NANOMATERIALS AND NANOSTRUCTURES FOR VARIOUS APPLICATIONS

Nanomateriale şi nanostructuri pentru diverse aplicații

NANOMATERIALS AND NANOSTRUCTURES FOR VARIOUS APPLICATIONS

EDITORS:

Gheorghe Brezeanu, Horia Iovu,
Cornel Cobianu, Dan Dascălu

EDITURA ACADEMIEI ROMÂNE

Bucureşti, 2012

The responsibility for originality and the contents of the articles lies exclusively with the authors.

Address: EDITURA ACADEMIEI ROMÂNE
Calea 13 Septembrie nr. 13, sector 5,
050 711, Bucureşti, România,
Tel. 4021-3188146, 4021-3188106
Fax: 4021-3182444
E-mail: edacad@ear.ro
Internet: http://www.ear.ro

Peer reviewers: Prof. Adrian Rusu, Prof. Dragoş Dobrescu

Descrierea CIP a Bibliotecii Naţionale a României

Nanomaterials and Nanostructures for Various Applications /
editors: Gheorghe Brezeanu, Horia Iovu, Cornel Cobianu,
Dan Dascălu - Bucureşti : Editura Academiei Române, 2011
ISBN: 978-973-27-2169-8

I. Gheorghe Brezeanu (ed.)
II. Horia Iovu (ed)
III. Cornel Cobianu (ed.)
IV. Dascălu, Dan (ed.)

62.002.3:539.24
539.26:621.9

Editorial assistant: Mihaela Marian
Computer operator: Elena Trică
Cover: Elena Trică

Passed for press: 03.2012. Size: 16 / 70 × 100.
Printed sheets: 16.5
D.L.C. for large libraries: 621.38.032; 007
539.23.08
for small libraries: 62.38

CONTENTS

FOREWORD 7

HIGH-K DIELECTRICS IN NANO & MICROELECTRONICS
G. BREZEANU, M. BREZEANU, F. BERNEA 9

A MICROWAVE FIELD EFFECT TRANSISTOR BASED ON GRAPHENE
M. DRAGOMAN, G. DELIGEORGIS, D. NECULOIU, D. DRAGOMAN, G. KONSTANTINIDIS, A. CISMARU, R. PLANA 23

CARBON-BASED NANOMATERIALS. ENVIRONMENTAL APPLICATIONS
A.C. ION, I. ION, A. CULETU 31

NOVEL CONCEPTS FOR CO_2 DETECTION BY DIFFERENTIAL RESONANT NANOSENSING
B. SERBAN, C. COBIANU, C. BOSTAN 57

SOLAR ENERGY MATERIALS OBTAINED BY SPRAY PYROLYSIS DEPOSITION
A. DUTA, D. PERNIU, L. ISAC, A. ENESCA 73

CONDUCTING POLYMERS FUNCTIONALIZED CARBON NANOTUBES FOR APPLICATIONS IN THE RECHARGEABLE LITHIUM BATTERIES
M. BAIBARAC, I. BALTOG, T. VELULA, P. GOMEZ ROMERO, S. LEFRANT 103

SOI BY SMART-CUT. TEM-HRTEM CHARACTERIZATION OF STRUCTURAL DEFECTS INDUCED IN Si BY PLASMA HYDROGENATION
C. GHICA, L.C. NISTOR 123

SPECTROSCOPY AND *AB INITIO* STUDIES OF OPTICAL TRANSITIONS IN NANOSTRUCTURED ZNO
*R. PLUGARU, A. DINESCU, F. COMANESCU, M. PURICA, S. MIHAIU, E. VASILE, N. PLUG*ARU 139

NANOSTRUCTURED, FUNCTIONAL FILMS PREPARED USING THERMIONIC VACUUM ARC
C.P. LUNGU, I. JEPU, I. MUSTATA, V. KUNCSER, V. IONESCU, V. CIUPINA, M. OSIAC, G.E. IACOBESCU 163

THE EUKARYOTE CELL INTERACTION WITH DOPED TiO_2 NANOPARTICLES

G.C. CORNEANU, C. CRĂCIUN, M. CORNEANU, C. LAZĂU, I. GROZESCU, S. TRIPON ……..……. 173

Ge NANODOTS EMBEDDED IN A SILICA MATRIX

I. STAVARACHE, A.-M. LEPADATU, M. L. CIUREA 193

DEFECT ASSISTED LOCALIZATION OF Mn^{2+} ACTIVATING IONS IN THE CORE OF THE ZnS QUANTUM DOTS

S.V. NISTOR, M. STEFAN, L.C. NISTOR, D. GHICA C.D. MATEESCU ….……..…… 213

GROWTH AND CHARACTERIZATION OF ULTRATHIN Fe MAGNETIC LAYERS DEPOSITED ON ATOMICALLY CLEAN Si(001) BY MOLECULAR BEAM EPITAXY

N.G. GHEORGHE, M.A. HUSANU, G.A. LUNGU, D. MACOVEI, V. KUNCSER, R.M. COSTESCU, D.G. POPESCU, C.M. TEODORESCU ……..... 225

MAGNETIC NANOCLUSTERS SYNTHESIZED BY A NOVEL METHOD OF AGGREGATION IN ULTRA HIGH VACUUM; APPLICATIONS IN NANOELECTRONICS AND NANOMEDICINE

O. CRISAN, A.D. CRISAN …….....…….……. 245

FOREWORD

This volume from the *Micro-and nanoengineering* series, edited by the Romanian Academy is containing papers related to selected presentations at the 9th National Seminar of Nanoscience and Nanotechnologies (16th of March, 2010, Romanian Academy).

We are briefly presenting below the content of the this volume.

The first group of papers is focused on a few application domains. One paper is related to materials (dielectrics) devoted to nanoelectronics, whereas the second one is reporting realization of graphene transistors.

Another couple of papers is devoted to nanomaterials related to environmental applications and to gas nanosensors, respectively.

The third couple of papers is related to energy: materials for solar energy, and nanomaterials for rechargeable lithium batteries, respectively.

The largest number of papers in the volume, however, are related to nanomaterials and their fabrication and characterization. Nanoparticles and nanodots are considered, whereas the last three papers are devoted to magnetic materials.

The content of the volume, with contributors from Romania, reflects the great progress made in infrastructure during the last years: state of the art equipments are now available in Romanian laboratories. The multidisciplinary character of the research reported in the papers is also obvious from the affiliation of coauthors.

Altogether, this new volume reflects the progress in the *nano* field in this country.

November 2011 *The editors*

High-K Dielectrics in Nano&Microelectronics

G. BREZEANU[1], M. BREZEANU[2], F. BERNEA[3]

[1]University "POLITEHNICA" Bucharest,
Splaiul Independentei 313, 040011, Bucharest, Romania
[2]Engineering Department, University of Cambridge,
9 JJ Thomson Avenue, Cambridge CB3 0FA, UK
[3]Carpatcement Holding, Romania

Abstract. For CMOS applications, as device scaling, obeying Moore's law reduces the active area of the devices to nearly atomic dimensions. The high-k dielectrics need to be used to prevent the tunnelling effects which increase the leakage currents. These insulators are also important for enabling high-performance nanoelectronic transistors built on high-mobility materials, such as diamond, carbon nanotubes or silicon carbide (SiC).

One of the major issues to be addressed when coming to power devices is the choice of the appropriate termination. An already, classical implementation of the field plate technique, widely used for Si, SiC and diamond power diodes, is the oxide ramp termination. This method requires the presence of a dielectric ramp smaller than 10º, etched around the anode, which assures the smoothness of the electric field at the contact's periphery. The main limitation of this termination is a premature oxide breakdown which is a killing factor for the yield. The paper presents improvements in the efficiency of this termination for Schottky Barrier Diodes (SBDs) on SiC and diamond, using high-k dielectrics. These insulators can reduce both the oxide and the surface semiconductor electric field.

Introduction

In recent years, several emerging high-k materials have attracted enormous attention as potential candidates for electronic devices. Silicon dioxide (SiO_2) has been used as dielectric for more than 40 years because of its manufacturability and ability to deliver continued transistor performance improvements as it has been made ever thinner [1-10].

Over decades of incremental improvements to CMOS processing, the limitations of the SiO_2 gate dielectric layer have hung over the silicon industry as its single biggest technical challenge [1-15].To improve MOS transistor

performance in the past, chip manufacturers have shrunk the thickness of the gate dielectric to as little as five atomic layers (1.2 nm). Although this has helped transistors reach very high speeds, the problem is that these very thin layers of SiO_2 tend to leak a lot of current, resulting in energy waste and a build-up of heat. In addition, SiO_2 thickness uniformity across a 12 inch wafer imposes even more crucial difficulty in the growth of such a thin film, since even a mono-layer difference in thickness represents a large percentage difference and thus can result in the variation of threshold voltage across the wafer [4]. Reliability also becomes a huge concern for a very thin layer SiO_2 film.

Intel have been integrated into a manufacturable 45nm process a combination of a high-k dielectric based on hafnium and a new metal gate material compatible with hafnium will reduces source-drain leakage substantially [1,9-10]. Gordon Moore described this new approach, as the *"biggest change in transistor technology since the introduction of polysilicon gate MOS transistors in the late 1960s"[10]*.

IBM has come up with a slightly different solution to the leakage problem, but is also using a high-k dielectric gate, [10].The latest developments at Intel and IBM will help III-V devices penetrate new markets, by instigating greater convergence of the compound and silicon industries. High-k dielectric is at the centre of this, and high-k compound semiconductor MOSFETs will be able to leverage the millions of man years of silicon circuit designs, [10].

Actually, there is an increasing interest in the use of wide band-gap semiconductors, such as silicon carbide (SiC) and diamond, for power switching, power conversion, motor drives and military and consumer electric vehicles [16-22]. An issue related to the design of SiC or diamond devices is the junction discontinuity at the sharp corners of the electrodes. These results in noticeable increase of the maximum electric field in semiconductor bulk compared with its one dimensional value. These field peaks can be reduced using edge terminations surrounding the electrodes periphery [16-17]. Field plate termination is widely used in power devices design due to a less complicated fabrication process. We proposed and already tested on Si, SiC and diamond diodes a simple, low temperature, field plate termination based on a small angle etching of a dielectric deposed around the anode contact [18-22].

The paper presents enhancements in this termination for Schottky barrier diodes (SBDs) on SiC and diamond, using high-k dielectrics. The use of high-k materials allows for the reduction of the electric field at the corner by minimizing the recess without losing electrode control.

Scaling limits of SiO_2

The prosperity of modern integrated circuits has been realized with continuous shrinkage of MOS transistors (Fig. 1). Miniaturization of transistors has not only

increased package densities, but also accelerated circuit speed and reduced power dissipation [1-15].

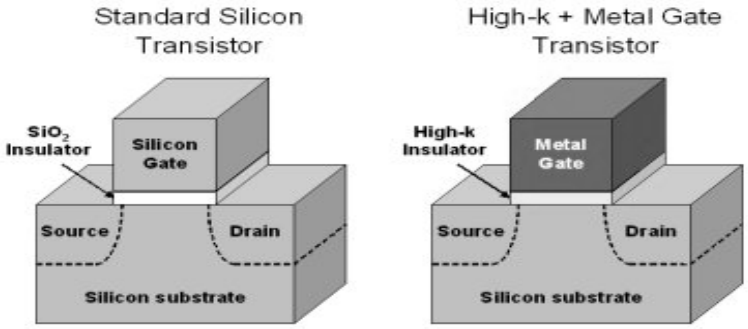

Fig. 1. MOS transistor structure with dielectric gate [10].

These improvements were achieved by scaling down of physical thickness of the gate dielectric (T_{ox}) and gate length (L_{GATE}). As shown in Fig.2, scaling of L_{GATE} and T_{ox} is slowing with technology nodes [6]. Fig. 3 plots channel length divided by gate oxide thickness for Intel's process technologies over the past 20 years [6]. Each data point represents a process technology, which was used to fabricate Intel's leading-edge microprocessors. A simple relationship between oxide thickness and the minimum channel length set by short channel effects is observed. Thermally grown silicon oxide (SiO_2) has been used as gate dielectric because it offers many desirable properties such as: an excellent interface, thickness controllability, high thermal stability and good reliability [2-4].

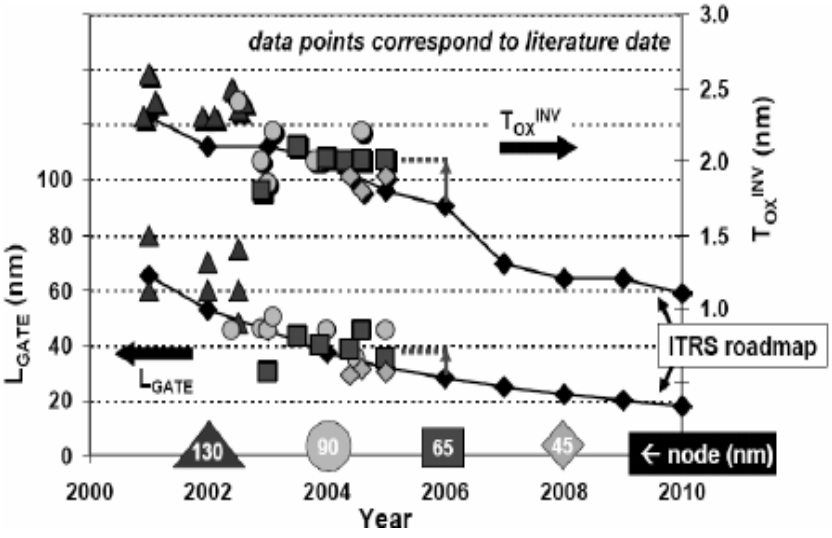

Fig. 2. Scaling trend of gate length and oxide thickness (ITRS International Technology Roadmap for Semiconductors) [6].

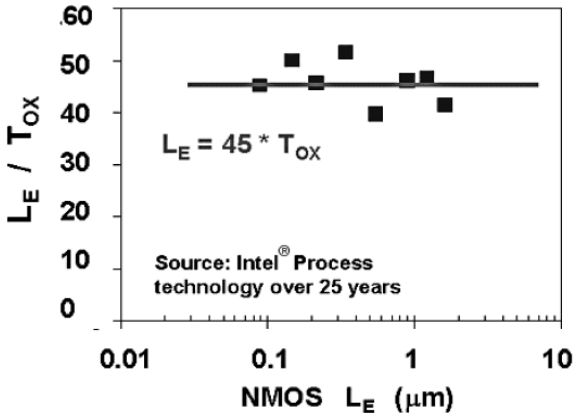

Fig. 3. Channel length to gate oxide thickness ratio versus channel length for some Intel process technologies [6].

For new CMOS nanotechnology (L_{GATE}< 90nm) SiO_2 has reached its physical limitations: higher leakage current and reliability concerns. A physical thickness of 11-15Å is so thin that electrons can directly tunnel through the oxide, resulting in excessively high gate leakage current. The forecasted leakage current is shown in Fig. 4 [5]. High leakage is a great concern, particularly for low power requests, and high performance applications as well. Due to the increase in the gate leakage, static power can exceed the active power as shown in Fig. 5, [6]. To reduce the increase in active power, V_{DD} needs to be reduced as well.

But as seen in Fig. 6 [6], V_{DD} is also falling behind the roadmap targets thus limiting the reduction of active power and increasing the electric field across the gate oxide, which decreases the reliability of the gate oxides.

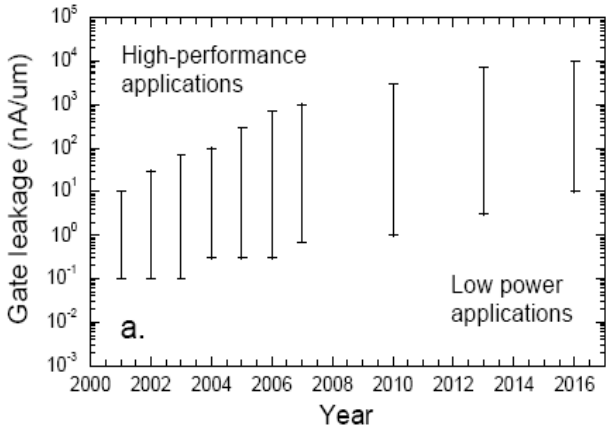

Fig. 4. The predicted range of acceptable gate leakage current over the years; the upper limit represents high performance and the lower limit represents low power applications [5].

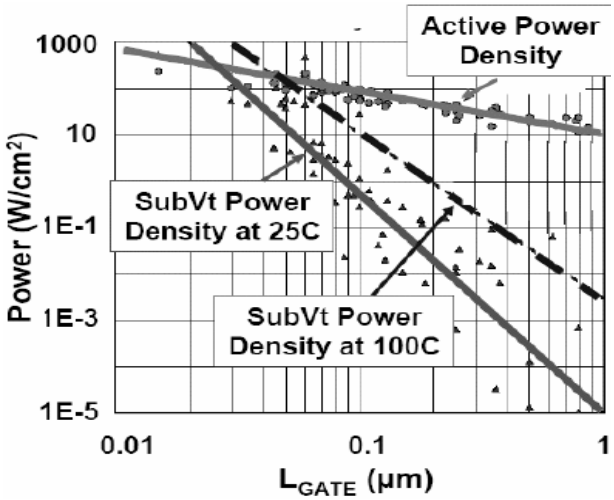

Fig. 5. Active and static power increase with scaling of L_{GATE}.

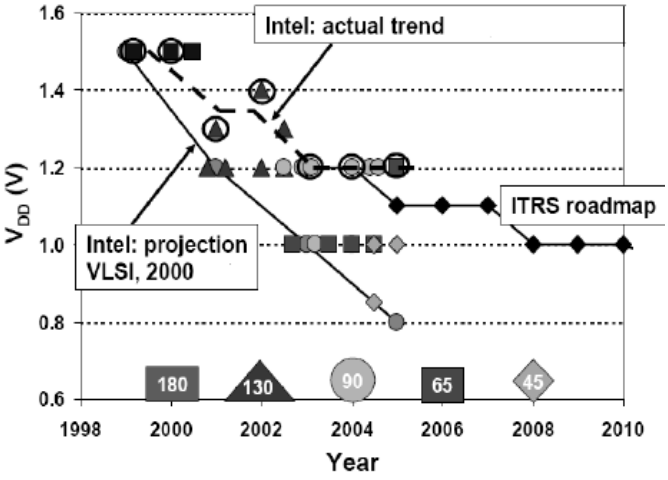

Fig. 6. Scaling of V_{DD} with technology nodes [6].

High-*k* dielectrics

High-*k* gate dielectrics have been studied as alternative gate dielectrics for the 65nm CMOS technology (Fig. 1) and beyond to replace conventional SiO_2 or silicon oxynitrides (SiO_xN_y). The requirements for high-k dielectric applications are [5]:

- high dielectric constant and large band gap
- high band offset with electrodes

- ❖ thermally and chemically stable in contact with semiconductor substrate
- ❖ scalable equivalent oxide thickness EOT < 10Å
- ❖ compatibility with gate electrode material
- ❖ density of interface states comparable to SiO_2
- ❖ low lattice mismatch and similar thermal expansion coefficient with Si
- ❖ mobility comparable to SiO_2
- ❖ negligible capacitance-voltage hysteresis (< 20mV)
- ❖ good reliability (no charge trapping, high breakdown voltage etc.)

In Fig. 7, dielectric constants of high-k candidates were summarized [4, 11-14]. TiO_2 and barium strontium titanate (BST) showing profoundly higher permittivity, were reported not to be thermally stable with silicon substrates [4]. It is worth mentioning that high-k dielectrics such as BST do not seem to be appropriate since the very high dielectric constant causes field induced barrier lowering (FIBL) which degrade short channel effects of MOS transistor [4]. A high density of surface states has been reported for $Al_2 O_3$.

In general, with the increase of the metal atomic number, the metal ionic radius increases, but the cohesive force decreases in the metal oxide, and results in a large dielectric constant. The bandgap energy decreases related to the dielectric constant [8].

$$E_G \propto \left(\frac{3}{2+\varepsilon_k} \right)^2 \tag{1}$$

Fig. 8 shows the bandgap and dielectric constant of some dielectric materials [7]. The inverse relationship suggested by above Eq. (1) is clearly demonstrated.

A narrow bandgap results in smaller energy band offsets with Si. Band offsets of high-k dielectrics with the conduction band edge (Φ_{Be}) and valence band edge Φ_{Bh} of Si is compared in Fig. 9 [4, 15]. The higher band offset indicates that the carrier generation and conduction can be minimized. A band offset less than 1.0 eV may lead to an unacceptably large leakage current. This current is more likely to be governed by direct tunneling current given by [4]:

$$J_{e(h)} = \frac{A}{T_k^2}\left[\left(\Phi_{Be(h)} - \frac{V}{2}\right)\cdot\exp\left(BT_k\sqrt{\Phi_{Be(h)} - \frac{V}{2}}\right) - \left(\Phi_{Be(h)} + \frac{V}{2}\right)\cdot\exp\left(BT_k\sqrt{\Phi_{Be(h)} + \frac{V}{2}}\right)\right] \tag{2}$$

where:

$$A = \frac{q^2}{2\pi h} \qquad B = \frac{4\pi}{h}\sqrt{2m^* q}$$

T_k is dielectric thickness and q, m^*, and h represent electron charge, effective mass of electron, and Plank's constant, respectively. Therefore, the leakage current

depends significantly on band offsets and to oxide thickness. Based on the band offset in Fig. 9, Ta_2O_5, which has been studied widely for the application in DRAM storage capacitors appears to be unsuitable for the gate electrode application. Al_2O_3 and Si_3N_4 have too low k to be used for several generations as shown in Fig.7-9. Among these materials, HfO_2 has been shown to be compatible with: poly-silicon gate, poly-SiGe and TaN gates [4]. In contrast, ZrO_2 has been reported that it was not compatible with poly-Si gate due to the reaction of Zr with poly-Si gate [4].

If a high-k dielectric can replace SiO_2, the dielectric thickness (T_k) increases proportionally to keep the same dielectric capacitance. A figure of merit to judge a high-k gate dielectric layer is the equivalent oxide thickness, defined as [2-8]

$$EOT = \frac{\varepsilon_{ox}}{\varepsilon_k} T_k \tag{3}$$

where $\varepsilon_{ox}/\varepsilon_k$ is the ratio of relative oxide and high-k dielectric permittivity, respectively. Since a thicker layer is used for insulating, the tunneling current is drastically reduced. However, a new high-k material can be integrated into the present ULSI process. In Fig.10 the expected EOT evolution for these processes is shown [5]. The upper limit corresponds to high performance and the lower limit denotes low power applications [5]. MOSFETs with HfO_2 dielectrics and TaN gate showed very low EOT and low leakage current even after the conventional CMOS process flow [9-10]. Considering the cost of development and implementation, HfO_2 gate dielectric needs to span two or three generations from the 65 nm to the 32 nm design rule. To meet the requirements for these generations, EOT should be scaled down to less than 10A while suppressing leakage current to below 1mA/cm^2 (Fig. 11), [9]. A combination of a high-k dielectric based on hafnium and a secret new metal gate material compatible with hafnium will cut gate leakage current density by more than 500 times (Fig. 11). The dielectric's high k value compensates for the thinning of the dielectric in smaller process geometries. A thinner dielectric enables higher drive and thus allows transistors to switch faster.

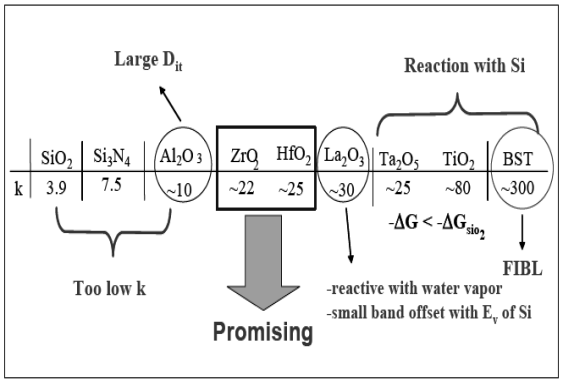

Fig. 7. Dielectric constant of some high-k dielectrics [4,11-14].

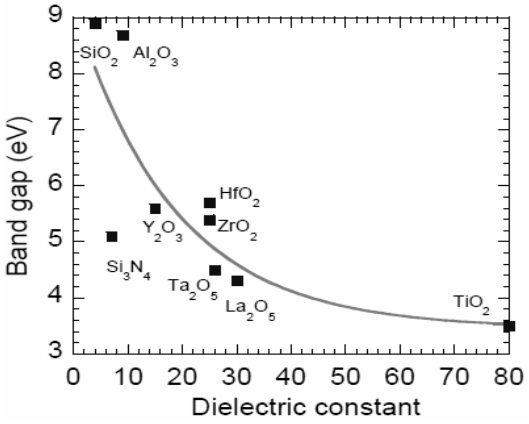

Fig. 8. Band gap dependence versus dielectric constant of some high-k dielectrics [4,11-14.

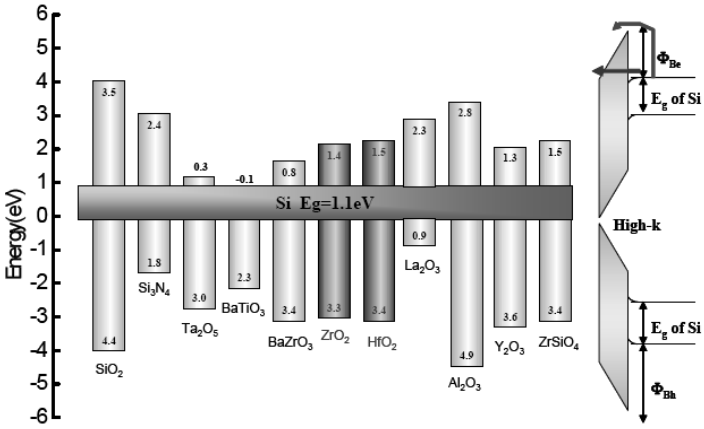

Fig. 9. Band offset of gate dielectric candidates with conduction band edge and valence band edge of Si substrate [4,15].

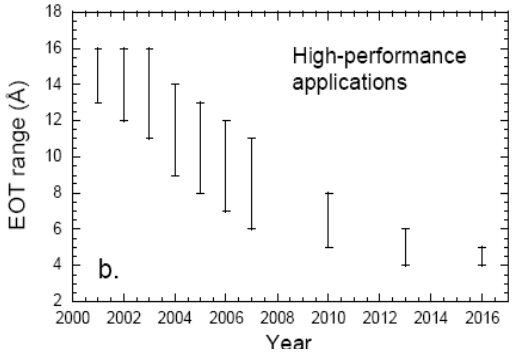

Fig. 10. The predicted evolution of equivalent oxide thickness [5].

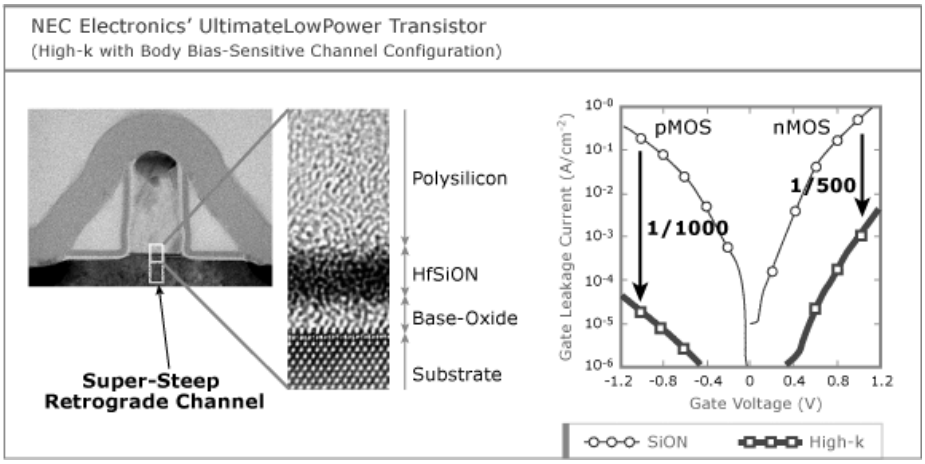

Fig. 11. Nano- MOS structure with high-k dielectric [9].

SiC and Diamond Electronics Devices With High-k Dielectrics

Wide band gap semiconductors such as diamond and SiC are the promising materials for new power devices. Over the last two decades, significant advances in the growth, doping, and processing technologies of these materials have been accomplished opening new promise for high power electronics. In real devices, the breakdown voltage of the devices is always less than that predicted by theory, since the material is not perfect (crystal defects) and the electric field is crowding at the electrode corner [16-22].

These high fields can be relieved by using edge termination surrounding the electrode periphery. An effective edge termination makes the electric field distribution uniform in the bulk and at the electrode corner and take the breakdown capability of the device closer to its theoretical limit. Traditionally, techniques like field plates, floating guard rings and junction termination extensions have been used [16-17].

We have already proposed the oxide ramp termination, an original implementation of the field plate concept, previously widely used for Si, SiC and diamond (Dia) diodes. This termination, shown in Fig. 12 for a Schottky Barrier diode (SBD), is based on a field plate overlapping on oxide ramp at the periphery of the device main electrode contact. The oxide ramp termination is acknowledged by the international community as a highly efficient termination for power devices [16-22]. In this paper, the high-k insulators are used with the ramp oxide termination of SiC and diamond diodes.

For power devices, due to the high voltages employed, the dielectric breakdown might appear before the semiconductor one. The use of alternative insulators, with high dielectric constants will reduce the electric field within the oxide and, as a

consequence, the risk of premature dielectric breakdown. In order to emphasize the effect of varying the relative permittivity (ε_r) on the performance of ramp oxide terminated structures, extensive simulations were performed on SiC and diamond diodes. In order to avoid dielectric breakdown, the maximum electric field in the oxide (E_{OX}), has to be lower than 5-6MV/cm, acceptable operating fields for high-k dielectrics like Si_3N_4, Ta_2O_5 or HfO_2 (the later having the highest product between the dielectric constant and the maximum electric field). The increase of ε_r not only reduces E_{OX}, but also improves the breakdown voltage (BV) of the diodes. The termination efficiency (η), defined as the ratio between the achieved BV and the ideal one, significantly increases for larger ε_r, regardless of the ramp angle.

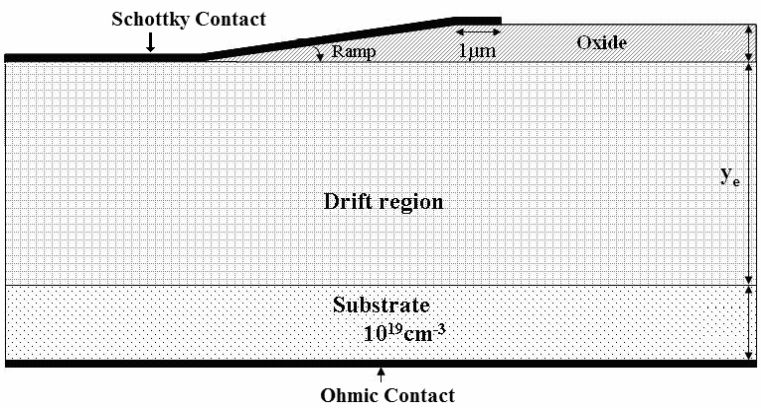

Fig. 12. Schottky barrier diode (SBD) with oxide ramp termination.

Fig. 13 presents the electric field distribution at the semiconductor surface for both SiC and Dia SBDs, having the same doping level in the drift layer ($7x10^{15}cm^{-3}$). Two peaks, are observed: one at the beginning and one at the end of the ramp. For both materials, the increase of ε_r results in a severe reduction of the field peak at the start of the ramp. An increase of the overall electric field at the interface and, a smooth electric field distribution at the Schottky contact and along of the oxide-semiconductor interface can be observed at higher permittivity. This is due to the increase of the voltage drop on the semiconductor when insulators with high permittivity are used.

Consequently, an increase of the termination efficiency is obtained. For SiC SBDs, the efficiency of termination increases strongly with ε_r, up to 96% (Fig.14). In the case of Dia, the effect of the insulator permittivity is reduced, mainly due to the much lower doping of the drift layer (used in these simulations), and the termination efficiency is around 92%. A mild decrease of the efficiency is observed for high permittivity value.

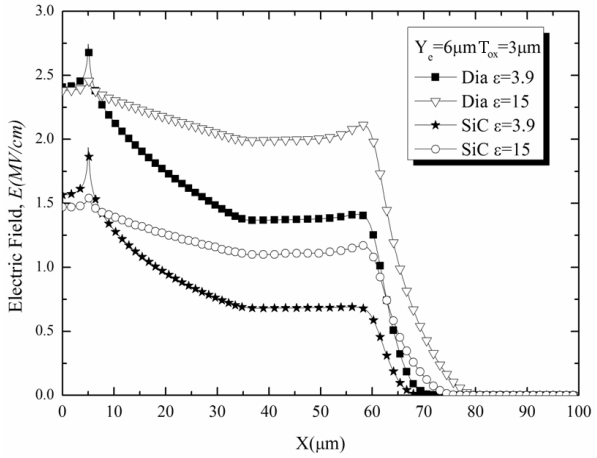

Fig. 13. Electric field along the interface Dia and SiC SBDs with the same drift doping.

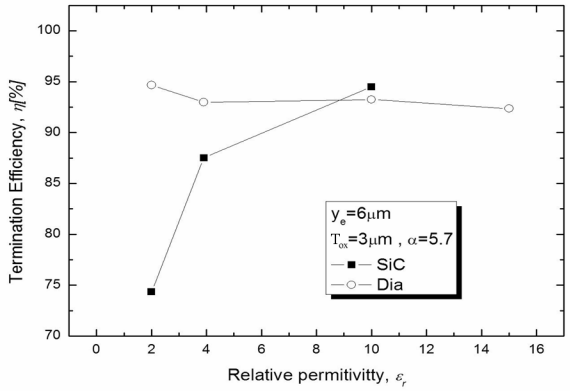

Fig. 14. Termination efficiency vs. dielectric relative permittivity for SiC and Dia SBDs.

Another important benefit of the relative permittivity growth is that the ramp angle can be increased up to 10^0, without affecting the value of the efficiency. This has a direct influence on the area consumption, taking into account the fact that the larger the angle, the smaller the area needed for the termination.

In order to confirm the predictions of the theoretical study presented above, a comparison between the performances of the Schottky diodes, when employing SiO_2 and Si_3N_4 as insulators for the ramp termination, was performed in Fig.15.The ramp angle was kept constant (5.7^0), while the thickness of the dielectric was varied in the range 0.5-5μm. The Si_3N_4 ramps show better performances both in terms of termination efficiencies and maximum electric field in insulator (Fig. 15). A very high efficiency of 95% can be obtained for this diode using the silicon

nitride for ramp termination (Fig. 15a).The fact that η is very high and practically constant with T_{OX}, enables the design to be focused only on reducing E_{OX}, which falls below the acceptable maximum for thicknesses larger than 3.5μm (Fig. 15b).

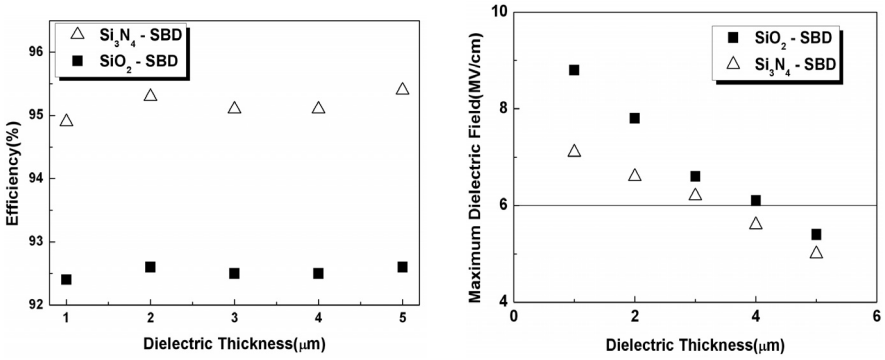

a) b)

Fig. 15. Comparison between SiO_2 and Si_3N_4 SBDs on SiC from the point of view of (a) termination efficiency and (b) maximum electric field in the dielectric.

We have also analyzed the impact of using two high-*k* dielectrics, (Si_3N_4 and HfO_2), as insulators for the ramp termination on diamond Schottky structures (Fig.16). As expected, the electric field in the dielectric decreases at breakdown when using high-*k* dielectrics (Fig.16b). Values of the maximum dielectric field comparable to the operational field are obtained for HfO_2 ramps with insulator thicknesses in excess of 3.5 μm. For these structures, the risk of premature dielectric breakdown is minimum. The price to pay for this improvement in reliability is a small degradation of the electrical performances of the termination. The efficiency drops by 5–7% to 85–87% when using HfO_2 instead of SiO_2 (Fig.16a), still high enough for a competitive termination structure.

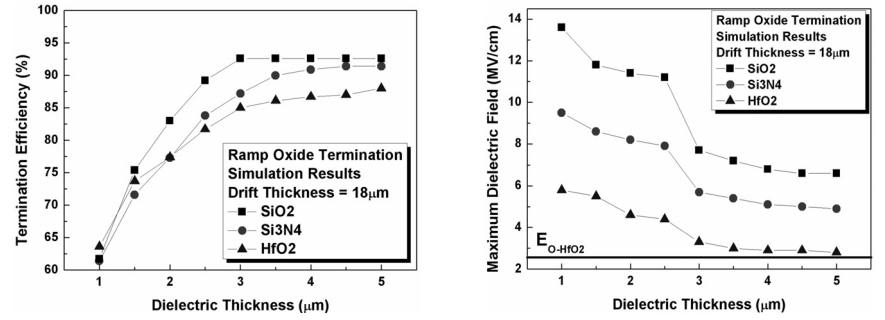

a) b)

Fig. 16. Oxide ramp termination with SiO_2, Si_3N_4 and HfO_2 for SBDs on diamond (a) termination efficiency and (b) maximum electric field in the dielectric.

Conclusions

The requirement of high performance, high reliability, high package density along with low voltage and low power application for submicron CMOS technology and device scaling has acted as the driving force. A continuing scaling down of the MOS device with the minimum feature size bellow 90 nm requires EOT less than 15 Å. A physical thickness of only some atomic layers of traditionally gate insulator (SiO_2) creates several problems. Electrons can directly tunnel through the SiO_2, resulting in excessively high gate leakage current. To solve this critical issue SiO_2 has been replaced with a thicker high-*k* material as HfO_2, in the gate dielectric, clamming reduction in leakage by more than two orders of magnitude.

The possibility of using high-k dielectrics for field plate terminations of Schottky on SiC and diamond in order to avoid a possible premature dielectric breakdown was investigated, too.

A high efficiency oxide ramp termination based on high-*k* insulators has been extensively studied. For SiC SBDs, the efficiency of termination increases strongly with relative permitivity, up to 96%. In the case of Dia, the effect of the insulator permittivity is less significant, and the termination efficiency is around 92%.

With an HfO_2 ramp, the premature dielectric breakdown risk can be avoided for dielectric thicknesses larger than 3.5 μm for diamond and SiC Schottky devices. A comparison between SiO_2 and Si_3N_4 ramps for SBDs on SiC showed that the latter exhibits superior performances.

In conclusion, high-k dielectrics are highly recommended for SiC devices, but have a lower impact in the case of low doping diodes on diamond.

References

[1] MUSCULAR Ann Stafford, *Intel, IBM embrace high-k metal gates for 45nm*, Electronic Weekly, January 2007.

[2] AGRAWAL R., *Fabrication, Characterization and Hall Mobility Analysis of MOS Devices with Low K and High K Dielectric Materials*, Thesis for degree of Master of Science in Electrical Engineering , University of Texas at Arlington, 2006.

[3] OK I., *A Study on Electrical and Material Characteristics of Hafnium Oxide with Silicon Interface Passivation on III-V substrate for Future Scaled CMOS Technology*, PhD Dissertation, University of Texas at Austin, 2008.

[4] KANG C., *A study on the material and device characteristics of hafnium oxynitride MOSFETs with TaN gate electrodes*, PhD Dissertation, University of Texas at Austin, 2004.

[5] NIEH R.E., *An evaluation of the electrical, material, and reliability characteristics and process viability of ZrO_2 and ZrO_xN_y for future generation MOS gate dielectric*, PhD Dissertation, University of Texas at Austin, 2002.

[6] AKBAR M.S., *Process Development, Characterization, Transient Relaxation, and Reliability Study of HfO_2 and $HfSi_xO_y$ Gate Oxide for 45nm Technology and Beyond*, PhD Dissertation, University of Texas at Austin, 2005.

[7] SCHAEFFER J.K., *Hafnium Dioxide Gate Dielectrics, Metal Gate Electrodes, and Phenomena Occurring at their Interfaces*, PhD Dissertation, University of Texas at Austin, 2004.
[8] YANG X., *Issues In Front-End Engineering Of Cmos Nanoelectronics*, PhD Dissertation, University of Texas at Arlington, 2007.
[9] *High-k Transistor, advanced process technology*, NEC Electronics Corporation , 2005.
[10] *IBM and Intel make high-k gate breakthrough*, Compound semiconductor net, 2007.
[11] SHANNON R.D., *Dielectric polarizabilities of ions in oxides and fluorides*, J. Appl. Phys., **73**(1), p. 348, 1993.
[12] WILK G.D., WALLACE R.M. and ANTHONY J.M., *Hafnium and zirconium silicates for advanced gate dielectrics*, J. Appl. Phys., **15**(1), p. 484, 2000.
[13] EZHILVALAVAN S. and TSENG T., *Conduction mechanisms in amorphous and crystalline Ta_2O_5 thin films*, J. Appl. Phys., **83**(9), p. 4797, 1998.
[14] PARK Donggun, KING Ya-chin, LU Qiang, KING Tsu-Jae, HU Chnming, KALNITSKY Alexander, TAY Sing-Pin, and CHENG Chia-Cheng, *Transistor Characteristics with Ta_2O_5 Gate Dielectric*, IEEE Electron Device Letters, **19**, p. 441, 1998.
[15] ROBERTSON John, *Band offsets of wide-band-gap oxides and implications for future electronic devices*, Journal of Vacuum Science & Technology B:Microelectronics and Nanometer Structures, **18**(3), p. 1785, 2000.
[16] TARPLEE M.C., MADANGAGLY V.P., ZHANG Q., SURDARSHAN T.S., *Design Rules for Field Pate Edge Termination in SiC Schottky Diodes*, IEEE Trans. El. Dev., **48**, p. 2659, 2001.
[17] SHERIDAN D.C., NIU G., MERRETT J.N., CRESLLER J.D., ELLIS C., TIN C.C., *Design and Fabrication of Planar Guard Ring Termination for High Voltage SiC Diodes*, Solid St. Electron., **44**, p. 1367, 2000.
[18] BREZEANU G., BADILA M., BREZEANU M., UDREA F., BOIANCEANU C., ENACHE I., DRAGHICI F., VISOREANU A., *Breakdown performances improvements of SiC diodes using high–k dielectrics*, in Proc. of the 28nd International Semiconductor Conference, p. 357, 2-4 Oct., Sinaia, Romania, 2005.
[19] BREZEANU M., BADILA M., BREZEANU G., UDREA F., BOIANCEANU C., AMARATUNGA G.A.J., ZEKENTES K., *An Effective Field Plate Termination for SiC Devices Based on High-k Dielectrics*, in Proc. of International Conference on Silicon Carbide and Related Materials-ICSCRM, p. 21, 18-23 Sept, Pittsburg, USA, 2005.
[20] BREZEANU M., AVRAM M., RASHID S.J., AMARATUNGA G.A.J., BUTLER T., RUPESINGHE N.L., UDREA F., TAJANI A., DIXON M., TWITCHEN D.J., GARRAWAY A., CHAMUND D., TAYLOR P., BREZEANU G., *Termination Structures for Diamond Schottky Barrier Diodes*, in Proc of the 18th International Symposium on Power Semiconductor Devices and ICs (ISPSD 2006**)**, p. 73, 4-8 June, Napoli, Italy, 2006.
[21] BREZEANU M., BUTLER T., RUPESINGHE N.L., AMARATUNGA G.A.J., RASHID S.J., UDREA F., AVRAM M., BREZEANU G., *Ramp Oxide Termination Structure using High-k Dielectrics for High Voltage Diamond Schottky Diodes*, Diamond and Related Materials, **16**, p. 1020, 2007.
[22] BREZEANU G., BREZEANU M., BOIANCEANU C., UDREA F., AMARATUNGA G.A.J., GODIGNON P., *Impact of High-k Dielectrics on Breakdown Performances of SiC and Diamond Schottky Diodes*, Material Science Forum, **600-603**, p. 983, 2009.

A Microwave Field Effect Transistor Based on Graphene

M. DRAGOMAN[1], G. DELIGEORGIS [2], D. NECULOIU[3],
D. DRAGOMAN[4], G. KONSTANTINIDIS[2], A. CISMARU[1], R. PLANA[5]

[1]National Institute for Research and Development in Microtechnology (IMT), P.O. Box 38-160, 023573 Bucharest, Romania
[2]Foundation for Research & Technology Hellas (FORTH) P.O. BOX 1527, Vassilika Vouton, Heraklion 711 10, Crete, Hellas
3Politehnica University of Bucharest, Electronics Dept., 1-3 Iuliu Maniu Av., 061071 Bucharest, Romania
[4]Univ. Bucharest, Physics Dept., P.O. Box MG-11, 077125 Bucharest, Romania
[5]LAAS CNRS, 7 Avenue du Colonel Roche, 31077 Toulouse Cedex 4, France

Abstract. We present dc and microwave experiments on a graphene-based top-gate field effect transistor. The transistor is acting as an active device far from the Dirac point, and turns into a passive device at the Dirac point, the transistor amplification being suppressed due to lack of carriers. In this way, microwave switches can be implemented based on the specific charge carrier transport in graphene. The maximum stable gain of the transistor is maintained up to 9 GHz, and the mobility of graphene FET is greater than 8000 cm^2/Vs far from the Dirac point.

1. Introduction

Graphene is an atom-thick sheet of graphite consisting of a honeycomb lattice in which carbon atoms bond covalently with their neighbours. The dispersion relation of graphene is linear, and consists of two cones that touch in one point, which is called Dirac point and corresponds to zero energy. The density of carriers in graphene and the Fermi level are tuned by the gate voltage [1]. The microwave graphene FET is a very new transistor [2], [3]. The graphene physical properties such as: (i) ballistic transport at room temperature over a distance of 0.4 μm [3], (ii) intrinsic mobility of carriers of 44 000 $cm^2V^{-1}s^{-1}$ at room temperature [4], and (iii) tunable input impedances around 50 Ω, specific for RF applications, in microwave devices based on graphene [5], make this material a good candidate for very high frequency devices.

The graphene properties are summarized in the Table 1.

Table 1: Graphene properties

Parameter	Value and units	Observations
Mobility	40 000 $cm^2V^{-1}s^{-1}$	At room temperature (intrinsic mobility 200 $cm^2V^{-1}s^{-1}$ in suspended structures)
Mean free path (ballistic transport)	200- 300 nm	At room temperature
Fermi velocity	c/300=1000000 m/s	At room temperature
Thermal conductivity	5000 W/mK	Better thermal conductivity than in most crystals

In the graphene microwave FET, graphene is the channel between the drain (D) and the grounded source (S) contacts. The graphene FET transistor reported below is a top gate FET that has two parallel channels controlled by a single gate electrode (G) to enhance the drain current. The graphene FET is ended by coplanar lines (CPWs), the source electrode is formed from two ground electrodes of the CPWs, while the gate and drain electrodes are the central conductors of the CPWs. The graphene channel is isolated with respect to the top gates by a 200 nm thick PMMA layer. PMMA was selected as gate dielectric due to its high mechanical and thermal stability, high resistivity, of 2×10^6 Ωcm, a similar dielectric constant as SiO_2 (tan $\delta \cong 0.07$ and $\varepsilon_r \cong 3$ at 10 GHz [7]), and easy deposition on a prescribed area.

2. The Fabrication of the Graphene FET

The single-layer graphene sheet was supplied by Graphene Industries and was placed on top of a 300 nm SiO_2 layer that was grown on a high resistivity Si substrate (the resistivity of which is 8 kΩcm) using mechanical exfoliation techniques. The identification of the single layer graphene was done optically and/or using Raman spectroscopy by the company mentioned above. A SEM photo of the microwave FET transistor is presented in Fig. 1.

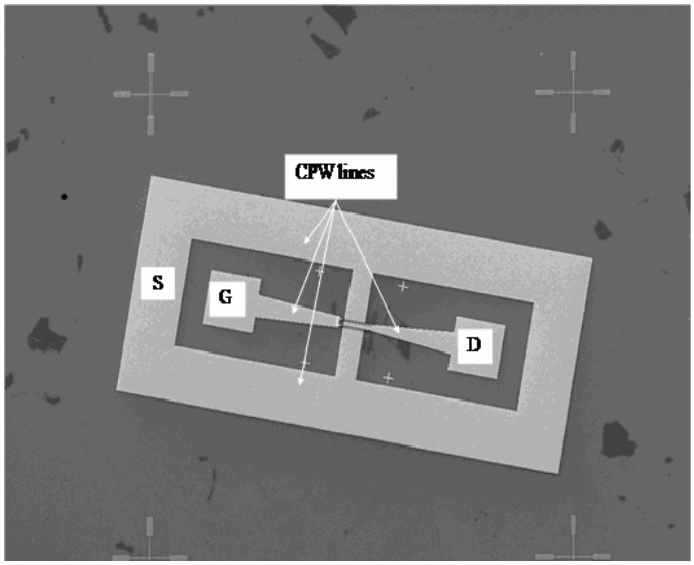

Fig. 1. The microwave graphene FET.

The graphene flake is first identified and mapped in SEM. Then, a set of alignment marks are located near each flake to enable precise alignment of subsequent metallization processes. The alignment marks and the subsequent metallizations were defined using standard e-beam bilayer PMMA lithography. Afterwards, 40 μm wide drain and source electrodes were defined using e-beam. Simultaneously, the CPW electrodes which end the graphene FET were patterned on the substrate. Finally, a 2 nm Ti/300nm Au metallization was evaporated using e-gun, the process being completed by lift-off in acetone. PMMA exhibits an image reversal effect if exposed to high electron doses, and this effect was utilized to get a stabilized PMMA that covers the area where the gate electrode was to be patterned. To complete the device, a fresh PMMA layer was deposited on the sample and a 200 nm thick gate was defined using the e-beam lithography technique. The same metallization, i.e. 2 nm Ti/300 nm Au, was also used to obtain the gate. The process was finalized by lifting off the excess metal in acetone. Acetone does not attack the stabilized PMMA layer during this step, so that the gate electrode can be placed on top of it. A SEM photo of the main area of the graphene FET is presented in Fig. 2. The dimensions of the transistor are: source-drain distance L = 2 μm, gate length L_G = 200 nm, and source/drain width W = 40 μm.

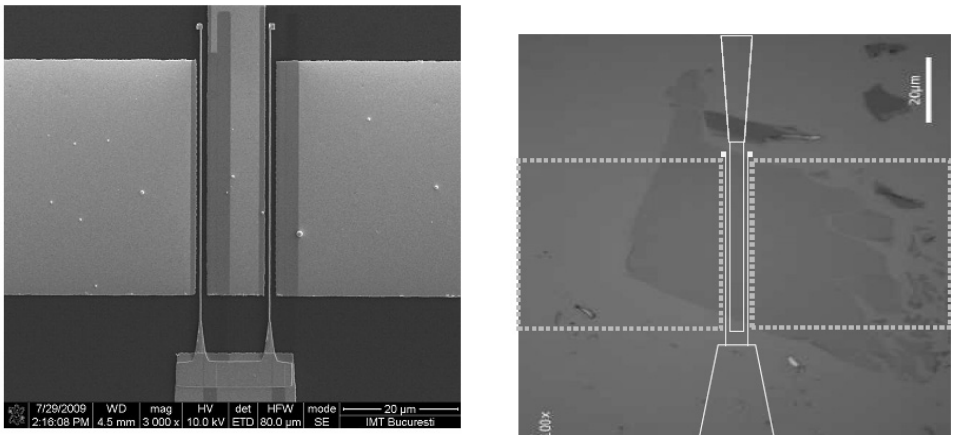

(a) (b)

Fig. 2. (a) SEM photo of the gate area of the graphene microwave FET (b) optical view of graphene with the marked lines of electrodes over it (not scaled).

3. DC and Microwave Characterization of the Graphene FET

We have first measured the dc characteristics of the graphene FET in order to find the Dirac point. The Dirac point displays a kink in the drain current versus drain voltage dependence, I_D–V_D, at a certain drain voltage [8]. Beneath the kink the conduction is unipolar, while at the kink it turns into ambipolar. In the ambipolar regime a pinch-off region travels between source and drain as V_D increases. In Fig. 3a we have displayed the $I_D - V_D$ dependence at $V_G = 2$ V. The kink that characterizes the presence of the Dirac point is located around $V_D = 4$ V. The mobility $\mu = (en)^{-1}(\partial I_D/\partial V_D)\times(L/W)$, where $n = 1.6\times10^{-11}$ cm^{-2} is the carrier concentration, is represented also in Fig. 3a. It can be seen that near the Dirac point the mobility decreases dramatically due to the recombination of carriers, but far from the Dirac point it becomes greater than 8000 cm^2/Vs. The drain current versus gate voltage characteristics, I_D–V_G, is displayed in Fig. 3b for $V_D = 2$ V. At positive gate voltages the charge transport is assumed by electrons, while whole transport takes place at negative gate voltages. The minimum value of the drain current occurs at the gate voltage associated to the Dirac point. In our case, the Dirac point is situated at $V_G = 0$ V. In Fig. 3b we have also shown the transconductance $g_m = \partial I_D / \partial V_G$, which attains a maximum value of 50 μS at a gate voltage of +1 V and has a minimum value of -200 μS around the gate voltage of -2 V. At the Dirac point, *i.e.* at $V_G = 0$ V, the transconductance almost vanishes.

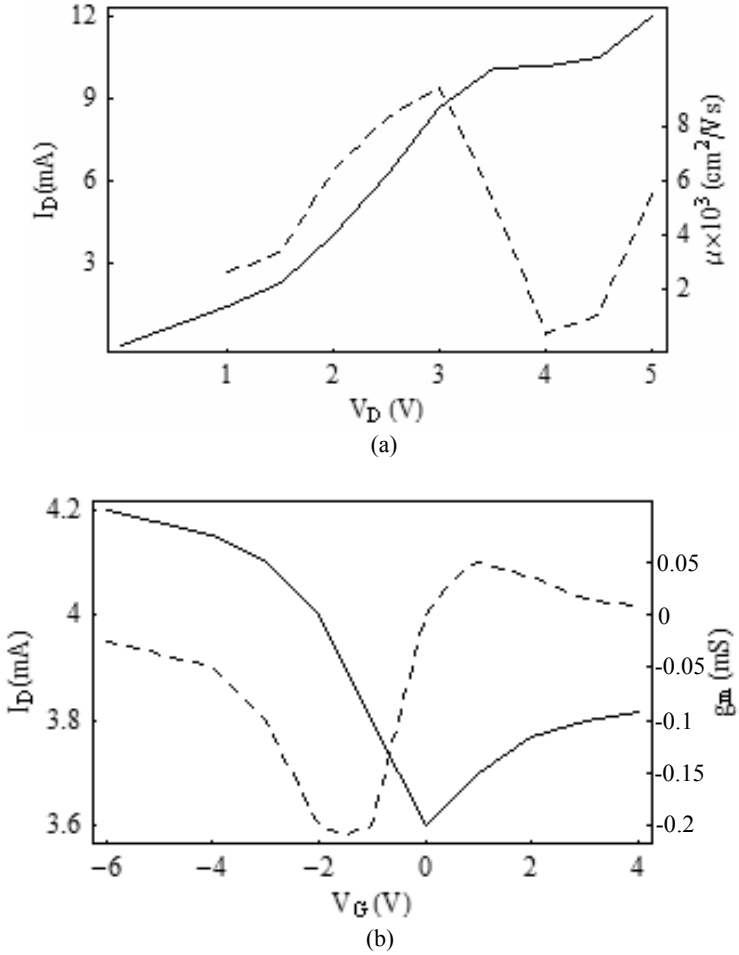

Fig. 3. (a) V_D dependence of I_D (solid line, left vertical axis) and mobility (dashed line, right vertical axis) at $V_G = 2$ V, and (b) V_G dependence of I_D (solid line, left vertical axis) and transconductance (dashed line, right vertical axis) at $V_D = 2$ V.

Working at the Dirac point is undesirable in dc because it worsens the dc parameters: the mobility decreases with orders of magnitude, while the transconductance vanishes and suppresses the FET graphene amplification, producing a quite strong reflection at the gate. However, tuning the drain and gate voltages of the FET graphene near and far from the Dirac point, its gain can be switched OFF and ON. The maximum stable gain, defined as MSG = $|S_{21}|/|S_{12}|$, is around 1 in the OFF state and greater than 1 in the ON state. To demonstrate this switching behavior we have measured the graphene transistor in the microwave spectral region. The measurements of the microwave graphene FET were performed directly on-wafer with a VNA-Anritsu-37397D connected to a

Karl–Suss PM5 on-wafer probe station. The system was calibrated with the SOLT calibration.

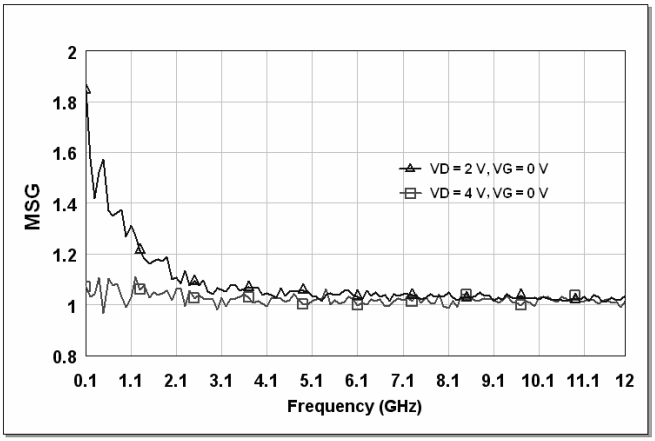

Fig. 4. Frequency dependence of the maximum stable gain at $V_G = 0$ V

In Fig. 4 the maximum stable gain of the microwave graphene FET at $V_G = 0$ is displayed at the drain-source voltages $V_D = 2$ V and 4 V. Two situations can be inferred from Fig. 4: the transistor behaves as a passive device with a MSG ≅ 1 for $V_D = 4$ V, i.e. at the Dirac point, and is an active (amplifying) device away from the Dirac point, for instance at $V_D = 2$ V. The amplification is present also for other drain-source voltages, of 1 V, 6 V and 8 V, but the results are not displayed here.

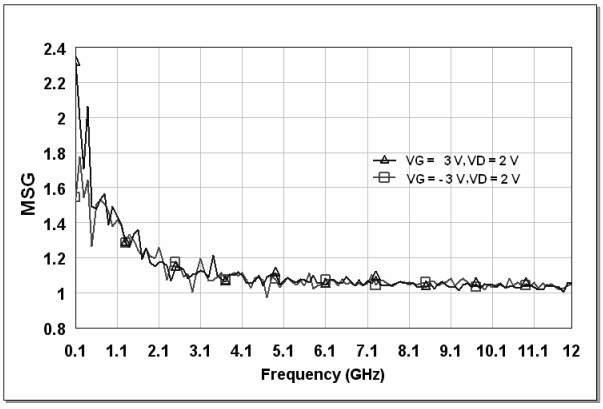

Fig. 5. Frequency dependence of MSG at $V_G \cong -3$ V and $V_G \cong +3$ V.

Far from the Dirac point, the maximum stable gain is almost the same if the polarization is reversed; for example, it is almost the same for $V_G \cong -3$ V and $V_G \cong +3$ V. The corresponding maximum stable gain is displayed in Fig. 5 for $V_D = 2$ V. The graphene transistor amplifies, i.e. has MSG>1, up to 9 GHz. From the results in Fig. 5 it follows that, away from the Dirac point, the microwave behavior of the device does not depend on the polarity of the gate voltage.

4. Conclusion

In conclusion, we have reported a graphene FET, which can switch its state in a reversible way from passive to active, when the drain and gate voltages are varied. This property will be further investigated and will be applied for designing microwave switches that are expected to have good performances taking into account that the switching time is less than 1 ns. Also, the cutoff frequency of the transistor, which is actually around 50 GHz, will be increased in further researches. Recent results [9], [10] have demonstrated that the intrinsic cutoff frequency ($f_c = g_m / 2\pi\, C_{gate}$) of the graphene FETs are exceeding 300 GHz. However, the extrinsic cutoff frequencies where are taken into account the parasitic capacitances ($f_c = g_m / 2\pi\, (C_{gate} + C_p)$) are few GHz and comparable with our results. The graphene FET quest will continue by imposing gate lengths within the ballistic transport limits and the decreasing of the parasitic capacitances.

Reference

[1] NOVOSELOVK.S., GEIM A.K., JIANG D., ZHANG Y., DUBONS S.V., GROGORIEVA I.V., and FIRSOV A.A., *Electric field effect in atomically thin carbon films*, *Science*, **306**, pp. pp. 666–669, 2004.

[2] LIN Y.-M., JENKINS K.A., VLADES-GARCIA A., SMALL J.P., FARMER D B., AND AVOURIS P., *Operation of graphene transistors at gigahertz frequencies*, Nano Letters, **9**, pp. 422–426, 2009.

[3] MERIC I., BAKLITSKAYA N., KIM P., AND SHEPARD K., *RF performances of top-gated, zero-bandgap graphene field-effect transistors*, IEEE Electron Devices Meeting, San Francisco, 15-17 December 2008.

[4] DRAGOMAN M., DRAGOMAN D., DELIGIORGIS G., KONSTANTINIDIS G., NECULOIU D., CISMARU A., and PLANA R., *Current oscillations in wide graphene sheet*, J. Appl. Phys., **106**, p. 044312, 2009.

[5] SHISHIR R.S. and FERRY D.K., *Instrinsic mobility in graphene*, J. Phys.: Condens. Matter., **21**, p. 23204, 2009.

[6] DELIGIORGIS G., DRAGOMAN M., DRAGOMAN D., KONSTANTINIDIS G., NECULOIU D., CISMARU A., AND PLANA R., Microwave propagation in graphene, Appl. Phys. Lett., **95**, p. 073107, 2009.

[7] SUBRAMANYAM G., MATHALA P., CHEVALIER C., DAVIES A., YANEY P., and GROTE J., *Microwave characterization of electro-optic polymers*, MRS Conference Fall, Symposium B, Boston 2002.

[8] MERIC I., HAN M.Y., YOUNG A.F., OZYILMAZ B., KIM P., and SHEPARD K.L., *Current saturation in zero-bandgap, top-gated graphene field-effect transistors*, Nature Nanotechnology, **3**, p. 654, 2008.

[9] LIN W., DIMITRAKOPOULOS C., JENKINS K.A., FARMER D.-B., CHIU H.Y., GRILL A., and AVOURIS P., *100 GHz transistor from wafer-scale epitaxial graphene*, Science **327**, (5966), p. 662, February 2010.

[10] LIAO L., LIN Y.-C., BAO M., CHENG R., BAI J., LIU Y., QU Y., WANG K.L., HUANG Y., DUAN X., *High-speed graphene transistors with a self-aligned gate*,"Nature **467**, pp. 305–308, September 2010.

Carbon-Based Nanomaterials. Environmental Applications

Alina Catrinel ION, Ion ION, Alina CULETU

Politehnica University of Bucharest, Department of Analytical Chemistry and Instrumental Analysis, Polizu Street no. 1-7, 07113, Bucharest, Romania
E-mail: ac_ion@yahoo.com

Abstract. In this review, environmental and agricultural applications of carbon-based nanomaterials, natural and engineered as possible environmental sorbents will be presented. The rather new applications of engineered carbon-based nanomaterials as sorbents for organic and inorganic contaminants in soil systems will be emphasized, as well as the behavior of natural carbon-based nanoparticles in soils. Possible enhancement of several organic and inorganic substances sorption through these nanoparticles in soils has to be regarded as well. A correlation between the type and amounts of nanoparticles in soils and the amounts of chemical substances delivered or retained have to be re-evaluated in the future.

Introduction

Nanotechnology is defined as understanding and control of matter at dimensions between 1 and 100 nm, where unique phenomena enable novel applications [1]. The application of nanotechnology to the environment and agriculture was addressed by the United State Department of Agriculture in a document published in September 2003 [2], rapidly evolving and revolutionizing the agriculture. Nanotechnology can play an important role in pollution sensing through surface-enhanced Raman scattering, surface plasmon resonance, fluorescent detection, electrochemical detection and optical detection, treatment through adsorption, photocatalysis treatment of pollutants, reduction by nanoparticles and bioremediation.

The implications of the nanotechnology research in the environment and agriculture are developed based on the identification of the nanoresearch thematic areas of relevance to the environmental and agricultural system. Nanomaterials like: nanoparticles, carbon nanotubes, fullerenes, biosensors, controlled delivery systems, nanofiltration find relevant applications in agri-food thematic areas like: natural resources management, delivery mechanisms in plants and soils, use of agricultural waste and biomass, in food processing and food packaging, risk

assessment being also evaluated.

Nanosensors in the environment and agriculture begin to have wide applications due to the **environmental monitoring** of pollutants present in the atmosphere, in soils and in wastewater. Different categories of sensors are used like: biosensors, electrochemical sensors, optical sensors. The nano-detection sensors and devices will be the main instruments for trace heavy metals and POPs detection and these can be applied to real samples, the need of commercializing nanosensors becoming in the next years a necessity.

In **treatment** applications, conventional water treatment methods include bio-sand, coagulation, flocculation, reverse osmosis, distillation and adsorptive filtration through ion-exchange resins, active alumina or iron oxide cannot remove all the contaminants. Widely used sorbents for water treatment include: nano-structured metal oxides, carbon nanomaterials, zero-valent iron nanoparticles. Nano iron oxides are well known for removing of toxic ions and organic pollutants from water [3, 4, 5] Carbon nanostructures have been studied because of their physical and chemical properties and their applications, presenting high capability for the removal of various inorganic and organic pollutants and radionuclides from large volumes of wastewaters. Heavy metal ions were removed from aqueous solutions being adsorbed on the surface of the oxidized carbon nanostructures [6, 7]. The adsorption isotherms show that different kinds of heavy metals have different affinity to the adsorbent depending on the material. Surface nano-scale modified carbon black present good affinity for Cu(II) and Cd(II) and Fe^0 nanoparticles for As(III) in groundwater [8].

Another application of nanomaterials in environmental and agricultural treatment is the **remediation** (pollutant transformation from toxic to less toxic in water and soil). Researchers have focused their attention on the remediation of water and soil using Fe^0 nanoparticles which can transform the pollutant (chlorinated organic chemicals) without leaving the chlorinated intermediate by-product [9, 10]. Fe^0 nanoparticles were already applied in the reduction of PCB [11], in the reductive debromination of diphenyl ethers [12], in the removal of alachlor and pretilalachlor [13] and catalysis of chlorinated ethenes. [14]. Simultaneous dechlorination of several pollutants is important for agriculture applications [15], as well as the exploration effective reduction nanoparticles [16] other than Fe^0 and bimetal nanoparticles for metal removal. [17].

Nanosorbents are very important for capturing heavy metal ions and organic contaminants. A smart application of carbon nanomaterials for the removal of heavy metals from soils is also emphasized. [18]. The encapsulation of carbon nanotubes to form a reconfigurable conglomerate with iron oxide microcapsules and their applications in Pb(II) removal was achieved, proving to be recyclable and environmentally friendly for the removal of heavy metals.

Photocatalysis in agriculture is another direction in which nanomaterials can play an important role. Different nanostructures of titanium dioxide (TiO_2) and zinc

oxide (ZnO) have been widely studied as photocatalysts [19, 20]. Methylene blue adsorbed on the surface of ZnO nanoparticle degrades it into leucomethylene blue [21], chemicals presented in pesticides are transformed in relatively harmless molecules such as CO_2, N_2 and H_2O.Under progress is also the removal of pesticides and herbicides on plants and the soil through photocatalysis [22]. Carbamate pesticides used in a variety of field crops are completely mineralized in the presence of ZnO and TiO_2, dichlorvos being an example of an often used pesticide. Apart from nanoparticles, there are reports on the use of nanotubes and nanostructures thin films for degrading pesticides. TiO_2 nanotubes were used for atrazine degradation [23] and TiO_2 thin films for the degradation of organochlorine pesticides [24].

Nanomaterials are (taking into account healthy aspects of nanotechnology) quite effective in detection and treatment systems of environmental pollutants. **Developing functional properties of nanomaterials** trace detection of inorganic and organic pollutants and treatment in water and soil can be tremendously improved. Nanomaterials can be used to detect pesticides, to selectively capture target pollutants and to treat them through reduction or oxidation operation of the nanomaterials. Through **the synergetic action of nanomaterials and through biological processes**, pollutants can be also removed, this methods being used in the environmental engineering of water and soil. Through **nano-photocatalysis** the removal of pollutants becomes another very important direction in environmental engineering, especially in treating pollutants from industrial areas.

In this review, we will be present environmental and agricultural applications of carbon nanomaterials, natural and engineered as sorbents. These materials unite the properties of sp2 hybridized carbon bonds with the characteristics of physics and chemistry at the nanoscale. The most common properties cited in environmental applications are size, shape and surface area, molecular interactions and sorption properties and electronic, optical and thermal ones.

Properties of Carbon-Based Nanomaterials

Molecular manipulation implies control over the structure and conformation of a material, for carbonaceous nanomaterials this includes size, length, chirality and the number of layers. Variations in synthesis technique, temperature, pressure, catalyst, electron field optimize nanomaterial structure, purity and physical orientation for specific applications [25]. Diameter is an important dimension in determining the properties and applications of tubular carbon nanostructures. Small single walled carbon nanotubes (SWNT) diameter is strongly correlated to synthesis technique [26], the diameter inducing higher strain energies, mixing of σ and α bonds and electron orbital rehybridization. These bond structure modifications induce fundamental alterations to the electronic, optical, mechanical, elastic and thermal properties of SWCNTs. The characteristic properties dependent

on nanotube diameter are complemented by physical size exclusion and capillary behavior relevant to environmental and agricultural systems. The narrow inner diameter of nanotubes has found application in novel molding, separation and size exclusion processes [27]. The combined characteristics of narrow diameters and long tubules also imply exceptional aspect ratios in nanotubular structures [28]. Across the spectrum of carbonaceous nanomaterials, the high surface area to volume ratio distinguishes nanomaterials from their micro-scale counterparts. The ratio of $\Delta G_{surface}/\Delta G_{volume}$ increases, where ΔG represents the difference in free energy between the bulk material and the nanoscale structure [29]. The size, shape and surface area of carbonaceous nanomaterials are highly dependent upon aggregation state and solvent chemistry. Impurities adsorbed to the surface of nanomaterials alter the aggregation behavior, thermal and electron characteristics, mechanical strength and physico-chemical properties of the nanomaterials.

Electronic, optical, thermal properties The bonding configuration of carbon based nanomaterials confers unique conductive, optical and thermal properties for applications in the electronic industry. Novel electronic properties will contribute to environmental sensing devices and to new environmental remediation techniques of persistent organics [30]. Tunable band gaps, remarkable stable and high-current carrying capacity, low ionization potential and efficient field emission properties [31] are highly cited electronic properties of SWCNTs, these properties being linked to chirality, diameter, length and the number of concentric tubules. Theoretical and experimental work demonstrates that band gaps are dependent upon the chirality and diameter of nanotubes. A reference coordinate system indexes the chirality of the SWCNTs by a pair of (n,m) integers corresponding to the specific atoms on a planar graphene sheet [32]. Armchair conformations denoted by (n, n) tubes are metallic and independent of tube diameter and curvature. The (n, m) nanotubes with carbon atoms arranged in a zigzag or helical conformation are small gap or large gap semiconductors. Conduction in MWCNTS is dominated by the electronic structure of the outermost tubules and resembles the electronic behavior of graphite [33].

The ionization potential of SWCNTs is below of common field emitters used in the electronic industry, the ionization potential referring to the energy necessary to excite an electron from the ground state to an excited state. In field emitters, a low ionization potential reduces the voltage necessary for exciting an electron and forcing its emission from the molecule. Further reduction in ionization potential is observed in the presence of certain adsorbates, including water. Reducing the voltage potential and enhancing the efficiency of field emission is an example of nanotube application in the green design of next generation devices.

Molecular interaction and sorption Elucidating the molecular interactions, sorption and partitioning properties governing carbon based nanomaterials is generally consistent with physical-chemical models and theories including electrostatics, adsorption, hydrophobicity, etc…Molecular modeling can provide

explanations about physical-chemical processes at the nanoscale. The potential energies of interaction between carbonaceous nanomaterials are already described in the literature [34], accounting for both van der Waals attractive forces and Pauli repulsion originating from overlapping electron orbitals at short separation distances. Hydrophobicity and capillarity will contribute to the adsorption behavior and orientation of sorbates in microporous carbon, physisorption being the dominant mechanism of sorption for not functionalized nanomaterials. Adsorption studies report rapid equilibrium rates, high adsorption capacity, low sensitivity to pH range, minimal hysteresis in dispersed nanoparticle sample [35] and consistency with Langmuir, BET or Freundlich isotherms. [36]. These studies are complicated by the unique properties of adsorption in micropores. In environmental applications, adsorptive capacity has broad implications for contaminant removal and hydrogen storage.

Sorption of environmental contaminants to sorbents such as NOM, clay and activated carbon accounts for an important sink in natural and engineered environmental systems. The sorptive capacity of conventional carbonaceous sorbents is limited by the density of surface active sites, the activation energy of sorptive bonds, the slow kinetics and the nonequilibrium of sorption in heterogeneous systems. The large dimensions of traditional sorbents also limit their transport through low porosity environments and complicate the subsurface remediation. Carbonaceous nanosorbents with their high surface area to volume ratio, controlled pore size distribution and their surface chemistry overcome many of these intrinsic limitations.

An integration of innovative use and existing knowledge and technologies in agriculture with nanotechnology and innovative partnerships between agricultural research institutions with nanoscience research institutions and universities and nanotech companies will help nanotechnology to be faster and efficient applied in agriculture.

Nanotechnology and The Environmental Soil Science

Soil science is concerned with the science of all the materials we find in soils; this being a complex mix of chemicals and organisms of which some are organized at the nanolevel and some not. The thorough analysis of natural nanoparticles (NPs) and engineered NPs in soils involves the sequence of detection, identification, quantification and detailed characterization, if possible. To study and to understand the properties and behavior of different size fractions in soils is a difficult task, each size fraction of the soil matrix, the colloidal fraction, the clay fraction, the slit fraction, the sand fraction and the gravel having specific properties and roles within this matrix. The nano fraction in soils can control or affect the soil physical or chemical properties, the understanding of the nanomaterials behavior being far from complete, from the physical chemistry point of view.

Natural nanoparticles in soils may occur as **nanominerals** e.g. certain clays and Fe and Mn oxyhydroxides or as **carbon containing** NPs [37, 38]. Soils and sediments contain many kinds of inorganic and organic particles such as: clay minerals, metal hydroxides and humic substances [39], nanoparticulate goethite, akaganeite, hematite [40], ferrihydrite and soil humic substance [41]. Hochella [42] classified the NPs present in terrestrial systems in three classes: nanofilms, nanorods and NPs. Nanosheets are usually products of the weathering processes that occur in soils, having very diverse compositions (usually mixtures of oxides and oxyhydroxides of Fe or of other elements) [43]. Nanorods result usually in the process of accelerated weathering of primary soil minerals induced by sediments at alkaline pH values, nanosize hematite and feldpathoids appearing [44, 45, 46]. Nanoparticles (NPs) founding soils can be biogenic uraninite [47], oxidized iron formed by biologically induced oxidation of Fe(II) [48], Fe(III) oxyhydroxides NPs which can constitute the ferric core of ferritine, the main iron storage protein in biological systems [49] As Hochella et al. has already shown, ferrihydrite in natural sediments behaves as a natural sorbent, but its structure and composition is still a matter of debate.

The organic nanomaterials in soils (considered by Nowack and Buchelli as carbon-containing natural NPs) [50] are divided into biogenic, geogenic and pyrogenic NPs. Examples of natural NPs are fullerenes and carbon nanotubes (CNTs) of interstellar origin [51]. Environmental colloids in soils include humic substances and large biopolymers such as polysaccharides and peptidoglycans and, although the knowledge of their structures increased in the last years, their precise function and composition is not very well defined [52]. Soot as product of re-condensation processes during incomplete combustion of fossils appears in soils and in the atmosphere, where from it is again deposited on soils [53]. Some of them can derive from polycyclic aromatic hydrocarbons (PAHs) at temperatures between 300 and 500^0C in the presence of elemental sulfur, or during natural combustion process [54].

Table 1. Classification of natural nanoparticles in soils

Formation				Examples
Natural	C-containing	Biogenic	Organic colloids	Humic, fulvic acids
		Geogenic	Soot	Fullerenes
		Atmospheric	Aerosols	Organic acids
		Pyrogenic	Soot	CNT Fullerenes
	Inorganic	Biogenic	Oxides	Magnetic
			Metals	Ag, Au
		Geogenic	Oxides	Fe-oxides
			Clays	Allophane
		Atmospheric	Aerosols	Sea salt

Nanoparticles (NPs) behavior in soils

The processes affected by nanoparticles presence in soils (the role of the nano-size fraction) seems to gain importance in the last years, the sorption capacity, the interfacial electron transfer reactions, the mobility and the diffusive mass transfer playing an important role in soils properties. Sorption capacity of the NPs refers to some topics such as: assessment of sorption capacity of the NPs in soils; assessment of the NPs interactions with other minerals of the soil matrix and the resulting effects on contaminant and nutrient adsorption/desorption in soils; usage of NPs for groundwater cleanup and remediation purposes; evaluation and quantification of the controls or effects of different variables (physical, chemical, biological) on these processes.

Contaminant or nutrient sorption on NP surfaces has attracted the attention of researchers, several studies in soil chemistry showing that NPs have high sorption capacities for metal and anionic contaminants [55, 56, 57]. It was found that the contaminant sequestration was accomplished mainly by surface complexation, but sorbed surface species can be encapsulated within interior surfaces of NP aggregates, a phenomenon with significant consequences for contaminant dispersion or remediation processes. Metallic species as Ni can be linked to natural short-ordered aluminosilicates [58], arsenate on TiO_2 surfaces [59], humic acids and aromatic compounds by multi walled carbon nanotubes MWCNTs [60].

Nanoparticles interactions with soil minerals and the effects on sorption and desorption of nutrients or contaminants were also studied. Research showed that Fe rich NPs competed efficiently with NOM for Pb binding in soils and water [61]. Another aspect of the same phenomenon is related to the NPs competition with the aqueous species of contaminants and nutrients for available sorption sites on different sorbents present in soils.

Another aspect concerns how the aggregation affects surface energy and the available surface area for sorption and the timescales of adsorption or desorption of contaminants or nutrients from exposed surface and remote sorption sites within the aggregate structures. Research results have demonstrated that the relative reactivity of 5 and 32 nm particles as determined from Langmuir adsorption parameters did not present important variations despite the differences in NP aggregation for these two different sizes. These results also suggested that the aggregation did not affect the extent of organic acid sorption, the challenge remaining the assessment the available surface area for NP sorption because of the aggregation [62]. NPs have been used for groundwater cleaning up and contaminated sites remediation. CuO NPs were found as being an effective material for As(III) and As(V) adsorption [63] Other possible applications investigated the potential of zero-valent FeNPs for treatment and remediation of persistent organic pollutants such as hexachlorocyclohexanes [64], phenantrene sorption by nano-TiO_2 and nano-ZnO particles for the adsorption of organic

contaminants [65], the concentration depending effects of single-walled CNTs or MWCNTs in terrestrial ecosystems on decreasing HOC accumulation by earthworms [66]. Factors such as soil solution pH and ionic strength, elemental substitution in the NPs crystal structure may have an important impact on NP sorption extent and timescales. Chemically oxidized nanoporous sorbents with very good lead adsorption performance were used in batch adsorption experiments were conducted to study the effect of adsorbent dose, initial concentration and temperature on the removal of Pb(II) from aqueous systems, the adsorption being maximum for the initial pH in the range of 6.5-8.0 [67].

The NPs mobility in soils would depend on the degree of the NP interactions with the mineral particles of the soil matrix. Recent studies demonstrated that NP may easily move through the soil profiles. For example, TiO_2 NPs transport behavior through saturated homogeneous soil columns showed that TiO_2 can remain suspended in soil suspension even after 10 days, the transport distances being about hundreds centimeters [68]. NPs such as CNTs can carry contaminants facilitating their transport through soil profiles via mass transfer [69]. Accelerated transport of Pb associated with Fe oxide NPs is observed in soil and river samples in Germany and Sweden [70], carbonaceous NPs enhancing the transport of hydrophobic organic contaminants HOCs in porous media. The movement of NPs in soils and through the soil profile is controlled by a number of geochemical variables: pH, ionic strength, content of NOM and clay in addition to NPs related properties: surface charge, size, charge, aggregation, surface coating and impurities. These facts clearly demonstrate the complexity associated with studies of this type with multiple variables and several effects. Soil pH is a major variable in controlling NP mobility. Research on CNTs showed the effects of acid treatment on: the surface properties, the colloidal stability, and the heavy metal sorption. The results showed that acid treatment increased the amount of acidic surface groups on the CNTs and controlled colloidal stability and their adsorption capacity. Other factors controlling NPs mobility are NP size, sorption kinetics and residence time. MWCNTs were expected to gain widespread usage in commercial products, but concerns about environmental and human risks have been raised [71]. Results from flow-through-column experiments in subsurface and drinking water systems demonstrated that pore water velocity influences MWCNTs transport with higher mobility at greater pore water velocities.

Separation and Characterization of Nanoparticles in Soils

The thorough analysis of NPs (natural and engineered) involves the sequence of detection, identification, quantification and characterization. In a complex or heterogeneous sample, each step of this sequence is an individual challenge, field-flow-fractionation (FFF) being one of the most promising techniques to achieve relevant characterization. It becomes clear that new analytical methods are needed

to quantify NPs in a wide variety of sample types. This task can be very difficult especially for impure and complex samples, like environmental, biological and food samples. Environmental samples (especially soils) are complex matrices, which may contain natural and engineered NPs besides other particles, varying in composition, size and shape. To solve the problem of detecting, identification, quantification and characterization of NPs a solution is to make use of an existing contrast between the NPs and the sample matrix or to create one. There are analytical tools available to obtain accurate results for simple matrices, but not too many for more complicated matrices. Detection by light-scattering (LS) techniques is based on the differences between the refractive index of the particles and of the medium [72]. LS is not substance specific and for dynamic light scattering (DLS) the polydispersity of the NPs in the sample limits its applicability [73]. Mass spectrometry can not be used alone for NPs measurement if the composition of NPs is identical to the sample [74] Electron microscopy (EM) makes use of spatial resolution and differences in composition and structure of the particles. It is good for identifying single particles, but it fails to provide a statistical representation of the whole sample [75] Separation using ultra-filtration apparatus are based on gradient filtration using membranes with different molecular weight cutoffs (MWCOs) for separating colloidal materials in soils into specific size-fractions.

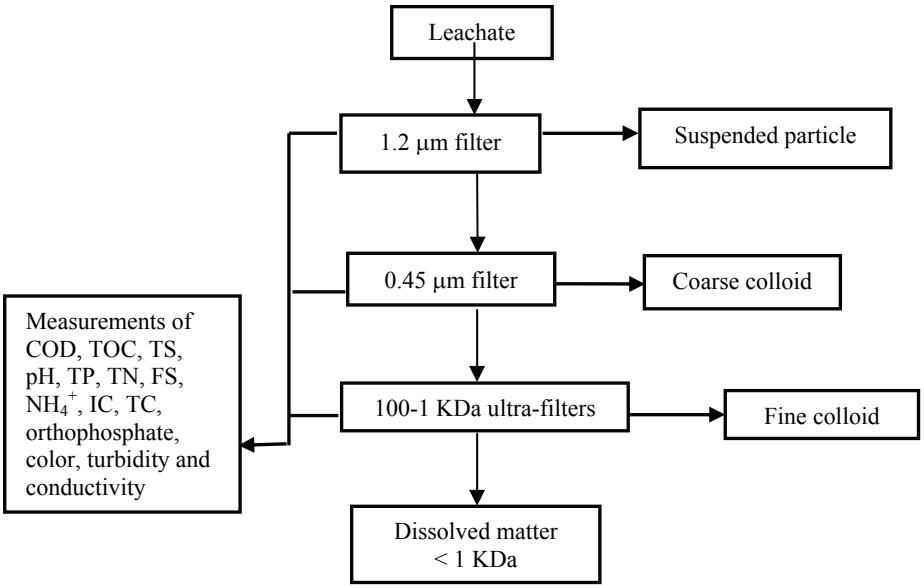

Fig. 1. Schematic separation of organic matter size fractionation using micro- and ultra-filtration.

The soils are initially filters using 1.2 μm, followed by 0.45 μm membranes made of mixed cellulose, 0.22 μm and then on membranes with nominal MWCOs

of 100, 30, 10 and 1 kDa (1 Da is equal to 1/16 of an O atomic mass unit). All membranes are made of polyether sulfone (PES).

The residue retained by the 1.2 μm membranes was defined as suspended solid, the residue retained by the 0.45 μm membranes as coarse colloids and the residue retained by the rest of the PES MWCO membranes as fine colloids. The materials remaining in solution after the 1 kDa MWCO membrane filtration step were defined as dissolved matter.

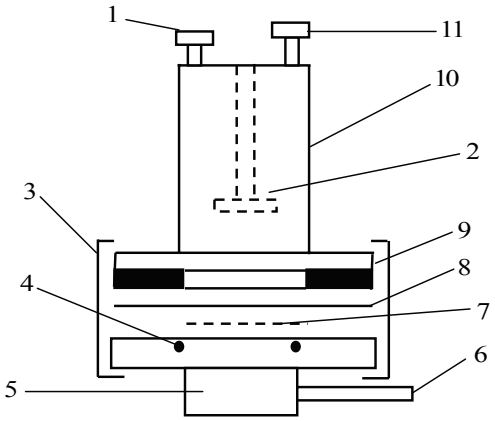

Fig. 2. Schema of an ultra-filter: 1. Admitting pipe; 2. Stirrer; 3. Fixator; 4. O-ring seal pack; 5. Seat; 6. Outlet; 7. Flow deflector; 8. Ultra membrane; 9. Scaling pipe; 10. Ultra filter cup; 11. Feed inlet.

The combination with a hydrodynamic separation technique (e.g. field-flow fractionation FFF) offers the possibility of using all the potential of the aforementioned techniques. By separating macromolecules and particles, FFF reduces sample poly-dispersity and complexity for each of the analytical devices and ideally also adds particle-size information [76].

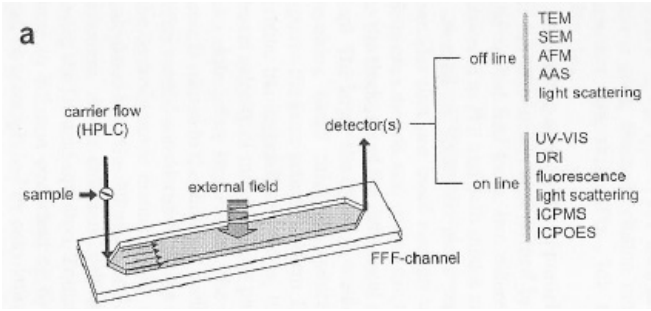

Fig. 3. Scheme of typical flow-field fractionation (reproduced with permission from F. van der Kammer et al., Trends in Anal. Chem. 2011, 30(3), 425-436.

Much of an FFF system resembles a classic liquid chromatography (LC) system (pumps, autosampler, detectors), FFF separates particles at low to medium pressure in an open channel without a stationary phase, the interactions of the NPs with the stationary phase being avoided. Since FFF is prone to interferences by large particles (> 1 μm), sample preparation is required for most samples, a suitable sample for FFF separation being a stable dispersion of NPs in a liquid medium, suitable sample-preparation technique playing a major role in FFF analysis.

Table 2. Example of application of FFF for characterization of nanoparticles in different matrices

Particle type	Size	Matrix	Separation	Detection	Ref.
Ni and U bound to humic acid	90-120 nm	Sediment extract	aF^4	UV-Vis 254 nm, ICP-MS	[77]
Metal bound to humic acid	1-10 nm	Sediment extract	sF^4	UV-Vis 254 nm, ICP-MS	[78]
Metal bound to humic substances	<10 nm	River sample	aF^4	MALLS, ICP-MS, TEM	[79]
Macromolecules	<1000kDa	Compost leachates	aF^4	ICP-MS	[80]
Polyethylene imine	25000 Da	Seawater	sF^4	UV-Vis 254 nm, ICP-MS,TEM	[81]
Humic acid	3790-3950 Da	Wastewater	sF^4	MALLS	[82]
Complex of extracellular metal with polymeric substances	52-737 kDa	Synthesized suspension medium	aF^4	MALLS, TEM	[83]

Sorption on Carbon Nanostructures in Soils

Sorption is a surface phenomenon which may be either absorption or adsorption or a combination of the two. Adsorption is the association of an adsorbate compound onto a surface (sorbent) usually in a liquid/solid or vapor/solid system, while absorption involves the redistribution of a compound from an aqueous phase into a volume of material. In geochemical systems, the two are indistinguishable and the term sorption is always used. Sorption is a fate mechanism that can be present in any aquatic or ground water system.

Sorption has been traditionally divided into two systems: weak physic-sorption and strong chemi-sorption. Each specific sorption interaction is usually somewhere in-between these two extremes. In order to understand these terms, we must understand first the molecular nature of the surface and of the sorbate.

Sorption is a term that includes several elementary reactions. Sorption can involve strong electrostatic interactions between ions or dipoles and surfaces, including ion exchange type reactions. Sorption can involve only weak

intermolecular forces such as van der Waals interactions. As used by geochemists, sorption to natural surfaces also generally includes adsorption on surfaces and absorption into the material. The surface of a solid represents an interface between the gas or solution phase and the mineral crystal. The nature of that interface depends on the nature of both the crystal phase and the solution or the gas phase. The solid surface can be represented as a surface of discrete sites and each one individually participates in a reaction resulting in sorption.

In general, nanoparticles can be used as sorbent materials in two configurations: chemically bonded, through a covalent bond to microparticles or directly used as raw materials. When these materials are used as sorbents, the interaction of the analyte can be produced directly on the nanoparticle surface or in the interstices of the aggregate. The non-covalent interaction established between the analyte and the nanoparticles or the nanostructured materials includes ionic interactions (dipole-dipole), hydrogen bonds, π-π stacking, dispersion forces, dative bonds and the hydrophobic effect. The presence of functionalized nanoparticles or supramolecular aggregates allows the possibility of incorporating one or more of these interactions.

In recent years, a large number of allotropic carbon nanoparticles have been described including: nanodiamonds [84], fullerene [85], nano-onions [86], carbon nanotubes (CNTs) [87], graphite nanosheets [88]. The sorptive capacity of conventional carbonaceous sorbents is limited by the density of the surface active sites, the activation energy of sorptive bonds, the slow kinetics and nonequilibrium of sorption in heterogeneous systems and the mass transfer rate to the sorbent surface. The large dimensions of traditional sorbents also limit their transport through low porosity environments and complicate the applications in subsurface remediation. Carbonaceous nanosorbents with their high surface area to volume ratio, controlled pore size distribution and surface chemistry overcome many of these intrinsic limitations. Sorption studies using carbon-based nanomaterials report rapid equilibrium rates, high adsorption capacity, being effective over a broad pH range and consistency with BET, Langmuir or Freundlich isotherms [89]. Direct sorption of organic contaminants to the nanomaterial surface is driven by the same fundamental hydrophobic, dispersion and weak dipolar forces to determine sorption energies in conventional systems [90] The higher equilibrium rates of carbonaceous nanosorbents over activated carbon are attributed to [91] π electron polarizability or π-π electron-donor acceptor interactions within aromatic sorbents, reduced heterogeneity of adsorption energies and the absence of pore diffusion as an intermediate mechanism in adsorption [92]. This conclusion is reinforced by Yang *et al*. [93] comparing a variety of carbonaceous nanosorbents. Another advantage to carbonaceous nanosorbents is the virtual absence of hysteresis between adsorption and desorption isotherms for liquids and gases under atmospheric pressure. Enhanced atmospheric pressure relevant to gas adsorption in hydrogen storage applications may restore hysteresis in the system by reducing the

energy barrier to fill nonwetting CNT pores and the intraparticle region of the nanoaggregates [94]. While rapid equilibrium rates and high sorbent capacity are powerful attributes of carbonaceous nanosorbents, their true revolutionary potential lies in the diverse pathways for tailored manipulations of their surface chemistry. Tailoring the dominant physical and chemical adsorption forces via selective functionalization yields carbonaceous nanomaterials that complement the existing suite of relatively unspecific conventional sorbents. Functionalized nanosorbents may provide an optimized approach for targeting micropollutants, removing contaminants [95]. CNTs functionalized with hydrophilic –OH and –COOH groups exhibited superior sorption of low molecular weight and polar compounds [96]. In contrast to the relatively nonspecific, hydrophobic sorption mechanisms describing organic sorption, inorganic sorption to carbonaceous nanostructures is characterized by specific complexation reactions. Surface functional group density rather than total surface area becomes the primary determinant of inorganic sorption capacity. Metal speciation or competing complexation reactions render sorption capacity sensitive to changes in pH [97].

Despite the synthesis costs, the cost effectiveness of carbon based nanomaterials vs. traditional activated carbon was demonstrated, the environmental applications of nanomaterials sorption capacity being not limited to the removal or remediation of contaminants, but to controlled delivery of fertilizers and pesticides as well.

The adsorption isotherms

Adsorption isotherms describe the equilibrium relationship between bulk activity of absorbate in solution and the moles adsorbed on the surface at constant temperature. Adsorption isotherm expressions are derived from fundamental principles of the adsorption process, experimental data fitting by isotherm expressions whether the experimental system satisfies the assumptions of the isotherm derivation or not. Brunauer described five general types of sorption isotherms:

1. **Langmuir type** offers a good representation of chemisorption and usually represents the low P portion of other isotherms. Adsorption sequentially fills surface sites until mono-layer coverage is achieved. No multi-layer coverage is included. Each site is equivalent in energy. Langmuir behavior assumes rapid reversible sorption and interaction only between sorbate molecules and a surface site. The lower portion is linear. The equation for the Langmuir isotherm is given by: $Q=Q_mbC_g/(1+bC_g)$, where Q is the amount sorbed, Q_m is the monolayer coverage, C_g is the gas phase concentration and b is a constant. While the Langmuir isotherm is rarely useful in real heterogeneous systems, it illustrates well the concept of monolayer coverage.
2. **BET type**. The BET equation is an extension of the Langmuir relationship

that accounts for multilayer coverage. Here, multiple layers can form before monolayer is complete with multiple layers forming as a condensation reaction. At high pressure, the adsorbate condenses to a bulk liquid on the surface; the number of layers becomes infinite. This isotherm describes well the physic sorption of an organic onto dry surface soils. The equation $Q=QmcP/(P^0-P)[1+(c-1)(P/P^0)]$, where P^0 is the saturated vapor pressure and c is a constant related to the energy (enthalpy) of adsorption. While this is effective in describing vapor-phase adsorption on dry soils, it does not describe electrostatic interactions of ions onto a heterogeneous surface in an aqueous system.

3. **Freundlich type**. A well-used empirical isotherm is the Freundlich relationship which allows a heterogeneous surface that is more often seen in natural systems. When $1/n > 1$, the sorption constant increases with increasing solution concentration, perhaps reflecting an increase in the hydrophobic character of the surface after a monolayer. When $1/n < 1$, K decreases with solution concentration as the low-energy sites are occupied. 1/n slightly greater than 1 is often found for organic solutes. The Freundlich equation is: $Q=K_F C_s^{1/n}$

Linear isotherms When 1/n=1, the isotherm becomes a linear relationship which often closely describes the absorption reaction of an organic molecule partitioning into soil organic matter, having no linear portion. In this case, the distribution coefficient Kd describes a linear relationship between the dissolved concentration of absorbate ion and the concentration adsorbed to the surface. Linear adsorption best describes systems at low concentrations where the Langmuir relationship is still linear. The end result assumes that the amount of a solute sorbed is proportional to the concentration in solution. The Kd expression is derived from the Langmuir isotherm, assuming a very small P and $KP<<1$. The measured Kd value is an operational parameter with no thermodynamic significance, but still useful in describing simple systems. The value of the Kd is restricted to the system for which the value was obtained.

Factors affecting sorption are the following ones: **surface area, mineral surface properties, organic carbon, solubility, temperature, pH, salinity, co-solvents** and **dissolved organic matter.**

Surface area. Adsorption is a surface phenomena directly related to surface area. When increasing the surface area the specific adsorption will increase, too. Sorption is usually reported as a bulk property on a per gram weight basis. Sorption should always be reported on an area basis, considering micropores and molecular porosity.

Mineral surfaces properties. Surface charge creates surface conditions in which there is an uneven charge distribution, creating a double-layer of ions, charged organic solutes exchanging with other counter-ions in the double layer, resulting in physisorption.

Organic carbon. It has been found that the sorption of hydrophobic organic compounds is strongly controlled by the presence of soil organic material. While the reaction resembles a sorption and will fit a sorption isotherm, it is partitioning.

Solubility. As the solubility of a hydrophobic compound decreases, the adsorption coefficient increases from entropy driven interaction with the surface.

Temperature. Since adsorption is an exothermic process, K values usually decrease with increasing temperature. In general, a 10% decrease in K sorp would occur with a temperature rise from 20 to 30^0C.

pH. Only chemicals that tend to ionize are affected by the pH, on neutral molecules the only change will be in the character of the surface, at low pH humic materials being nearly neutral, for example and more hydrophobic. Changes in pH will affect organic acids and bases by changing solubility. Cations resulting from the protonation of an organic base may more strongly adsorb to soils than neutral species. Sorption of charged species will be affected by the pH.

Salinity. An increase in salinity can lower the adsorption coefficient of cations due to the replacement/exchange by alkali cations. The adsorption of acid herbicides increases with salinity at pH values above the pKa of the acid, pH influencing the affects of salinity. Neutral molecules are generally less affected by salinity, but often show an increased adsorption with increasing salt concentration, probably due to the increase in the activity coefficient of neutral molecules and resulting decrease in aqueous solubility. Increasing salinity may also change the interlayer spacing of layer clays as well as the morphology of the soil organic matter.

Co-solvents. Co-solvents are water soluble organic solvents such as methanol or acetone and they can decrease the sorption constant Ksorp by increasing the apparent solubility. The pyrene Ksorp decreases by 30% in 10% methanol.

Natural Nanoparticles in Soils and Environmental and Agricultural Applications as Sorbents

Nanoparticles in soils can be divided into natural and anthropogenic particles, being further separated into carbon-containing and inorganic NPs. Natural and anthropogenic combustion processes that take place both in stationary and in mobile sources emit a variety of particles. From these particles the soot fraction of the black carbon correspond to the nano-sized BC. Soot as a product of re-condensation processes during incomplete combustion of fossil and renewable fuels is emitted into the atmosphere from where it is deposited onto soils and water bodies. Although fullerenes and CNT are considered as engineered NP, they are also natural particles (fullerenes) or CNTs. The majority is believed to have formed from polycyclic aromatic hydrocarbons (PAH) during metamorphosis at high temperatures and in the presence of elemental sulfur [98].

Dissolved organic carbon and organic colloids in the sub-micron size range

have been recognized as distinct organic phase to which pollutants are partitioning. By their shear abundance such sorbents may attenuate the truly dissolved exposures of organic pollutants. Soot is an important adsorbent for organic compound, the nonlinear adsorption of organic compounds onto BC completely dominating total sorption at low aqueous concentrations in soils and sediments [99]. The efficient sorption to BC pulls toxic polycyclic aromatic hydrocarbons, polychlorinated biphenyls, dioxins, polybrominated diphenylethers and pesticides into sediments and soils [100], the presence of BC explaining that the sorption of organic compounds into soils and sediments is much higher in comparison with the absorption into the organic matter alone.

CNTs have proved to be adsorbents for organic compounds from water, examples including dioxin [101], PAH [102], DDT [103], chlorobenzenes and chlorophenols [104, 105] dyes [106], pesticides [107], herbicides [108, 109]. In all cases, the available adsorption space was found to be the cylindrical external surface, neither the inner cavity, nor the inter-wall space of multi-walled CNT.

Oxidized CNTs are also good adsorbents for metals such as: Cu [110], Ni [111], Cd [112, 113], Pb [114], Ag [115] and rare earth metals [116]. In all the cases, adsorption is pH dependent increasing sorption by increasing pH.

Fullerenes have also been tested for the adsorption of organic compounds, adsorption depending to a great extent on the dispersion state of the C60 [117]. Incomplete dispersion leading to significant adsorption-desorption hystheresis [118]. Ballesteros *et al*., [119], found that fullerenes are not very good sorbents for organic compounds, but they are efficient for the removal of organometallic contaminants.

There are some examples till the moment concerning sorption of several contaminants on natural carbon based nanomaterials in soils, these applications being listed in the table below.

Table 3. Natural carbon containing nanoparticles in soils as sorbents for contaminants

Formation	Type	Sorbent	Contaminant	Ref.
Biogenic	Organic colloids	Humic and fulvic acids	phenantrene	[120]
Biogenic	Organic colloids	Humic and fulvic acids	atrazine	[121]
Biogenic	Organic colloids	Humic and fulvic acids	Th(IV)	[122]
Geogenic	Soot	fullerenes	Organic contaminants	[123]
Pyrogenic	Soot	CNTs	14C-phenantrene 14C-benzo[a]pyrene	[124]
Pyrogenic	Soot	CNTs	arsenate	[125]
Pyrogenic	Soot	CNTs	pesticides	[126]
Pyrogenic	Soot	CNTs	pyrene	[127]
Pyrogenic	Soot	CNTs	1,2-dichlorobenzene	[128]
Pyrogenic	Soot	CNTs	Organic contaminnats	[129]
Pyrogenic	Soot	CNTs	243 Am(III)	[130]

Engineered Carbon Nanomaterials (CNM) in Soils as Sorbents for Environmental Contaminants

The environmental applications of engineered carbonaceous nanomaterials are both proactive (preventing environmental degradation, improving public health, optimizing energy efficiency) and retroactive (remediation, wastewater reuse, pollutant transformation). Carbon unique hybridization properties and the sensitivity of carbon's structure to perturbations in synthesis conditions allow for tailored manipulation to a degree not yet achieved by inorganic nanostructures [131].

Wetting plays a key role in the nanototube capillarity. Hydrophobicity and capillarity also contribute to the adsorption behavior and orientation of sorbates in micro-porous carbons. Physi-sorption is the dominant mechanism of sorption for not functionalized nanomaterials. Adsorption studies report rapid equilibrium rates, high adsorption capacity, low sensitivity to pH range, minimal hysteresis in dispersed nanoparticle samples and consistency with traditional Langmuir, BET or Freundlich isotherms [132].

Functionalized nanosorbents may provide an optimized approach for targeting specific micropollutants, removing low concentration contaminants or improving subsurface mobility. For instance, when compared to activated carbon, carbon nanotubes functionalized with hydrophilic –OH and –COOH groups exhibited superior sorption of low molecular weight and polar compounds. In contrast to the relatively non-specific, hydrophobic sorption mechanisms describing organic sorption, inorganic sorption to carbonaceous nanostructures is characterized by specific complexation reactions. Surface functional group density, rather than total surface area becomes the primary determinant of inorganic sorption capacity. Metal speciation or competing complexation reactions also render sorption capacity sensitive to changes in pH.

Although there are several examples in the literature illustrating the promising sorption properties of carbon based nanomaterials, their applications in real environmental samples and particularly in agriculture are very scarce. In this regards, this project will contribute to filling the existing gap between theory and experimental results by carrying out a comprehensive study of a wide range of novel nanosorbents with a truly multidisciplinary approach.

Nanotubes (CNTs) conceptually represent a micrometer-scale graphene sheet rolled into a cylinder nanoscale diameter and capped with spherical fullerenes. Extensive reviews have been published on the synthesis and structural conformation of CNTs, highlighting their position on the spectrum of carbon hybridization and the effect that this conformation has one property relevant to environmental applications.

The development of various methods for producing **graphene** - a single layer of carbon atoms bonded together in a hexagonal lattice and graphitic nanoplatelets -

multilayer of carbon atoms bonded together in a hexagonal lattice has stimulated a vast amount of research in recent years. Graphene and chemically modified graphene (CMG) are promising candidates as components in applications, such as energy-storage materials, paper-like materials, polymer composites, environmental sorbent materials [133].

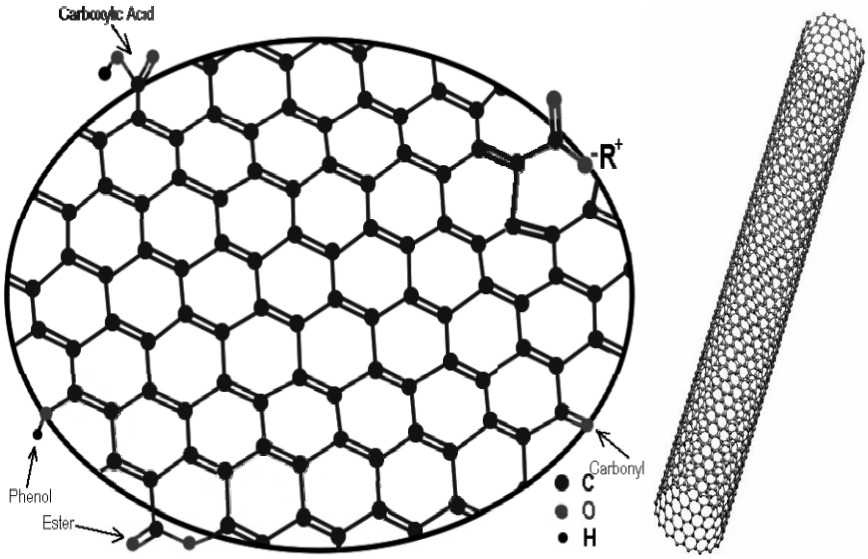

Fig. 4. Schema of carbon based nanomaterials: functionalized graphene and CNT.

Functionalized CNTs, graphitic nanoplatelets and graphene can be used to bind contaminants such as heavy metals, organochlorine remanent pesticides, organophosphate pesticides and polychlorinated biphenyls (PCBs). The amount of the contaminant that binds to the nanotube is up to ten times higher than the weight of the CNM. Both CNTs and graphene will be embedded in liquid permeable materials.

Direct sorption of organic contaminants at the nanomaterial surface is driven by the same fundamental hydrophobic dispersion and weak dipolar forces that determine sorption energies in conventional systems. The higher equilibrium rates of carbonaceous nanosorbents over activated carbon are attributed to π-π electron-donor acceptor. Interactions with aromatic sorbates reduced heterogeneity of adsorption energies and the absence of pore diffusion as an intermediate mechanism in adsorption [134]. This conclusion is reinforced by results comparing a variety of carbon nanosorbents. Another advantage to carbon nanosorbents is the virtual absence of hysteresis between adsorption and desorption isotherms for liquid and gases under atmospheric pressure.

Table 4. Engineered based carbon nanoparticles CNTs as sorbents for contaminants (inorganic and organic ones)

Sorbent	Application	Contaminant	Ref
Iminodiacetic acid functionalized MWCNTs	Separation and preconcentratin	Heavy metals	[135]
CNTs and carbon encapsulated magnetic nanoparticles	Kinetics of sorption	Copper ions	[136]
CNTs doped with metal impurities	Sorption from aqueous solutions	Pb(II)	[137]
Modified MWCNTs	Sorbents	Traces of gold (III)	[138]
CNTs and carbon encapsulated magnetic nanoparticles	Sorbents	Heavy metals	[139]
Carbon-nanotube silver composite	Sorbent for capture and analysis	Hg(II)	[140]
Ag-CNTs	Mercury trap	Hg(II)	[141]
Oxidized MWCNTs	Sorption from aqueous solutions	Pb(II)	[142]
L-cysteine functionalized MWCNTs	Selective sorption and preconcentration	Heavy metals	[143]
Non-oxidized MWCNTs	Enrichment efficiency of sorption	Metal ions	[144]
CNTs	Sorption from aqueous solutions	Divalent metal ions	[145]
Carbon nanosorbents	Concentration and separation	Metal ions	[146]
Carbon nanotubes	Sorbent for aqueous solutions	Ni(II)	[147]
Modified CNTs	adsorption	sulfamethoxazole	[148]
MWCNTs	Competitive adsorption	Naphthalene, 2,4-dichlorophenol, 4-chloroaniline	[149]
Natural organic matter (NOM) CNTs	Sorption in natural samples in the presence of NOM	Organic contaminants	[150]
CNTs	Adsorption	phenolic compounds	[151]
CNTs	Sorption in the presence of NOM	Organic contaminants	[152]
MWCNTs	Competitive sorption	Pyrene, phenantrene, naphtalene	[153]

Table 5. Engineered based carbon nanoparticles (graphene) as sorbents for contaminants (inorganic and organic ones)

Sorbent	Application	Contaminant	Ref
Lignite activated nanstructured carbon	Fixed-bed results	$HgCl_2$	[154]
Oxidized MWCNTs and graphene	Mixed sorbents	Zn(II) and naphtalene	[155]
Nanostructured wood charcoal	Natural sorption	Hydrophobic organic compounds	[156]
Surface modified graphite nanosheets	Adsorbent for water samples	1,2-dichlorobenzene	[157]
Graphite and soot	Mediated reduction	2,4-dinitrotoluene, hexahydro-1,3,5-trinitro-1,3,5-triazine	[158]
Nanoporous carbon xerogels	sorbent	Organic contaminants	[159]
Wood charcoals	Different thermochemical conditions	Single-ring organic compounds	[160]
Nanostructured black carbon	sorbent	Aromatic compounds	[161]
Nanostructured charcoal	Competitive experiments	Aromatic compounds	[162]
Exfoliated graphite nanoplatelets (xGnP)	Sorption from aqueous solutions	Phenolic compounds	[163]
Exfoliated oxidized graphite nanoplatelets (xGnP)	Sorption from aqueous solutions	Pb(II)	[164]
Nanostructured wood charcoal	sorbents	Hydrophobic contaminants	[165]

Fig. 5. Possible solution for water decontamination using nanomaterials impregnated curtains.

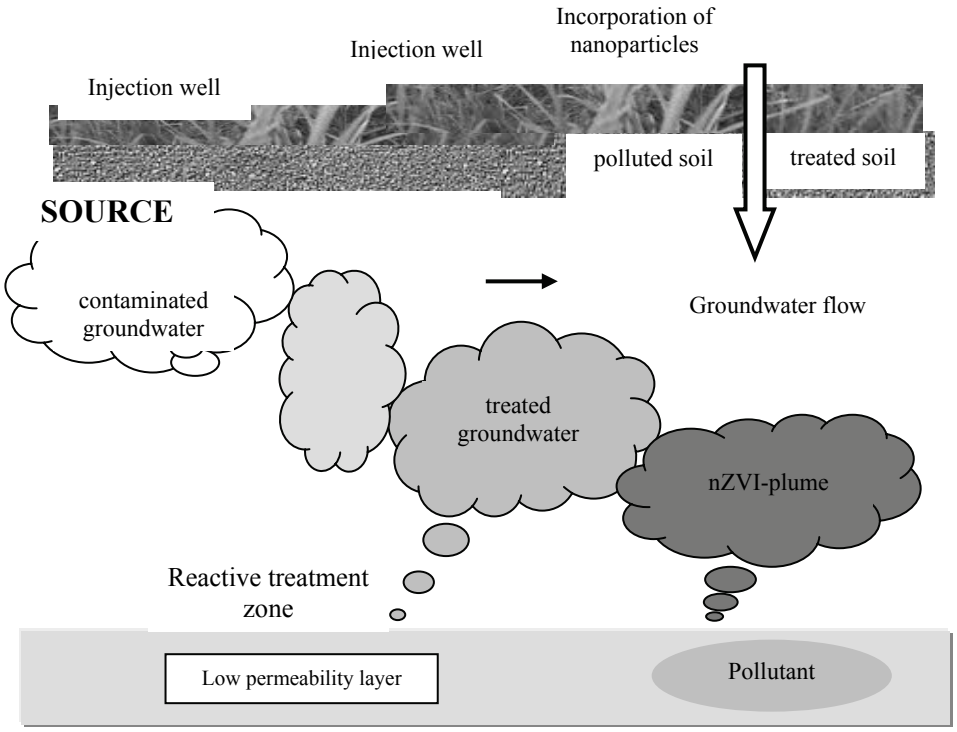

Fig. 6. Solution for soil decontamination using nanoparticles.

The decontamination processes will take place simultaneously by entrapping the proposed nanomaterials (mixing as grown and oxidized CNTs or graphene) in combination on different supports and introducing these tools in the flow path of contaminated waters. Their performance will be assessed by testing samples from contaminated areas before and after decontamination using the developed filtration methods and tools.

Conclusions

Nanotechnologies can find applications in many other environmental and agri-food thematic areas:

- in **efficient use of soil resources** (nanoparticles in soil in situ remediation, absorption and release of contaminants in soils; nanoscale iron particles in rapid destruction of chlorinated hydrocarbons in soil and groundwater; nanosensors in monitoring of heavy metals)
- in **efficient use of water resources** (nanotechnology in desalination and water purification; nanoporous membranes in filtration of viruses; nano-sponges in the absorption of toxic metals)

- in **delivering mechanism in plant, soil and animal systems** (mesoporous silica nanoparticles in delivering DNA and chemicals into plants; smart magnetic silica core-shell nanomaterials in specific targeting, cell sorting and bio-imaging; organically modified silica nanoparticles as DNA carriers; carbon nanofibers in gene therapy of plants; carbon nanotubes as molecular transporters)
- in **using agricultural waste/biomass** (biosynthesis of nanoparticles by microbes, biosynthesis of nanoparticles by the utilization of agriculture residues)
- in **food processing** (nanotechnology in food safety and quality control and in the production of functional and nutritive food; in biosensors, nanocantilevers, carbon nanotubes)
- in **food packaging** (nanoscale titanium dioxide particles in plastic packaging, nanosensors, bio-polymers based nanocomposites for safe storage)

This review treated in the first part the applications of natural and engineered carbon-based nanomaterials as sorbents for environmental contaminants, the second part offering a synthesis of carbon-based nanomaterials with applications in sensors for pesticides.

References

[1] ROCO M.C., NANOPART J.. Res. **5**(3-4), pp. 181–189, 2003.
[2] *USDA Nanoscale Science and Engineering for Agriculture and Food Systems*, Dept. of Agriculture, United States 2003.
[3] PONDER S.M., DARBAB J.G., MALLOUK T.E., Environ. Sci. Technol. **34**, p. 2564, 2000.
[4] LI X., ZHANG W., Langmuir **22**, p. 4638, 2006.
[5] HU J.S., ZHONG L.S., SONG W.G., WAN L.J., Adv. Mater. **20**, p. 2977, 2008.
[6] KALFA O.M., YALCIKAYA O., TURKER A.R., J. Hazard. Mater. **166**, p. 455, 2009.
[7] TAN X., CHEN C., YU S., WANG X., Appl. Geochem. **23**, p. 2767, 2008.
[8] KANEL S.R., MANNING B., CHARLET L., CHOI H., Environ, Sci. Technol. **39**, p. 1291, 2005.
[9] SONG H., CARRAWAY E.R., Appl. Catal. B: Environ. **78**, p. 53, 2008.
[10] PHENRAT T., SALEH N., SIRK K., TILTON R.D., LOWRY G.W., Environ. Sci. Technol. **41**, p. 284, 2007.
[11] LI C., CHEN Y., CHIU K., YAK H.K., Surf. Sci. **600**, p. 1382, 2006.
[12] KEUM Y.S., LI Q.X., Environ. Sci. Technol. **39**, p. 2280, 2005.
[13] KIM H.Y., KIM I.K., SHIM J.H., KIM Y.C., HAN T.H., CHUNG K.C., KIM P.I., OH B.T., KIM I.S., Bull. Environ. Contam. Toxicol. **77**, p. 826, 2006.
[14] ALESSI D.S., LI Z., Environ. Sci. Technol. **35**, p. 3713, 2001.
[15] WANG C.B., ZHANG W.X., Environ. Sci. Technol. **31**, p. 2154, 1997.
[16] KIM J.H., TRATNYEK P.G., CHANG Y.S., Environ. Sci. Technol. **42**, p. 4106, 2008.
[17] LAI K.C.K., LO I.M.C., Environ. Sci. Technol. **42**, p. 1238, 2008.
[18] CHOI B.W.S., *et al*., Adv. Funct. Mater. **20**, pp. 820–825, 2010.
[19] PREVOT A.B., FABBRI D., PRAMAURO E., RUBIO A.M., GUARDIA la De M., Chemosphere **44**, pp. 249–255, 2001.
[20] ULLAH R., DUTTA J., J. Hazard Mater. **156**, p. 194, 2008.
[21] BARUAH S., DUTTA J., Sci. Technol. Adv. Mater. **10**(013001 :18), 2009.

[22] RAHMAN M.A., MUNEER M., Desalination **181**, pp. 161–172, 2005.
[23] ZHANQI G., SHAOGUI Y., NA T., CHENG S., HAZARD J., Mater. **145**, pp. 424–430, 2007.
[24] YU B., ZENG J., GONG L., ZHANG M., ZHANG L., CHEN X., Talanta **72**, pp. 1667–1674, 2002.
[25] JOST O., GORBUNOV A., LIU X.J., POMPE W., FINK J., J. Nanosci. Nanotechnol. **4**, 433–440, 2004.
[26] ANDREAS H., Angew. Chem. Int. Ed. **41**, pp. 1853–1859, 2002.
[27] HOLT J., PARK H., WANG Y., STADERMANN, M. ARTYUKHIN A., GRIGOROPOULOS C., NOY A., BAKAJIN O., Science **312**, 312, pp. 1034–1037, 2006.
[28] C.H. Jin, K. Suenaga, S. Iijima, Nat. Nanotechnol. 3 (2008), 17-21.
[29] HUNTER R.J., *Foundation of the Colloidal Science*, 2nd ed., Oxfor University Press: oxford; New York, 2001.
[30] COLVIN V.L., *Clean water from small materials in Nanotechnology of the environment MRS: Boston MA*, 2007.
[31] SAITO Y., UEMURA S., Carbon **38**, pp. 169–182, 2000.
[32] *Carbon Nanotubes: Synthesis, structure, properties and applications*, Dresselhaus M.S. Ed.; Springer: Berlin, **80**, NY, 2001.
[33] HU Y., SHENDEROVA O., BRENNER D., COMPUT J., Theor. Nanosci. **4**, pp. 199–221, 2007.
[34] HUNTER R.J., *Foundation of Colloid Science*, 2nd Ed; Oxford University Press: Oxford; New York, 2001.
[35] HILDING J., GRULKE E.A., SINNOT S.B., QIAN D., ANDREWS R., m. Jagtoyen, Langmuir **17**, pp. 7540–7544, 2001.
[36] CHEN W., DUAN L., ZHU D., ZHU D.Q., Environ. Sci. Technol. **41**, pp. 8295–8300, 2007.
[37] HOCHELLA M.F., Geochim. Cosmochim. Acta **71**, p. A 408, 2007.
[38] MAURICE P.A., HOCHELLA M.F., Adv. Agron. **100**, pp. 123–153, 2008.
[39] THENG B.K.G. and YUAN G.D., Elements **4**, pp. 395–309, 2008.
[40] WAYCHUNAS G.A., KIM C.S., BANFIELD J.F., NANOPART J., Res. **7**, pp. 409–433, 2005.
[41] ADANI F., SALATI S., SPAGNOL M., TAMBONE F., GENEVINI P., PILU R., Chromosphere **76**, pp. 523–528, 2009.
[42] HOCHELLA M.F., LOWER S.K., MAURICE P.A., PENN R.L., SAHAI N., SPARKS D.L., TWINING B.S., Science **319**, pp. 1631–1635, 2008.
[43] QUAFOKU N.P., *Impact of Environmental Nanoparticles on Physical, Chemical, Biological and Hydrological Processes in Terrestrial ecosystems Handbook of Soil Science*, 2010.
[44] QAFOKU N.P., AINSWORTH C.C., SZECSODY J.E., QAFOKU O.S., J. Environ. Qual. **32**, pp. 2354–2363, 2003.
[45] QAFOKU N.P., AINSWORTH C.C., SZECSOD J.E., BISH D.L., YOUNG J.S., MCCREADY D.E. and QAFOKU O.S., J. Environ. Qual. **32**, pp. 2364–2372, 2003.
[46] QAFOKU N.P., QAFOKU O.S., AINSWORTH C.C., DOHNALKOVA A. and McKINLEY S.G., Appl. Geochem. **22**, pp. 2054–2064, 2007.
[47] SINGER D.M., FARGES F. and BROWN Jr. G.E., Geochim. Cosmochim. Acta **73**, pp. 3593–3611, 2009.
[48] MIOT J., BENZERARA K., MORIN G., KAPPLER A., BERNARD S., OBST M., FERARD C., SKOURI-PANET F., GUIGNER J.M., POSTH N., GALVEZ M., BROWN G.E. and GUYOT F., Geochim. Cosmochim. Acta **73**, pp. 696–711, 2009.
[49] CARTA D., CASULA M.F., CORRIAS A., FALQUI A., NAVARRA G., PINNA G., Mater. Chem. Phys. **113**, pp. 349–355, 2009.
[50] NOWACK B., BUCHELI T.D., Environ. Pollut. **150**, pp. 150, 5–22, 2007.
[51] BECKER L., POREDA R.J., HUNT A.G., BUNCH T.E., RAMPINO M., Science **291**, pp. 1530–1533, 2001.
[52] BUFFLE J., Environ. Chem. **3**, pp. 155–158, 2006.
[53] GOLDBERG E.D., *Black carbon in the environment*, 1985 John Wiley&Sons, NewYork.
[54] HEYMANN D., JENNESKENS L.W., JEHLICKA J., KOPER C., VLIETSTRA E., Fuller. Nanotub. Carbonnn Nanostruct. **11**, pp. 333–370, 2003.
[55] WAYCHUNAS G.A., KIM C.S., BANFIELD J.F., NANOPART J., Res. **7**, pp. 409–433, 2005.
[56] DOMINGOS R.F., TUFENKJII N., WILKINSON K.J., Environ. Sci. Technol. **43**, pp. 1282–1286, 2009.

[57] MENDIVE C.B., BREDOW T., FELDHOFF A., BLESA M.A., BAHNEMANN D., Phys. Chem. Phys. **11**, pp. 1794–1808, 2009.
[58] LEVARD C., DOELSCH E., ROSE J., MASION A., BASILE-DOELSCH I., PROUX O., HAZEMAN J.-L., BORSCHNECK D., BOTTERO J.-Y., Geochim. Cosmochim. **73**, pp. 4750–4760, 2009.
[59] ZHANG H.J., CHEN G.H., Environ. Sci. Technol. **43**, pp. 2905–2910, 2009.
[60] WANG X., TAO S., XING B., Environ. Sci. Technol. **43**, pp. 6214–6219, 2009.
[61] HASSELOV M., KAMMER von der F., Elements **4**, pp. 401–406, 2008.
[62] PETTIBONE J.M., CWIERTNY D.M., SCHERER D.M., GRASSIA V.H., Langmuir, **24**, pp. 6659–6667, 2008.
[63] MARTINSON C.A., REDDY K.J., J. Colloid Interface Sci. **336**, pp. 406–411, 2009.
[64] ELLIOT D.W., LIEN H.L., ZHANG W.X., J. Environ. Qual. **37**, pp. 2192–2201, 2009.
[65] YANG K., XIN B.S., Environ. Sci. Technol. **43**, pp. 1845–1851, 2009.
[66] PETERSEN E.J., PINTO R.A., LANDRUM P.F., WEBER J., WALTER J., Environ. Sci. Technol. **43**, pp. 4181–4187, 2009.
[67] BANIAMERIAN M.J., MORADI S.E., NOORI A., SALAHI H., Appl. Surf. Sci. **256**, pp. 1347–1354, 2009.
[68] FANG J., SHAN X.-Q., WEN B., LIN J.-M., OWENS G., Environ. Pollut. **157**, pp. 1101–1109, 2009.
[69] SCHIERZ A., ZANKER H., Environ. Pollut. **157**, pp. 1088–1094, 2009.
[70] HOFMANN T., KAMMER von der F., Environ. Pollut. **209**, pp. 1117–1126, 2009.
[71] LIU X., O'CAROLL D.M., PETERSEN E.J., HUANG Q., ANDERSON C.L., Environ. Sci. Technol. **43**, pp. 8153–8158, 2009.
[72] CAO A., Anal. Lett. **36**, p. 3185, 2003.
[73] TIEDE K., HASSELOV M., BREITBARTH E., CHAUDRY Q., BOXALL A.B.A., J. Chromatogr. A, 503, 2009.
[74] PLATHE K., KAMMER VON DER F., HASSELOV M., MOORE J., MURAYAMA M., HOFMANN T., HOCHELLA M.F., Environ. Chem. **7**, p. 82, 2010.
[75] TIEDE K., BOXALL A.B.A., TEAR S.P., LEWIS J., DAVID H., HASSELOV M., Food Addit. Contam. p. 795, 2008.
[76] GIDDINS J.C., *The field-flow fractionaltion family: underlying principles*, in Field-flow fractionation handbook, pp. 3–29, Wiley, New York USA, 2000.
[77] JACKSON B.P., RANVILLE J.F., BERTSCH P.M., SOWDER A.G., Environ. Sci. Technol. **39**, p. 2478, 2005.
[78] SIRIPINYANOND A., BARNES R.M., AMARASIRIWARDENA D., J. Anal. Atom. Spectrom. **17**, p. 1055, 2002.
[79] BAALOUSHA M., KAMMER F.V.D., MOTELICA-HEINO M., BABOROWSKI M., HOFMEISTER C., COUSTUMER Le P., J. Chromatogr. A, **109**, p. 3156, 2005.
[80] BOLEA E., LABORDA F., CASTILO J.R., Anal. Chim. Acta **661**, p. 206, 2010.
[81] DUBASCOUX S., KAMMER Von Der F., Le HÉCHO I., GAUTIER M.P., LESPES G., J. Chromatogr. A **1206**, p. 160, 2008.
[82] AMARASIRIWARDENA D., SIRIPINYANOND A., BARNES R.M., J. Anal. Atom. Spectrom. **16**, p. 978, 2001.
[83] ALASONATI E., DUBASCOUX S., LESPES G., SLAVEYKOVA V.I., Environ.Chem. **7**, p. 215, 2010.
[84] RATY J.Y., GALLI G., J. Electroanal. Chem. **9**, p. 584, 2005.
[85] JIANG G., ZHENG Q., J. Appl. Polymer Sci. **97**, p. 2182, 2005.
[86] ROY D., CHHOWALLA M., WANG H., SANO N., ALEXANDROU I., CLAINE T.W., AMARATUNGA G.A.J., Chem. Phys. Lett. **373**, p. 52, 2003.
[87] DAI H., Surf. Sci. **500**, p. 218, 2002.
[88] LI X., CHEN G., Mat. Let. **63**, pp. 930–932, 2009.
[89] YANG K., WANG X.L., ZHU L.Z., XING B.S., Environ. Sci. Technol. **40**, pp. 1855–1861, 2006.
[90] ALLEN-KING R.M., GRATHWOLL P., BALL W.P., Adv. Water Resour. **25**, p. 985–1016, 2002.
[91] GOTOVAC S., HATTORI Y., NOGUCHI D., MIYAMOTO J, KANAMARU M., UTSUMI S., KANOH H., KANEKO K., J. Phys. Chem. B **110**, pp. 6236–6244, 206.

[92] PENG X.J., LI Y.H., LUAN Z.K., DI Z.C., WANG H.Y., TIAN B.H., JIA Z.P., Chem. Phys. Lett. **376**, pp. 154–158, 2003.
[93] YANG F.H., LACHAWIEK A.J., YANG R.T., J. Phys. Chem. B **110**, pp. 6236–6244, 2006.
[94] PUNYAMURTULA V.K., QIAO Y., Mater. Res. Innovation **11**, pp. 37–39, 2007.
[95] YAN H., GONG A J., HE H.S., ZHOU J., WEI Y.X., LV I., Chemosphere **62**, pp. 142–148, 2006.
[96] LU C.S., CHUNG Y.L., CHANG C.F., Water Res. **39**, (2005), pp. 1183–1189, 2005.
[97] WANG X.K., CHEN C.L., HU W.P., DING A.P., XU D., ZHOU X., Environ. Sci. Technol. **39**, pp. 2856–2860, 2005.
[98] HEYMANN D., JENNESKENS L.W., JEHLICKA J., KOPER C., VLIETSTRA E., Fuller. Nanotub. Carbon Nanostruct. **11**, pp. 333–370, 2003.
[99] CORNELISSEN G., GUSTAFSSON O., BUCHELI T.D., JONKER M.T.O., KOELMANS A.A., NOORT van P.C.M., Environ. Sci. Technol. **39**, pp. 6881–6885, 2005.
[100] KOELMANS A.A., JONKER M.T.O., CORNELISSEN G., BUCHELI T.D., NOORT Van P.C.M., GUSTAFSSON O., Chemosphere **63**, pp. 365–377, 2006.
[101] LONG R.Q., YANG R.T., J. Am. Chem .Soc. **123**, pp. 2058–2059, 2001.
[102] GOTOVAC S., HATTORI Y., NOGUCHI D., MIYAMOTO J., KANAMARU M., UTSUMI S., KANOH H., KANEKO K., J. Phys. Chem. B **110**, pp. 16219–16224, 2006.
[103] ZHOU Q.X., XIAO J.P., WANG W.D., J. Chromatogr. A **1125**, pp. 152–158, 2006.
[104] PENG X.J., LI Y.H., LUAN Z.K., DI Z.C., WANG H.Y., TIAN B.H., JIA Z.P., Chem. Phys. Lett. **376**, pp. 154–158, 2003.
[105] CAI Y.Q., CAI Y.E., MOU S.F., LU Y.Q., J. Chromatogr. A. **1081**, pp. 245–247, 2005.
[106] FUGETSU B., SATOH S., SHIBA T., MIZUTANI T., LIN B., TERUI N., NODASAKA Y., SASA K., SHIMIZU K., AKASAKA T., SHINDOH M., SHIBATA K.I., YOKOYAMA A., MORI M., TANAKA K., SATO Y., TOHJI K., TANAKA S., NISHI N., WATARI F., Environ.Sci.Technol. **38**, pp. 6890–6896, 2004.
[107] ZHOU Q.X., DING X.J., XIAO J.P., Anal. Bioanal. Chem. **385**, pp. 1520–1525, 2006.
[108] ZHOU Q.X., XIAO J.P., WANG W.D., Microchim.Acta **157**, pp. 93–98, 2007.
[109] BIESAGA M., PYRZYNSKA K., J. Sep. Sci. **29**, pp. 2241–2244, 2006.
[110] LIANG P., DING Q., SONG F., J.Sep.Sci. **28**, pp. 2339–2343, 2005.
[111] CHEN C.L., WANG X.K., Ind. Eng. Chem. Res. **45**, pp. 9144–9149, 2006.
[112] LI Y.H., WANG S.G., LUAN Z.K., DING J., XU C.L., WU D.H., Carbon **41**, pp. 1057–1062, 2003.
[113] LIANG P., LIU Y., GUO L., ZENG J., LU H.B., J. Anal. At. Spectrom. **19**, pp. 1489–1492, 2004.
[114] Li Y.H., Zhu Y.Q., Zhao Y.M., Wu D.H., Luan Z.K., Diam. Relat. Mater. **15**, pp. 90–94, 2006.
[115] DING Q., LIANG P., SONG F., XIANG A., Sep. Sci. Technol. **41**, pp. 2723–2732, 2006.
[116] LIANG P., YU Y., GUO L., Spectrochim.Acta B **60**, pp. 125–129, 2005.
[117] CHENG X., KAN A.T., TOMSON M.B., J. Nanopart. Res. **7,** pp. 555–567, 2005.
[118] YANG K., XING B., Environ. Pollut. **145**, pp. 529–537, 2007.
[119] BALLESTEROS E., GALLEGO M., VARCARCEL M., J. Chromatogr. A **869**, pp. 101–110, 2000.
[120] YANG K., ZHU L., XING B., Environ. Sci. Pollut. Research **17**(2), pp. 410–419, 2010.
[121] LU J., LI Y., YAN X., SHI B., WANG D., TANG H., Colloids and Surfaces A: Physicochemcial and Engineering Aspects **347**(1-3), p. 90–96, 2009.
[122] TAN X., WANG X., CHEN C., SUN A., Applied Radiation and Isotopes **65**(4), pp. 375–381, 2007.
[123] LI D., LYON D.Y., LI Q., ALVAREZ P.J.J., Environ. Toxicol. And Chemistry **27**(9), pp. 1888–1894, 2008.
[124] TOWELL M.G., BROWNE L.A., PATON G.I., SEMPLE K.T., Environ. Pollut. **159**, pp. 706–715, 2011.
[125] YUAN C., HUNG C.-H., CHEN K.-C., J. Haz. Mat. (1-3), pp. 563–570, 2009.
[126] ASSENSIO-RAMOS M., BORGES-HERNANDEZ J., BORGES-MIGUEL T.M., RODRIGUEZ-DELGADO M.A., Anal. Chim. Acta **647**(2), pp. 167–176, 209.
[127] PETERSEN E.J., PINTO R.A., LANDRUM P.F., WELER Jr.W.J., Environ. Sci. Technol. **43**(11), pp. 4181–4187, 2009.

[128] YUAN C., HUNG C.-H, HUANG W.-L., Separation Sci. Technol. **44**(10), pp. 2284–2303, 2009.
[129] WANG X., JIALONG L.U., XING B., Environ. Sci. Technol. **42**(9), pp. 3207–3212, 2008.
[130] WANG X., CHEN C., HU W., DING A., XU D., ZHOU X., Environ. Sci. Technol. **39**(8), pp. 2856–2860, 2005.
[131] NOWACK B., BUCHELI T.D., Environ. Pollut. **150**(1), pp. 5–22, 2007.
[132] CHEN W., DUAN L., ZHU D.Q., Environ. Sci. Technol. **41**, pp. 8295–8300, 2007.
[133] PARK S., RUOFF R.S., Nature nanotechnology **58**, pp. 217–224, 2009.
[134] GOTOVAC S., HATTORI Y., NOGUCHI D., MIYAMOTO J., KANAMARU M., UTSUMI S., KANOH H., KANEKO K., J. Phys. Chem. B **110**, pp. 16219–16224, 2006.
[135] WANG J., MAX X., FANG G., PAN M., YE X., WANG S., J. Haz. Mat. **186**(2-3), pp. 1985–1992, 2011.
[136] M. Bystrzejewski, K. Pyrzynska, Colloids and Surfaces A: Physicochemical and Engineering Aspects, 2011 in press.
[137] TIAN X., ZHOU S., ZHANG Z., HE X., YU M., LIN D., Environ. Sci. Technol. **44**, pp. 8144–8149, 2010.
[138] AFZALI D., GHASEMINEZHAD S., TAHER M.A., J. AOAC International **93**(4), pp. 1287–1292, 2010.
[139] PYRZYNSKA K., BYSTRZEJEWSKI M., Colloids and Surfaces: Physicochemical and Engineering Aspects **362**(1-3), pp. 102–109, 2010.
[140] LUO G., YAO H., XU M., CIU X., CHEN W., GUPTA R., XU Z., Energy and Fuels **24**(1), pp. 419–426, 2010.
[141] LUO G., YAO H., XU M., XU Z., J. Huazhong Univ. of Science and Technology **38**(1), pp. 129–132, 2010.
[142] XU D., TAN X., CHEN C., WANG X., J. Haz. Mat. **154**(1-3), pp. 407–416, 2008.
[143] LIU Y., LI Y., YAN X.-P., Advanced Functional Materials **18**(10), pp. 1536–1543, 2008.
[144] El-SHEIKH A.H., Talanta **7591**, pp. 127–134, 2008.
[145] RAO G.P., LU C., SU F., Separation and Purification Technology **58**(1), pp. 224–231, 2007.
[146] PYRZYNSKA K., Anal. Sci. **23**(6), pp. 631–637, 2007.
[147] LU C., LIU C., J. Chem. Technol. **81**(12), pp. 1932–1940, 2006.
[148] ZHANG X., PAN B., YANG K., ZHANG D., HO J., J. Environ. Sci. And Health(A)/Toxic hazardous substances&environmental engineering **45**(12), pp. 1625–1634, 2010.
[149] YANG K., WU W., JING O., JIANG W., XING B., Environ. Sci. Technol. **44**(8), pp. 3021–3027, 2010.
[150] WANG X., XING B., ACS National Meeting Book of Abstracts, 2008.
[151] LIN D., XING B., Environ. Sci. Technol. **42**(19), pp. 7254–7259, 2008.
[152] WANG X., JIALONG L.U., XING B., Environ. Sci. Technol. **42**(9), pp. 3207–3219, 2008.
[153] YANG K., WANG X., ZHU L., Environ. Sci. Technol. **40**(18), pp. 5804–5810, 2006.
[154] MIBECK B.A.F., OLSON E.S., MILLER S.J., Fuel Processing Technology **9**(11), pp. 1364–1371, 2009.
[155] CHO H.-H., SMITH B., FAIRBROTHER K.A., BALL W.P., ACS National Meeting Book of Abstracts, 2008.
[156] CHEN J., ZHU D., SUN C., Environ. Sci. Technol. **41**(7), pp. 2536–2541, 2007.
[157] LI X., CHEN G.H., Mater. Lett. **63**, pp. 930–932, 2009.
[158] OH S.-Y., CHIU P.C., Environ. Sci. Technol. **4**3(18), pp. 6983–6988, 2009.
[159] MOLCHANOV V.V., SHCHUCHKIN M.N., ZAIKOVSKII V.I., BOGDANOF S.V., ZAITSEVA N.A., Kinetic and Catalysis **49**(5), pp. 702–707, 2009.
[160] ZHU D., KVON S., PIGNATELO J.J., Environ. Sci. Technol. **39**(11), pp. 3990–3998, 2005.
[161] ZHU D., PIGNATELO J.J., Environ. Sci. Technol. **3**9(7), pp. 2033–2041, 2005.
[162] PIGNATELLO J.J., Environ. Sci. Technol. **39**(6), pp. 1606–1615, 2005.
[163] ION A.C., ALPATOVA A., ION I., CULETU A., Mat. Sci. Eng. B, 2011, doi: 10.1016/j.mseb.2011.01.018.
[164] ION A.C., ION I., CULETU A., Mat. Sci. Eng. B, 2010, doi: 10.1016/j.mseb.2010.07.021.
[165] CHEN J., ZHU D., SUN C., Environ. Sci. Technol. **41**(7), pp. 2536–2541, 2007.

Novel Concepts for CO_2 Detection by Differential Resonant Nanosensing

Bogdan SERBAN, Cornel COBIANU, Cazimir BOSTAN

Sensors &Wireless Laboratory Bucharest, 169A
Floreasca Street, Building A, 014459, Honeywell Romania, Bucharest, Romania
E-mail: bogdan.serban@honeywell.com

Abstract. In this paper we present two general approaches for silicon surface functionalization to be used in carbon dioxide detection by means of MEMS/NEMS nano-cantilever based resonant sensors. In the first chemical route, the synthesis of sensing layer can be performed using 1,8 diazabicyclo[5,4,0] undec-7-ene (DBU) or 1,5 diaza [3,4,0]-non-5-ene (DBN), as sensing terminal groups. This functionalization is according to Bronsted –Lowry theory. In the second chemical route, the functionalized monolayer involves amino groups as sensitive pendant groups, according to HSAB theory. A comparison between both types of functionalization in terms of sensing mechanism, reversibility, response time, temperature operation, cross sensitivity, versatility of synthesis is presented. We propose novel resonant differential sensing principles aiming at further improving the performances of the resonant differential sensors in terms of drift reduction.

1. Introduction

Low cost detection and monitoring of carbon dioxide (CO_2) has a crucial importance in the area of gas sensors, considering the huge impact of CO_2 emissions to the global warming and the need to survey large ground where the greenhouse gas is generated and even the underground areas, where it is sequestrated.

Chemical CO_2 gas sensors with sensitive layers based on polymers or small molecules exhibit some advantages in comparison with spectroscopic sensors, e.g. low energy consumption, simplicity , small size. In the last decade, much attention has been paid to find or design new CO_2 sensitive compounds which could ensure specificity, ambient conditions operations, fast and reversible response, high sensitivity[1].

Among the many organic and inorganic compounds known to have carbon dioxide sensing properties, amino group-based polymers and small molecules containing nitrogen atoms has been extensively studied[1-3].

Synthesis and selection of these CO_2 sensitive compounds were performed using two different approaches.

Hard soft acid bases (HSAB) theory has been introduced as useful tool for design/selection of different carbon dioxide sensing layers.

A lot of older proposed solutions such as polyethyleneimine, Versamid 900, BMBT, monoethanolamine (MEA), diethanolamine (DEA), diisopropilamine (DIPA), triethanolamine (TEA), n-methyldiethanolamine (MDEA) polyallylamine, polyvinylamine, polyetyleneimine –amino carbon nanotubes matrix nanocomposites, polyallylamine –aminocarbon nanotubes matrix nanocomposites, ionic liquid with amino groups can be understood in the view of this principle [4-13].

Acid-bases Bronsted-Lowry theory is another useful method to select potential carbon dioxide sensitive layers. Taking into account the basicity of nitrogen atoms –based organic compounds[14] several compounds has been tested: 1,8 diazabicyclo[5, 4, 0] undec-7-ene (DBU) or 1,5 diaza [3, 4, 0]-non-5-ene (DBN), polyguanidines, polyamidines, DBU- methyl phenylsilica, polyether DBU, etc [15-20]

In this paper we report the functionalization of silicon surface of vibrating nanobeams of resonant sensors for CO_2 detection. Design of this functionalization can be performed according to Bronsted –Lowry theory (as it will be shown in section 3A) and HSAB theory (as it will be shown in section 3B).

In addition, we describe our concept of all-differential resonant gas sensing, aiming at an increased accuracy of sensing by minimizing the baseline drift of the detector, and thus preserving long term operation stability [21-27]. Our functionalization method based on HSAB theory is in agreement with the results shown in Ref. [28].

2. Resonant MEMS/NEMS GAS Sensing

After more than three decades of research, the Micro (Nano)-Electro-Mechanical Systems (MEMS/NEMS) for resonant sensing are becoming a mature principle, with high expectations in the field of chemical detection for biomolecules and gases monitoring [29-32]. The resonant chemical detection principle consists in the shift of the natural resonance frequency of a vibrating beam as a function of the mass loading created by the analyte which has to be selectively adsorbed on the functionalized sensing surface. With the increasing demand for very highly sensitive and selective sensors, the emerging Nano-Electro-Mechanical Systems (NEMS) are pushing the gas sensing limits much beyond the state of the art, and where the mass of the adsorbed gases on the

sensing surface is below 1 zeptogram [32]. As this detection is performed at room temperature, the loading effect of humidity should be eliminated, as well as any influence of ambient temperature variation on the resonance frequency. Traditionally, these "common mode" signals, like temperature and humidity, with deleterious effect on sensor accuracy and its baseline drift have been rejected by using a differential resonant approach, as shown in Fig. 1. In this figure, one can see a sensing loop containing an electronic oscillator and the coated MEMS/NEMS vibrating beam in the feed-back, and an "identical" reference loop, which is containing an identical oscillator and an uncoated vibrating beam. The resonance frequency of the vibrating beam is determining the frequency of the oscillator. The two loops are tuned so that to have the same resonance frequency in the absence of the analyte to be detected, but they will become different in the presence of the gas to be detected, as shown in Fig.1. Subtraction of the two resonance frequencies, at the level of the mixer, will provide a frequency difference which will be proportional to the gas to be measured. Such a classical differential approach is using only one functionalized layer on the vibrating sensing beam, while the uncoated surface of a similar vibrating beam is performing the reference function. Unfortunately, this approach does not compensate the sensor response for the sensing layer ageing; moreover, it is limited in compensating the humidity effect, when the uncoated surface has a different humidity response compared to the surface of the functionalized sensing layer. In order to solve these drawbacks of the classical differential resonant chemical sensors, we have proposed a novel differential resonant concept, as shown in Fig. 2, where a reference layer is added on the reference vibrating beam. This layer is designed to have a humidity and visco-elastic behavior similar to that of the sensing layer, but no sensing properties.

The novelty of our approach comes from the chemical functionalization of the silicon surface of nanoresonator and by the use of the reference sensing monolayer, which will have the same physical properties as the sensing layer, but no sensing capabilities. Such an all differential sensing principle, where a reference layer is added on the surface is solving the prior-art drift issues specific to differential resonant chemical sensors, where the reference loop had only an uncoated surface, which could not eliminate the humidity and aging effects of sensing layer from the sensor response.

The good thing is that such reference layers have almost similar physical response to temperature, humidity and aging in general, which make them very suitable for the differential sensing where the above "common mode signals" can be eliminated, while the differential signal (containing only CO_2 response) may be accurate and drift-free.

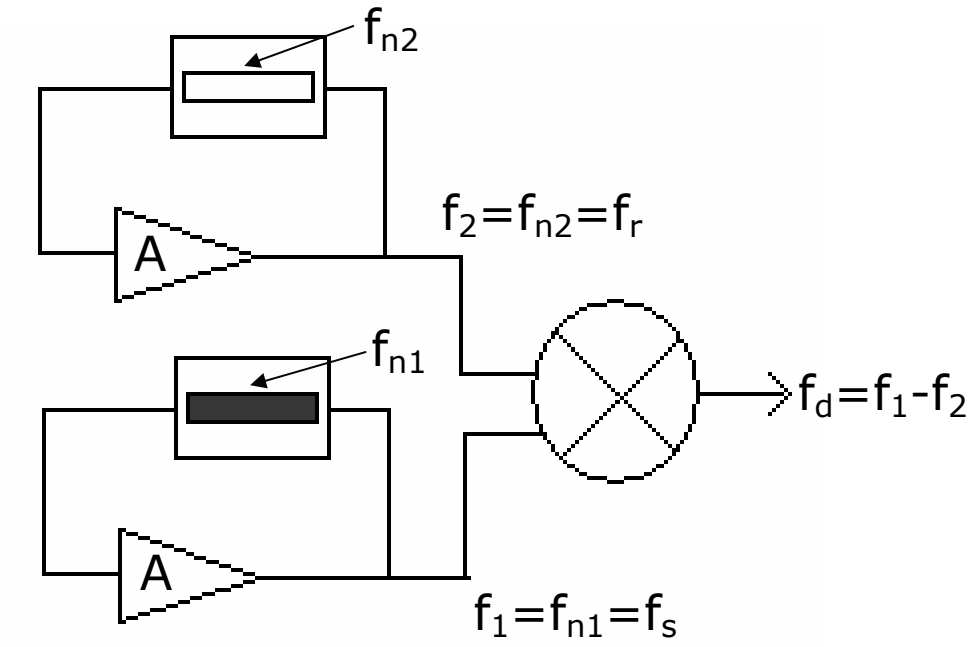

Fig. 1. Differential resonant MEMS/NEMS gas sensor with uncoated reference beam

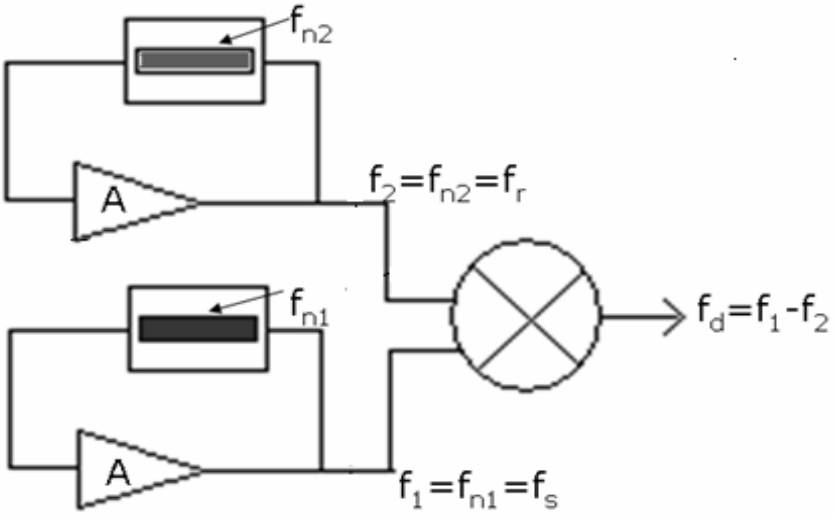

Fig. 2. Differential resonant MEMS/NEMS gas sensor with coated reference beam.

3. Results and Discussions

Self-assembled monolayers (SAMs) have been the subject of an intense study because of their potential in chemical sensing applications. Such a sensing monolayer is made of molecules that have a terminal group which is attached to the suspended silicon beam and the other which is functionalized for CO_2 recognition and detection.

A. Functionalization of silicon resonant nanosensor according to Bronsted- Lowry theory.

The chemical design of the sensing monolayer with main focus on the functional sensing group was based on Bronsted–Lowry theory. The proposed sensing layers contain CO_2 sensitive pendant groups such as 1,8 diazabicyclo [5,4,0] undec-7-ene (DBU) or 1,5 diaza [3,4,0]-non-5-ene (DBN)[21-26], which are presented in Fig.3 from below.

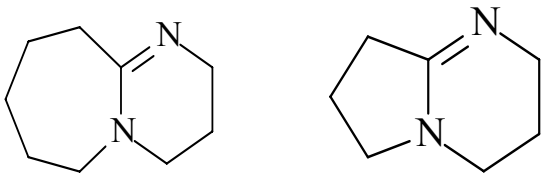

DBU DBN

Fig. 3. The structure of DBU and DBN.

Both DBU and DBN are highly basic (high pKa values) and are able to react at room temperature simultaneously with carbon dioxide and water according to the following equations, from Figs. 4 and 5.

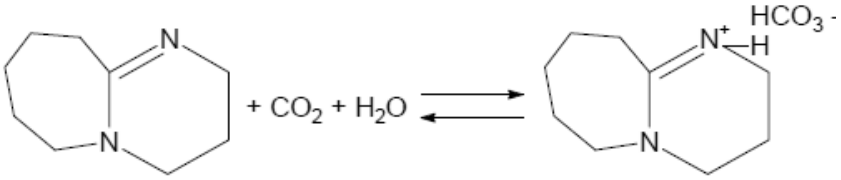

Fig. 4. The reaction of DBU with carbon dioxide and water at room temperature.

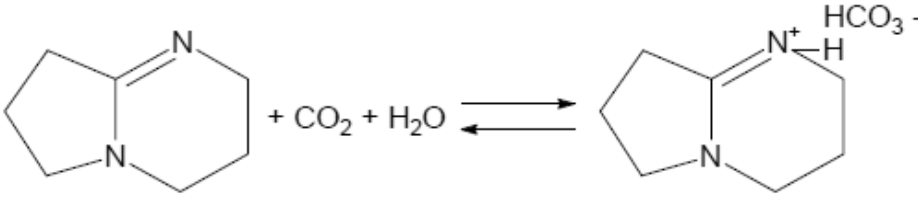

Fig. 5. The reaction of DBN with carbon dioxide and water at room temperature.

The DBU and DBN sensing moieties are covalently bonded to the Si surface by means of either alkyl chain groups (route I) or styrene moiety (route II).

The sequence of DBU functionalization processes by route I is as follows:

1) Wafer cleaning avoiding sticking of the suspended membrane to the substrate.
2) Native oxide removal from suspended Si beam in 1% HF in order to create hydrogen -terminated Si beam surface (Fig. 6a).
3) Immersion of the wafers containing suspended beam having its hydrogen-terminated surface in a flask containing unsaturated alkyl halide such as alkyl chloride and toluene followed by heating the sealed flask for formation of alkyl monolayer on the Si surface (Fig. 6b).
4) Rinsing the wafers in isopropyl alcohol, followed by their cleaning and drying so as to avoid suspended beam sticking to the substrate.
5) Deprotonation of the DBU at low temperatures, in the presence of butyl lithium (Fig. 6c).
6) Reaction of deprotonated DBU with alkyl chloride monolayer from the silicon surface in order to obtain the CO2 sensing layer (Fig. 6d).

The scheme of this synthesis is shown below in Figs.6 a-d:

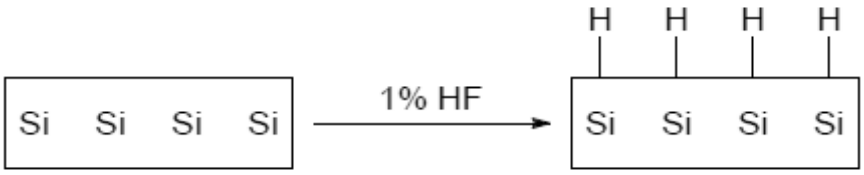

Fig. 6a. Hydrogenation of the silicon surface.

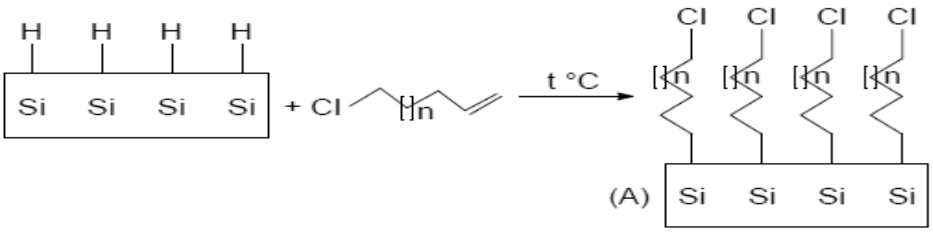

Fig. 6b. Formation of alkyl monolayer on the Si surface.

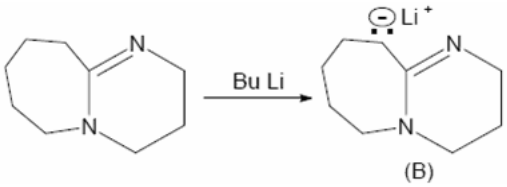

Fig. 6c. Deprotonation of DBU in butyl lithium in order to obtain the compound B (deprotonated DBU)

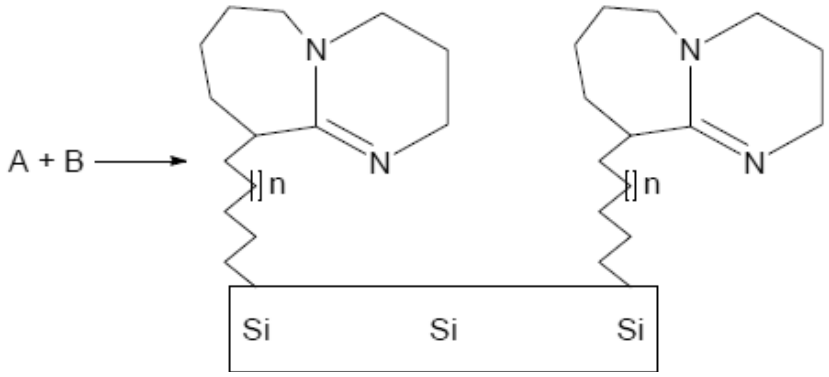

Fig. 6d. Attachment of DBU sensing moieties from the silicon surface through covalent bonding.

A similar approach is followed for the DBN functionalization process where deprotonated DBN (Fig. 7a) is reacting with alkyl chloride monolayer from Si surface in order to obtain a surface with DBN moiety (Fig.7b), which is sensitive to the CO_2 gas.

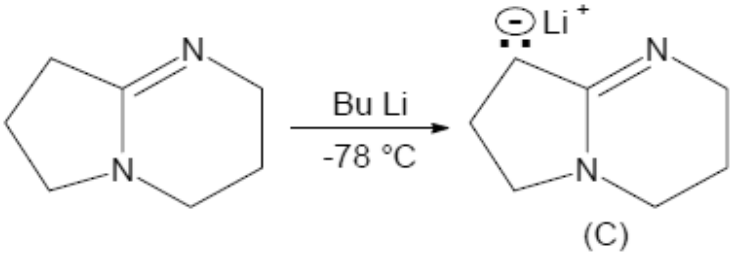

Fig. 7a. Deprotonation of DBN.

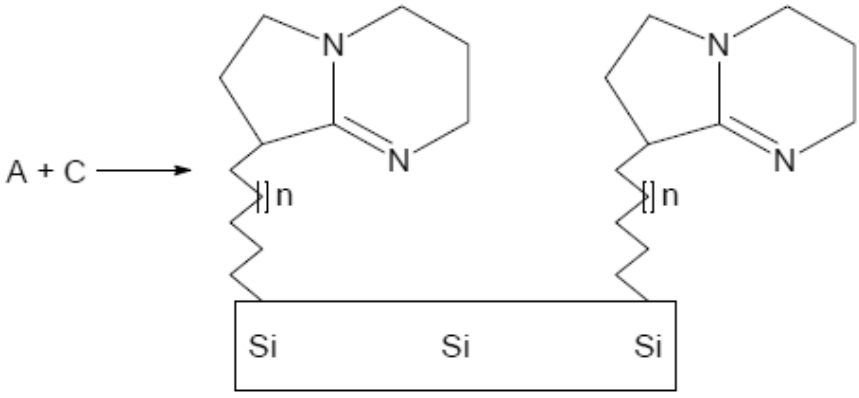

Fig. 7b. Attachment of DBN sensing moieties from the silicon surface through covalent bonding.

The reference layers have almost similar nature like the above DBN and BDU, because they originate from the above sensing layer but in this case, the amidine moieties are converted into hydrochlorides, and thus, we get no sensitivity to CO_2 on the reference channel.

The sequence of DBU functionalization process by route II (Figs. 8a-c) is as follows:

1) Wafer cleaning avoiding sticking of the suspended membrane to the substrate.
2) Native oxide removal from suspended Si beam in 1% HF for getting H-terminated Si beam surface
3) Immersion of the wafers containing suspended beam having its hydrogen-terminated surface in flask containing chloromethylated styrene and toluene followed by heating the sealed flask for getting a monolayer of chloromethylated styrene connected to the Si surface by styrene moiety (Fig. 8a).
4) Rinsing the wafers in isopropyl alcohol, followed by their cleaning and drying so as to avoid suspended beam sticking to the substrate.
5) Deprotonation of the DBU at low temperature , in the presence of butyl lithium
6) Reaction of deprotonated DBU with compound A' in order to synthesize the DBU based sensing layer connected by styrene moiety to the Si surface (Fig. 8b).

The reference layer for the DBU based sensing layer connected by styrene moiety to Si surface is obtained by the reaction of the above DBU based sensing layer with HCl, by selectively printing liquid HCl only on the surface of the future reference beams.

A similar approach is followed by the DBN functionalization process by the route II (Fig. 8c)

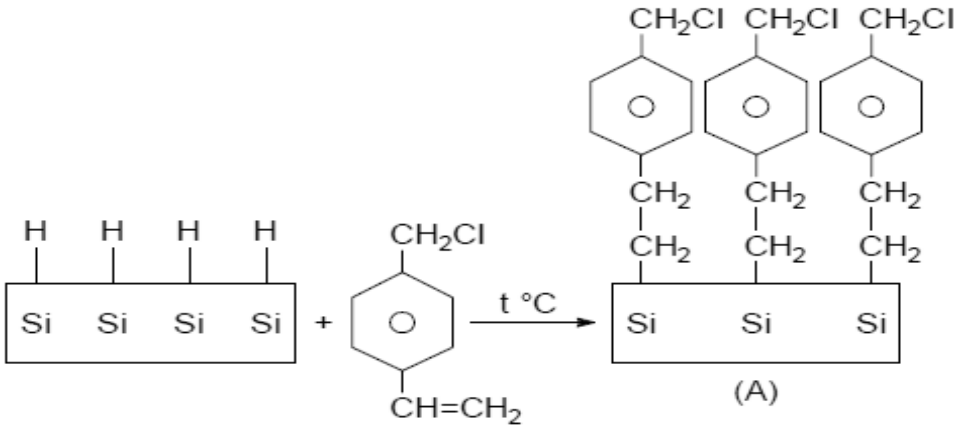

Fig. 8a. Formation of a monolayer of chloromethylated styrene on Si surface.

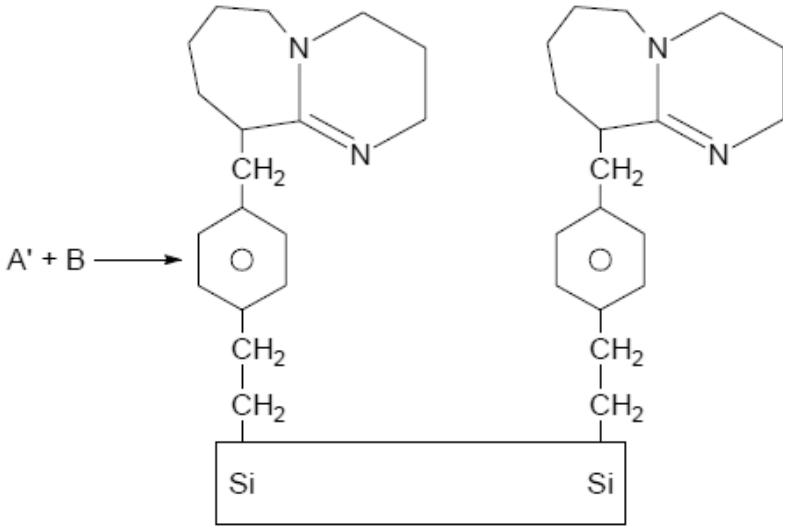

Fig. 8b. DBU based layer connected to Si surface by styrene moiety.

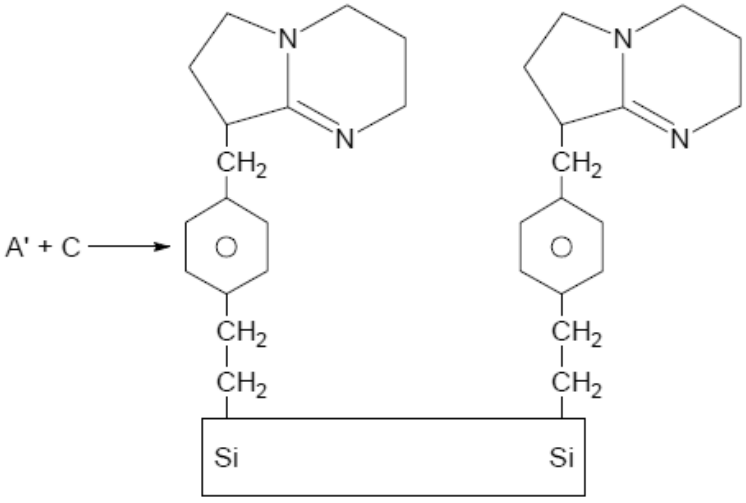

Fig. 8c. Attachment of DBN sensing moieties from the silicon surface through covalent bonding

B. Functionalization of silicon resonant nanosensor according to HSAB theory[27-28]

The selection and design of sensitive terminal groups which are incorporated in the SAMs was based on the Hard Soft Acid Base (HSAB) rule. According to this

theory, a hard Lewis base prefers to bond to a hard Lewis acid, and a soft Lewis base prefer to bond to a soft Lewis acid. Carbon dioxide is a hard acid, and, according to HSAB rule, it can interact with amino groups, which are hard bases. This interaction is an acid-base equilibrium, which is reversible and it leads to the formation of carbamates.

Thus, we obtain the CO2 sensing SAM which is functionalized with amino-terminated groups to be used as anchors for CO2 detection. We have also chemically designed the molecular composition of the reference SAM, so that this will not respond to CO2 but will have the same response to humidity and similar ageing properties, as the sensing SAM.

The whole process is following the steps presented in Figs.9a-c.

1) Cleaning of processed silicon wafers (samples) containing suspended Si nano-beam and AuCr metallization for 1 h in isopropyl alcohol.
2) Rinsing with deionizated water.
3) Immersion in 2% HF in DI water for five minutes in order to remove the native SiO_2 from the Si surface and to generate Si-H bonds on the Si surface (Fig. 9a).
4) Exposure to a flow of ozone for a short period of time in order to obtain a hydroxyl terminated surface (Fig. 9b).
5) Immersion of the hydroxyl terminated samples in a sealed flask containing one of the possible amino alcohols (4 amino- 1 butanol, 4- N-methyl amino- 1 – butanol, 5 amino 1- pentanol, 5 N-methyl amino- 1 pentanol, 6 amino- 1 hexanol, 6 methylamino-1 hexanol, ethanol amine, diethanolamine, 1, 3 diamino 2- propanol) heated in dry nitrogen, in order to allow the polycondensation reaction to happen (Fig. 9c) and a CO_2 sensing SAM monolayer to be formed on the Si surface.
6) Rinsing with isopropyl alcohol, DI water and drying in N_2 stream.

If all the amino groups react at room temperature with hydrochloric acid, the obtained hydrochloride possess the same properties, except the sensing toward carbon dioxide molecules (Fig.10).

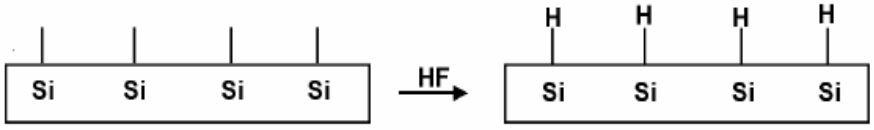

Fig. 9a. Hydrogenation of silicon surface.

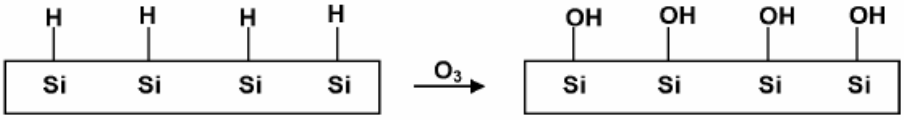

Fig. 9b. Formation of hydroxyl terminated silicon surface.

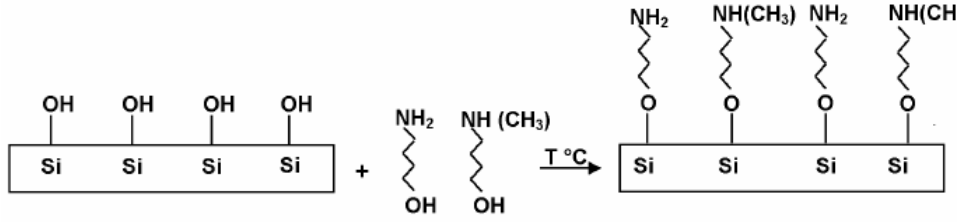

Fig. 9c. Functionalization of CO_2 sensing silicon surface with pendant amino groups.

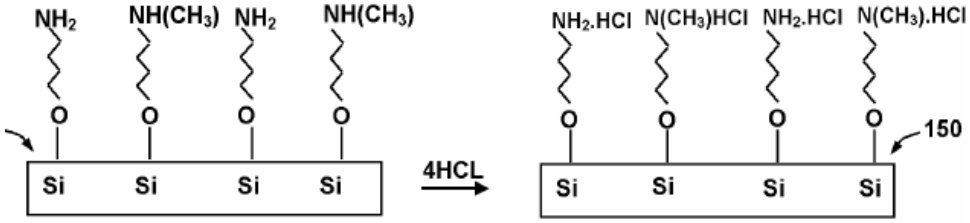

Fig. 10. Synthesis of reference layer by conversion of all amino groups into hydrochloride.

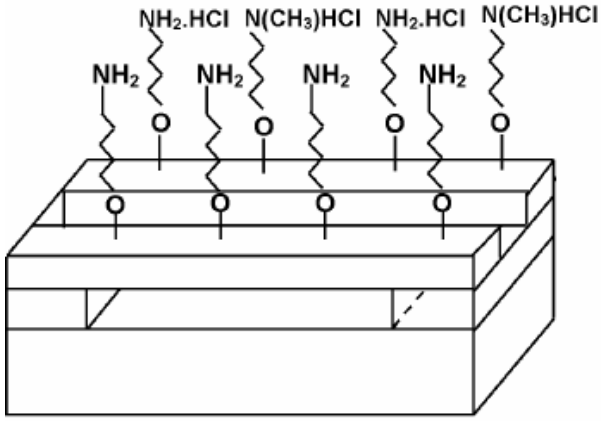

Fig. 11. Silicon suspended beam with sensing layer (which contains terminal amino groups) and reference layer (in which all amino groups are converted into hydrochloride).

In order to increase the number of available amino groups, polycondensation can be performed with 1, 3 diamino-2-propanol (Fig.12).

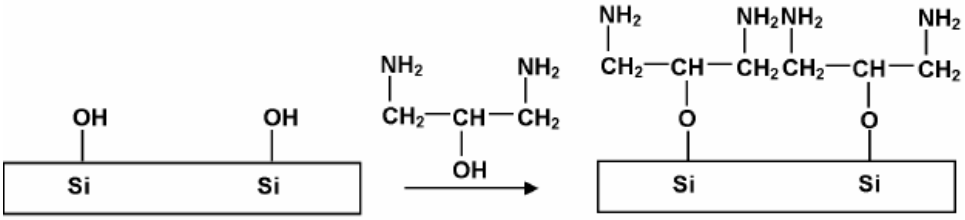

Fig. 12. Polycondensation of OH-terminated silicon surface with 1,3 diamino-2 propanol.

Functionalization with amidines moieties (according to Bronsted–Lowry theory) and functionalization with amino groups (according to HSAB theory) exhibit some differences, which will be analyzed, below in terms of sensing properties .

	DBU and DBN functionalization based on Bronsted–Lowry theory	Amino groups Functionalization based on HSAB theory
Sensing mechanism	Reaction of DBU and DBN with CO_2 and H_2O with the formation of bicarbonate salt; Molar ratio DBU (or DBN):CO2 : H2O is 1:1:1.	Reaction of amino groups with CO_2 with formation of carbamates The molar ratio NH_2 : CO_2 is 2:1
Reversibility	Both reactions are reversible, the trapped CO_2 molecules being released by heating or flowing the inert gas such as N_2	
Response time	Few seconds - in the case of functionalization with amidine moieties	Few seconds - in the case of functionalization with amino groups
Operating Temperature	Both types of sensors at room temperature	
Cross sensitivity	Possible interferences with other acidic gases, such as CS_2, SO_2, COS	Possible interferences with other acidic gases, such as H_2S, SO_2
Versatility of synthesis	Sophisticated and costly synthesis**.** The manipulation of amidines and organometallic compounds must be performed with caution.	more versatile synthesis

DBU and DBN are bases with low pKb.

1. Aliphatic amino groups are hard bases, according to HSAB theory and can react with carbon dioxide which is hard acid.

4. Conclusions

Two general approaches for functionalization of silicon surface to be used for carbon dioxide silicon detection by resonant nanosensors were presented.

Synthesis of sensing layer can be performed using 1,8 diazabicyclo[5,4,0] undec-7-ene (DBU) or 1,5 diaza [3,4,0]-non-5-ene (DBN), as sensing terminal groups. This functionalization is according to Bronsted –Lowry theory.

Other functionalization of silicon surface involves amino groups as sensitive pendant groups, according to HSAB theory.

Novel resonant sensing principles were proposed for further improving the performances of the resonant differential sensors in terms of sensor drift reduction.

A comparison between both type of functionalization in terms of sensing mechanism, reversibility, response time, temperature operation, cross sensitivity, versatility of synthesis was made.

Acknowledgement. The authors are expressing their gratitude to EU-FP-7-NEMSIC project and Honeywell International for their support with developing this research.

References

[1] KORSAH K., MA C.L., DRESS B., *Harmonic frequency analysis of SAW resonator chemical sensors: application to the detection of carbon dioxide and humidity*, Sensors and actuators B **50**, pp. 110–116, 1998.

[2] NIEUWENHUIZEN M.S., NEDERLOF A.J., *A SAW Gas Sensor for Carbon Dioxide and Water. Preliminary Experiments*, Sensors and actuators B **2**, pp. 97–101, 1990.

[3] GABRIELJ.C., GRUNER G., STAR A., *Carbon dioxide nanoelectronic sensor*, WO 2005/026694, A2.

[4] PEARSONR.G., *Hard and soft acids and bases*, J.Am. Chem. Soc., **85**(22), pp. 3533–3539, 1963.

[5] SERBAN B., MIHAILA M., COSTEA S., BUIU O., *New ligand selection rule for quantum dot functionalization*, Proceedings of the International Semiconductor Conference CAS, pp. 81–84, 2009.

[6] SERBAN B., A. SARIN KUMAR K., COBIANU C., BUIU O., COSTEA S., BOSTAN,C. VARACHIU N., *Selection of gas sensing materials using the hard soft acid base theory; Application to surface acoustic wave CO_2 detection,* Proceedings of the International Semiconductor Conference CAS, pp. 247–250, 2010.

[7] COBIANU C., SERBAN B., PETRESCU V., PETTINE J., KARABACAK D., OFFERMAN P., BRONGERSMA S., CHERMAN V., ARMINI S., HASSANI F.A., GHIASS M.A., TSUCHIYA Y., MIZUTA H., DUPRE C., DURRAFOURG L., KOUMELA A., MERCIER D., OLLIER E., TSAMADOS D., and IONESCU A., *Towards nano-scale resonant gas sensors*, Annals of the Academy of Romanian Scientists, Series on Science and Technology of Information, **3**(2), p. 39–50. 2010.

[8] SERBAN B., MIHAILA M., BUIU O., COSTEA S., *A new approach for quantum dot-polymer nanocomposite design*, Nanomeasure, pp.12, 3-4 June, Krakow, 2010.

[9] BUIUO., SERBAN B., MIHAILA M., BREZEANU M. and COSTEA S., *New design approach for quantum dot solar cell*, Second workshop on Size- dependent Effects in Materials for environmental protection, Nessebar, **22**, September 19-21, Bulgaria, 2010.

[10] SERBAN B., SARIN KUMAR A.K., COSTEA S., MIHAILA M., BUIU O., BREZEANU M., VARACHIU N., COBIANU C., *Surface acoustic wave CO_2 sensing with polymer-amino carbon nanotube composites*, Proceedings of the International Semiconductor Conference CAS, pp. 73–76, 2008.

[11] SERBAN B., SARIN KUMAR A.K., COSTEA S., MIHAILA M., BUIU O., BREZEANU M., VARACHIU N., COBIANU C., *Polymer–amino carbon nanotubes nanocomposites for surface acoustic wave CO_2 detection*, Romanian Journal of Information science and technology, **12**(3), p. 376, 2009.

[12] SERBAN B., COBIANU C., BERCU M., VARACHIU N., MIHAILA M., BOSTAN C., VOICU S., *Matrix nanocomposite containing aminocarbon nanotubes for carbon dioxide sensor detection* , Pub.No.: US 2008/0264147 A1, Pub. Date: Oct. 30, 2008.

[13] AVRAMESCU V., BOSTAN C., SERBAN B., GEORGESCU I., COSTEA S., VARACHIU N., COBIANU C., *Surface acoustic wave devices and their sensing capabilities,* Proceedings of the International Semiconductor Conference CAS, pp. 27–36, 2009.

[14] http://evans.harvard.edu/pdf/evans_pKa_table.pdf

[15] HELDEBRANT D.J, JESSOP P.G., THOMAS C.A., ECKERT C.A. and LIOTTA C.L., *The reaction of 1,8-diazabicyclo[5.4.0]undec-7-ene (DBU) with carbon dioxide,* J.Org.Chem. **70**, pp. 5335–5338, 2005.

[16] OCHIAI B., YOKOTA K., FUJII A., NAGAI D., ENDO T., *Reversible trap-release of CO_2 by polymers bearing DBU and DBN moieties,* Macromolecules, **41**, pp. 1229–1236, 2008.

[17] GATTUSO S.A., *Carbon dioxide capture by tertiary amidine functional adsorbents,* PhD Thesis, University of Pittsburg, 2007.

[18] TOMOI M., KATO Y., KAKIUCHI H., *Polystyrene-supported 1,8-diazabicyclo [5,4,0]undec-7-ene as reagent in organic synthesis*, Macromol. Chem. **185**, pp. 2117–2124, 1984.

[19] BOHME F., KLINGER C., BELMANN C., *Surface properties of polyamidines. Colloids and surfaces* A. **189**, pp. 21–279, 2001.

[20] LITTLE R.J., SWAAIJ van W.P.M, VERSTEEG G.F., *Kinetics of carbon dioxide with tertiary amines in aqueous solutions,* AICHEJ **36**, pp. 1633–1640, 1990.

[21] COBIANU C., SERBAN B., *Novel concepts for CO_2 detection by differential resonant nanosensing* (invited paper)**,** a 9-a editie a seminarului national de nanostiinta si nanotehnologie, 16 martie 2010, biblioteca Academiei Romane. Abstract: http://www.romnet.net/ro/seminar16martie2010/brosura%20final%2018%20martie_c1f.pdf

[22] SERBAN B., COBIANU C., MIHAILA M., DUMITRU V., US Patent Aplication, *Carbon Dioxide Sensor With Functionalized Resonating Beams,*

[23] C. COBIANU and B. SERBAN, *"All-differential resonant nanosensor apparatus and method*, U.S patent application, Application number: 12/617,893, Filing date: 11/13/09.

[24] SERBAN B., COBIANU C., MIHAILA M., DUMITRU V., BUIU O., U.S Patent Application, *Carbon Dioxide Sensor*, No.: 10196990.5 Filing Date: December 24, 2010.

[25] COBIANU C., SERBAN B., GEORGESCUI., COSTEA S., BOSTAN C., *A novel concept for low drift chemical sensing at micro and nano scale*, Proceedings of the International Semiconductor Conference, CAS, pp. 217–220**,** 2010.

[26] SERBAN B. and COBIANU C., *Novel concepts for NO2 detection by differential resonant nanosensing*, Nano-Electro-Mechanical Devices for Integrated Sensing and Switching Satellite workshop to ESSDERC/ESSCIRC 2010.

[27] SERBAN B., COBIANU C., MIHAILA M., DUMITRU V.G., US Patent Application No. 12/856891, Filed on 16 August, 2010, *Functionalized Monolayers For Carbon Dioxide Detection by a Resonant Nanosensor.*

[28] ROCCHIA M., GARRONE E., GEOBALDO F., BOARINO L., SAILOR M.J., *Sensing CO_2 in a chemically modified porous silicon film.,* Phys.stat.sol, (a), **197**(2), pp. 365–369, 2003.

[29] BURG T.P., GODIN M., KNUDSEN S.M., SHEN W., CARLSON G., FOSTER J.S., BABCOK K., MANALIS S.R., *Weighing of biomolecules, single cells and single nanoparticles in fluid*, Nature, **446**, pp. 1066–1069, 26 April 2007.

[30] HUANG X.M.H., MANOLIDIS M., JUN S.C. and HONE J., *Nanomechanical Hydrogen Sensing*, Applied Physical Letters, **86**, p. 143104, 2005.

[31] PINNADDUWAGE L.A., BOIADJIEV V., HAWK J.E., and THUNDAT T., *Sensitive Detection of Plastic Explosives with Self-assembled Monolayer-Coated Microcantilevers*, Applied Physics Letters, **83**(7), pp. 1471–1473, 18 August 2003.

[32] LI Mo, TANG H.X. and ROUKES M.L., *Ultra-sensitive NEMS based Cantilevers for Sensing, Scanned Probe, and very High-Frequency Applications*, Nature Nanotechnology, **2**, pp. 114–120, 2007.

Solar Energy Materials Obtained by Spray Pyrolysis Deposition

Anca DUTA, Dana PERNIU, Luminita ISAC, Alexandru ENESCA

Transilvania University of Brasov, Dept. Renewable Energy Systems and Recycling,
Eroilor 29, 500036 Brasov, Romania
E-mail: a.duta@unitbv.ro

Abstract. Efficient and low-cost solar energy conversion devices require large active surfaces of thin oxide films with controlled properties. By increasing the deposition surface, the properties are increasingly difficult to maintain, therefore a careful choice of the deposition technique is required. Spray pyrolysis deposition is a low-cost, up-scalable technique that allows to obtain thin (poly)crystalline films over large surface areas. This paper presents a review on the most important control parameters in SPD, with a focus on organic and polymeric additives. Thin films of TiO_2, CuO, $CuInS_2$ and $CuSbS_2$ are used as case studies in the presentation.

Keywords: spray pyrolisys deposition, thin films, solid state solar cells, solar absorbers, photocatalyst, electrochromic oxides.

1. Introduction

Fossil fuel depletion - but mainly greenhouse gas emissions - drive the attention of the researchers, companies and officials towards alternative energy resources, and solar energy plays in this future scenario a key-role. As such, solar energy is of relatively limited use, in the so-called passive solar applications (buildings, drying, etc.). Heat, power and chemical conversion of solar energy can be designed using the full spectrum of the solar radiation in specific devices and installations. The reasons that limit the use of the solar energy today are strongly related to the conversion devices' efficiency and costs. Integrated solutions for solving these two problems represent a subject of interdisciplinary research, involving advances in materials, equipment design, process design, cost-benefit analysis, marketing and political decisions.

In any conversion installation/equipment, the active conversion element represents the bottle neck for the conversion efficiency, due to (physical) constrains, and mainly related to the materials. Therefore, a careful control of the materials properties is targeted and this can be reached by controlling the

composition, the structure and the morphology. Market-affordable devices also require low amounts of low-cost materials, and metal oxides and sulphides etc., and represent eligible candidates for most of the applications. For a given initial precursor system, these basic properties can be controlled by the deposition/obtaining technique(s) and parameters. For large area devices, the deposition technique must comply with the industrial needs, preferably using already existent manufacturing technologies and equipments. Most of the applications need thin films, most of them as stacked layers.

Several deposition techniques are complying (in certain extent) with these requests: tape casting (doctor blade), hydrothermal synthesis, sol-gel, dipping, chemical bath deposition and spray pyrolysis deposition (SPD). The latest allows the kinetic (nucleation/growth) and thermodynamic control, by fine tuning the deposition parameters, thus allowing tailoring materials for the designed applications.

This paper presents a synthesis of the relevant aspects on obtaining solar energy materials obtained via SPD, detailing on the correlation: materials properties – conversion efficiency for solid state solar cells.

2. Opto-Electric Properties and Defects Chemistry

The fundamental optical and electrical properties of solar energy materials are strongly influenced by their defects chemistry. Usually, defects' formation in the lattice reactions uses the Kröger –Vink notation to outline the point defects, [1]: S_p^q representing:

- the point defect symbol – S, which can be the symbol of an existing ion in the lattice or of an ion vacancy;
- defect electrical charge - q (as super-script) which is represented by dot (.) for an effective positive charge, dash (') for the effective negative charge and (x) for zero-effective charge.
- defect position - p (as subscript) – which can be a regular ion place from the lattice, or in an interstitial position.

One interesting example could be considered the $CuInS_2$ material, where different situations from defect chemistry of solar cell materials are encountered [2].

The $CuInS_2$ (CIS) is a ternary compound and following types of defects can be expected in the lattice:

- cation and anion vacancies (VCu', VIn''',$VS^{\cdot\cdot}$) [3];
- interstitial ions ($Cu_i^{\cdot}$, $In_i^{\cdot\cdot\cdot}$, Si''), [3];
- cation anti-site disorder (Cu-Au ordering), [4].

Intrinsic point defects are most likely thermally generated in CIS according to the Schottky mechanism (the formation of cation and anion vacancies, eq. 12), the Frenkel mechanism (the displacement of a cation in an interstitial position, leaving behind a cation vacancy, eq. 13 and 14), or anti-Frenkel mechanism (the

displacement of an anion in an interstitial position, leaving behind an anion vacancy, eq. 15). The anti-site disorder occurs when cations exchange places in the lattice, i.e. CuIn'' and $InCu^{\cdot\cdot}$. The anti-site defects can form an ordered arrangement, which is referred to as the Cu-Au ordering (Cu-AuCIS), which practically has no semiconductor behaviour, thus being an internal source of shunts.

$$0 \leftrightarrow V_{cu}^{'} + V_{In}^{'''} + 2V_{S}^{\cdot\cdot} \tag{1}$$

$$0 \leftrightarrow \mathrm{Cu_i^{\bullet}} + \mathrm{V_{Cu}^{'}} \tag{2}$$

$$0 \leftrightarrow \mathrm{In_i^{\bullet\bullet\bullet}} + \mathrm{V_{In}^{'''}} \tag{3}$$

$$0 \leftrightarrow S_i^{''} + V_S^{\bullet\bullet} \tag{4}$$

The formation mechanism of the Cu-AuCIS phase can be explained considering the simultaneous formation of Frenkel disorder in both cation sub-lattices of the CIS lattice.

The defect occurrence is under thermodynamic control; for example, the formation of the In interstitial and In vacancy (eq. 14) are not energetically favourable, because of the high electric charge of the point defect, although this reaction is formally possible.

At (too) high temperatures, Cu and In interstitial ions can occupy the neighbouring vacancies either passivating the defects or occupying the vacancies according to eq. 16:

$$\mathrm{Cu_i^{\bullet}} + \mathrm{V_{Cu}^{'}} + \mathrm{In_i^{\bullet\bullet\bullet}} + \mathrm{V_{In}^{'''}} \rightarrow \mathrm{Cu_{In}^{''}} + \mathrm{In_{Cu}^{\bullet\bullet}} \tag{5}$$

The likelihood of these reactions in a solid film depends on the ion mobility, hence on their dimension and on temperature.

During synthesis, especially in open atmosphere as it is the SPD case, deviations from molecularity and/or from stoichiometry are expected, resulting in extrinsic defects. In the CIS case, deviation from stoichiometry, that is the sulphur incorporation or loss from the CIS lattice, is according to the reaction:

$$\frac{1}{2}\mathrm{S_{2(g)}} + \mathrm{V_S^{\bullet\bullet}} \rightarrow \mathrm{S_S^{x}} + 2\mathrm{h^{\bullet}} \tag{6}$$

The equation explains the p-type conductivity of CIS, which is increased when post deposition treatment is done in sulphur atmosphere.

The deviations from molecularity, describe the Cu_2S and In_2S_3 incorporation (not as supplementary phases) which result in Cu-rich / In-rich material:

$$\mathrm{Cu_2S} \xrightarrow{2\mathrm{CuInS_2}} 2\mathrm{Cu_{Cu}^{x}} + 2\mathrm{V_{In}^{'''}} + \mathrm{S_S^{x}} + 3\mathrm{V_S^{\bullet\bullet}} \tag{7}$$

$$In_2S_3 \xrightarrow{2CuInS_2} 2V_{Cu}^{'} + 2In_{In}^{x} + 3S_S^{x} + V_S^{\bullet\bullet} \tag{8}$$

Literature mentions the segregation of Cu_2S or In_2S_3 phases in CIS thin films and their formation can be explained based on the Frenkel disorders in CIS lattice:

$$2Cu_i^{\bullet} + S_S^x \rightarrow Cu_2S_{(s)} + V_S^{\bullet\bullet} \quad (9)$$

$$2In_i^{\bullet\bullet\bullet} + 3S_S^x \rightarrow In_2S_{3(s)} + 3V_S^{\bullet\bullet} \quad (10)$$

Combining deviation from stoichiometry and from molecularity, the p-type conduction of the CIS material can again be explained. It has to be mentioned that deviation from stoichiometry is more likely to occur when the materials are annealed in sulphur or at a large excess of sulphur in the precursor solution.

$$Cu_2S + \frac{1}{2}S_{2(g)} \xrightarrow{CuInS2} Cu_{Cu}^x + Cu_{In}^{''} + 2S_S^x + 2h^{\bullet} \quad (11)$$

$$In_2S_3 + \frac{1}{2}S_{2(g)} \xrightarrow{CuInS2} 2V_{Cu}^{'} + 2In_{In}^x + 4S_S^x + 2h^{\bullet} \quad (12)$$

From these equations correlations between the material synthesis and properties can be drawn:

- depending on the deposition technique, doping and post treatment, the solar energy materials can exhibit ionic, electronic (p-type or n-type) or mixed electronic-ionic conduction.
- the point defects in the crystal lattice result in deep levels in the material's bad gap, which value can deviate from the theoretical value;
- large specific surfaces/interfaces are well accommodating point defects, explaining the band gap variation with the morphology.

3. Spray Pyrolysis Deposition Technique

Spray pyrolysis proved to be a suitable method for the deposition of large-area metal oxide, spinel oxide, chalcogenide, and different sulphide films, [5, 6]. The process is already widely applied and is attractive for the deposition of low-cost, thin-film photovoltaic solar cells [7].

The technique offers the possibility to deposit layered films and films with composition gradients throughout the thickness by changing the composition of the spray solution and deposition parameters.

During the SPD process, a precursor aerosol is sprayed towards the substrate. The components in the precursor droplets react to form a new chemical compound on the substrate surface and usually some by-products that should be vaporized in the open atmosphere.

The properties of the deposited film depend on the precursors' solution qualitative and quantitative composition, spraying rate, substrate temperature, ambient atmosphere, carrier gas, droplet size, and the cooling rate after deposition. The film thickness is influenced by the spray nozzle-substrate distance, the

substrate temperature, the concentration of the precursor solution, and the amount of the sprayed precursor solution.

The film formation depends on the reactant/solvent evaporation and on the process of droplet landing. The ideal deposition condition is considered when the solvent is completely removed at the moment the droplet approaches the substrate where the chemical reaction occurs [8]. The reactant molecules undergo processes of absorption, surface diffusion and chemical reaction, leading to nucleation and layer growth, while volatile by-products evaporate and diffuse away from the surface [9].

3.1. *Precursors' solution composition*

As precursor solutions are typically used inexpensive materials such as metal nitrate, chloride, acetate.

A widely used solar energy material is titania. Hundreds of papers report the deposition of TiO_2 thin films starting from alcoholic solution of titanium(IV)isopropoxide (TTIP). The addition of acetilacetone, proved to influence the thin film morphology and also its adherence to the substrate [10, 11], by lowering the chemical reactivity of the TTIP, avoiding its partial polycondensation due to steric hindering. The physical properties of acetilacetone (viscosity, surface tension, density, volatility) increase the aerosol stability and support a convenient flow rate [12].

Special care is required in handling the solution because of the possible by-reactions between the precursors (hydrolysis, polycondensation, etc) [12] leading to solubility problems and phase segregation, where the different components precipitate close to the working conditions. These reactions may develop in the thin film additional chemical phases such as oxides in sulphides thin layers [5], or carbon as a result of incomplete decomposition and removal of the organic components [13]; in extreme situations they make impossible SPD. The deposition temperature mainly controls the concentration of the residues from the precursors. To eliminate the solubility problems, alcoholic solutions are used (for TiO_2 deposition [10]) or highly acidic solutions (for $CuSbS_2$ deposition [14, 15].

To enhance thin film properties, polymer additives or surfactants can also be used [11], but the most important influence on thin films, for solar energy conversion optoelectronic properties, is the addition of doping agent(s) [16, 17]. Replacing TTIP can be successfully done with $TiCl_4$, when SPD homogeneous thin films can be obtained, with various structure and density, again depending on the additive types and concentration.

3.2. *Thin film deposition*

The production of droplets and their dispersion into the gas influences the size and morphology of the aggregates in the thin film due to the concentration and

velocity of the generated droplet. Depending on spray parameters (e.g. nozzle diameter, carrier gas pressure, distance between nozzle and substrate), the droplet size and distribution may be controlled. The cone-jet mode is obtained when the liquid is distorted at the tip of the tube type nozzle into a conical shape (Taylor cone). This cone is extended at its apex by a permanent jet of very small diameter. If the electric field is used for the atomization, the jet may be split, forming a multi-jet mode spray [18].

The aerosol flow rate (F_a) is influenced by the liquid properties as vapour pressure (P), viscosity (η) and surface tension (σ), as follows, [12]:

$$F_a = K\sqrt{\frac{P}{\eta\sigma}} \tag{13}$$

where K: is a coefficient depending on the power necessary to generate the aerosol.

Based on this equation, the influence of additives in the precursors' solutions can be explained: the addition of acetylacetone lowers the solution viscosity and the addition of the surfactants lowers the solution surface tension, thus increasing the aerosol flow rate.

During transportation, different forces act on the droplets, influencing the trajectory and flow rate: gravitational, Stokes, thermophoretic, electric [12]. The thermophoretic force pushes the droplet away from a hot surface, and due to this force, the thin film grows also from vapour-containing droplets passing very close to the hot substrate. The droplets spread on the substrate and initially form a powdery deposit.

From the aerosol droplets the solvent can evaporate during transport to substrate. This leads to a size reduction of the droplet and to the development of the concentration gradient within the droplet. The precursor precipitates on the surface of the droplet when the surface exceeds the solubility limit. Precipitation occurs due to rapid solvent evaporation and slow solute diffusion. This results in a porous crust [12].

When the droplets are large and the droplet concentration is low, undesired hollow particles are formed. Smaller droplets produce solid particles because the diffusion distance of the solute is shorter, leading to a more uniform concentration distribution within the droplet. Increasing the number of droplets results in a larger solvent vapour concentration in the carrier gas. Consequently, the evaporation rate decreases and precipitation is delayed. Therefore, an increase in the droplets number decreases the probability of forming hollow particles.

3.3. *Precursors reaction*

The thermodynamic control of SPD allows tailoring the films structure and texture:

- in the low temperature regime, the droplet splashes onto the substrate and the reaction occurs fully there, some of the heat being consumed for vaporizing the solvent. This process usually conduct to rough or non-adherent thin films;
- at higher temperatures the solvent evaporates completely during the aerosol transport and dry precipitate hits the substrate, where the decomposition occurs;
- at very high temperatures, after the solvent vaporizes, the solid precursors can melt or sublimate before reacting and the resulting vapours diffuse to the substrate (as in the CVD processes).

Normally, well chosen temperatures used in SPD do not allow these processes.

3.4. *Film growth*

During film growth, the precursor particles reach the substrate, developing aggregates that will either grow in size or disintegrate into smaller entities through dissociation processes [19].

When the aerosol droplets hit the solid surface, the collision decreases the energy of the chemical entities, and they may partially bind to the surface. Isolated nuclei are then formed from groups of such chemical entities (molecules or atoms), aggregated due to the thermal motion. The "new" arriving atoms are integrated in the structure at edge of the crystal nuclei, since they strongly interact with the existing atoms. The energy of the local surface allows these interactions at the unsaturated surface bonds. For the thin film growth three basic models were developed:

- Island growth (Volmer-Weber)–specific for the chemical entities which are bound to each other more strongly than to the substrate. During the growth small stable clusters nucleate on the surface and then grow in the three dimension, forming islands;
- Layer-by-layer growth (Frank-van der Merwe)–for the chemical entities more strongly bound to the substrate than to each other. During the process, the small stable nuclei extend, growing in two dimensions, forming planar sheets. A first monolayer forms, and further layers cover, but the bonds between atoms are less strong.
- Layer-plus-island growth (Stranski–Krastanow)–involves an intermediate combination of the previous two models. During the thin film growth, after monolayer(s) formation on the substrate, islands formation occurs, probably as result of the decreased bonding energy of the chemical species to the existing layers.

It is important to notice that, depending on the deposition conditions, each of these mechanism is likely to occur for a given precursor system.

3.5. *Chemical reactions*

During the deposition process, the precursors interact and/or react with the environment. For example, in the TiO_2 thin films deposition using ethanol solution of TTIP and acetylacetone (AcAc), hydrolysis and condensation of titanium alcoxide occurs [20, 21]:

- hydrolysis of the metal alcoxide:

$$Ti(i\text{-}OPr)_4 + x\ H_2O \rightarrow Ti(i\text{-}OPr)_{4-x}(OH)_x + x\ HOC_3H_7 \quad (14)$$

Metal complexes, as $Ti(i\text{-}OPr)_{4-x}(Acac)_x$, are also reported in solutions over 2 mol/L [12].

- condensation of the hydrolyzed products result in species containing bridging oxygen:

$$2Ti(i\text{-}OPr)_{4-x}(OH)_x \rightarrow [Ti(i\text{-}OPr)_{4-x}(OH)_{1-x}\text{–}O - Ti(i\text{-}OPr)_{4-x}\text{-}(OH)_x] + HOC_3H_7 \quad (15)$$

During the deposition process the amorphous hydrous oxide $TiO_2.nH_2O$ is formed and, depending on the deposition and post deposition temperature, anatase and/or rutile can be formed. The rutile phase is attributed to the $TiO(OH)_2(OH)_2$ linear chains which, after internal proton transfer lead to corner-sharing octahedral chains (Ti_3O bridges) [21].

- If the pH is adjusted, the deoxolation reaction is favored, and the condensation leads to skewed chains typical for the anatase structure [19]: $O{=}Ti - OH_2 \rightarrow HO\text{-}Ti\text{-}Ti\text{-}OH$

4. Additives for Crystallinity and Morphology Control

Developing thin films for solar energy conversion requires a careful control of the composition, crystalline structure and morphology, which can be obtained by using various additives. Basically, an additive in the precursor system interacts with the metal ion(s) and develops new structures with controlled stability. In aqueous solutions the metal cations are usually hydrated; the additives can develop physical and/or chemical bonds with the cations with (partial) dehydration, developing complex with different and predictable stability.

Their decomposition during SPD is controlled in order to develop the optimum oxide thin film, Fig. 1.

Additives can also develop various structures within the solvent, changing the specific surface within the aerosol droplets, thus modifying the vaporisation rate and the work of adhesion of the droplet with the substrate. Depending on this, the mechanisms presented in 2.4 can be particularly imposed. This is valid for any additive but has strong effect when using surfactants.

Concluding, by adding surfactants into the precursors' solutions, interactions are expected with the metal cation and with the solvent(s), influencing the cation reactivity and the thermal behaviour of the entire system.

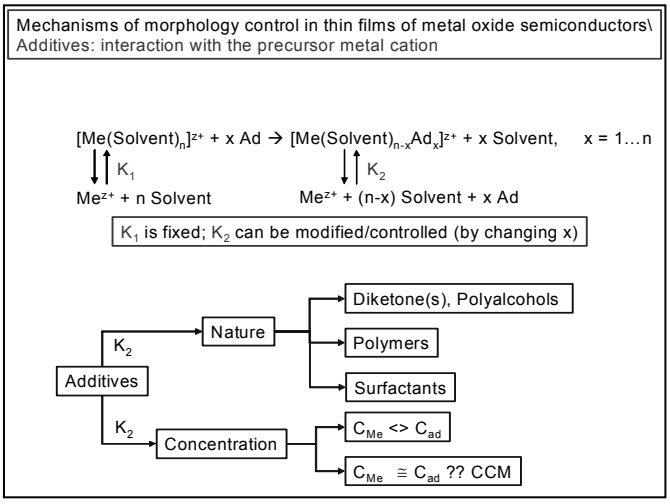

Fig. 1. The role of additives in developing photocatalysts.

Using various surfactant additives, a wide range of morphologies can be obtained, as exemplified for TiO_2, prepared from $TiCl_4$ or TTIP, as presented in Fig. 2.

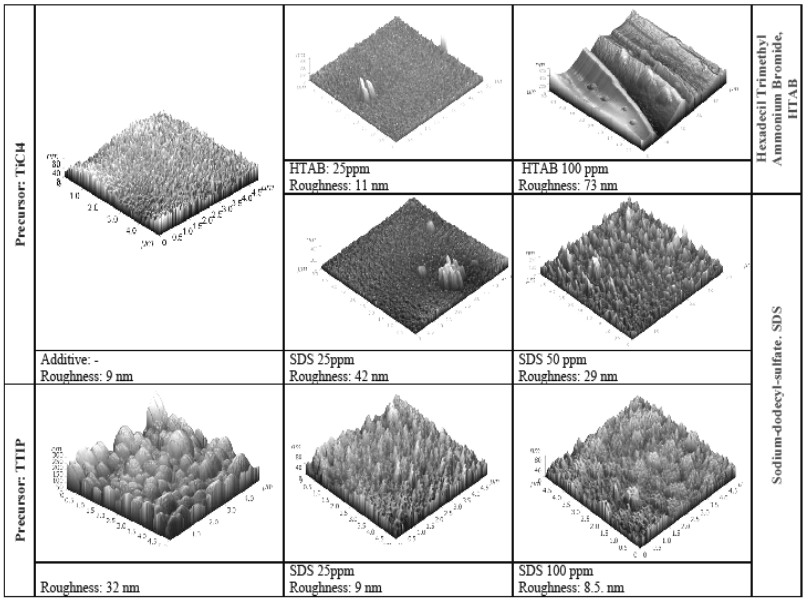

Fig. 2. Morphology control of TiO_2 by using additives.

Thin TiO_2 anatase layers, with various morphologies were also prepared by SPD using $TiCl_4$ precursor and hydrophilic and hydrophobic polymeric additives.

The polymeric additives increases de porosity and induce a faster absorption rate [22]. The samples obtained from the precursor which contain hydrophobic copolymer are characterized by high electrical conductivity and a band gap of 3.2 eV, Fig. 3. The hydrophilic copolymer induces a shift in the band gap value (3.5 eV) and decreases the electrical conduction of the layers [22].

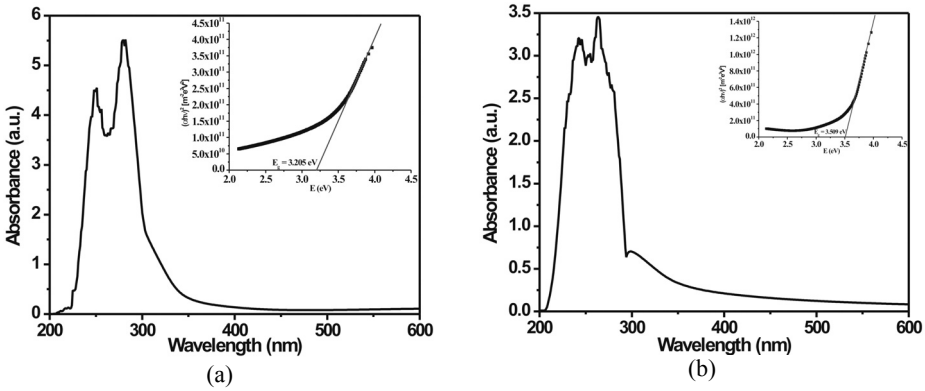

Fig. 3. The band gap value of TiO_2: **(**a**)** prepared with 25ppm hydrophobic copolymer **(**b**)** prepared with 25ppm hydrophilic copolymer [22]

The film thickness also plays an important role. Rather thick porous films are effective in advanced wastewater treatment but there is an optimum value that insures also the adherence on the substrate. Thin films of SnO_2 were obtained via SPD, at 400°C, using air as carrier gas at the pressure of 1.4 bar [22, 23]. The samples were annealed at 500° during 6 hours. Various layer thicknesses were obtained by increasing the number of deposition sequences, as presented in Table 1.

Increasing the number of deposition sequences obviously will increase the film thickness but this is not a linear process; a larger number of sequences implies a longer stationary time on the heater, resulting in the film densification, with consequences on the specific surface. Still, a linear control of the film thickness is necessary and this can be obtained by varying the precursor concentration. Using similar deposition parameters but varying the tin precursor concentration an almost linear variation of the film thickness (obtained from reflectance measurements) could be reached, Fig. 4. The annealing process will decrease the amount of oxygen vacancies into the lattice by increasing the amount of free electrons.

Table 1. Film thickness variation with the number of deposition sequences [23]

Sample	SnO_2_1	SnO_2_2	SnO_2_3	SnO_2_4
No. of deposition sequences	10	15	20	25
Film thickness, [nm]	20	80	100	130

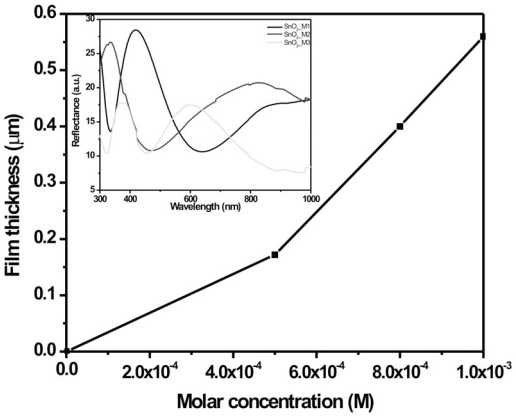

Fig. 4. Film thickness and the corresponding reflectance measurements [24].

5. Case Study: Materials for Photovoltaics Obtained by SPD

The discovery of the photovoltaic effect and the development of the first Si based cells are the fundaments on which the photovoltaic systems have evolved in the past decades. Still, the costs of the "photovoltaic kW" is the highest comparing to all the renewable energy systems, which – in turn - is significantly higher comparing to the power obtained from fossil or nuclear fuels. Therefore, plenty of research is devoted to developing low-cost, high-efficiency photovoltaic devices that can be used in a variety of applications.

Rather new developments in photovoltaics are the Solid State Solar Cells (SSSC) as promising alternatives to the Dye-Sensitized Solar Cells (DSSC) in the trend firstly stated by Graetzel and O'Reagen (1991) [25]. In a SSSC, all the components are inorganic and solid materials. Depending on the structure, two types of SSSC were developed until now: Extremely Thin Absorber (ETA) and 3D (nano-structured) solar cells. These types of solar cells are based on semiconductor thin films associations, using low-cost materials (precursors), deposited with up-scalable techniques.

The first ETA cell was developed by Kaiser et al. [26] as a stack of three thin layers: n-type semiconductor / light absorber / p-type semiconductor, following the observation that diffusion length of charge carriers within the absorber materials is a limiting property in the solar cells efficiency.

For good light absorption, the extremely thin absorber layer is embedded in a porous and transparent solid state structure, between a transparent n-type and a transparent p-type semiconductor [27]. The general structure of an ETA cell is presented in Fig. 5. As n-type semiconductor mostly reported is TiO_2 (anatase), but ZnO [28-33] or SnO_2 [34] can also be used; the absorber material ($CuInS_2$ [32, 33],

CdTe [28]) is a film with a thickness of a few tenths of nanometers and as solid-state p-type semiconductor CuSCN can be, for example, used [35].

The main advantage of this device is that the transport distance inside the absorber is strongly reduced, therefore the quality requirements for these materials are less strict and low-cost materials may be used. In order to provide sufficient light absorption, highly structured p–n heterojunctions (nanoporous or microporous) must be used [27]. Due to some disadvantages, such as relatively slow electron transfer reactions at the (two) interfaces and the recombination of the carrier charges (with a corresponding efficiency loss) [36], the ETA concept was further advanced by the development of the 3D or nano-structured solar cells, firstly reported by Goossens and co-workers [27, 36].

In a 3D solar cell concept, the absorber replaces one of the partner semiconductors (usually the p-type one); the n-type nanoporous wide band gap semiconductor and the p-type absorber are mixed on a nanometer scale to form an interpenetrating network [27]. The general structure of the 3D cell (Fig. 6) is: front contact / n-type semiconductor / p-type semiconductor absorber / back contact. In this cell, light absorption occurs near the interface thus, the minority carrier diffusion length is limited to tens of nanometers and this offer large tolerance against electron-hole recombination in the photoactive material.

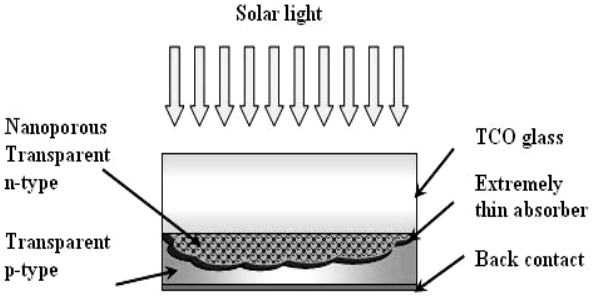

Fig. 5. The structure of a ETA solar cell.

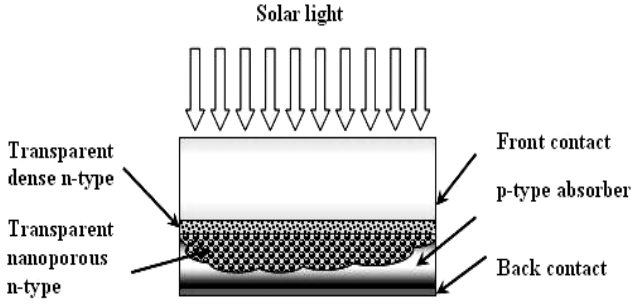

Fig. 6. The structure of a 3D solar cell.

The best efficiencies for a 3D cell reported were of 4% in a system containing dense TiO_2 anatase (100 nm thickness), nanoporous TiO_2 anatase layer (2 μm thick) obtained by doctor blade, In_2S_3 as buffer layer and $CuInS_2$ as absorber layer, deposited by ALD (Atomic Layer Deposition), [27]. The In_2S_3 buffer layer used between the TiO_2 (n-type) and $CuInS_2$ (p-type) semiconductors to prevent the recombination process by a better alignment of the conduction bands of the two semiconductors [37].

One important difference between the ETA and the 3D solar cells is the p-type semiconductor which, for the latest, has limited optical band gap, being able to absorb in the visible range of the solar spectrum. This corresponds to a rather limited group of materials, considering the needs of bands alignment and the electrochemical potential equilibrium, Fig. 5 [38].

The diagrams in Fig.7 suppose an intimate contact between the n- and p-type semiconductors (and with the interim buffer or tunnelling layers, if any) for avoiding shunts. Parallel processes (mainly recombination) are responsible for the (still) low efficiencies in the SSSC. A buffer layer (n- or p-type semiconductor) is therefore proposed, to limit mainly the back recombination. This supplementary layer must be very thin, allowing the charge carrier diffusion.

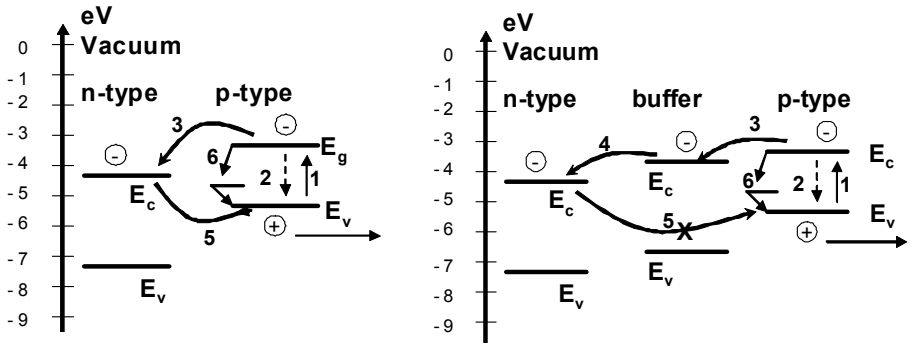

(1) photo-excitation; (2) intrinsic recombination; (3) electron transfer at the interface; (4) electron diffusion; (5) back recombination; (6)interface recombination.

Fig. 7. Band alignment and processes in a 3D solar cell [37].

The major problem in these devices is the difficulty of obtaining a homogeneous composition of the materials, with reasonable reproducibility. One should take notice that crystalline structure and morphology influences the band gap value, while the composition (polyomorphism, non-stoichiometry) influence both the band gap value and position.

The band gap value can be estimated using the optical transmittance spectra, Fig. 8 [39] and, using these data, the absorption coefficient and the band gap of the semiconductor thin film can be evaluated.

The absorption coefficient can be calculated using the equation:

$$\alpha = \ln(1/T)/t \tag{16}$$

The bandgap energy Eg can be obtained by plotting the optical absorption, $(\alpha h\nu)^2$ vs. the photon energy, (hν), and extrapolating the linear portion of the curve to $(\alpha h\nu)^2 = 0$. An example is presented in Fig. 9 for nanoporous anatase TiO_2, obtained by SPD.

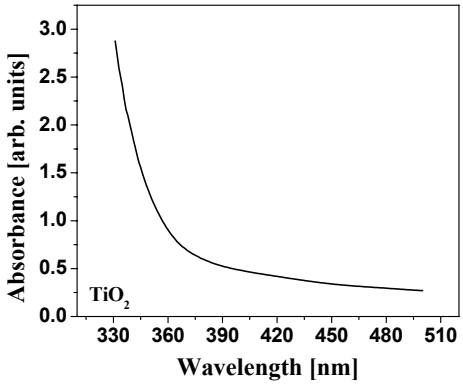

Fig. 8. Optical absorbance spectra of TiO_2 film.

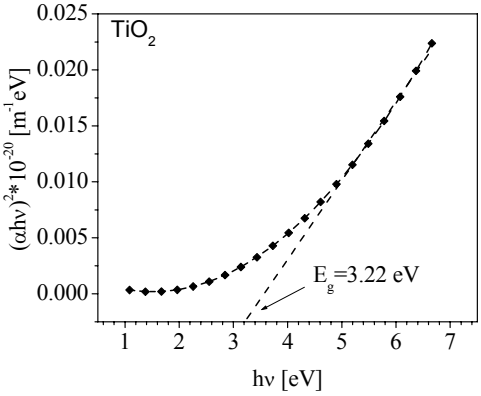

Fig. 9. Calculation of Eg in TiO_2 nanostructured film.

The band gap energy can further be used to calculate the conduction (ECB) and valence (EVB) band edges of the films by the following empirical equations [40]:

$$E_{VB} = \chi_{semiconductor} - E_e + 0.5E_g \tag{17}$$

where: E_{VB} is the valence band edge potential, E_e is the energy of free electrons (4.5 eV), E_g is the band gap energy of the semiconductor (calculated from experimental data as described above), $\chi_{semiconductor}$ is the semiconductor electronegativity calculated as [41]:

$$\chi_{cation}(eV) = \frac{\chi_{cation}(P.u) + 0.206}{0.336} \tag{18}$$

$$\chi_{semiconductor}(eV) = 0.45 \cdot \chi_{cation}(eV) + 3.36 \tag{19}$$

where: χ_{cation} (P.u.) is the cationic electronegativity (P.u. Pauling units), χ_{cation} (eV) is the absolute cationic electronegativity (eV) and $\chi_{semiconductor}$ (eV) is the absolute semiconductor electronegativity (eV).

Next the conduction band edge potential E_{CB} can be evaluated using:

$$E_{CB} = E_{VB} - E_g \tag{20}$$

For some of the semiconductor materials obtained by Spray Pyrolysis Deposition (SPD), the E_{VB} and E_{CB} are calculated and the results are presented in Table 2.

Table 2. Values of the band gap, valence band and conduction band of the thin films prepared by SPD

Semiconductor	E_g (eV)	E_{VB} (eV)	E_{CB} (eV)
TiO_2	3.22	2.81	-0.41
Cu_xS	2.16	2.76	0.60
Sb_2S_3	1.56	2.66	1.10
In_2S_3	3.11	3.07	-0.04

According to these data, the p–n junction formation model and the schematic diagram of the electron-hole separation process of the $CuInS_2/TiO_2$ junction are presented in Fig. 10.

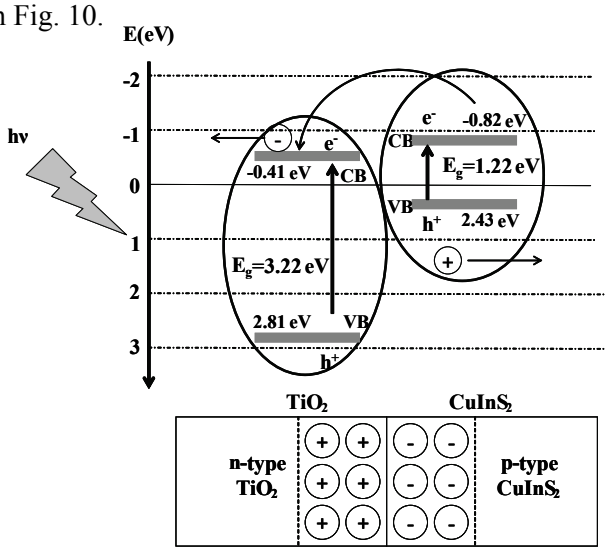

Fig. 10. The schematic diagram of the p-n heterojunction $CuInS_2/TiO_2$ and the electron-hole separation.

The 3D solar cell consists of several layers of different inorganic solid-state materials in thin-film form: window layer (n-type semiconductor), absorber layer (p-type semiconductor) and contacts (front and back contacts). A brief review on the design and optimization of different 3D SSSC components, using SPD as single deposition technique are further presented.

5.1. *The Window layer (n-type semiconductor)*

The primary function of a window layer in a photovoltaic device is to form a hetero-junction with the absorber layer [42]. The n-type semiconductor film has to be highly transparent and conductive, which is difficult to obtain because of the optical absorption of the free carriers in the infrared region. Therefore, it is necessary to increase the mobility in the material to get larger conductivity while keeping the carrier concentration low. The band gap of the materials should be large enough to show a high transmission also for the blue light. The problems of obtaining a good layer are often related to the requirement of a low temperature deposition process, imposed by the substrate or by the previously deposited layers.

As n-type semiconductor different wide band gap oxides are reported; among them, the most frequently used is TiO_2 anatase (E_g = 3.26 eV [43]), which has chemical stability, non-toxicity and low-cost. It is deposited, using different techniques onto conductive glass (TCO, FTO, ITO). Most frequently TiO_2 thin layers are obtained CVD, ALD, sol-gel, doctor blade and SPD.

Using SPD, dense or nanostructured TiO_2 anatase layers can be obtained; actually, for SSSC, a sequence of a thin dense layer (improved contact with FTO) followed by a mezzo-porous layer able to be infiltrated by the absorber is necessary. It was previously reported [10, 44] that, using the same precursor system (absolute ethanol solutions of TTIP, and acetylacetonate - AcAc), both morphologies can be obtained (Fig. 11), by modifying the deposition and annealing parameters, Table 3.

Small band gap variations could also be registered by morphology changing, with variations between 3.22 to 3.28 eV.

Table 3. Optimized deposition conditions for TiO_2 material obtained by SPD

Thin film	Precursors composition (weight ratio)	T [^oC]	n_{sp}	p [bar]	H [cm]	T_{ann} [^oC]	t_{ann} [h]
dense-TiO_2	TTIP:AcAc:Et = 1:1.5:22.5	350	20	1.2	17	450	2
nanoporous-TiO_2	TTIP:AcAc:Et = 1.3:1:20.8	400	20	1.2	30	550	6

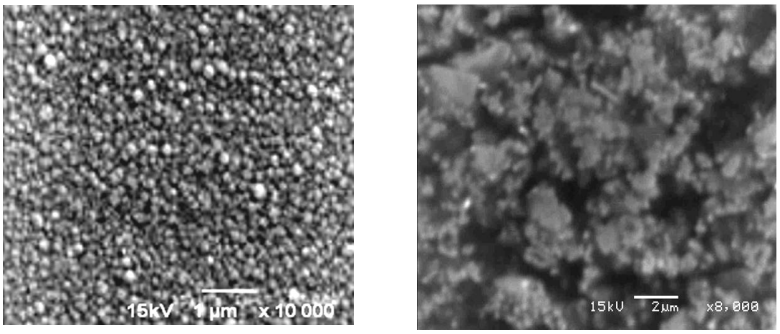

(a) (b)

Fig. 11. SEM images of **(a)** dense and **(b)** mezzo-porous anatase TiO_2 films obtained by SPD.

The current–voltage (I-V) dark curves of the dense, nanoporous and dens/nanoporous TiO_2 anatase layer(s) (Fig. 12) show the diode behaviour of the films, confirming that homogenous films, free of pinholes are obtained. The differences in the I-V response can be correlated with the amount of defects that is differently modified during the growth and annealing steps, according to the porosity of the thin layer and the oxygen diffusion rate.

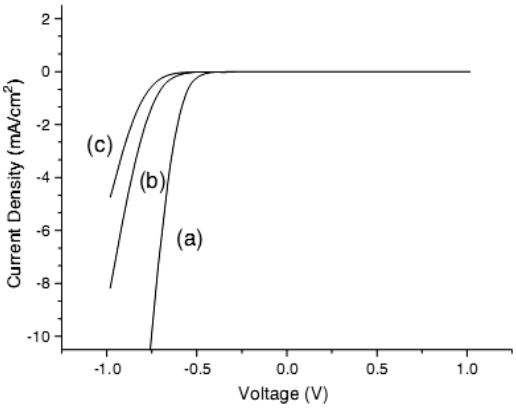

Fig. 12. I–V dark curves of (a) dense; (b) nanoporous and (c) dens/nanoporous TiO_2 anatase layers.

5.2. *The absorber layer (p-type semiconductor)*

An ideal absorber solar cell material should be a semiconductor (usually p-type) with the band gap in the range of 1-1.5 eV (for efficiencies over 30%, at AM 1.5), with a high light absorption coefficient (~105/cm), high quantum efficiency of excited carriers, long diffusion length, low recombination velocity, and, most important, it should be able to form a good electronic junction

(homo/hetero/Schottky) with suitably compatible materials [50]. In addition, non-toxicity, long-term and chemical stability, readily availability and an easy, low-cost and reproducible deposition technique are also requirements for a good absorber material [45, 46].

The absorber material largely reported for 3D SSSC is $CuInS_2$ (CIS), but other alternatives are also possible, mainly in the group of metal sulphides, Table 4.

Considering the need of lowering the production costs, low energetic, up-scalable techniques, such as Chemical Bath Deposition (CBD, [47, 48]), Photochemical Deposition (PCD [49]), Successive Ionic Layer Absorption and Reaction (SILAR [50]), or Spray Pyrolysis Deposition (SPD, [32, 33, 51-53]) are used for thin sulphide films.

Table 4. Binary and ternary sulphides - possible absorbers in a 3D SSSC

Material	E_g [eV]	Ref.	Material	E_g [eV]	Ref.
SnS	1.3	40	MoS_2	1.9	46
Cu_xS (x =1.8-2)	1.2÷2.48	31, 41-43	$CuInS_2$	1.55	21
Sb_2S_3	1.3÷2.13	44-45	$CuSbS_2$	1.52	39, 47

Dense films, containing SnS and SnS_2 crystalline phases, were obtained from aqueous solutions of $SnCl_2 \cdot 2H_2O$ and thioureea, in a weight ratio of 1.44:1 [54]. The study showed that modifying the deposition/substrate temperature (T = 250-350^oC), films with different compositions, morphologies and diode behaviour were obtained. Best morphology (dens and homogenous film, Fig. 13) and electrical response (Fig. 14) were obtained for films deposited at 250^oC, considered as optimized films (Table 4).

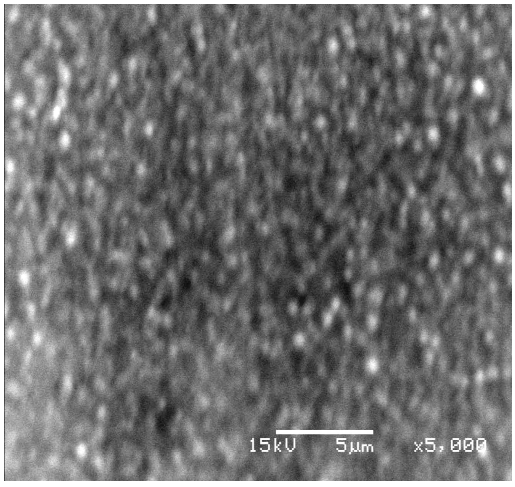

Fig. 13. SEM images of SnS thin films deposited deposited onto FTO glass substrate at 250°C.

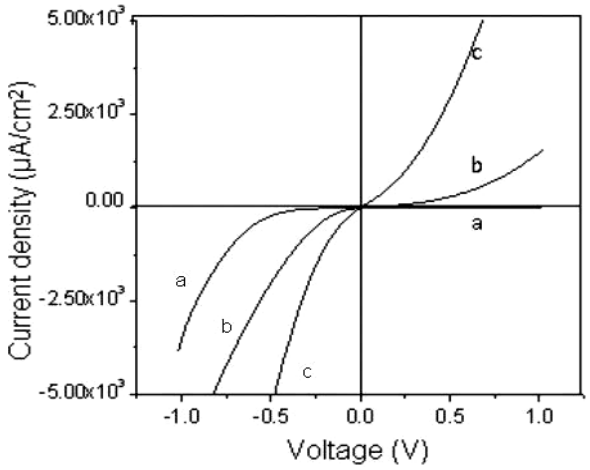

Fig. 14. I-V dark curves of SnS thin films deposited onto FTO glass substrate at: a) 250°C, b) 300°C, and c) 350°C.

Crystalline thin films of Sb_2S_3, with orthorhombic structure, were deposited onto FTO glass substrate from aqueous and mixed water-ethanol (W-Et) solutions using as precursors $(CH_3COO)_3Sb$ and thioureea [55]. The composition, the crystalline structure, the morphology, the optical (Eg) and electrical properties (I-V curves in dark) of the layers were tailored by varying the deposition parameters (substrate temperature and number of spraying sequences) and the solvent composition, using water (W) and mixed water-ethanol (W-Et) solvents, Table 4.

Table 5. Optimized deposition conditions for sulphides absorbers materials obtained by SPD

Sulphide absorber	Precursors solution		T [°C]	n_{sp}	p [bar]	H [cm]
	Precursors ratio	Solvents				
SnS	Sn:S = 1.44:1	W	250	15	1.2 (N_2)	25
Sb_2S_3	Sb:S = 1:2.22	W:Et = 4:1	260	16	1.2 (N_2)	25
Cu_xS	Cu:S = 1:3	W:Et:Gly = 7:2:1	300	90	1.2 (air)	15
$CuInS_2$	Cu:In:S=1:1.16:2.16	W:Et = 3:2	315	25	1.2 (air)	15
$CuSbS_2$	Cu:Sb:S=1:2.57:5.71	W	240	25	1.2 (air)	25

These films were integrated (tested) in 3D cells with the structure: FTO/ TiO_2 (n-type semiconductor) / Sb_2S_3 (absorber layer, deposited at the varied parameters)/ graphite. The I-V curves recorded in dark and under illumination for the cells showed the diode behaviour, without shunts. The best characteristics (V_{oc} = 264.22 mV, $I_{sc} = 2.63 \times 10^{-6}$ A and FF = 0.383), Fig. 15, were obtained for the cell with the Sb_2S_3 film obtained at 260ºC, after 16 numbers of spraying sequences, with 20% ethanol in the sprayed solution (optimized film, Table 5). The best photovoltaic response registered for the optimized sample is the result of: (a) a denser film (Fig. 16), which means better TiO_2/ Sb_2S_3 interface, and (b) a lower

band gap value, 1.56 eV, that insures reduced recombination and a better injection of the electrons from the conduction band of the Sb_2S_3 in the conduction band of the TiO_2 (anatase).

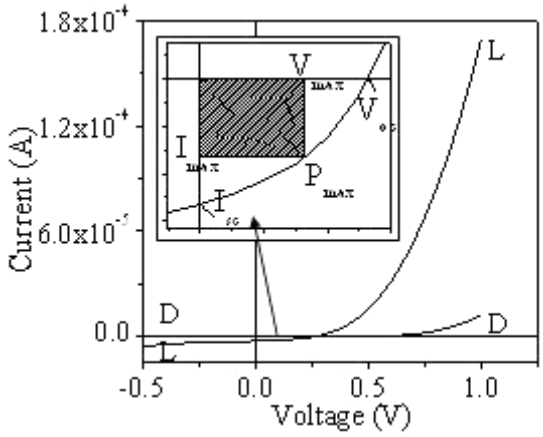

Fig. 15. I-V curves measured in dark and under illumination of 3D cell: FTO/ TiO_2/ Sb_2S_3 (optimized film)/ graphite.

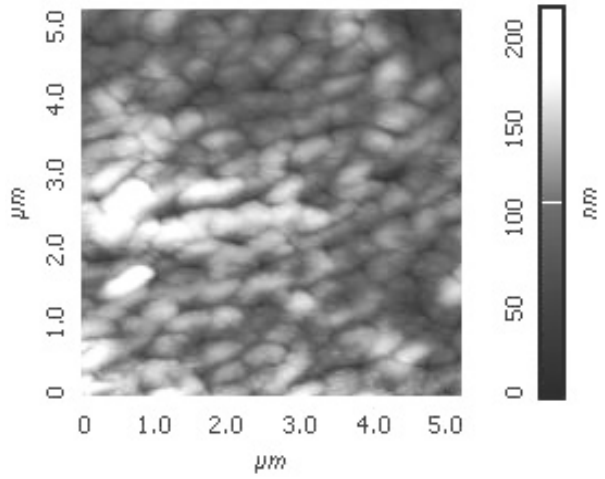

Fig. 16. AFM image of Sb_2S_3 film deposited at 260°C from water-ethanol solutions with 20% ethanol.

Stoichiometric and non-stoichiometric copper sulphides, ranging from Cu_2S to CuS were prepared using hydrated copper chloride and thioureea in water and water-based solvents (water-ethanol-glycerol mixed solvents) [5, 56, 57]. Modifying the precursor's concentration the Cu:S ratio, the deposition temperature (T) and the number of spraying sequences (nsp), thin films of Cu_xS (x = 1-2), with

various compositions and E_g values, in the range 2.28-3.1 eV, were obtained, Table 6. Changing the deposition parameters also allow tailoring the morphology, Fig. 17 a and b.

Table 6. Copper sulfides thin films obtained by SPD

Cu:S	$CuCl_2$ [mol/L]	T [°C]	n_{sp}	Crystalline phase composition	E_g [eV]
1:2.5	0.3	300	25	$Cu_{1.8}S + Cu_2S$	2.67
1:3	0.25	300	25	$Cu_{1.8}S$	2.69
1:3	0.3	275	25	$CuS + Cu_{1.8}S$	2.59
1:3	0.3	300	15	$Cu_{1.8}S + Cu_2S$	3.01
1:3	0.3	300	25	$Cu_{1.8}S + Cu_2S$	2.73
1:3	0.3	300	35	$Cu_{1.8}S + Cu_2S$	2.53
1:3	0.3	300	90	$Cu_{1.96}S$	2.28
1:3	0.3	325	25	$Cu_{1.8}S$	3.10
1:3	0.35	300	25	$Cu_{1.8}S + Cu_2S$	2.68
1:3.5	0.3	300	25	$CuS + Cu_{1.8}S$	2.46

Films containing copper-rich phases with photovoltaic properties (Cu_xS, x = 1.8-2) were obtained in depositions at higher temperatures (T = 300-325ºC), using a high number of spraying sequences (90), from precursors' solutions with Cu:S = 1:2.5, respectively Cu:S = 1:3 at Cu^{2+} concentration of 0.3 mol/L.

As in case of Sb_2S_3 absorber prepared via SPD, tailoring the morphology of the Cu_xS thin films by using water-alcohols mixed solvents represents a path to obtain dense and homogenous layers, as result of faster solvent vaporising and therefore a higher reaction rate. Dense and homogenous (Fig. 17) films assure a good n-p interface (good contact on large surfaces) and avoid recombination.

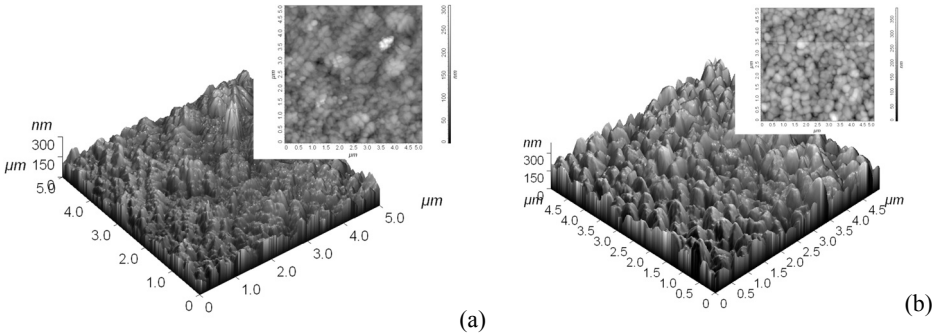

Fig. 17. AFM images of Cu_xS obtained at 300°C, with 25 spraying sequences, from precursors solution with: **(a)** Cu:S = 1:3, C_{Cu}^{2+} = 0.25 mol/L, and **(b)** Cu:S = 1:3.5, C_{Cu}^{2+} = 0.3 mol/L

5.3. *Chalcopyrite-based absorbers*

The absorber material $CuInS_2$ (CIS) is part of the I-III-VI group of semiconductors, with chalcopyrite structure. CIS is a suitable absorber in 3D SSSC because it is chemically stable, non-toxic, has a high absorption coefficient

($\Omega > 104$ cm^{-1}) and a direct band gap energy of about 1.5 eV. The CIS based solar cells with conversion efficiency over 11% have already been reported [52]. Pure CIS is a p-type semiconductor, but n-type conduction can be obtained by doping with Sn [58].

Thin films of CIS were obtained via SPD, from solutions containing $CuCl_2.2H_2O$, $InCl_3$ and thioureea in water and water-ethanol mixed solvents [59]. Water (partially) soluble copolymers of maleic anhydride were investigated as morphology controllers of copper-based sulphides. Hyfrophilic (Hfl) and hydrophobic (Hfb) co-polymers having different conformation in the working conditions were investigated and proved to be efficient in changing the morphology, even at very low concentrations (25ppm), Fig. 18. The addition of hydrophilic co-polymer resulted in polycrystalline, porous thin films, while the films obtained from solutions where hydrophobic co-polymer was added, had a lower crystalline degree, a columnar preferred growth and lower electrical response.

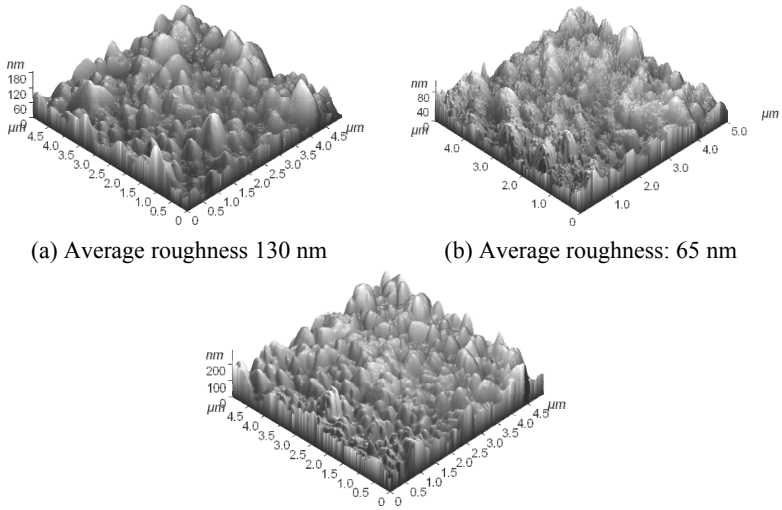

(a) Average roughness 130 nm (b) Average roughness: 65 nm

(c) Average roughness: 48 nm

Fig. 18. AFM images of CIS films deposited from precursors solutions (a) without copolymeric additives, (b) with Hfl, and (c) with Hfb copolymers

By adding an In_2S_3 buffer layer, also deposited via SPD, a solar cell was obtained, having the structure: FTO/TiO_2dense-nanoporous/In_2S_3/$CuInS_2$/C (graphite) and the characteristics: V_{oc}=305 mV, J=1.145 mA/cm^2 and FF = 0.0.256.

An alternative to replace $CuInS_2$ in a 3D SSSSC is $CuSbS_2$, which is part of the same group of chalcopyrite materials and with the indium and the antimony ionic radius almost equals. The lower price of antimony, comparing to indium, the direct band gap energy of 1.52 eV and the convenient photovoltaic properties make

$CuSbS_2$ a promising candidate as absorber material in SSSC.

The $CuSbS_2$ was–to the best of our knowledge - for the first time prepared by SPD in our group [14, 15, 60-64]. The copper chloride and thioureea were used, as previously, while different antimony precursors were tested, the best results corresponding to antimony acetate $Sb(CH_3COO)_3$. Dense, crystalline films of $CuSbS_2$ with orthorhombic structure can be obtained using an antimony excess in the precursor's solutions, but the result is the development of supplementary phases (Sb_2S_3 with orthorhombic structures), leading to a decrease in the photovoltaic response.

The deposition temperature plays a key-role in improving the I-V response by decreasing the Sb_2S_3 content in the layer and allowing long-range crystalline ordering. Fine properties tuning can be done by modifying the deposition height (H = 25-35 cm) and the break between two deposition pulses (τ = 60, 90s). Variations in the band gap energies, from 1.1 eV to 1.8 eV were registered for different deposition conditions and different morphologies, (Fig. 19).

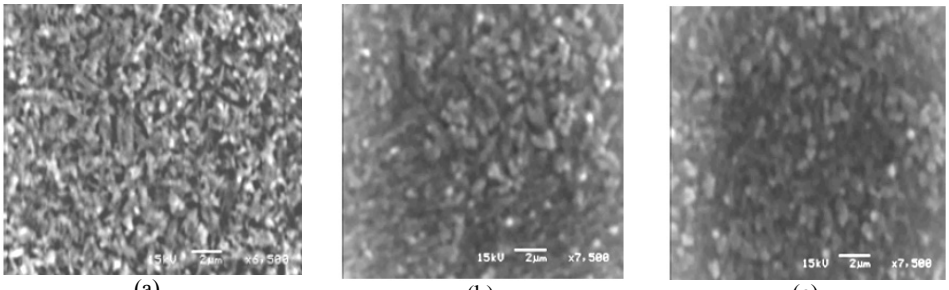

(a) (b) (c)

Fig. 19. SEM images of $CuSbS_2$ deposited by SPD at 240°C from precursors solutions with Cu:Sb:S weight ratios: **(a)** 1:2.57:5.71, **(b)** 1:4.29:5.71, **(c)** 1:6:5.71.

During all the studies, cells consisting of TiO_2–$CuSbS_2$ junctions were developed and tested, Fig. 20.

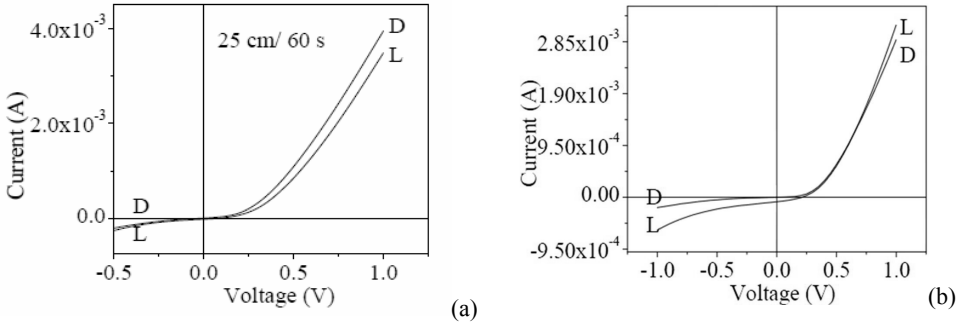

(a) (b)

Fig. 20. I-V curves measured in dark (D) and under illumination (L) for **(a)** FTO/dense TiO_2/$CuSbS_2$(optimized)/C (graphite) and **(b)** 3D cell: FTO/denseTiO_2/nanoporous TiO_2/In_2S_3/ $CuSbS_2$/C (graphite)

The results show that the thin nanoporous TiO_2 film increase the cell performances (FF), comparing to the cell containing only dense anatase. This can be related to a better infiltration of $CuSbS_2$ in the TiO_2 matrix. The cell is working at a rather low FF (0.318), thus improvements on the materials side are further expected for enhancing crystallinity and for decreasing the secondary phases [38]. Beside the quest for highly efficient photovoltaic materials, supplementary solutions may support the increase in the conversion efficiency, as increasing the amount of solar radiation (photons) reaching the module, by tracking and/or by using light concentrators.

5.4. *Interim layers obtained by SPD*

Increased efficiency of 3D SSSC was reported when using interim layers (Al_2O_3 and/or In_2S_3) between the n-type semiconductor TiO_2 (anatase) and the p-type semiconductor $CuInS_2$. These films can prevent the electron-hole pair recombination (by a better alignment of the n- and p-semiconductors energy bands) and the dopability of the n-type semiconductor when infiltrated with the p-type absorber [27, 37].

The 3D cell is obtained by successive deposition of the components. Thus, the buffer layer will be in contact with both, the n-type and the p-type semiconductor and for reason of controlled nucleation/growth it is preferable a structure/composition rather related to one of them, e.g. if the p-type semiconductor is CIS, a possible buffer can be In_2S_3. Indium sulphide, In_2S_3 is an n-type semiconductor, with the band gap reported between 1.8-3.3 eV and with high transmittance in the visible region [65, 66].

Indium sulphide was deposited by SPD as an n-type conduction with a band gap varying between 3–3.78 eV according to the sulphur excess ratio in the precursor system (up to 1:7.5 compared to In). The large E_g values make these films suitable for an extremely thin buffer layer in SSSC, supporting the electron injection [67].

Aluminium oxide (alumina, Al_2O_3) has received much attention as material with excellent mechanical, optical, chemical, thermal and electrical properties. It exhibits physical properties such as (average) high refractive index (1.74 at 500 nm), large dielectric constant and wide band gap energy (7-9 eV) [68].

Solar cells with $CuSbS_2$ absorber were developed [59, 69]. via SPD, using interim layers of Al_2O_3 and/or In_2S_3 , with the following structures:

(1) FTO/ dense TiO_2/ nanoporous TiO_2/ $CuSbS_2$/C(graphite),

(2) FTO/ dense TiO_2/ nanoporous TiO_2/ In_2S_3/ $CuSbS_2$/C(graphite),

(3) FTO/ dense TiO_2/ nanoporous TiO_2/Al_2O_3/ In_2S_3/ $CuSbS_2$/C(graphite).

The cell characteristics obtained for the 3 D cells are presented in Table 7.

The cells developed with In_2S_3 buffer layer present an improved photovoltaic response confirming the limitation of recombination. By introducing the Al_2O_3 tunnel layer in the structure, the photovoltaic response is affected, supporting that

idea that the TiO_2 thin layer is not doped with cooper ions during the infiltration process.

Table 7. Cells parameters obtained for the developed 3D cells

Cell	V_{oc} (mV)	I_{sc} (mA)	V_{max} (mV)	I_{max} (mA)	FF	$V_{max} \cdot I_{max}$ (mV·mA)
1	90	0.024	50	0.012	0.280	0.60
2	343	0.127	196	0.070	0.315	13.72
3	174	0.004	100	0.002	0.240	0.17

Conclusions

Spray pyrolisys deposition represents a versatile technique, allowing the development of large area thin films for solar energy conversion devices. The paper reviews the parameters that have significant influence on the crystalline structure and morphology, with a focus on the most important output properties for opto-electronic devices. A case study is detailed for the new generation of photovoltaics, particularly, on the solid state solar cells. Deposition and annealing temperatures, spraying geometry and sequences, the precursor concentration and solvent(s) are discussed and the importance of the additives is outlined as important tools in tuning the precursors' stability/reactivity, thus the nucleation and growth processes.

Acknowledgement. Significant results presented in the paper were obtained under the frame of the ID_840/2008 project, financed by the Romanian Council for Research in Higher Education, which is gratefully acknowledged.

References

[1] KRÖGER F.A., *The Chemistry of Imperfect Crystals*; North-Holland Publishing Co, Holland, 1964.

[2] PERNIU, D., DUTA, A., SCHOONMAN, J., *The Defect Structure of Copper Indium Disulfide*, Functionalized Nanoscale Materials, Devices and Systems, NATO Publishing Unit, 2008.

[3] BINSMA J.J.M., *Defect chemistry of $CuInS_2$, investigated by electrical measurements and Mössbauer spectroscopy*, Journal of Physics and Chemistry of Solids, **44**, pp. 237–244, 1983.

[4] UENG H.Y., HWANG H.L., *The defect structure of $CuInS_2$. part III: Extrinsic impurities*. Journal of Physics and Chemistry of Solids, **51**, pp. 11–18, 1990.

[5] ISAC L., DUTA A., KRIZA A., *Copper sulfides obtained by spray pyrolysis - Possible absorbers in solid-state solar cells*, Thin Solid Films, **15**, pp. 5755–5758, 2007.

[6] IENEI E., ISAC L., DUTA A., *Synthesis of alumina thin films by spray pyrolysis*, Revue Roumaine de Chimie, **3**, pp. 161–165, 2010.

[7] KRUNKS M., BIJAKINA O., MIKLI V., REBANE H., VAREMA T., ALTOSAAR M., MELLIKOV E., *Sprayed $CuInS_2$ thin films for solar cells: The effect of solution composition and post-deposition treatments*, Solar Energy Materials & Solar Cells, **69**, pp. 93–98, 2001.

[8] PATIL P.S., *Versatility of chemical spray pyrolysis technique*, Materials Chemistry and Physics, **59**, pp. 185–198, 1999.

[9] OKTIK S., RUSSELL G.J., BRINKMAN A.W., *Properties of ZnO layers deposited by "photo-assisted" spray pyrolysis*, Journal of Crystal Growth, **159**, pp. 195–199, 1996.
[10] DUTA A., *TiO_2 thin layers with controlled morphology for ETA (extremely thin absorber) solar cells*, Thin Solid Films, **511-512**, pp. 195–198, 2006.
[11] ANDRONIC L., MANOLACHE S., DUTA A., *TiO_2 thin films prepared by spray pyrolysis deposition (SPD) and their photocatalytic activities*, Journal of Optoelectronics and Advanced Materials, **5**, pp. 1403–1406, 2007.
[12] DUMINICA F.D., MAURY F., ABISSET S., *Pyrosol deposition of anatase TiO_2 thin films starting from $Ti(OPr)_4$/acetilacetone solutions*, Thin Solid Films, **515**, pp. 7732–7739, 2007.
[13] ISAC L., DUTA A., PURGHEL E., *Tailoring alumina thin film properties using hydrophilic/hydrophobic copolymer additives*, Physica Status Solidi A, **205**, pp. 2413–2416, 2008.
[14] MANOLACHE S., ANDRONIC L., DUTA A., *The influence of the deposition condition on crystal growth and on the band gap of CuSbS2 thin film absorber used for Solid State Solar Cells (SSSC)*, Journal of Optoelectronics and Advanced Materials, **5**, pp. 1269–1272, 2007.
[15] MANOLACHE S., DUTA A., ISAC L., *The influence of the precursor concentration on $CuSbS_2$ thin films deposited from aqueous solutions*, Thin Solid Films, **15**, pp. 5957–5960, 2007.
[16] ENESCA A., ANDRONIC L., DUTA A., *Influence of sodium ions (Na+) dopant on the efficiency of the tungsten trioxide photoelectride*, Revue Roumaine de Chimie, **1**, pp. 11–15, 2010.
[17] ENESCA A., DUTA A., SCHOONMAN J., *Influence of tantalum dopant ions (Ta5+) on the efficiency of the tungsten trioxide photoelectrode*, Physica Status Solidi A, **8**, pp. 2038–2041, 2008.
[18] PEREDNIS D., GAUCKLER L.J., *Thin Film Deposition Using Spray Pyrolysis*, Journal of Electroceramics, **14**, pp. 103–111, 2005.
[19] BARRY CARTER C., GRANT NORTON M., Ceramic Materials Science and Engineering, Springer, New York, USA, pp. 112–132, 2007.
[20] MEDINA-VALTIERRA J., FAUSTO-REYES C., CALIXO S., BOSCH P., LARA V.H., *The influence of surfactants on the roughness of titania sol-gel films*, Materials Characterization, **58**, pp. 233–242, 2007.
[21] MAHSHID S., ASKARI M., GHAMSARI M.S., *Synthesis of TiO_2 nanoparticles by hydrolysis and peptization of titanium isopropoxide solution*, Journal of Materials Processing Technology, **189**, pp. 296–300, 2007.
[22] ENESCA A., ANDRONIC L., DUTA A., *Wastewater Treatment using optimized TiO_2 photocatalytic properties*, Environmental Engineering and Management Journal, **8**, pp. 753–758, 2009.
[23] ENESCA A., BOGATU C., VOINEA M., DUTA A., *Opto-electronic properties of SnO_2 layers obtained by SPD and ECD techniques*, Thin Solid Film, **519**, pp. 563–567, 2010.
[24] ENESCA A., DUTA A., *The influence of the precursor concentration on the properties of SnO_2 thin films*, Thin Solid Film, **519**, pp. 568–572, 2010.
[25] O' REAGAN B., GRATZEL M., *A low-cost, high-efficiency solar cell based on dye-sensitized colloidal TiO_2 films*, Nature, **353**, pp. 737–739, 1991.
[26] KAISER I., ERNST K., FISCHER CH.-H., KONENKAMP R., ROST C., SIEBER I., LUX-STEINER M.Ch., *The ETA – Solar Cells with $CuInS_2$: A Photovoltaic Cell Concept using an Extremely Thin Absorber (eta)*, Solar Energy Materials&Solar cells, **67**, pp. 89–96, 2001.
[27] NANU M., SCHOONMAN J., GOOSSENS A., *Inorganic Nanocomposite of n- and p- Type Semiconductors: A new Type of Three-Dimensional Solar Cell*, Advanced Materials, **16**, pp. 453–456, 2004.
[28] LEVY-CLEMENT C., KATTY A., BASTIDE S., ZENIA F., MORA I., MUNOZ-SANJOSE, *A new CdTe/ZnO columnar composite film for Eta-solar cells*, Physica E, **14**, pp. 229–232, 2002.

[29] DUTA A., NANU M., POPA M., MANOLACHE S.A., GOOSSENS A., SCHOONMAN J., *ZnO Based Materials for the ETA Solar Cells*, Bulletin of the Transilvania University of Brasov, **10**, pp. 133–140, 2004.

[30] FAY S., KROLL U., BUCHER C., VALLAT-SAUVAIN E., SHAH A., *Low pressure chemical vapour deposition of ZnO layers for thin-film solar cells: temperature-induced morphological changes*, Solar Energy Materials & Solar Cells, **86**, pp. 385–397, 2005.

[31] DHANANJAY D., NAGARAJU J., KRUPANIDHI S.B., *Temperature dependent transport properties of CuInSe2–ZnO heterostructure solar Cell*, Journal of Physics and Chemistry of Solids, **67**, pp. 1636–1642, 2006.

[32] OJA ACIK I., KATERSKI A., MERE A., AARIK J., AIDLA A., DEDOVA T., KRUNKS M., *Nanostructured solar cell by spray pyrolysis: Effect of titania barrier layer on the cell performances*, Thin Solid Films, **517**, pp. 2443–2447, 2009.

[33] KRUNKS M., KATERSKI A., DEDOVA T., OJA ACIK I., MERE A., *Nanostructured solar cell based on spray pyrolysis deposited ZnO*, Solar Energy Materials & Solar Cells, **92**, pp. 1016–1019, 2008.

[34] TENNAKONE K., BANDARANAYAKE P.K.M., JAYAWEERA P.V.V., KONNO A., KUMARA G.R.R.A., *Dye-sensitized composite semiconductor nanostructures*, Physica E, **14**, pp. 190–196, 2002.

[35] O'REGAN B., LENZMANN F., MUIS R., WIENKE J., *Solid-State Dye-Sensitized Solar Cell Fabricated with Pressure-Treated P25−TiO_2 and CuSCN: Analysis of Pore Filling and IV Characteristics*, Chemistry of Materials, **14**, pp. 5023–5029, 2002.

[36] GOOSSENS A., *Nanocomposite 3D Solar Cell*, Proceedings of The International Conference on Materials Science and Engineering (BRAMAT), Braşov, România, **2005**.

[37] NAKAYAMA N., ITO K., *Sprayed films of stannite Cu_2ZnSnS_4*, Applied Surface Science, **92**, pp. 171–175, 1996.

[38] DUTA A., VISA I., MANOLACHE S.A., ISAC L., *p-Type semiconductors for Solid State Solar Cells*, Proceedings of 23th European Photovoltaic Solar Energy Conference, **1**, pp. 716–719, 2008.

[39] ANDRONIC L., DUTA A., *TiO_2 thin films for dyes photodegradation*, Thin Solid Film, **515**, pp. 6294–6297, 2007.

[40] GAO C., LI J., SHAN Z., HUANG F., SHEN H., *Preparation and visible-light photocatalytic activity of In_2S_3/TiO_2 composite, Mater*, Chem. Phys., **122**, pp. 183–187, 2010.

[41] KWON C.-W., POQUET A., MORNET S., CAMPET G., DELVILLE M.-H., TREGUER M., PORTIER J., *Electronegativity and chemical hardness: two helpful concepts for understanding oxide nanochemistry*, Mater. Lett., **51**, pp. 402–413, 2001.

[42] CHOPRA K.L., PAULSON P.D., DUTA V., *Progress in Photovoltaics: Research and Applications*, Progress in Photovoltaics: Research Applied, **12**, pp. 69–92, 2004.

[43] ZILVERENTANT C.L., *Hybrid Solar Cells of Titanium Dioxide Sensitized with Organic Semiconductors*, *PhD. Thesis, TUDelft University*, Netherlands, 2003.

[44] DUTA A., VISA M., MANOLACHE S.A., NANU M., *Anatase (TiO_2) Thin Layers for Solid-State Solar Cells*, IEEE proceeding on the International Conference on Optimization of Electrical and Electronic Equipment, 2008.

[45] GREEN M.A., *Solar cells Operating Principles, Technology and System Applications, Prentice Hall*, New York, USA, 1982.

[46] GOETZERBERGER A., HEBLING C., SHOCK H.V., *Photovoltaic materials, history, status and outlook*, Materials Science and Engineering R, **40**, pp. 1–46, 2003.

[47] RODRIGUEZ LAZCANO Y., NAIR M.T.S., NAIR P.K., *$CuSbS_2$ Thin Film Formed Through Annealing Chemically Deposited Sb_2S_3-CuS Thin Films*, Journal of Crystal, **223**, pp. 399–406. 2001.

[48] NAIR P.K., NAIR M.T.S., GARCÍA V.M., ARENAS O.L., PEÑA Y., CASTILLO *A., Semiconductor thin films by chemical bath deposition for solar energy related applications*, Solar Energy Materials and Solar Cells, **52**, pp. 313–344, 1998.

[49] PODDER J., KOBAYASHI R., ICHIMURA M., *Photochemical deposition of Cu_xS thin films from aqueous solutions*, Thin Solid Films, **472**, pp. 71–75, 2005.
[50] SARTALE S.D., LOKHANDE C.D., *Growth of copper sulphide thin films by successive ionic layer adsorption and reaction (SILAR) method*, Materials Chemistry and Physics, **65**, pp. 63–67, 2000.
[51] WANG S-Y., WANG W., LU Z-H., *Asynchronous-pulse ultrasonic spray pyrolysis deposition of Cu_xS (x=1, 2) thin films*, Materials Science and Engineering B, **103**, pp. 184–188. 2003.
[52] ALLOUCHE N.K., NASR T.B., TURKI N.K., CASTAGNE M., *Characterization of heterojunctions based on airless spray deposited $CuInS_2$ thin films on different underlayers*, Energy Procedia, **2**, pp. 91–101, 2010.
[53] KATERSKI A., DANILSON M.A., MERE M., KRUNKS M., *Effect of the growth temperature on chemical composition of sprey deposited $CuInS_2$ thin films*, Energy Procedia, **2**, pp. 103–107, 2010.
[54] MANOLACHE S.A., ISAC L.A., DUTA A., KRIZA A., NANU M., *Metal Based Sulfides, p-Type Semiconductors in Solid State Solar Cells*, Proceeding of International Semiconductor Conference, Sinaia, Romania, pp. 141–144, 2006.
[55] MANOLACHE S.A., DUTA A., *The development of crystalline Sb2S3 thin films as buffer layer or as absorber material for three-dimensional (3D) solar cells*, Proceeding of International Semiconductor Conference, Sinaia, Romania, pp. 373–376, 2007.
[56] ISAC L.A., DUTA A., KRIZA A., NANU M., SCHOONMAN J., *Crystal order in Cu_2S obtained by spray pyrolysis*, Journal of Optoelectronics and Advanced Materials, **5**, pp. 1265–1268. 2007.
[57] ISAC L., POPOVICI I., ENESCA A., DUTA, A., *Copper Sulfides (Cu_xS) Thin Films as Possible p-type Absorbers in 3D Solar Cells*, Energy Procedia, **2**, pp. 71–78, 2010.
[58] PERNIU D., MANCIU A., ISAC L., SHOONMAN J., *Gallium and tin doped $CuInS_2$*, Journal of Optoelectronics and Advanced Materials – Symposia, **6**, pp. 992–995, 2009.
[59] POPOVICI I., PERNIU D., ISAC L., ENESCA A., DUTA A., *The influence of different n-type semiconductors on solid state solar cells with $CuIns_2$ p-type absorber*, Proceeding oh the 24th European Photovoltaic Solar Energy Conference, Germany, pp. 3020–3023, 2009.
[60] MANOLACHE S.A., ENESCA A., DUTA A., *Three-dimensional (3D) solar cell TCO/ TiO_2/$CuSbS_2$/ graphite*, Proceeding of the 22 European Photovoltaic Solar Energy Conference and Exhibition, Milano, Italy, 2007.
[61] MANOLACHE S.A., DUTA A., NANU M., GOOSSENS A., SCHOONMAN J., *The Limitation given by the n-Type Semiconductor TiO_2 in the Choice of the Absorber Material used for Solid State Solar Cells*, Proceeding of the International Conference on Sustainable Energy, Brasov, Romania, 2005.
[62] MANOLACHE S.A., NANU M., DUTA A., GOOSSENS A., SCHOONMAN J., *$CuSbS_2$ a New Absorber for Solid State Solar Cells (SSSC)*, Proceeding of the Romanian International Conference on Chemistry and Chemical Engineering - RICCCE XIV, Bucharest, Romania, 2005.
[63] MANOLACHE S.A., NANU M., DUTA A., ENESCA A., GOOSSENS A., SCHOONMAN J., *$CuSbS_2$, a Possible Absorber for Extremely Thin Absorber Solar Cells*, Proceeding of the 20th European Photovoltaic Solar Energy Conference and Exhibition, Barcelona, Spania, pp. 1906–1909, 2005.
[64] MANOLACHE S.A., DUTA A., *The Influence Of The Spray Deposition Parameters In The Photovoltaic Response of The Three-Dimensional (3d) Solar Cell: TCO/ TiO_2/ $CuSbS_2$/Graphite*, Journal of Optoelectronics and Advanced Materials, **10**, pp. 3219–3222, 2007.
[65] BÖRNSTEIN L., *Ternary Compounds, Organic Semiconductors,* **41**Ed.; Springer-Verlag, New York, USA, 2000.

[66] YOUSFI E.B., WEINBERG B., DONSANTI F.P., COWACHE D., LINCOT D., *Atomic layer deposition of zinc oxide and indium sulfide layers for Cu(In,Ga)Se2 thin-film solar cells*, Thin Solid Films, **387**, pp. 29–32, 2006.

[67] ISAC L., PERNIU D., NANU M., DUTA A., *Thin films of In_2S_3as alternatives to CdS layers in solar cells*, Journal of Optoelectronics and Advanced Materials – Symposia, **6**, pp. 986–991, 2009.

[68] BALAKRISHNAN G., KUPPUSAMI P., TRIPURA SUNDARI S., *Thirumurugesan, R.; Ganesan, G.; Mohandas, E.; Sastikumar, D. Structural and optical properties of γ-alumina thin films prepared by pulsed laser deposition*, Thin Solid Films, **518**, pp. 3898–3902, 2010.

[69] MANOLACHE S.A., ISAC L., PURGHEL(IENEI) E., DUTA A., *Three dimensional solar cell*, Proceedings of the 23th European Photovoltaic Solar Energy Conference, **1**, pp. 563–566, 2008.

Conducting Polymers Functionalized Carbon Nanotubes for Applications in the Rechargeable Lithium Batteries

M. BAIBARAC[1], I. BALTOG[1], T. VELULA[1],
P. GOMEZ ROMERO[2], S. LEFRANT[3]

[1]National Institute of Materials Physics, Atomistilor Street 105 Bis, Magurele,
PO Box MG-7, R-77125, Romania
E-mail: barac@infim.ro

[2]Centre d'Investigacio en Nanociencia i Nanotecnologia, CIN2 (CSIC-ICN),
Campus de la UAB, 08193, Bellaterra, Spain

[3]Institut des Materiaux Jean Rouxel, 2 rue de la Houssiniere, Nantes, France

Abstract. This work deals with recent progress in the rechargeable lithium batteries field using as active material composites based on conducting polymers (CPs) and carbon nanotubes (CNTs). A brief review of the synthesis and vibrational properties of composites of the type poly (3,4-ethylenedioxythiophene)/ single-walled carbon nanotubes (PEDOT/SWNTs) and polydiphenylamine (PDPA)/SWNTs is shown in this work. The performances of the two composites and the mechanism which explain the insertion/de-insertion of Li^+ ions during charge/discharge tests of cells using as active materials PEDOT and PDPA functionalized SWNTs, respectively is reported.

1. Introduction

In the last ten years many publications have gathered the tremendous progress made in the knowledge of physical and chemical properties of CNTs and their composites having conjugated polymers (CPs) as host matrices [1-5]. This is a consequence of the various and numerous applications reported for CPs/CNTs composites in different fields such as those of supercapacitors, rechargeable batteries, sensors, photovoltaic cells and photodiodes, optical limiting devices, solar cells, high-resolution printable conductors, electromagnetic absorbers and, last but not least, advanced transistors [3, 5]. In this context, the first studies concerning the use of the CPs/CNTs composites as active materials in lithium rechargeable batteries have started in 2006 [6]. Thus, using an electrolytic solution containing $LiPF_6$, a current density of 10 mA g^{-1} and a potential range between 1 and 3.5 V, during the first 20^{th} charge–discharge cycles, high specific discharge

capacities of about 45 and 115 mA h g^{-1} were reported for a positive electrode based on single-walled carbon nanotubes (SWNTs) and multi- wall carbon nanotubes (MWNTs) functionalized with poly N-vinyl carbazole (PVK), respectively. M. Baibarac et al. report a striking difference between PVK/SWNTs and PVK/MWNTs composites in the range of 1.5-2.5 V. In the case of PVK/MWNTs composite, they invoke a two stage interaction process, which increases in intensity with the number of cycles. These results indicate that the electrochemical performance of the PVK battery is much improved when a CNT functionalized with PVK composite is used as active material because of the apparent synergy between the host polymeric matrix and guest nanoparticles [6]. One year later, J. Chen et al. indicate that a membrane electrode based on "free-standing" aligned carbon nanotubes (ACN), PEDOT and polyvinilidene fluoride (PVDF), which is lightweight, flexible, highly conductive and mechanically robust, can be easily fabricated into a rechargeable battery without using a metal substrate or binder [7]. In this Li ion battery, the weight of the electrode is reduced significantly compared with a conventional electrode made by coating a mixture containing an active material onto the metal substrate. The results published in Ref. 8 show that the capacity of the ACN/PEDOT/PVDF electrode is 50% higher than that observed for free-standing SWNT paper. In fact, a highly stable dischargeable capacity of 265 mA hg^{-1} was reported after 50 cycles when ACN/PEDOT/PVDF electrode in a Li-ion cell was tested under a constant current density of 0.1 mA cm^{-2}. This is significantly higher than the value obtained previously for SWNT paper (173 mA h g^{-1}) under identical working conditions [9]. This result was attributed to the high accessible surface area (140 cm^2/cm^2) of the aligned CNTs, which coupled to the robust polymer layer provides a mechanically stable array.

In 2009, the performance of polyaniline (PANI) /MWNTs composites as cathode for rechargeable lithium batteries was tested by B.L. He *et al.* [5]. The discharge capacity of PANI/MWNTs composites is high as 122.8 mA h g^{-1} compared to 98.9 mA h g^{-1} for PANI. The composites show a stable discharge behavior, while the discharge capacity of pure PANI exhibits during 50 cycles a decreasing tendency. The results reported of B.L. He *et al.* [10] are much better than those obtained on PANI nanotubes or nanofibers as the cathode for lithium/PANI rechargeable batteries reported by Wang *et al.* [11]. The main reason may be that the addition of MWNTs to PANI makes the composites similar to an interwoven fibrous structure, which improves the conductivity and facilitates access of the electrolyte. A particular result of these studies is that the specific capacity and coulombic efficiency values are much higher than other rechargeable lithium-PANI cells assembled with gel polymer electrolyte [12, 13]. The promising results reported until now in the Li rechargeable batteries field make this application of primary importance. Therefore, in this paper, our attention is concentrated on testing the PEDOT/SWNTs and PDPA/SWNTs composites as an active material for cathodes in Li rechargeable batteries.

2. Experimental

Composites based on PEDOT and SWNTs were synthesized by the chemical polymerization of
EDOT in the presence of SWNTs according to Ref. [14]. Despite the low EDOT solubility in water, the chemical polymerization was carried out in aqueous solution containing 2.1 g dm^{-3} of monomer. The oxidizing agent, i.e. $FeCl_3$, was added to the monomer solution, and the whole mixture was stirred for 24 hours at 25^0C. Using stoichiometric amounts of $FeCl_3$, slow rates of polymerization were noted, with low yields of about 14% after 24 hours. [14] According to the paper of R. Corradi et al. [14], an increase of the PEDOT yield was obtained by a synthesis carried out with an excess of oxidant (from 2.33:1 up to 25.63:1, *i.e.*, ten fold excess over the stoichiometric amount). In this case, for the chemical synthesis of PEDOT, a mass of monomer of 0.1 g was used. Afterwards, the dark blue PEDOT suspensions was washed with 1000 ml of de-ionized water and then dried under vacuum at 65^0C. For the PEDOT/SWNTs composite synthesis, different masses of CNs, *i.e.*, 0.005, 0.01 and 0.02 g were added to the reaction mixture.

Composites based on PDPA and SWNTs were obtained by the electrochemical polymerization of DPA in a conventional three-electrode one-compartment cell having Pt or a SWNT film deposited onto a 1 cm^2 Pt plate as working electrodes. The counter electrode was a spiral Pt wire. The area of counter electrode was greater than that of the working electrode. The potential of the working electrode was measured vs. saturated calomel reference electrode (SCE). The polymerization solution consisted of 10^{-2} M DPA and 1M HCl in DMF-H_2O (1:1 vol). PDPA was electrochemically synthesized by cyclic voltammetry in the potential range (+100; +960) mV vs. SCE with a sweep rate varied from 5 to 100 mV s^{-1} applied both on a blank Pt electrode and a Pt electrode coated with a SWNTs film. The electrochemical measurements were carried out using a potentiostat/galvanostat, VOLTALAB 80 model, from Radiometer Analytical.

Surface enhanced Raman scattering (SERS) spectra were recorded at room temperature and in ambient air in a backscattering geometry under excitation wavelengths of 676 and 1064 nm. For the two excitation wavelengths, 676 and 1064 nm, we used a spectrophotometer Jobin Yvon T 64000 and a FT Raman Bruker RFS 100, respectively.

Fourier Transform Infrared (FTIR) spectra in the attenuated total reflexion (ATR) geometry were recorded using a Bruker FTIR spectrophotometer, Vertex 70 model.

Charge/discharge tests were carried out using a multichannel potentiostat-galvanostat (Arbin Instruments, College Station, USA) for two-electrode cells. To fabricate the positive electrode (cathode), we used the PEDOT/SWNTs or PDPA/SWNTs composite or CPs of the type PEDOT or PDPA (80 wt.% as active material), poly(vinylidene fluoride) (PVDF; 5 wt%) as binder, super-P carbon

(15 wt.%), dibutyl phthalate (DBP, 2 drops) and acetone (1 ml), all of which were mixed and stirred for 12 h to yield a homogeneous paste. The paste was tape-cast onto a glass surface and acetone allowed to evaporate. After peeling off the resulting film, it was washed with diethyl ether in order to remove the DBP. Lithium foil 0.38 mm thick with an area of 2.03 cm^2 was used as the negative electrode (anode). A solution of $LiPF_6$ (1M) in a 50:50 mixture (by volume) of ethylene carbonate and dimethyl carbonate was used as the electrolyte. Cell assembly was carried out under a purified argon atmosphere in a MBraun glove box. Electrochemical testing of the cells was performed using constant-current cycles. The current density was 10 mA g^{-1}. The cells were cycled between: i) 2 and 4.4 V in the case of PEDOT and the PEDOT/SWNTs composite and ii) 2 and 4 V in the case of PDPA and the PDPA/SWNTs composite.

3. Results and Discussions

3.1 *Composites based on PEDOT and SWNTs*

Figs. 1 and 2 show SERS spectra of SWNTs films at excitation wavelengths 1064 and 676 nm, before and after functionalization process with PEDOT. Spectra exhibit the well known two main groups of bands whose relative intensities and peak positions vary with excitation wavelength. The first group, from 100 to 350 cm^{-1} is associated with the radial breathing modes (RBM). The intensity and peak position of these bands, related to the tube diameter through the relation ν (cm^{-1}) = 223.75/d (nm) [1] are very sensitive to the excitation wavelength. The two strong bands situated at 174 and 164 cm^{-1}, observed at excitation wavelengths of 676 and 1064 nm, indicate that resonance occurs over a narrow range of diameters of about 1.36 and 1.27 nm, respectively. At the excitation wavelength of 1064 nm, the two Raman lines at 164 and 176 cm^{-1} have been associated with the RBM activated in isolated and bundled nanotubes, respectively.[15] The second group, consisting of the TM and D bands, is found from 1000 to 1700 cm^{-1}. These bands are not only related to the nanotube structure; the former, peaking at about 1595 cm^{-1} and attributed to the tangential vibration mode, is also seen in the Raman spectra of other graphitic materials such as HOPG. [1] The analysis of the group of bands associated with TM vibration at 676 nm excitation wavelength reveals four components, three of Lorentzian type at about 1606, 1588 and 1560 cm^{-1}, with widths at half maximum of about 32, 26 and 26 cm^{-1} and the fourth, at about 1542 cm^{-1}, asymmetrical in its lower energy side. This Breit-Wigner-Fano (BWF) profile has been related until recently as originating from an electron-phonon interaction [1], but recent calculations describe it as the G^- band which is in metallic tubes strongly dependent upon the tube diameters [16]. The D band is frequently associated with a disorder in the graphitic lattice or defects in nanotubes [1].

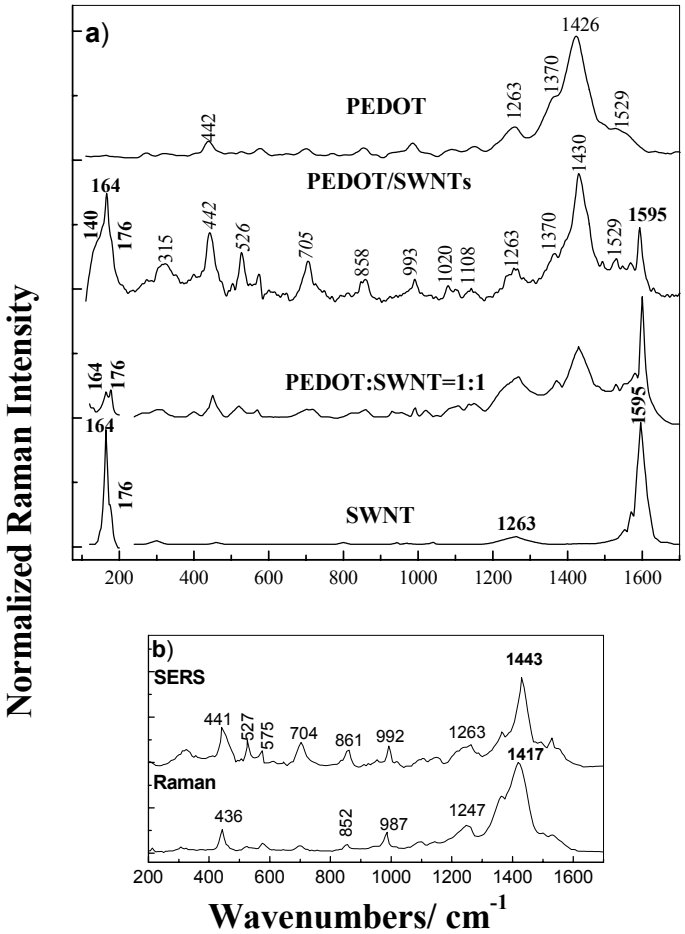

Fig. 1. SERS spectra (λ_{exc} = 1064 nm) of the films of SWNTs, PEDOT in undoped state and composite materials obtained by: i) the chemical synthesis of 0.1 g EDOT and 0.02 g SWNTs (PEDOT/SWNTs) and ii) the mixture of the two constituents in the massic ratio of PEDOT:SWNTs of 1:1 (a). Raman and SERS spectra of PEDOT doped with $FeCl_4^-$ ions (b).

Figs. 1 and 2 also show the SERS spectra of the PEDOT film. We note that the main Raman lines of the PEDOT are localized at 439-575, 698, 860, 990, 1250, 1365, 1412-1450, and 1545 cm^{-1}, being associated to the following vibration modes: oxyethylene ring deformation, symmetric C-S-C deformation, asymmetric C-S-C deformation, oxyethylene ring deformation, C_α- $C_{\alpha'}$ stretching +C-H bending, C_β- $C_{\beta'}$ stretching, symmetric C-C stretching and asymmetric C-C stretching, respectively [17] An interesting behavior of the C=C stretching vibration of PEDOT is worth noting. This band, located at 1424 cm^{-1} in the

un-doped polymer is firstly shifted to 1410 cm^{-1} and then to 1450 cm^{-1} with the doping level. [17]

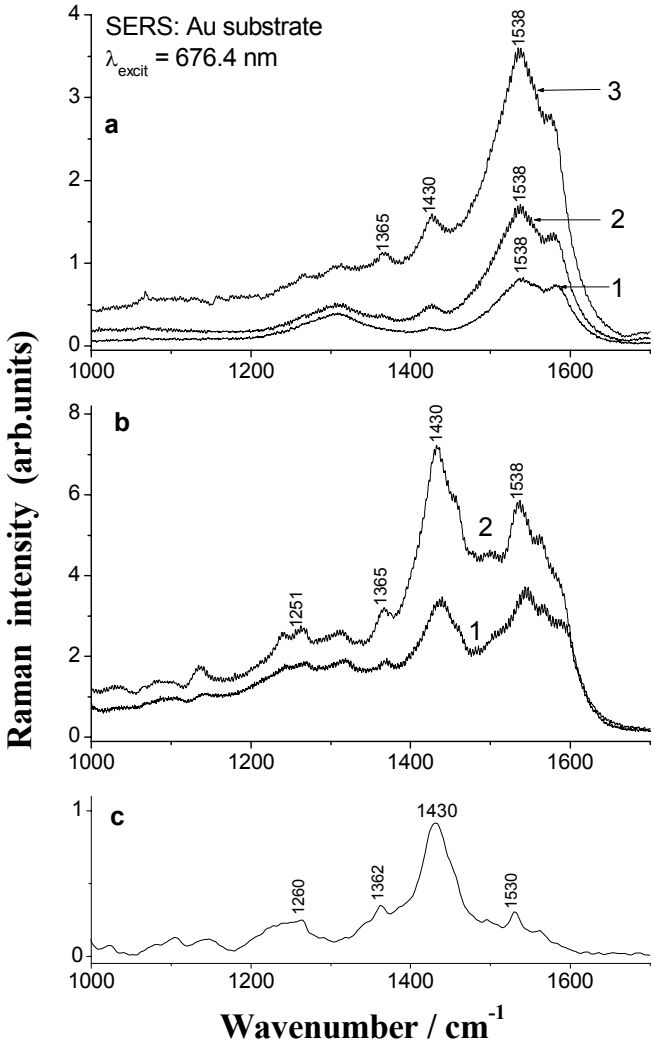

Fig. 2. SERS spectra (λ_{exc} = 676 nm) of films of SWNTs (curve 1a), PEDOT in un-doped state (c) and the composite materials obtained by the chemical synthesis of i) 0.1 g EDOT and 0.01 g SWNTs (2a) and ii) 0.1 g EDOT and 0.02 g SWNTs (3a). Curves 1b and 2b correspond to SERS spectra of composites obtained by the mixture of the two constituents PEDOT:SWNTs in the massic ratio of 1:1 and 2:1, respectively.

Concerning the C=C stretching vibration of PEDOT, Fig. 1 shows an intriguing experimental fact. The position of Raman band associated to the C=C stretching vibration is changed when the Raman spectrum is carried out on a PEDOT sample

in the powder state and thin film, respectively (of. ca. 50 nm) deposited on the rough Au support. At first sight, this variation is difficult to understand. However, the modification can be explained if one takes into account the mechanisms which govern SERS. It is well known that the SERS spectrum originates in two basic enhancement mechanisms: i) electromagnetic, achieved by the resonant excitation of the surface plasmons and ii) chemical, mainly due to charge transfer processes between the metallic substrate and adsorbed molecules. In our case, we think that electrons of the SERS metal support, excited by the incident photons, are transferred by tunneling into an excited state of the adsorbed polymer. In this way, the charge transfer process induces another equilibrium geometry in the excited molecule. The return of the electron to the metal leaves PEDOT into another vibrational excited state than the partially doped polymer molecule leading to the emission of a Raman shifted phonon. Consequently, the SERS spectrum of PEDOT deposited on the Au support appears as being different from the standard Raman spectrum because of the symmetry lowering effect produced by the laser excitation. We note that such variations for the PEDOT films with thickness bigger of 100 nm are not observed. Therefore, in all SERS studies are used the films with thickness around of 120 nm. As observed in Figs. 1 and 2, the different SERS spectra for the PEDOT/SWNTs composites are obtained, resulting from the mixture of the two constituents and from the chemical polymerization of EDOT in the presence of CNTs,. The main variations observed in the SERS spectra from Figs. 1 and 2 are: i) in comparison with SERS spectra of SWNTs, an enlargement of the RBM band at 1064 nm excitation wavelength is observed in the case of the PEDOT/SWNTs composite obtained by chemical polymerization of monomers in the presence of CNTs. A detailed analysis of the 100 - 250 cm^{-1} spectral range shows that this band is formed from three Raman lines localized at 140, 164 and 176 cm^{-1}. We note that all these Raman lines belong to SWNTs. Besides, for the chemical synthesis, a change of the ratio between the intensities of the Raman bands with the maximum situated at 164 and 1595 cm^{-1} is noted, too. When mixing the two constituents (PEDOT and SWNTs) is carried out, a significant decrease in the intensity of the RBM band is observed. At the 676 nm excitation wavelength, an increase in the intensity of the G^- component, independently on the way of preparation of the PEDOT/SWNTs composite, is observed; ii) in comparison with SERS spectrum of PEDOT doped with $FeCl_4^-$ ions, one observes that for the PEDOT/SWNTs composite: a) in the case of the two synthesis ways, the most intense Raman line is peaked at 1430 cm^{-1} not longer by those of the un-doped polymer; b) the ratio between the intensities of the Raman bands with maxima at 1263 and 699-705 cm^{-1} ($I_{1260}/I_{699\text{-}705}$) changes from 3:1 to 1:2 for the PEDOT/SWNTs composite prepared by the mixture route and chemical polymerization, respectively; c) in the case of the chemical polymerization of EDOT in the presence of SWNTs, the increase of the Raman bands intensity located at 442-526 and 705 cm^{-1} indicate the presence of some steric hindrance effects. An explanation for all these variations is not easy to

be given at the present time. In our opinion, the increase in the intensity of G^- component indicates the existence of an electron-phonon interaction enhanced by a supplementary roping of nanotubes through their functionalization with conducting polymer molecules. In the case of the chemical polymerization of EDOT in the presence of SWNTs, we think that a covalent functionalization takes place according with the following reaction from Scheme 1.

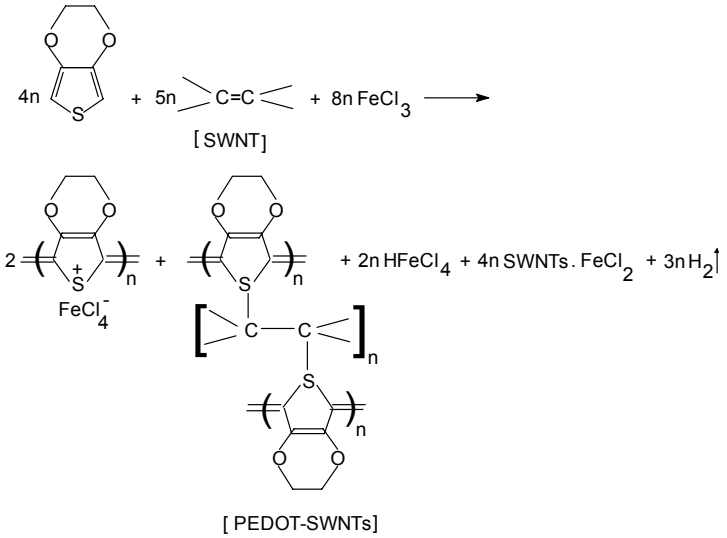

Scheme 1. The chemical polymerization reaction of EDOT in the presence of $FeCl_3$ and SWNTs.

The reaction shown in Scheme 1 is supported by the following experimental facts: i) the increase in the intensity of the deformation vibration modes of the oxyethylene ring and the C-S-C bond noticed by the Raman line at 442-526 and 705 cm^{-1}, respectively as a result of the steric hindrance effects induced by the formation of the new covalent bonds between PEDOT and SWNTs; ii) the localization of the most intense Raman line of PEDOT at 1430 cm^{-1}, situated always for un-doped polymer at 1426 cm^{-1} suggests that the reaction product contains mainly PEDOT covalently functionalized SWNTs and to a smaller extent PEDOT doped with $FeCl_4^-$ ions; iii) the appearance of the Raman line at 140 cm^{-1} is a consequence of the formation of a new covalent bond between PEDOT and SWNTs.

For the availability of high power density battery systems, it is important to increase the active surface area of the electrodes. Such an example is shown in this paper by the use of new cathode active materials based on the composites of the type PEDOT/SWNTs. Our studies concerning the use of the derivatives of PEDOT in the Li rechargeable batteries field indicate better performances than for the cell $Li/LiPF_6$/PEDOT by substituting the polymer with the PEDOT/SWNTs composite

obtained by chemical polymerization of EDOT in the presence of CNTs. Fig. 3 is rather illustrative in this respect.

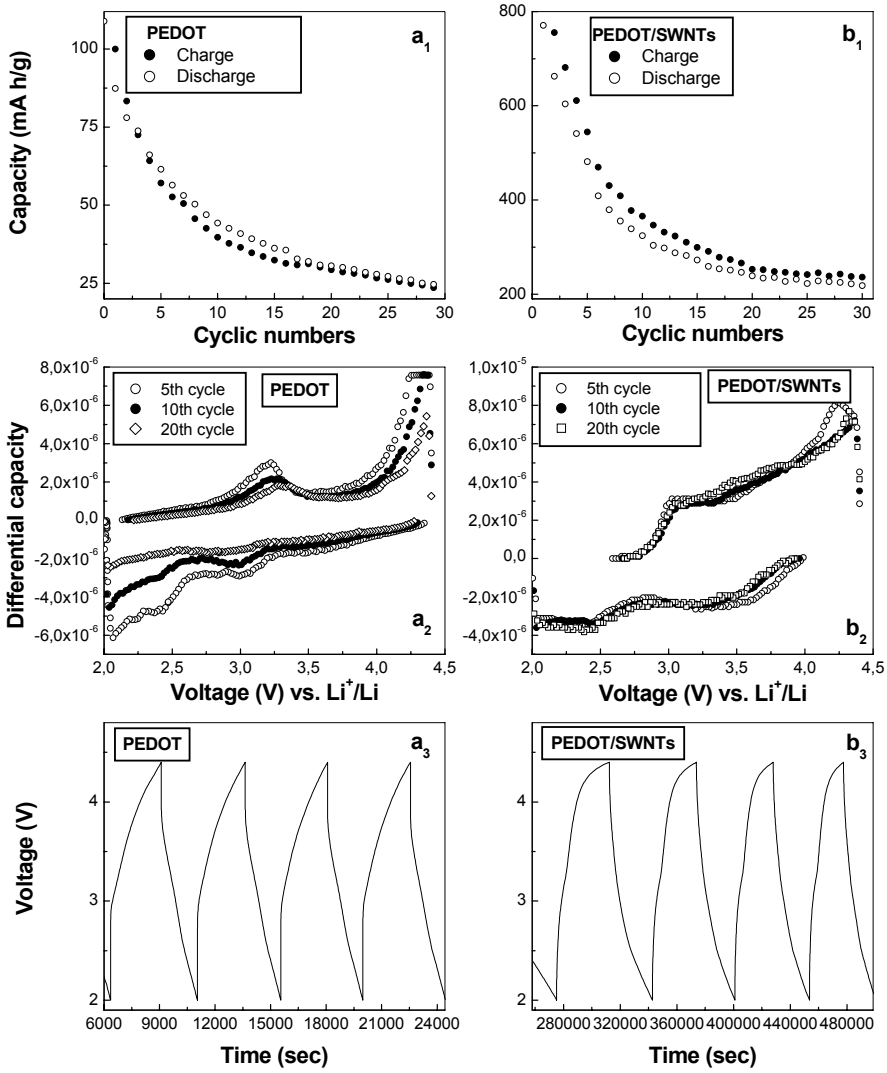

Fig. 3. The evolution of specific capacities vs. cycle number for PEDOT and PEDOT functionalized SWNTs electrodes in lithium cells is shown in a_1 and b_1, respectively. Fig. a_2 and b_2 show incremental capacity curves (for the 5th cycle (open circles), the 10th cycle (full circles) and the 20th cycle (open square) of PEDOT and PEDOT functionalized SWNTs battery. Fig. a_3 and b_3 show the voltage profile of PEDOT and PEDOT functionalized SWNTs batteries.

The first remarkable result is the very large specific capacity of the hybrid PEDOT/SWNT material in the first cycle (close to 800 mAh/g) which decreases

and gets stabilized above 200mAh/g. Indeed, for the two compounds (PEDOT doped with $FeCl_4^-$ ions and PEDOT functionalized SWNTs), a significant decrease of the capacity during the first twelve charge-discharge cycles is observed. Afterwards, an increase of the number of charge-discharge cycles leads to a smaller decrease of the cell capacity in the case of battery having PEDOT functionalized SWNTs as active cathode material. We believe that these results can be related to a more pronounced degradation of the PEDOT in comparison with the composites based on PEDOT and SWNTs. After 30 charge-discharge cycles, discharge capacities of ca. 25 and 200 mA h g^{-1} in the case of PEDOT and PEDOT functionalized SWNTs, respectively, are recorded. This result demonstrates a better performance of the $Li/LiPF_6$/PEDOT-functionalized SWNTs battery in comparison with that of the type $Li/LiPF_6$/PEDOT.

3.2 *Composites based on PDPA and SWNTs*

Fig. 4a shows the Raman spectrum of PDPA in bipolaronic state deposited on blank Pt electrode with the main lines situated at 412 - 612, 1174, 1204, 1372, 1491-1580 and 1609 cm^{-1}, which are assigned to the following vibration modes: benzene ring deformation, C-H bending in benzoid ring (B)-A_g mode, C-N stretching, semiquinone radical structure, C=C stretch, in quinoid ring (Q) and C-C stretch. (B), respectively [4, 18].

The interaction of PDPA in bipolaronic state with NH_4OH solution leads to modifications of the Raman spectrum as follows: i) the change in the relative intensities of the Raman lines located in the spectral ranges 1100-1200, 1300-1400 and 1550-1625 cm^{-1} ($I_{1100-1200}$: $I_{1300-1400}$: $I_{1550-1625}$) from 1:2:1 to 1:1:1.5 and ii) the change in the position of the above mentioned Raman lines. Fig. 4b shows that increasing the cycle number from 25 to 50 and 100 the Raman lines of PDPA in bipolaronic state are observed more and more clearly. The interaction between the polymer and SWNTs is evidenced also by the narrowing of G band profile. In the first 50 cycles, the asymmetric component of G band, with a maximum at 1540 cm^{-1}, decreases simultaneously with the disappearance of the Raman line associated to RBM. After 100 cycles, the Raman spectrum shows only vibrational features of PDPA in bipolaronic state. In the literature devoted to composites based on CPs and CNTs, the interaction with NH_4OH solution was used often to prove the functionalization of SWNTs with the polymers. Thus, as reported in Ref. 4, when there is no interaction between both components, a polymer/carbon nanotubes bilayer structure is obtained, leading to a Raman spectrum that appears as a sum spectrum of the two constituents. According to Ref. 4 such a behavior is also observed when the composite material interacts with NH_4OH solution. As it can be seen in Fig. 4b, this is not our case. The post-treatment of the sample with an aqueous NH_4OH solution results in the disappearance of all Raman lines of

PDPA and the total recovery of the Raman spectrum of SWNTs. An explanation for this behavior may come from a different Raman activity of PDPA and SWNTs.

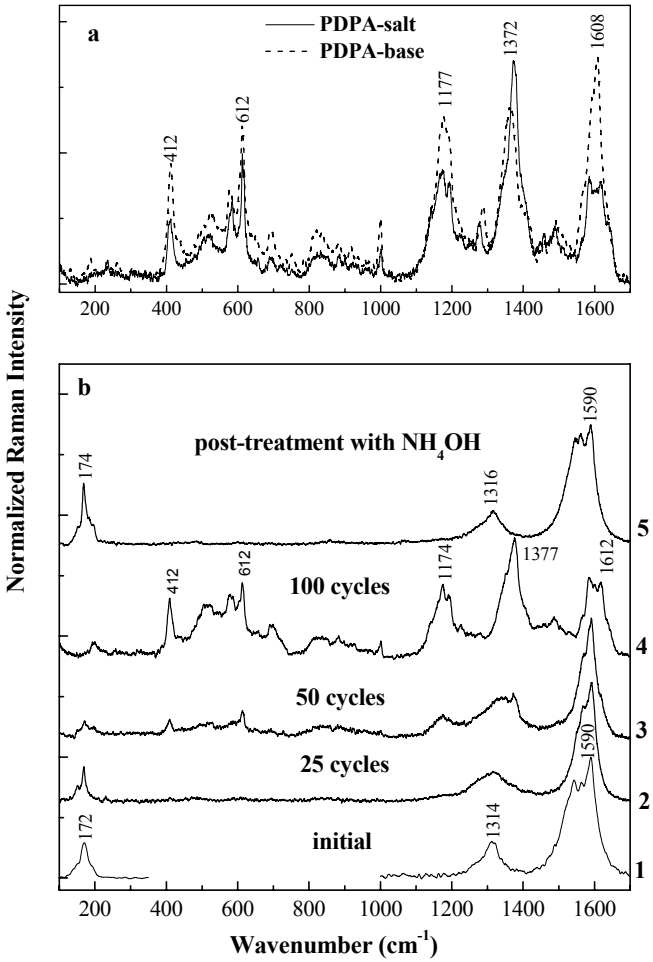

Fig. 4. Raman spectra at λ_{exc} = 647 nm of PDPA deposited on: (a) Pt support in doped (dotted line) and un-doped state (solid line) and (b) SWNTs film before (spectrum 1) and a fter electrochemical synthesis of PDPA-salt upon 25 (spectrum 2), 50 (spectrum 3) and 100 cycles (spectrum 4). Raman spectrum of the PDPA-base/SWNTs composite obtained by the interaction of PDPA-salt/SWNT film with NH_4OH 1M is shown in Fig. b as curve 5.

A confirmation of this hypothesis is shown in Fig. 5, where the ATR IR spectra of PDPA-salt (curve 1), PDPA-base (curve 2), PDPA-salt functionalized SWNTs (curve 3) and PDPA-base functionalized SWNTs (curve 4) are presented. As observed in Fig. 5, the main absorption bands of PDPA-salt deposited onto a blank

Pt support are located at 698, 752, 1161, 1178, 1317, 1497, 1595 and 1668 cm^{-1}, and are assigned to the following vibrational modes: inter-ring deformation, ring deformation, C-H in plane bending quinoid (Q), C-H bending benzene (B), $C_{aromatic}$-N stretching, C-C stretching + C-H bending, C-C stretching vibration of the B ring and $–NH^{+}=Q=Q=NH^{+}$-, respectively. [19, 20] The interaction of PDPA-salt with NH_4OH solution leads to the formation of PDPA-base, and the disappearance of the band at 1668 cm^{-1} in the ATR-IR spectrum (curve 2, Fig. 5). In comparison with PDPA-salt deposited onto Pt electrode (curve 1, Fig. 5), the main change shown by the ATR IR spectrum of PDPA-salt functionalized SWNTs, (curve 3 in Fig. 5) is a down-shift of the bands associated to the inter-ring deformation, ring deformation, C-H bending and $–NH^{+}=Q=Q=NH^{+}$- vibration modes, from 698, 752, 1498, 1668 cm^{-1} to 692, 744, 1487 and 1660 cm^{-1}, respectively. A careful analysis of the ATR-IR spectra of PDPA-salt (Fig. 5, curve 1) and the PDPA-salt/SWNT composite (Fig. 5, curve 2) reveals down-shifts of ca. 8 - 10 cm^{-1} for the absorption bands located in the ranges 600-800, 1400-1550 and 1600-1700 cm^{-1}. These bands are associated with vibrational modes of the ring or inter-ring deformation type, C-C stretching vibration of the benzene ring and $NH^{+}=Q=Q=NH^{+}$- (Q= quinoide ring).

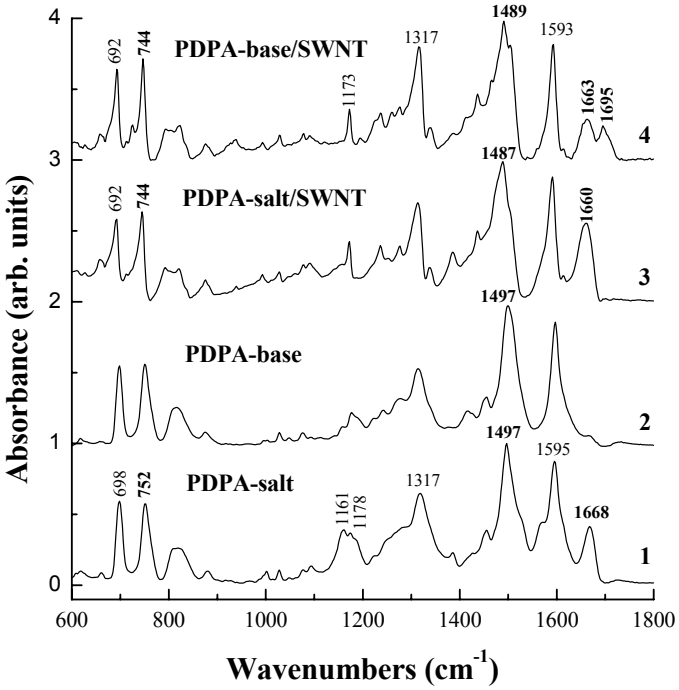

Fig. 5. ATR IR spectra of PDPA-salt (curve 1), PDPA-base (curve 2), PDPA-salt functionalized SWNTs (curve 3) and PDPA-base functionalized SWNTs (curve 4).

The change in the position of these bands indicates a modification of the force constants, which can be explained only on the basis of a covalent functionalization process of SWNT with PDPA-salt. Such a functionalization induces significant steric hindrance effects, which must be detected in the spectral range of the aromatic rings deformation ((600-800 cm^{-1} as reported above). The chemical interaction of PDPA-salt functionalized SWNTs with NH_4OH solution results in PDPA-base functionalized SWNTs. As it could be expected, the ATR IR spectrum of PDPA-base functionalized SWNTs (curve 4, Fig. 5) shows all IR bands of PDPA. Besides, in the spectral range 1600-1700 cm^{-1}, we detect an up-shift of the absorption bands from 1660 to 1663 cm^{-1} that is accompanied by the appearance of a new band with maximum at 1695 cm^{-1}. This new band indicates the appearance of C=O groups onto SWNTs. [21]. Having all these considerations in mind, we conclude that when electrochemical polymerization of DPA onto SWNTs film takes place, it results in SWNTs covalently functionalized with PDPA-salt.

In the following paragraph we can see the application of PDPA-salt functionalized SWNTs as active material for the positive electrode rechargeable lithium cells. Analyzing incremental capacity curves (Fig.6), we found different characteristics for the PDPA-salt and PDPA-salt covalently functionalized SWNTs composite. A significant decrease of capacity during the first 10 charge-discharge cycles is observed for the two materials. A decrease in capacity, of about 40% and 50%, is noted in Figs. $6a_1$ and $6b_1$ during the first 10 charge/discharge cycles of the cells (-) Li / PDPA-salt/SWNTs composite (+) and (-) Li / PDPA-salt (+), respectively.

A careful analysis of Figs. $6a_1$ and $6b_1$ reveals that during the first charge/discharge cycle irreversible capacity losses of 5 and 21 mA h g^{-1} are detected for PDPA-salt and PDPA-salt/SWNTs composite, respectively. This irreversible capacity is connected both to the reduction of the active materials, PDPA-salt and PDPA-salt/SWNTs composite, and the decomposition of the electrolyte with the formation of a passive protecting layer (labeled as solid electrolyte interface (SEI) film) takes place according to the following reaction [22, 23]:

$$C_3H_4O_3 + 2e^- + 2\,Li^+ = Li_2CO_3 + CH_2{=}CH_2$$

The charge spent in the formation of the passive layer is strictly connected to the surface area of the electrode material. Significant differences in capacity are noted for the two cells after 20 charge/discharge cycles. In the case of the (-) Li/ the PDPA-salt/SWNT composite (+) cell, the capacity remains unchanged and at a high value. On the other hand, in the case of the (-) Li/PDPA-salt (+) cell specific capacity values are lower and suffer a second drop from cycles 20 to 28 approximately. After that the capacity remains constant until the end of the 35 cycles are completed.

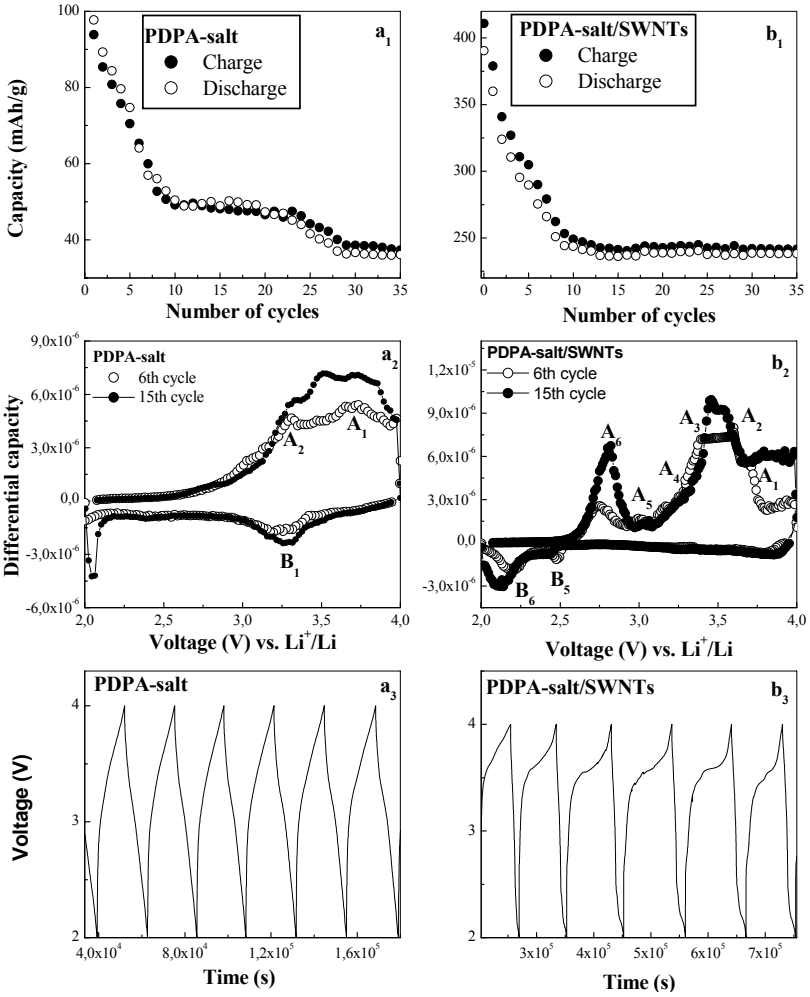

Fig. 6. The evolution of specific capacities vs. cycle number for PDPA-salt and PDPA-salt functionalized SWNTs electrodes in lithium cells is shown in a_1 and b_1, respectively. Fig. a_2 and b_2 show incremental capacity curves (for the 6th cycle (open circles) and the 15th cycle (full circles)) of PDPA-salt and PDPA-salt functionalized SWNTs battery. Fig. a_3 and b_3 show the voltage profile of PDPA-salt and PDPA-salt functionalized SWNTs batteries.

The reactions taking place at each of the cells studied ((-) Li/PDPA-salt (+) and (-) Li/ PDPA-salt/SWNT composite (+)) during the charge/discharge tests are shown in Scheme 1.

a) Negative electrode:

$$2n\ Li \underset{charge}{\overset{discharge}{\rightleftharpoons}} 2n\ Li^{+} + 2n\ e^{-}$$

b) Positive electrode of (-) Li/PDPA-salt (+) cell:

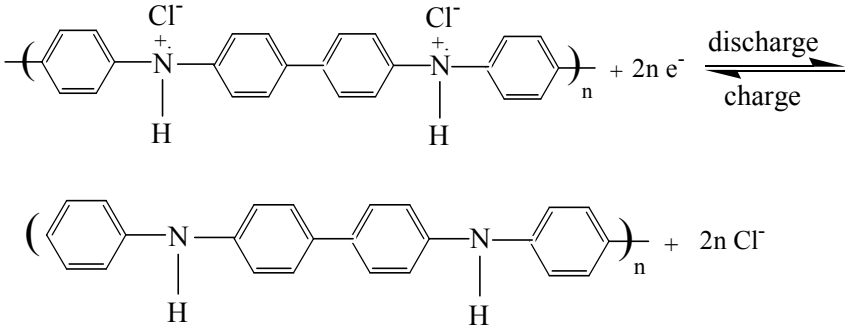

Total reaction of the (-) Li/PDPA-salt (+) cell:

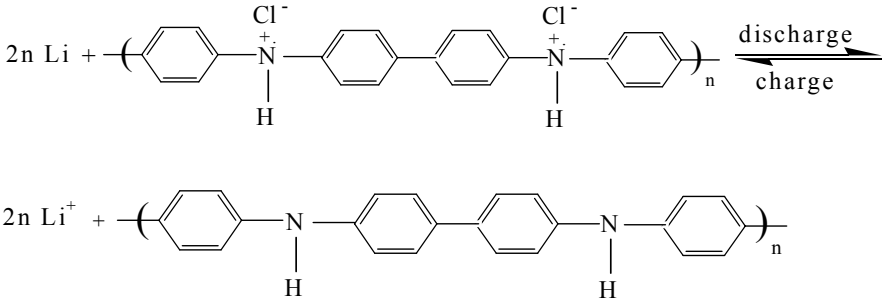

c) Positive electrode of the (-) Li/ the PDPA-salt/SWNTs composite (+) cell:

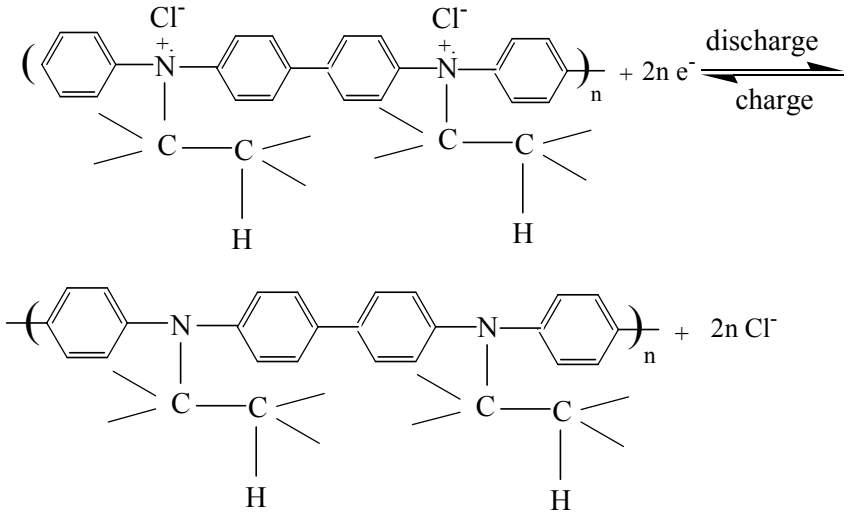

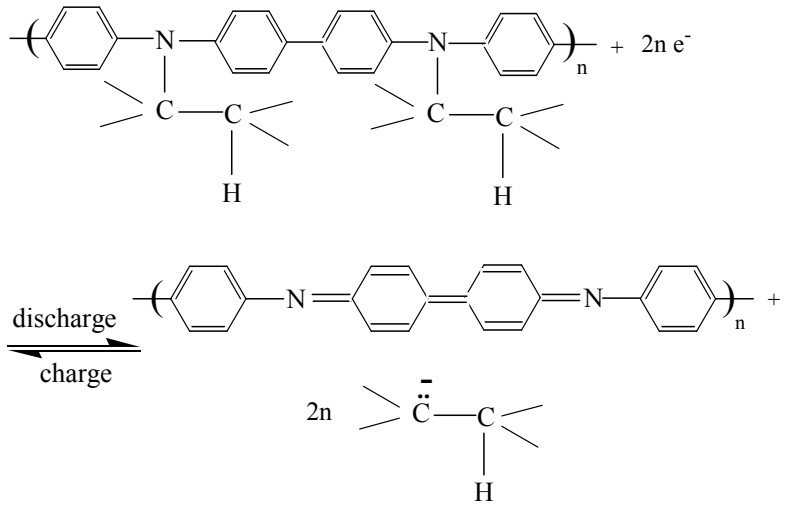

Total reaction of the (-) Li/ the PDPA-salt/SWNTs composite (+) cell:

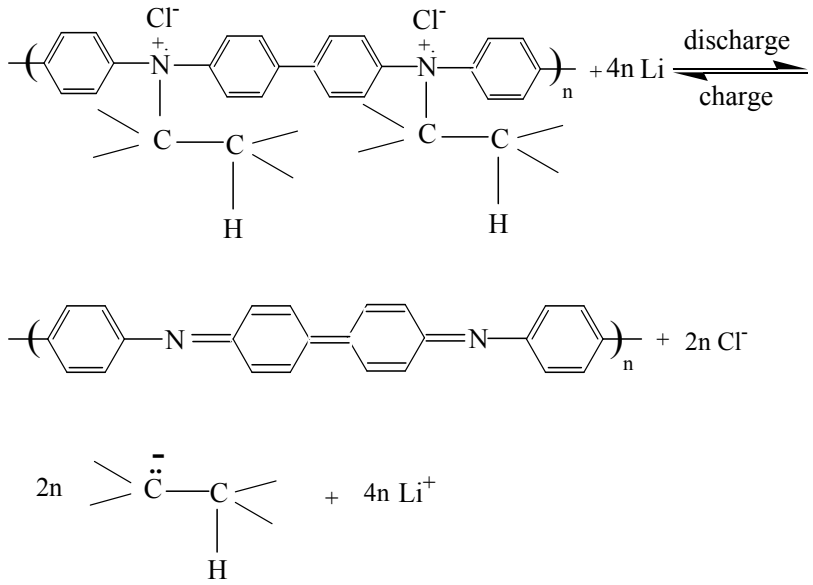

Scheme 1. Reactions at the two electrodes for the batteries (-) Li/PDPA-salt (+) and (-) Li/ the PDPA-salt/SWNTs composite (+): (a) the positive electrode, (b) and (c) the negative electrode containing as active material PDPA-salt and the PDPA-salt/SWNTs composite, respectively.

We believe that the second capacity drop could be related with a decomposition of the electrode surface. In the case of the (-) Li/ PDPA-salt/SWNTs composite (+) cell, the absence of the second capacity drop indicates an inhibiting role of SWNT

towards a further decomposition of the electrode surface. At the end of the final 35th charge-discharge cycle, discharge capacities of 35 and 245 mA h g^{-1} were recorded for PDPA-salt and the PDPA-salt/SWNTs composite, respectively. These results indicate that the electrochemical performance of a lithium battery based on PDPA-salt is substantially surpassed by the PDPA-salt/SWNTs composite as active material. This suggests a synergism between the host polymer matrix and guest nanoparticles, as detected in other hybrid systems. [24] The effect of the two active materials on the lithium cell potential is shown in Fig. 6. Analyzing the incremental curves of the two materials, electrochemical activity associated to Li insertion in the range 3-4 V (during discharge) is detected in both cases. For the PDPA-salt active material, the peaks associated to Li insertion and Li de-insertion noted in Fig. 6 as A_1-A_2 and B_1, respectively are found at 3.73 - 3.31 and 3.19 V vs. Li/Li^+. In the case of the PDPA-salt/SWNTs composite, the Li insertion is characterized by the maxima labeled A_1, A_2, A_3 and A_4 localized at potentials of about 3.7, 3.6, 3.41 and 3.17 V vs. Li/Li^+. On the other hand, a striking difference between PDPA and the PDPA/SWNTs composite is observed in the potential range 2-3 V, the latter active material showing a process characterized by two couples of intercalation/de-intercalation. These are characterized by the peaks associated to the Li insertion/Li de-insertion noted as A_5/B_5 and A_6/B_6 having potentials at 3.01/2.19 and 2.75/2.48 V, respectively. In the case of the (-) Li/ PDPA-salt/SWNTs composite (+) cell, as increasing of the charge/discharge cycles number (Fig. $6b_2$), it is interesting to note: i) the change in the relative intensities of the peaks situated in the potential range (2; 3) V and (3; 4) V and ii) an up-shift of the A_6 peak accompanied by a down-shift of the B_5 and B_6 peaks. Understanding of this particular behavior needs further research. However, the data presented here are more than sufficient to show that the PDPA-salt/SWNTs composite performs better in rechargeable Li batteries than the PDPA-salt material alone, and maintains a remarkably high value of specific charge of 245 mAh g^{-1} after 35 cycles which makes it worth of further studies for this particular application.

4. Conclusions

In this work, we have reported new results concerning the performances of the PEDOT/SWNTs and PDPA/SWNTs type composites as active materials in Li rechargeable batteries. Our results lead to the following conclusions:

i) the chemical polymerization of EDOT in the presence of SWNTs and $FeCl_3$ results in a covalent functionalization of SWNTs with PEDOT molecules, which is evidenced in the SERS spectra of PEDOT and SWNTs by: a) the appearance of a Raman line at 140 cm^{-1} indicating the formation of a new covalent bond between PEDOT and SWNTs; b) an increase in the intensity of the Raman line at 705 cm^{-1}, associated with the deformation vibration mode of C-S-C bond, the result of a steric hindrance effect induced by the bonding of PEDOT on SWNTs; and c) the

enhancement of the Raman band with maximum at 1540 cm^{-1} (G^- component) in SWNTs when the PEDOT weight in the PEDOT/SWNTs composite increases.

ii) using the PEDOT/SWNTs composite as a positive electrode and an electrolytic solution containing $LiPF_6$ into a Li rechargeable battery, a high specific discharge capacity (stabilized at ca. 200 mA h g^{-1}) is reported for the cathode active material;

iii) a covalent functionalization of SWNTs with PDPA in bipolaronic state takes place when electropolymerization of DPA onto SWNTs film occurs. The covalent functionalization process is probed by Raman and ATR IR spectroscopy studies;

iv) optimization of the electrochemical synthesis of the PDPA-salt functionalized SWNTs composite, as performed here, may improve their electrochemical performance in different applications. In this paper, such an example is given by an improvement of the specific capacity of PDPA-salt/SWNTs (steady at 245 $mAhg^{-1}$ after 35 cycles) with respect to pure PDPA-salt (35 $mAhg^{-1}$) in rechargeable Li cells.

Acknowledgment. This research was financed by projects PNII 72-182/2008 and PNII 62-081/2008.

References

[1] DRESSELHAUS M.S., DRESSELHAUS G., EKLUND P.C., *Science of fullerene and carbon nanotubes*, Academic Press, New York, 1996.

[2] BAIBARAC M., BALTOG I., LeFRANT S., Chapter 5, *Composites based on conducting polymers and carbon nanotubes in Book Nanostructured conductive polymers*, Ali Eftekhari Ed., Wiley-Blackwell Interscience, pp. 209–260, 2010.

[3] BAIBARAC M., GOMEZ-ROMERO P., NANOSCI J., Nanotech. **6**, p. 289, 2006.

[4] LEFRANT S., BAIBARAC M., BALTOG I., J. Mater. Chem. **19**, p. 5690, 2009.

[5] BAIBARAC M., BALTOG I., LeFRANT S., Current Organic Chemistry **17**, 2011.

[6] BAIBARAC M., LIRA CANTU M., ORO-SOLE J., CASAN-PASTOR N., GOMEZ ROMERO P., Small 2, 1075, 2006.

[7] CHEN J., LIU Y., MINETT A.I., LYNAM C., WAG J., WALLACE G.G., Chem. Mater **19**, p. 3595, 2007.

[8] WANG J., XU Y., SUN X., LI X., DU X., J. Solid State Electrochem. **12**, p. 947, 2008.

[9] NG S.H., WANG J., GUO Z.P., CHEN J., WANG G.X., LIU H.K., Electrochim. Acta **51**, p. 23, 2005.

[10] HE B.L., DONG B., WANG W., LI H.L., Materials Chemistry and Physics **114**, p. 371, 2009.

[11] WANG C.Y., MOTTAGHITALAB V., TOV C.O., SPINKS G.M., WALLACE G.G., J. Power Sources **163**, p. 1105, 2007.

[12] SIVAKKUMAR S.R., KIMA W.J., CHOI J.A., MacFARLANE D.R., FORSYTH M., KIM D.W., J. Power Sources **171**, p. 1062, 2007.

[13] CHENG F., TANG W., LI C., CHEN J., LIUM H., SHEN P., DOU S., Chem. Eur. J. **12**, p. 3082, 2006.

[14] CORRADI R., ARMES S.P., Synth. Met. **84**, p. 453, 1997.

[15] MARCOUX P.R., SCHREIBER J., BATAIL P., LEFRANT S., RENOURD J., JACOB G., ALBERTINI D., MEVELLEC J.Y., Phys. Chem. Chem.Phys. **4**, p. 2278, 2002.

[16] PISCANEC S., LAZZERI M., ROBERTSON J., CHASE B., FERRARI A.C., MAURI F., Phys. Rev. B **75**, p. 035427, 2007.
[17] GARREAU S., DUVAIL J.L., LOUARN G., Synth. Met. **125**, p. 325, 2002.
[18] LAPKOWSKI M., BERRADA K., QUILLARD S., LOUARN G., LEFRANT S., PRON A., Macromolecules **28**, p. 1233, 1995.
[19] QUILLARD S., LOUARN G., LEFRANT S., MacDIARMID A.G., Phys. REv. B **50**, p. 12496, 1994.
[20] KUO C.T., CHIUL W.K., Synth. Met. **88**, p. 23, 1997.
[21] DAIMAG L.V., COLTHUP N.B., FATELY W.G., GRASSELI J.G., *The Handbook of infrared and Raman characteristic frequencies of organic molecules*, Academic Press, New York, 1991.

SOI by Smart-Cut. TEM-HRTEM Characterization of Structural Defects Induced in Si by Plasma Hydrogenation

Corneliu GHICA, Leona Cristina NISTOR

National Institute for Materials Physics, PO Box MG-7 Magurele, Bucharest, Romania
E-mail: cghica@infim.ro, leonis@infim.ro

Abstract. Silicon wafers have been submitted to hydrogen RF-plasma treatment in various experimental conditions. Three types of induced extended defects are identified and characterized by transmission electron microscopy: planar defects in the {111} and {100} planes and nanometric voids. The parameters of the plasma treatment have been varied in order to confine the induced defects in a 50 nm band below the surface. Laser treatment has been applied on the as-hydrogenated Si wafers. We will show laser annealing results in the formation of a well defined layer of nanometric cavities, favoring the peel off of a layer thinner than 50 nm.

1. Introduction

Silicon hydrogenation has a history of a few decades in the silicon industry. It has been intensively studied some decades ago as an important step in silicon technology. The role played by hydrogen atoms inserted in a silicon matrix, concerning the control of doping atoms activity, defect passivation or suppression of carrier traps, was evidenced and characterized [1-4]. Nowadays, silicon hydrogenation is studied in a new context, namely with the aim of developing and improving a technological method known as smart-cut^{TM} used in the fabrication of 'silicon-on-insulator'(SOI) substrates [5]. The smart cut technique consists in creating a high density of crystal defects at a certain depth under the surface of a Si wafer, and then, to remove, by an appropriate method, the Si layer situated above the mechanically weakened region, which contains a high density of defects. The as-removed Si layer should remain single crystalline and, ideally, free of defects, in order to be used in a multilayer architecture of the kind 'single crystal layer / amorphous insulating layer / single crystal substrate'. The practical way used to induce crystal defects with a certain distribution profile under the Si wafer surface is either by ion implantation or by treatment in plasma of light atomic species, such as H or He [5-10]. Successful experiments have been reported concerning the smart-cut procedure by hydrogen ion implantation, where layers as thin as 200 nm have been removed from the Si wafers [5]. In our research we employ hydrogen

plasma in order to induce the necessary amount of defects. Apart from the lower cost, the use of H-plasma instead of H ion implantation could be, under appropriate conditions, less harmful for the Si layer to be removed by smart cut. Also, the possibility of peeling off even thinner layers is taken into consideration [11]. In general, the defects induced in Si by H ion implantation or H-plasma treatment, are planar defects, bubbles and dislocation loops [12, 13]. The high levels of H concentration in the Si lattice somehow complicate the problem, in the sense that the resulting defects are decorated with hydrogen and, therefore, different from the classical crystal defects encountered in Si. In order to be able to control the type of defects to be induced either by ion implantation or plasma treatment, the identification and characterization of defects in hydrogenated Si is necessary. This work contains qualitative and quantitative structural results obtained by conventional and high-resolution transmission electron microscopy (CTEM / HRTEM) on the defects in H-plasma treated Si wafers. We also present TEM results showing the evolution of the H-plasma induced structural defects in Si, in the case of surface laser annealing, with the aim to obtain a transferable single crystal Si layer thinner than 50 nm.

2. Experimental

p and *n*-type (001) Si wafers have been submitted to hydrogen RF-plasma treatments using a 13.56 MHz and a 110 MHz RF generator. The hydrogen partial pressure has been varied in the 10-10^4 Pa range and the discharge power between 50-200W. The sample temperature did not exceed 200 ^oC during the treatment, the heating being caused by the interaction with the RF-plasma. The treatment duration varied from 1 h to 4 h. Transmission Electron Microscopy (TEM) investigations have been performed using the JEOL 200 CX and JEOL 4000 EX electron microscopes on specimens prepared by mechanical thinning and ion milling on a Gatan PIPS machine.

3. Results and Discussions

The effects of the hydrogen plasma treatment on the Si wafers may be immediately observed by TEM investigation on cross-section specimens. These effects can be summarized into two main categories: surface effects and subsurface effects. The surface effects consist in the appearance of a surface roughness due to the etching action of hydrogen plasma against Si. The subsurface effects consist in the formation of extended structural defects such as planar defects and nanocavities.

3.1. *{111} defects*

The most frequently encountered defects in hydrogenated Si wafers are disposed along the {111} planes. The slip system in Si is <110>{111}, meaning that dislocations lie along the <110> directions and can slip across the dense {111} planes. The typical example of a planar defect in materials with diamond structure is the stacking fault, resulting from the dissociation of a perfect dislocation into partials. However, the {111} defects in the hydrogenated Si wafers show features

which make them different from the classical {111} defects in materials having diamond structure.

Figure 1 reveals typical conventional TEM images of the {111} defects encountered in the plasma hydrogenated Si samples. The bright field (BF) and dark field (DF) images in Fig. 1 a and b, respectively, are obtained in Bragg condition with the $1\bar{1}1$ spot strongly excited.

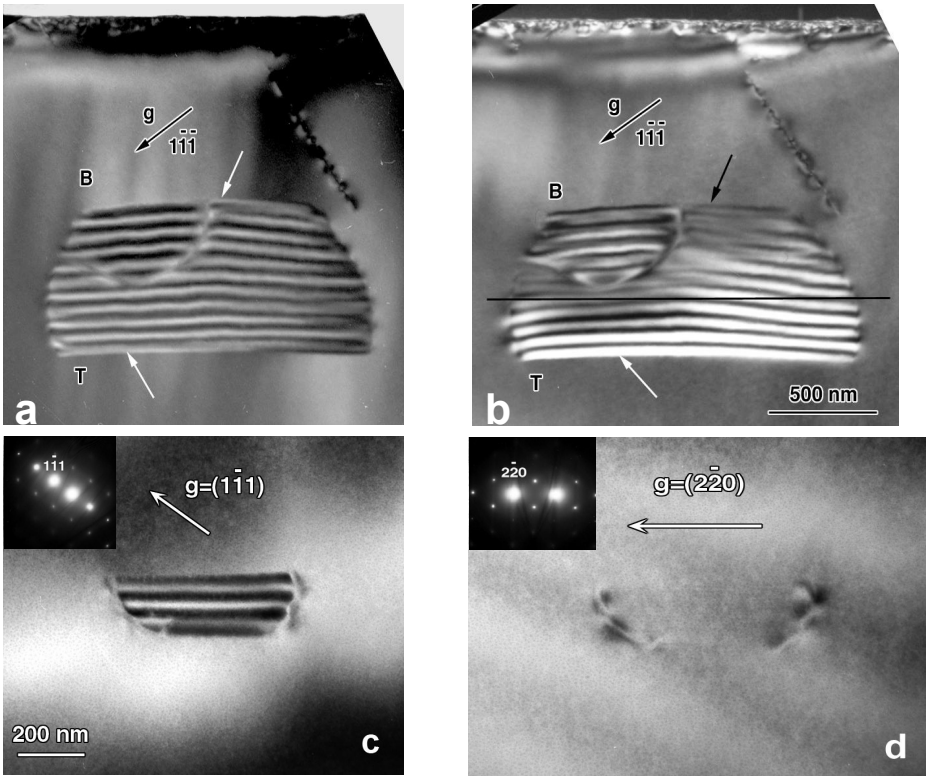

Fig. 1. Bright field (a) and dark field (b) images of a planar {111} defect. 'T' and 'B' denote, respectively, the top and bottom ends of the planar defect intercepting the specimen surfaces. The black line on the DF image has been added as a reference in order to evidence the fringe curvature. (c), (d) Bright field TEM images in Bragg condition of a {111} planar defect using the $1\bar{1}1$ and $2\bar{2}0$ reflections.

Two {111} defects can be observed. One of them, showing fringes, is buried at about 800 nm under the surface. By specimen tilting experiments, we have identified the habit plane for this defect as the (111) plane. The orientation of the reflection vector $\boldsymbol{g} = (1\bar{1}\bar{1})$ with respect to the bright outer fringe of the planar defect on the dark field image indicates that the defect has an intrinsic character,

i.e. has a missing silicon plane [14]. The second defect is seen in edge-on orientation. It is disposed in the $(1\bar{1}\bar{1})$ plane and intercepts the wafer surface. As a typical feature for this kind of defects, the characteristic contrast fringes are not straight, but slightly curved, as can be noticed by comparison with the line drawn on figure 1b. It indicates that the defect is not limited to a single crystallographic plane, but it affects several adjacent planes.

Information about the displacement vector characterizing the {111} planar defects can be extracted by imaging a defect in Bragg condition using the diffraction spots for which it becomes invisible. Two beam bright field images of such a defect are presented in figure 1 c and d, where the $1\bar{1}1$ and $2\bar{2}0$ reflections have been excited. The characteristic fringes of the defect became invisible for $\boldsymbol{g} = (2\bar{2}0)$, showing that the characteristic displacement vector $\boldsymbol{R}$ has no components along $[2\bar{2}0]$ and is most probably oriented perpendicular to the habit plane, as in the case of regular stacking faults [15].

In order to accede to the structure of defects at atomic level, HRTEM observations have been performed on {111} defects in edge-on orientation. Figure 2 a shows the HRTEM image of a {111} planar defect in the plasma hydrogenated silicon wafer, revealed in a very thin part of the specimen. Figure 2a shows a sharp contrast variation in the defect plane where the columns of atoms are revealed by a much brighter row of dots. In the centre of the figure the defect migrates over two adjacent {111} planes leaving a jog behind. This fact explains the curvature and deformations of the fringes on the diffraction contrast images of the {111} defects. In this situation, proposing a defect structure at atomic level is not an easy task. Several atomic models of the {111} defects in hydrogenated silicon have been proposed, all of them taking into consideration the breaking of the Si-Si bonds along {111} planes and the saturation of the resulting dangling bonds with hydrogen atoms, accompanied by longitudinal and/or transversal shifts of the Si lattice on each side of the defect. Atomic models proposed by Ponce et al. [16], Deák and Snyder [17], Van de Walle *et al*. [18], Zhang and Jackson [19], Heyman et al. [20] are summarized and simulated as HRTEM images by Muto et al. in [21].

To decide for a structural model of the {111} defect in plasma hydrogenated Si, we processed the experimental HRTEM image of the {111} defect to determine the strain field around the defect using the geometrical phase method (GPM) [22].

Figure 2 b gives the Fourier transform of the HRTEM image of the {111} defect. An XY coordinate system has been chosen and indicated near the left low corner of the HR picture. The phase images in figures 2 c and d have been obtained by selecting with a Gaussian mask the $\bar{1}11$ and $\bar{2}2\bar{4}$ spots in figure 2 b, respectively. The local geometrical phase across the images is calculated with

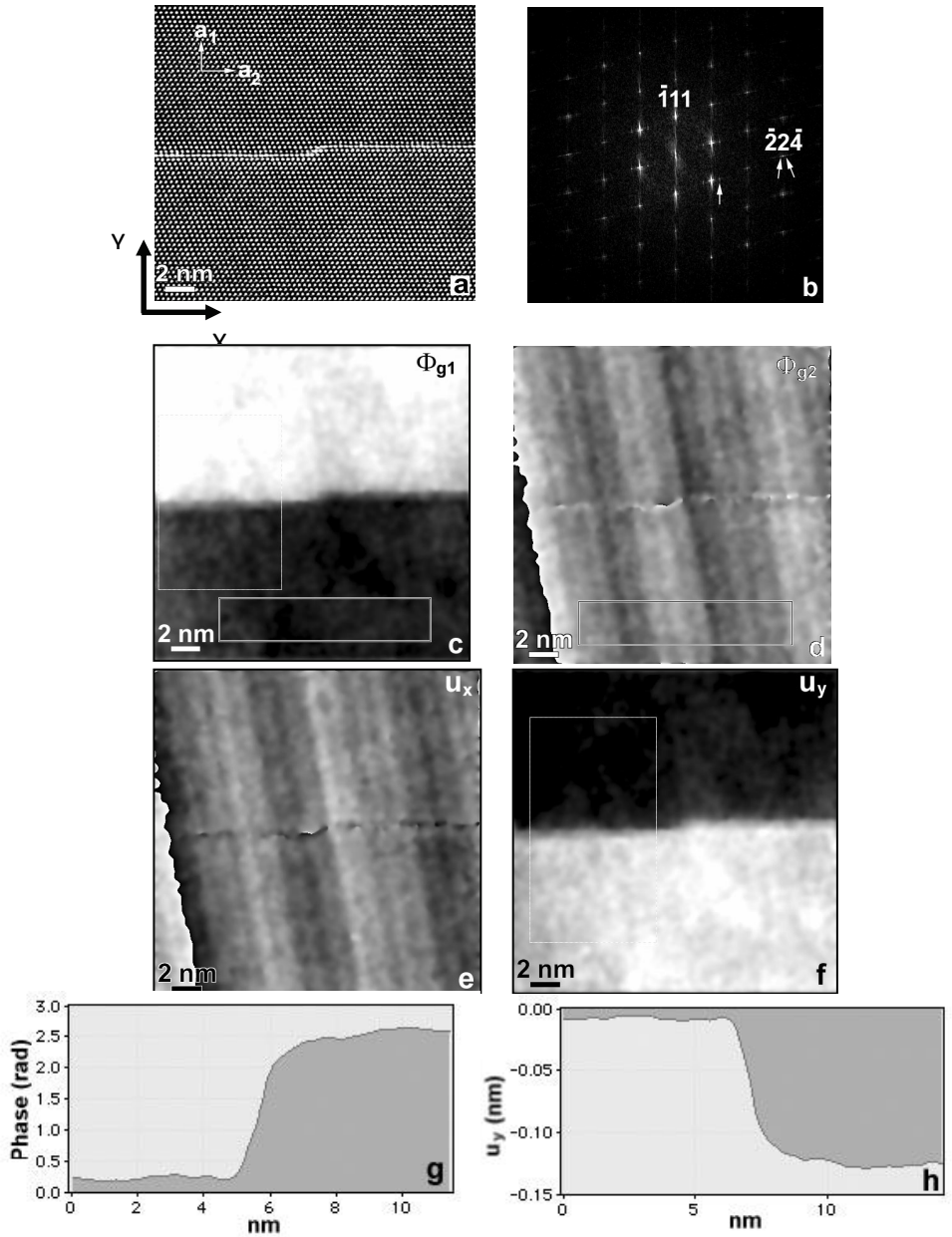

Fig. 2. (a) HRTEM image of the {111} defect in the thin region; the assigned XY coordinate system is figured; (b) Fourier transform of the HRTEM image; (c), (d) Phase images Φ_{g1} and Φ_{g2} obtained by FFT^{-1} using a Gaussian mask around $\boldsymbol{g}_1 = \bar{(111)}$ and $\boldsymbol{g}_2 = \bar{(2\,2\,4)}$, respectively; (e), (f) $u_x(\boldsymbol{r})$ and $u_y(\boldsymbol{r})$ components of the displacement field $\boldsymbol{u}(\boldsymbol{r})$ around the defect; (g) line profile of the phase across the defect in the Φ_{g1} phase image averaged over the 8 nm width of the rectangle in the left part of the image; (h) line profile of the $u_y(\boldsymbol{r})$ component across the defect in the positive sense of the OY axis.

respect to the average phase value corresponding to a reference area delimited by a rectangle in the low part of the phase images. On the phase images white / black areas correspond to regions of higher (positive) / lower (negative) phase, while grey areas are in phase (zero) with the reference area. One can notice on figure 2 c, on the $\boldsymbol{g}_1$ phase image (Φ_{g1}), a clear phase jump of the $\bar{1}11$ fringes across the defect with respect to the reference area.

Using the two phase images, the displacement field $\boldsymbol{u}(\boldsymbol{r})$ can be calculated using the two real space vectors $\boldsymbol{a}_1$ = 1/3 $[\bar{1}11]$ and $\boldsymbol{a}_2$ = 1/12 $[\bar{1}1\bar{2}]$ corresponding to the reciprocal $\boldsymbol{g}_1 = [\bar{1}11]^*$ and $\boldsymbol{g}_2 = [\bar{2}\,2\,\bar{4}]^*$ vectors. The displacement field $\boldsymbol{u}(\boldsymbol{r})$ can be mapped by imaging its $u_x(\boldsymbol{r})$ and $u_y(\boldsymbol{r})$ components according to the equations:

$$\begin{aligned} u_x(\boldsymbol{r}) &= (-1/2\pi)[\Phi_{g1}(\boldsymbol{r})a_{1x} + \Phi_{g2}(\boldsymbol{r})a_{2x}] \\ u_y(\boldsymbol{r}) &= (-1/2\pi)[\Phi_{g1}(\boldsymbol{r})a_{1y} + \Phi_{g2}(\boldsymbol{r})a_{2y}] \end{aligned} \tag{1}$$

In our picture coordinate system $a_{1x} = 0$, $a_{1y} = |\boldsymbol{a}_1| = \sqrt{3}/3$ and $a_{2x} = |\boldsymbol{a}_2| = \sqrt{6}/12$, $a_{2y} = 0$, which turns equation (1) into:

$$\begin{aligned} u_x(\boldsymbol{r}) &= -(\sqrt{6}/24\pi)\Phi_{g2}(\boldsymbol{r}) \\ u_y(\boldsymbol{r}) &= -(\sqrt{3}/6\pi)\Phi_{g1}(\boldsymbol{r}) \end{aligned} \tag{2}$$

expressed in fractions of the lattice parameter, a, or:

$$\begin{aligned} u_x(\boldsymbol{r}) &= -0.176\Phi_{g2}(\boldsymbol{r}) \\ u_y(\boldsymbol{r}) &= -0.499\Phi_{g1}(\boldsymbol{r}) \end{aligned} \tag{3}$$

expressed in nm (the lattice parameter of Si is a_{Si}=0.543 nm).

The u_x and u_y components of the strain field calculated with (3) are depicted in figures 2 e and f where, again, grey means no displacement, white means positive displacement (in the positive sense of the coordinate axis) and dark means negative displacement. In figure 2 f one can notice a uniform negative rigid body displacement along OY (or $[\bar{1}11]$ direction) of the upper part of the image with respect to the reference area. The phase jump as well as the displacement field can be quantitatively expressed using line profiles across the defect.

Thus, the phase jump across the defect in the positive sense of the OY axis (Figure 2 g) measures $0.72\pi \pm 0.044$ radians. Correspondingly, the value of the u_y displacement measured on the line profile (Figure 2 h) is 0.116 ± 0.002 nm.

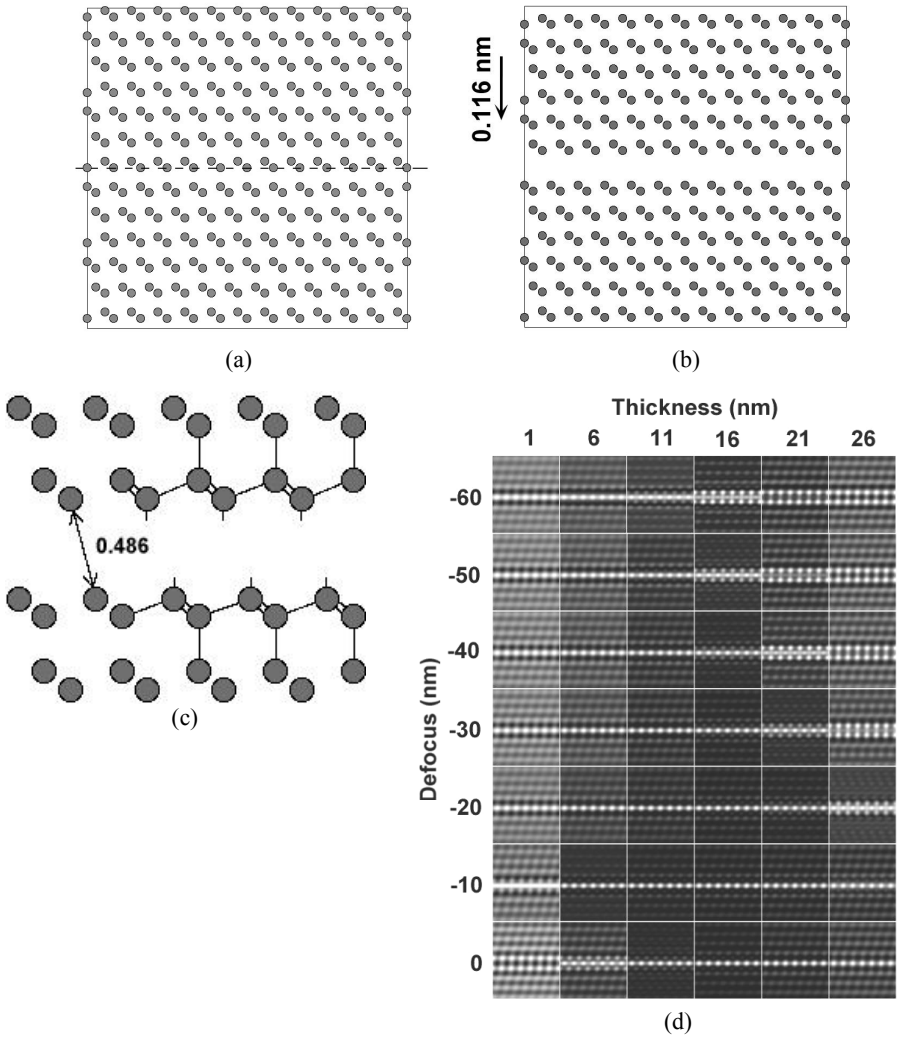

Fig. 3. Structural model of the {111} defect based on the displacement values obtained by the GPM analysis. (a) Undistorted Si structure projected along [110]; the horizontal line marks the interface between the bottom fixed part of the crystal and the upper part which the displacement vector is applied to; (b) structural model *B* of the {111} defect where two Si layers have been removed; (c) enlarged view of the atomic arrangement close to the defect plane for models *A* and *B*, respectively; interatomic distances in nm are indicated; (d) Matrix of simulated HR images for various thickness and defocus values based on the structural model (b).

We used the Crystal Kit software for the structural modelling of the defect. Starting from the undistorted Si crystal structure projected along [110] (Figure 3 a), the 0.116 nm rigid body displacement has been applied to the upper part of the matrix with respect to the fixed bottom part, and two Si layers at the interface have

been removed (Figure 3 c). We consider that the resulting dangling bonds are saturated with hydrogen. A unit cell has been defined and simulated HR images have been calculated using the Mac Tempas software. In figures 3 d we present a series of simulated images obtained for different values for the lens defocus and specimen thickness. At a visual inspection of the simulated images we can conclude that the proposed structural model provides a perfect fit for the HR images of the defect. Thus, the defect is imaged as a single row of brighter dots in the thin areas of the specimen, as in the experimental image in figure 2 a.

3.2. *{100} defects*

A second category of defects introduced by RF-plasma hydrogenation in silicon are the planar defects oriented along {100} planes. In principle, {100} planar defects are not encountered in diamond cubic materials, as {100} is not a slip plane in these crystallographic systems. However, {100} platelets have been reported for Si and Ge wafers submitted to deuteron irradiation [23, 24].

As in the case of the {111} defects, the interpretation of the HRTEM images of the {100} defects in hydrogenated Si wafers is rather difficult due to the presence of a high strain field around them. Moreover, unlike the {111} defects, the {001} defects proved to be rather unstable when imaged at 400 kV in HR conditions. Therefore, special precautions have been taken in order to record the HR images, such as performing the fine imaging adjustments on a different thin area away from the defect and, especially, working fast by taking HRTEM images within the first 20 seconds of defect imaging. It is well known that for accelerating voltages higher than 300 kV, the electron beam creates defects in Si by a knock-off mechanism. We noticed this effect in our specimens during observation in HR conditions at 400 kV. However, while the {111} defects were not beam sensitive, the {001} defects disappeared after about 20 seconds of observation in HR conditions at 400 kV and the Si matrix was healed.

A fragment from the central region of such a defect in edge-on orientation is imaged in Figure 4 a. The defect is not limited to a single crystallographic plane. It has a diffuse aspect affecting two or three neighboring (001) planes. Like the {111} defects, it migrates to adjacent planes, which gives it a slightly curved lens-like shape. Fourier filtered images obtained by selecting the $\bar{1}11$ and 002 spots from the power spectrum (Figure 4 b) are displayed in Figures 4 c and d, respectively. The $(\bar{1}\bar{1}1)$ family of planes is only weakly affected by the presence of the defect and the corresponding Fourier-filtered image has not been included here. However, for the $(\bar{1}11)$ planes, a phase shift can be observed in the upper part of the image with respect to the bottom part across the defect (Figure 4 c).

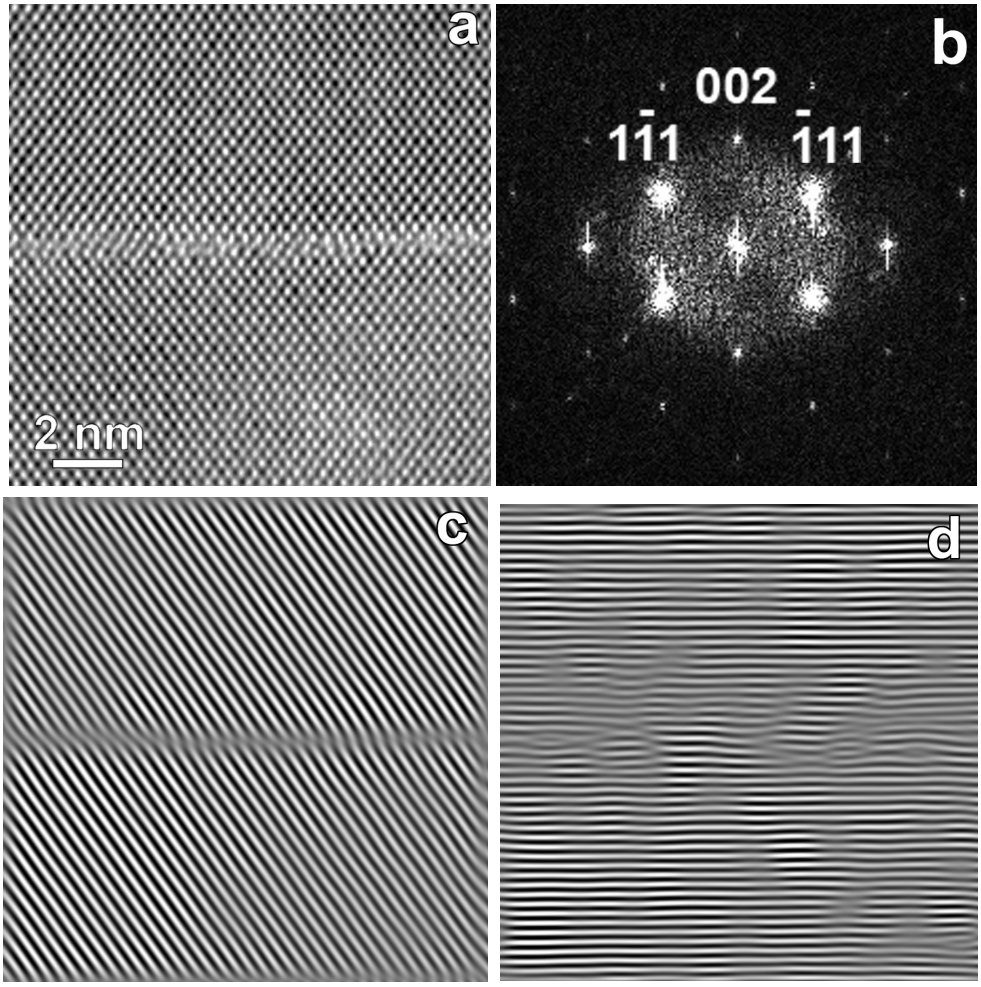

Fig. 4. (a) HRTEM image of an (001) defect; (b) the corresponding power spectrum; (c), (d) Fourier filtered images showing the $(\bar{1}11)$ and (002) planes, respectively.

The 002 filtered image (Figure 4 d) shows important distortions especially along the defect, where fragments of interstitial (002) planes can be observed. The defect has not a unique extrinsic or intrinsic character, but rather a mixed one, resulting probably from accumulation of vacancies and self-interstitials followed by their condensation on a {001} plane, as revealed by the 002 filtered image. It is well known in literature that this mechanism represents the way in which prismatic dislocation loops are formed [25]. The loss of fringe contrast can be related to a high degree of disorder in the lattice. Since this kind of defect is not characteristic

to silicon, but it occurs only in hydrogenated wafers, one could infer that the vacancies and interstitials involved are generated from the interaction between the Si lattice and the in-diffused H atoms.

3.3. *Nano-cavities*

From previous observations on He implanted silicon [26], bubbles were expected to appear in hydrogenated Si, as well. However, TEM observations revealed their rather seldom presence both in plan-view and cross-section specimens. In general, they appear as agglomerations of bubbles around 5-20 nm in size and they are surrounded by long range strain field; when imaged in plan-view close to the [001] zone axis, a 4-fold symmetry contrast surrounds them. In order to elucidate the origin of this contrast, we have performed tilting and defocus variation experiments.

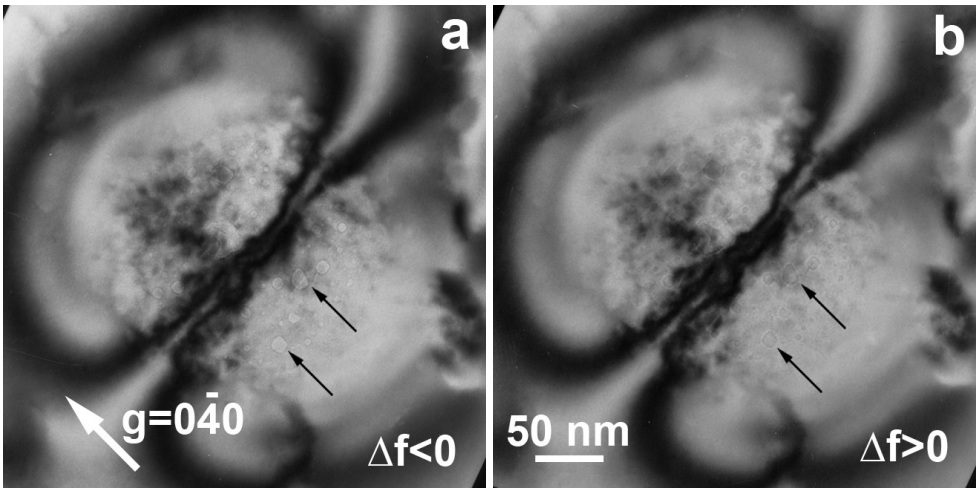

Fig. 5. TEM images on a plan-view specimen showing the strain field contrast around the defect in two-beam condition ($0\bar{4}0$ reflection excited): under focused (a) and over focused (b) images showing nanometric bubbles with, respectively, bright and dark inner fringe contrast.

Figure 5 shows two-beam images of the defect, $\mathbf{g}=(0\bar{4}0)$, in a plan-view specimen prepared from a hydrogenated Si(001) wafer. The two images present a bubble agglomeration surrounded by a 2-lobed strain field contour. The nature of the defect can be resolved on over focused ($\Delta f>0$) and under focused ($\Delta f<0$) images. For negative defocus the bubbles show a bright inner fringe, while for positive defocus the inner fringe becomes dark. This contrast behavior is characteristic for cavities inside a solid matrix [27]. The formation mechanism seems to be the same as in the case of the {001} defects, namely an accumulation

of in-excess vacancies. The interaction between the in-diffused H atoms and the Si lattice, based on the high chemical reactivity of the H atoms against the Si-Si bonds, is at the origin of the lattice vacancies and self-interstitials formation. These agglomerations of nano-cavities are always surrounded by long-range strain-field contours, demonstrating that high mechanical tensions are concentrated here.

3.4. *Plasma treatment optimization*

Si{001} wafers have been submitted to hydrogen RF-plasma treatment in optimized experimental conditions in order to avoid roughness increase and to create a thin subsurface layer (50 nm thin or less) containing a high density of structural defects [28]. The hydrogen RF-plasma has been created inside a discharge chamber between two flat electrodes separated at adjustable distance, with the Si wafer between the two electrodes. We have used two parallel disk-shaped electrodes with a diameter of 30 mm, separated at a distance of 30 mm. One of the two electrodes was grounded, while the RF signal with a power of 50 W or 200 W at 13.56 MHz was applied on the second electrode. The value of the hydrogen dynamical pressure inside the chamber was set in the 7.5–55 Pa range using a hydrogen flow of 10–20 sccm. The Si wafers were mounted on the grounded electrode and the treatment duration was 1 h. The temperature of the Si wafers during the treatment was less than 250^{o}C, the increase from room temperature being due to the plasma bombardment.

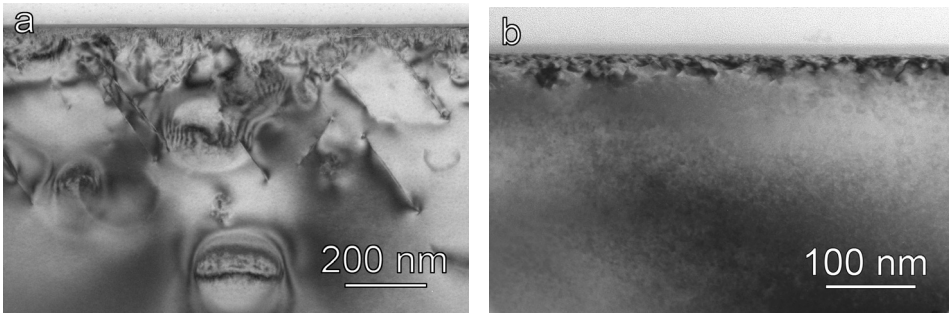

Fig. 6. Cross-section TEM images of Si wafers treated in hydrogen RF-plasma showing the extent of the defect-containing region as a function of the RF-discharge power: 200 W in (a) and 50 W in (b).

Figure 6 shows the cross-section TEM image of as-hydrogenated Si(001) wafers treated in the RF plasma at 50 W and 200 W. Two surface-related features of the as-hydrogenated sample are noticeable: i. a thin amorphous layer on the surface; ii. the roughness of the crystalline Si surface is of the order of the nanometer (peak-to-valley amplitude). Investigating samples treated at different plasma power values, we have noticed that the thickness of the amorphous surface layer after the RF-plasma treatment diminishes by increasing the RF-plasma power, from ca. 15 nm for the RF-plasma at 50 W down to 10 nm or thinner for

plasma treatment at 100 W and 200 W. Regarding the origin and history of this amorphous layer, we believe that it comes from the native SiO_2 layer on top of the Si wafer which has been chemically reduced to Si during the H-plasma treatment and then re-oxidized, once exposed to the air. In addition, the diminishing of its thickness with the increase of the plasma power is caused by the etching effect of hydrogen plasma, being more effective in the case of more energetic plasmas. Therefore, the presence of this thin SiO_2 layer on top of the hydrogen-containing Si single crystal characterizes the initial state of surface for the as-hydrogenated Si wafers when further submitted to thermal treatment or laser annealing. From the point of view of the final SOI architecture, we consider that the presence of this amorphous SiO_2 layer does not represent a major drawback, since the peeled-off layer will include a Si layer with a thin SiO_2 layer on top of it and the target substrate will be also a SiO_2-terminated Si wafer.

Below the surface, one can notice a region with a high density of structural defects. Most of the defects are planar defects situated in the {111} and {001} crystallographic planes. The extent of this faulted region is strongly dependent on the power of the RF discharge during the plasma treatment. It decreases from almost 1 μm in the case of the 200 W RF plasma (Figure 6 a) down to about 50 nm for the 50 W RF plasma (Figure 6 b). The high density of structural defects concentrates a significant strain field which can be noticed as a strong dark diffraction contrast. The structural defects induced by the hydrogen plasma treatment represent a straightforward indication regarding the depth range where hydrogen is present in a significant quantity.

3.5. *Laser annealing*

The difficulty posed by the plasma treatment in comparison with the ion implantation regarding the induced defects is that, in the case of plasma treatment, the induced defects intercept the wafer free surface. This does not occur for the ion implantation where the damaged layer is buried at a certain depth under the implanted surface, well separated from it. Therefore, in the case of plasma-hydrogenated wafers, where the defected region is adjacent to the surface, the after-hydrogenation treatment should result in a clear separation between the defect-containing region and the surface. The obtained defect configuration would be, this way, similar to the implanted samples, with the possibility to peel-off layers thinner than 50 nm. Several attempts to obtain such a result by classical thermal treatments of the plasma hydrogenated Si wafers failed, because, especially the {111]-type defects, which might intersect the wafer surface, are not annealed out. Therefore, we proposed to study laser annealing as an alternative method of after-hydrogenation treatment. The very principle of the laser annealing differs fundamentally from the thermal annealing. As in the case of any surface treatment using various energy sources, the energy transfer towards the material occurs

through the exposed surface. Depending on the experimental parameters, the energy transfer may be restricted to a narrow region of material in the surface vicinity, as opposed to classical thermal annealing which affects the whole volume of the sample.

In the case of our laser annealing experiments we used as irradiation laser beam the 3-rd harmonic λ=355 nm, corresponding to 3.49 eV photon energy, from a YAG:Nd source (λ=1.06 μm). At this wavelength, the optical absorption coefficient of Si is ca. 10^6 cm^{-1} [29]. From the Beer-Lambert law of radiation absorption, $I(x)=I_0\exp(-\alpha x)$, where α is the optical absorption coefficient, applied to a Si wafer under 355 nm laser radiation, it turns out that 90% of the absorbed incident beam energy (after subtracting the reflected beam) is confined to the first 23 nm of material. This preliminary information attests the fact that laser annealing offers the premises to concentrate a high density of energy into a very thin layer of Si with a thickness comparable or even less than that of the defect-containing layer after hydrogenation. In case the amount of laser energy deposited into the first 23 nm is enough to heal the defects encountered in this region, then the laser annealed sample would contain a certain density of defects embedded under a very thin (ca. 20 nm) layer of defect-free Si, which is exactly the desired distribution of structural defects needed for the smart-cut procedure. For our laser annealing experiments, the laser fluence on the surface of the as-hydrogenated wafers was 0.15 J/cm^2, with the laser beam spread over an area of ca. 1 cm^2. This fluence value is an order of magnitude below the ablation threshold of Si, reported to be around 1.8 J/cm^2 [30, 31].

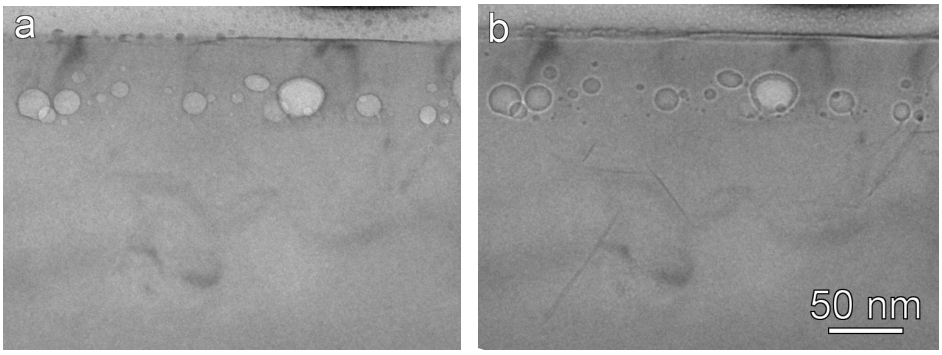

Fig. 7. Cross-section TEM images at low-magnification of a Si wafer after hydrogenation in RF-plasma at 200 W and subsequent pulsed laser annealing, for $\Delta f<0$ (a) and $\Delta f>0$ (b).

The consequences of the laser treatment on the surface of the Si wafer hydrogenated at 200 W can be immediately noticed in Figure 7. One can see that some of the planar defects are still present, in a region running deep (ca. 800 nm) under the treated surface, while the region close to wafer surface is defect free.

However, in addition to the hydrogen induced defects, a string of circular features right below the surface becomes visible after the laser treatment.

The nature of these features is rapidly identified in electron microscopy by comparing pairs of images obtained under opposite objective lens defocus conditions, meaning underfocused image ($\Delta f<0$) and overfocused image ($\Delta f>0$). By comparing the two underfocused and overfocused images, it becomes clear that the effect of the laser annealing is the formation of nanometric cavities with sizes ranging from 5-6 nm up to 50-60 nm. It is interesting to note that these nanocavities are distributed at a high density within a narrow layer of material (about 50 nm thick) below the surface. It is important to observe, also, that there is an even narrower layer of material (about 35 nm thick), between the free surface and the string of nanocavities, which contains no nanocavities at all. The concentration of the laser-formed nanocavities in a narrow band below the surface determines the mechanical weakening of the Si matrix in that region and creates the premises to lift off layers thinner than 50 nm.

4. Conclusions

Our work has demonstrated that laser annealing of RF-plasma hydrogenated Si wafers represents a reliable method of inducing appropriated structural defects in terms of density and spatial distribution for the subsequent removal of thin layers by the smart-cut procedure. The method combines RF-plasma treatment and UV laser annealing, which are sensibly cheaper than other techniques employed so far, such as ion implantation or molecular beam epitaxy. Hydrogen diffusion into the Si structure during the treatment in the RF-plasma is accompanied by the formation of extended structural defects (mostly {111} and {100} planar defects) and surface corrugation. The amplitude of these effects as well as the hydrogen quantity inside the Si matrix may be controlled through the experimental parameters such as set-up geometry, discharge power, etc. Pulsed laser annealing has been applied to as-hydrogenated Si wafers using the 3-rd harmonic of a YAG:Nd laser source. The rapid absorption of the UV laser radiation into the first tens of nm of Si results in the formation of a well defined layer of nanometric voids placed at a depth of 25-50 nm, depending on the experimental conditions. The highly populated layer of laser induced nanocavities determines an increased structural fragility of the Si matrix favoring the smart-cut process. These results are highly encouraging in considering RF-plasma treatment corroborated with laser annealing as an alternative reliable method to induce structural defects in a controllable manner below the surface of a Si wafer and to favor the peel off by smart-cut of Si layers thinner than 50 nm. For further understanding the mechanism of the nanocavity generation by vacancy diffusion under the thermal gradient induced by the laser treatment, the calculation of the temperature field inside the Si target in function of the laser beam parameters (wavelength, fluence, power, repetition rate, number of

shots) corroborated with the vacancy transient diffusion process will be performed as future work.

Acknowledgements. This work has been partially supported by CNCSIS in the frame of the national research program PN II Ideas (Contract No. 233/2007).

References

[1] PANKOVE J.I., CARLSON D.E., BERKEYHEISER J.E., WANCE R.O., Phys. Rev. Lett. **51**, p. 2224, 1983.
[2] JOHNSON N.M., Phys. Rev. B **31**, p. 5525, 1985.
[3] JOHNSON N.M., HAHN S.K., Appl. Phys. Lett. **48,** p. 709, 1986.
[4] SPEAR W.E., LeCOMBER P.G., Solid State Comm. **17**, p. 1193, 1975.
[5] BRUEL M., Nucl. Instr. and Meth. in Phys. Reas. B **108**, p. 313, 1996.
[6] JOHNSON N.M., PONCE F.A., STREET R.A., NEMANICH R.J., Phys. Rev. B **35**, p. 4166, 1987.
[7] JENG S.J., OEHRLEIN G.S., SCILLA G.J., Appl. Phys. Lett. **53**, p. 1735, 1988.
[8] RANGAN S., ASHOK S., CHEN G., THEODORE D., Nucl. Instr. and Meth. in Phys. Reas. B **206**, p. 417, 2003.
[9] QIAN C., TERREAULT B., GUJRATHI S.C., Nucl. Instr. and Meth. in Phys. Reas. B **175-177**, p. 711, 2001.
[10] FICHTNER P.F.P., KASCHNY J.R., BEHAR M., YANKOV R.A., MÜCKLICH A., SKORUPA W., Nucl. Instr. and Meth. in Phys. Reas. B **148**, p. 329, 1999.
[11] USHENKO A.Y., ULYASHIN A.G., Jpn. J. Appl. Phys. **41**, p. 5021, 2002.
[12] GHICA C., NISTOR L.C., BENDER H., RICHARD O., TENDELOO Van G., ULYASHIN A., Phil. Mag. **86**, p. 5137, 2006.
[13] GHICA C., NISTOR L.C., BENDER H., RICHARD O., TENDELOO Van G, ULYASHIN A., J. Phys. D: Appl. Phys. **40**, p. 395, 2007.
[14] SAADA G., *Microscopie électronique des lames minces cristallines* (Masson & C^{ie}, Paris, pp. 235–237, 1966.
[15] HIRSCH P.B., HOWIE A., NICHOLSON R.B., PASHLEY D.W., WHELAN M.J., *Electron Microscopy of Thin Crystals*, Butterworth & Co., pp. 165, London, 1967.
[16] PONCE F.A., JOHNSON N.M., TRAMONTANA J.C., WALKER J., Inst. Phys. Conf. Ser. **87**, p. 49, 1987.
[17] DEÁK P., SNYDER L.C., Radiat. Effects **111-112**, p. 77, 1989.
[18] WALLE De Van C.G., DENTENEER P.J.H., BAR-YAM Y., PANTELIDES S., Phys. Rev. Lett. **60**, p. 2761, 1989.
[19] ZHANG S.B., JACKSON W.B., Phys Rev. B **43**, p. 12142, 1991.
[20] HEYMAN J.N., AGER III J.W., HALLER E.E., JOHNSON N.M., WALKER J., DOLAND C.M., Phys. Rev. B **45**, p. 13363, 1992.
[21] MUTO S., TAKEDA S., HIRATA M., Phil. Mag. A **72**, p. 1057, 1995.
[22] HŸTCH M.J., SNOECK E., KILAAS R., Ultramicroscopy **74**, p. 131, 1998.
[23] MUTO S., TAKEDA S., Phil. Mag. Lett. **72**, 99, 1995.
[24] AKATSU T., BOURDELLE K.K., RICHTARCH C., FAURE B., LETERTRE F., Appl. Phys. Lett. **86**, p. 181910, 2005.
[25] HULL D., *Introduction to Dislocations*, 2nd edition, Oxford: Pergamon 1975.
[26] CEROFOLINI G.F., CORNI F., FRABBONI S., NOBILI C., OTTAVIANI G., TONINI R., Mat. Sci. Eng. **27**, p. 1, 2000.
[27] WILLIAMS D., CARTER C.B., *Transmission Electron Microscopy*, **3**, New York and London: Plenum 1996.

[28] GHICA C., NISTOR L.C., VIZIREANU S., DINESCU G., MOLDOVAN A., DINESCU M., Plasma Proc. Polym. **7**, p. 986, 2010.
[29] JELLISON Jr.G.E., MODINE F.A., J. Appl. Phys. **53**, p. 3745, 1982.
[30] WAKATA H., TASEV E., TUDA M., ONO K., HARUTA K., and UEDA Y., Appl. Surf. Sci. **79-80**, p. 152, 1994.
[31] TORRISI L., BORRIELLI A., and MARGARONE D., Nucl. Instr. Meth. B **255**, p. 373, 2007.

Spectroscopy and *ab Initio* Studies of Optical Transitions in Nanostructured ZnO

R. PLUGARU[a], A. DINESCU[a], F. COMANESCU[a], M. PURICA[a], S. MIHAIU[b], E. VASILE[c], N. PLUGARU[d]

[a]National Institute for Research and Development in Microtechnologies-IMT Bucharest
[b]Institute of Physical Chemistry "I.G. Murgulescu" Romanian Academy
[c]METAV S.A.-CD, Bucharest
[d]National Institute for Materials Physics, Bucharest-Magurele

1. Introduction

Oxide semiconductors are presently investigated for a wide range of potential device applications, from transistors to optical detection and emission. In this context, zinc oxide (ZnO) is of a particular interest because of its characteristics (wide direct bandgap energy of 3.37 eV and a large binding energy, 60 meV), that makes it one of the best candidates for transparent electronics, sensors and solar cells [1].

A great effort has been brought out to improve the electrical and optical properties of ZnO films, through a diversity of material synthesis techniques, substrates, doping and processing. Electrical conductivity control by Al-doping has received a particular interest, since it may provide a convenient mean for changing the carrier density and mobility [2, 4] combined with useful effects on optical properties in the blue and UV regions of the spectrum [5, 6]. Recently, resistivity values of the order of 10^{-3} - 10^{-4} Ω·cm were reported for Al-doped ZnO thin films with Al concentration between 0.25 and 3.5 at. % [7-10]. For a given Al concentration in the film the resistivity values strongly depend on the method of synthesis and processing, which determine the nanostructure and the defective state. Also, some experiments underscore the fact that increasing Al concentration above approximately 4 at. % has a detrimental effect on conduction and determines an increase in resistivity [8,11]. Still, there is no firm explanation to relate the local structural details in $Zn_{1-x}Al_xO$ to the electrical conduction mechanisms.

On the theoretical side, several comprehensive first principles studies of the electronic structure have attempted to find justifications for the intrinsic n-type

conductivity, the role of defects, as well as the difficulty in achieving p-type conductivity in ZnO (see, e.g., [12-14]). Although there is a conceptual agreement of these studies regarding the role of defects on the electrical and optical properties, one can not yet draw specific conclusions of practical relevance for the control of the conductivity mechanisms. The structure and the way of the dopant impurities incorporated in the films are still under investigation in order to better control the doping process [15-18].

In this contribution, we present results of an investigation on the structure, composition, optical and electrical properties of multilayered ZnO thin films doped with 0.5 at.% Al, prepared by the sol-gel method. The sol–gel process for ZnO and ZnO:Al doped thin films preparation is particularly advantageous because of its simplicity and low cost, composition control, homogeneity on the molecular level. However the crystalline quality of the ZnO prepared by sol–gel process might be inferior to other methods [19]. This effect is caused by the low temperature annealing performed in the sol-gel process that affects the structural and optical characteristics of the thin films. On the other hand, the sol-gel deposition process could present some particularities related to nucleation and growth of nanocrystallites in the thin films formed by multilayers deposition. We bring experimental evidence that when Al^{3+} replaces Zn^{2+} the local structure and the bonding are perturbed so that the defect states favour the electrical and optical conductivity enhancement.

We performed calculations in the Local (Spin) Density Approximation, L(S)DA, of the electronic structure in wurtzite-type ZnO modified by Al doping, aimed at revealing the impurity effects on the conductivity in the disordered matrix. A comparative, first principles study of the electronic structure in wurtzite-type ZnO, modified by M= Al, Ti, Mn doping is also presented, in an attempt to comprehend the impurity effects on conductivity and magnetism in these disordered matrices. Thus, we carried out self consistent calculations on $M_xZn_{1-x}O$ systems (x=0.02, 0.05 and 0.10) using the FPLO release 5.00-20 band structure code. The chemical disorder was treated in the Coherent Potential Approximation, CPA, in the multiscattering formalism of Blackman–Esterling–Berk [20, 21].

2. Experimental

Thin films of Al doped ZnO have been prepared by 1-10 successive layers deposition by sol-gel method on Si/SiO_2 wafers (200 nm SiO_2) and glass substrates (borosilicate glass slides). The starting materials used in the films deposition process were: zinc acetate dihydrate (p.a) $Zn(CH_3COO)_2$ x $2H_2O$ (**ZAD**) (Merck), aluminiumnitrat-nonahydrat $Al(NO_3)3$ x $9H_2O$ (**ANN**), absolute ethanol CH_3CH_2OH (Riedel-deHaen) and triethanolamine $(CH_3CH_2OH)_3N$ (**TEA**) (BAKER ANALYZED). The chart of the deposition process is presented in Figure 1.

Zinc and Aluminium solutions of 0.1 M and 1 M were obtained by dissolving **ZAD** and **ANN** into absolute ethyl alcohol. Zinc acetate solution was stirred up at

60˚C for 15 minutes, then **TEA** was slowly added drop wise in molar ratio of **TEA**/**ZAD**=1/5 and 1/0.5. The Al-Zn-sol was obtained by adding the appropriate quantity of **ANN** solution to the zinc acetate solution, so that finally represents 0.5% and 5% aluminum atoms in the Al - Zn mixture (ZnO:0.5% at. Al and ZnO:5% at. Al).

The clear and homogenous Al-Zn solution was stored at room temperature for 24 hours before being used for the deposition. After deposition on Si/SiO_2 and glass substrates by dip-coating, each layer was treated at 500^{o}C for 5 min with a heating rate of 5°C/min for reaching the dwell treatment level.

The thermal treatment was performed in air, by using a Nabertherm type oven. This densification treatment was carried out according to the results of **DTA** and **TG**/**DTG** analysis presented in Figure 2. **DTA** and **TG**/**DTG** investigations were performed with a Mettler Derivatograph in the temperature range 20-1000˚C with a heating rate of 5˚C/min.

The thermal analysis of the Al-doped ZnO-dried gel indicates that the total elimination of the organic component occurs at a temperature higher by more than 80˚ than in the case of the zinc acetate (429˚C for the gel and 347˚C for zinc acetate) suggesting the stronger stability of the gel network. The experimental conditions of the films deposition and densification were previously presented in [22]. The coating was repeated 1–10 times. The films were finally annealed at 500^{o}C for 1 h (post-deposition treatment).

The structural and compozitional characteristics of the films were studied by x-ray diffraction (XRD) (X-ray Diffraction System with triple axis rotating anode-Rigaku SmartLab with Cu Kα radiation) at grazing incidence, transmission electron microscopy (TEM) and high resolution TEM (HRTEM) (TENCAI F30 operated at 300 kV) and energy dispersive x-ray spectroscopy (EDX) in the TEM. The surface morphology was analised by scanning electron microscopy (Field Emission Gun Scanning Electron Microscope (FEG-SEM) - Nova NanoSEM 630) and micro-Raman confocal microscopy (Micro Raman LabRAM HR 800 Horiba). Raman spectroscopy investigation of the successively deposited layers has been performed by using a Micro Raman LabRAM HR 800 Horiba equipment. The Raman spectra, in the 100-1000 cm^{-1} wavenumber range were recorded under laser excitation at 632 nm wavelength and at low incident power (< 5 mW) to avoid sample damage or laser induced heating. The beam diameter was of ~ 1 μm and the laser beam was focused on the sample by a 100 x microscope objective lens. The transmittance and reflectance measurements were carried out by using an UV-Vis-NIR Spectrophotometer-SPECORD M42 equipment, in the wavelength range 200-900 nm. The refractive index and the thickness of the films were determined by spectro ellipsometry method. The ellisopmetric (Ψ, Δ) spectra were recorded with a Spectroscopic ellipsometer SE 800 XUV SENTECH equipment, in the wavelegth range 250-850 nm, with the variable beam diameter (4 to 0.1 mm) and angular variation (0 to 900) with a precision of 0.01^o.

3. Results and Discussion

3.1. *Synthesis of Al doped ZnO multilayered thin films by sol-gel method*

The 1-10 successive layers were deposited by sol-gel method on both Si/SiO_2 wafers and glass substrates. A schematic diagram of the process for Al-doped ZnO multilayered thin films deposition is presented in Figure 1. The thermal treatments were performed using the results of the thermal analysis curves of zinc acetate dihydrate, aluminium nitrate-nonahydrate and Al doped ZnO gel. Thermal analysis provided informations on both the purity of the reagents used as precrusors and on subsequent thermal treatments to be used in order to obtain zinc oxide films doped with aluminum [23].

The thermal effects recorded by DTA up to 1000°C for the zinc acetate dihydrate decomposition and for the prepared ZnO and Al-doped gels are presented in the *Table 1*. For the Zn $(CH_3COO)_2$ x $2H_2O$ sample the endothermic effect at 92°C indicates the H_2O evolution. The next endothermic effect at 247°C corresponds to the decomposition of acetate. Those two exothermic effects at 322°C and 347°C correspond to the oxidation reaction of the high amount of organics resulted by acetate decomposition, and, probably, crystallization of ZnO.

Table 1. DTA analysis of the Zinc acetate dihydrate and as prepared ZnO and Al-doped gels

Ample	Thermal effects		Assignments
	Endo (°C)	Exo (°C)	
$Zn(CH3COO)_2$ x$2H_2O$	92 247	322 347	Water evolution Acetate decomposition Oxidation of CO to CO_2 Combustion of organic part
Zn-O-gel	76 133 295	311 347 427	Alcohol evolution Water evolution Decomposition of the gel Oxidation of CO to CO_2 Combustion of organic part Crystallization of ZnO
Zn-Al-O gel	79 130 296	429	Alcohol evolution Water evolution Decomposition of the gel Combustion of organic part and crystallization of ZnO

The ZnO and Al-doped ZnO gels present quite similar thermal effects up to 300°C. The first two endothermic effects at 76°C and 133°C, respectively, are assigned to the evolution of ethanol and water. The decomposition of the Zn-hidroxo-acetate gel takes place simultaneously with the oxidation of the resulted CO to CO_2 at about 300°C. The two reactions are accompanied by two small thermal effects, one at 295°C (endothermic peak) assigned to decomposition of the

gel and the other 311°C (exothermic peak) assigned to CO oxidation. The low intensity of the peaks may be explained by the fact that a superposition and a compensation of the two phenomena take place. The exothermic peak at around 387 and 427°C may be assigned to the combustion of organic component and crystallization of ZnO from the studied ZnO gel. In the case of Al-doped ZnO gel appears only one peak at 429°C assigned to the combustion of organic component and crystallization of ZnO. This can be accounted for by the influence of a small amount of nitrate from the aluminium precursor (aluminium nitrate nonahydrate).

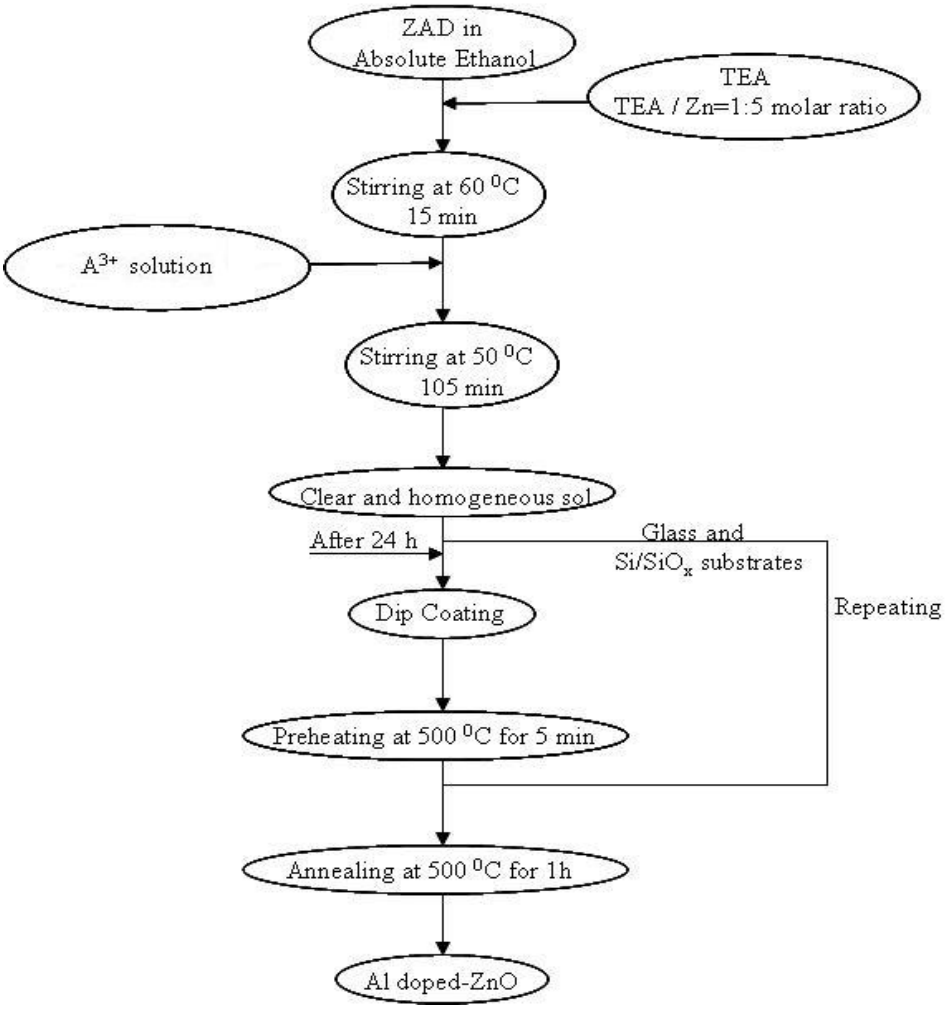

Fig. 1. Flow chart of Al doped ZnO multilayers deposition by sol-gel method.

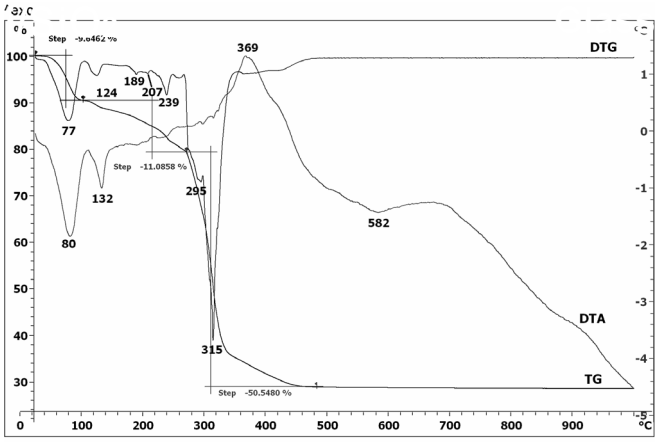

Fig. 2. The DTG, DTA and TG evolution of Al doped ZnO gel.

3.2. *Surface morphology*

The SEM images displayed in Figures 3 (a) and (b) show the morphology of the 0.5% Al doped ZnO films formed by 10 layers successively deposited on Si/SiO_2 and glass substrates, respectively. In both cases the films present a uniform, compactly packed polycrystalline structure, with the larger grain size between 44.5 and 48.7 nm. A slight unevenness of the films surface may be observed. Regions with a diameter of about 100 nm with smaller grain size occur over the entire surface, suggesting a non-uniform growth process.

The morphology of the films with N=1, 2, 3, 5 and 10 layers successively deposited on Si/SiO_2 and glass substrates is shown in Figures 4 (a) and (b).

The SEM images in Fig. 4 (a) and the Raman optical microscopy images presented in Fig.4 (b) demonstrate that the growth process takes place through the nucleation and coalescence of dendritic crystallized areas. All the layers show dendritic structures randomly distributed on their surfaces. The size of the dendritic regions is about 2-4 μm for films with 2 and 3 layers, then, decreases to less than 2 μm for the films with 4 and 10 layers, when films are deposited on a Si/SiO_2 substrate (see the sequence of the films from Fig. 4 (a)). Dendritic regions with the size of 1-2 μm for the films with 2 and 3 layers and about 100-200 nm for the films with 4 and 5 layers appear on the surface of the films deposited on glass (see Fig. 4 (b)). In this later case, the film consisting of 10 layers shows a porous structure with pore size of less than 100 nm rather than clusters of separate dendritic structures. Nano-star formation in ZnO: Al (5.0 at. wt.%) thin film deposited by dip-dry method have been reported previously [24].

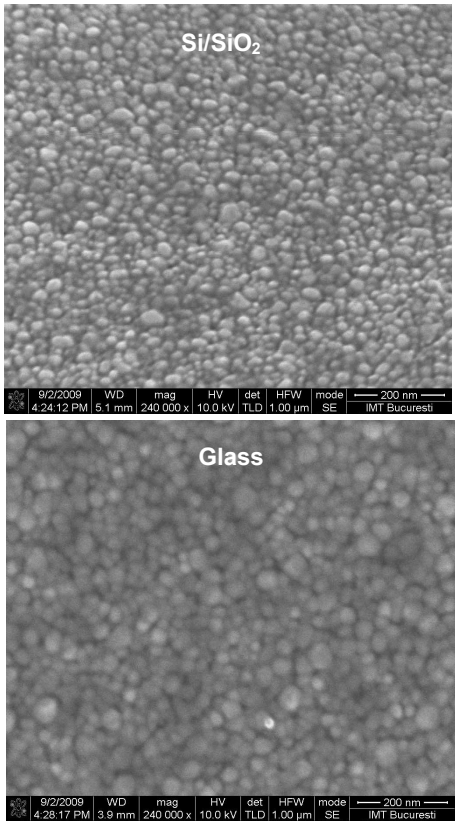

Fig. 3. SEM images of the surface of ZnO:0.5%Al 10 layers films. grown on Si/SiO_2 (a) and glass substrates (b).

The star-shaped structures are considered to be arising from the coalescence of crystallographically oriented ZnO nanoparticles. Doping with Al favors the aggregation of the crystallites and the formation of microstructures. Previous studies have shown that dendrite-like growths of ZnO can be obtained by controlling the aggregated ZnO seeds, [25, 26]. However, for the same nucleation conditions, the morphology of ZnO structures is determined by the rate of aggregation. The anisotropic microstructures with dendritic shape observed in our experiment require a higher growth rate compared with filamentary structures such as the nanowires. Thus, the structure of the films in this work suggests a fast crystallization process. The relatively high temperature, $500^{o}C$, used for the consolidation of each deposited layer, can be considered as a dominant factor which controls the agreggation and growth of our polycrystalline films.

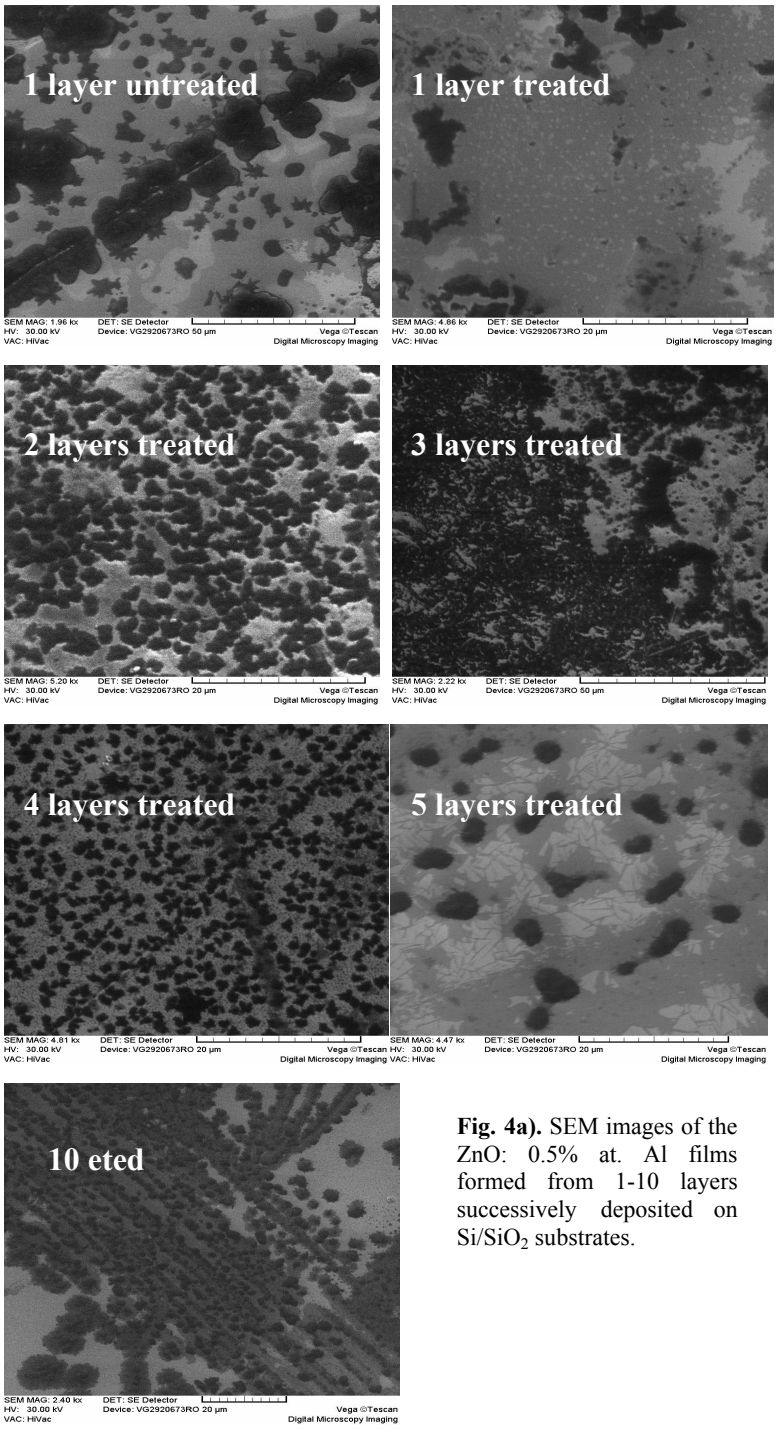

Fig. 4a). SEM images of the ZnO: 0.5% at. Al films formed from 1-10 layers successively deposited on Si/SiO_2 substrates.

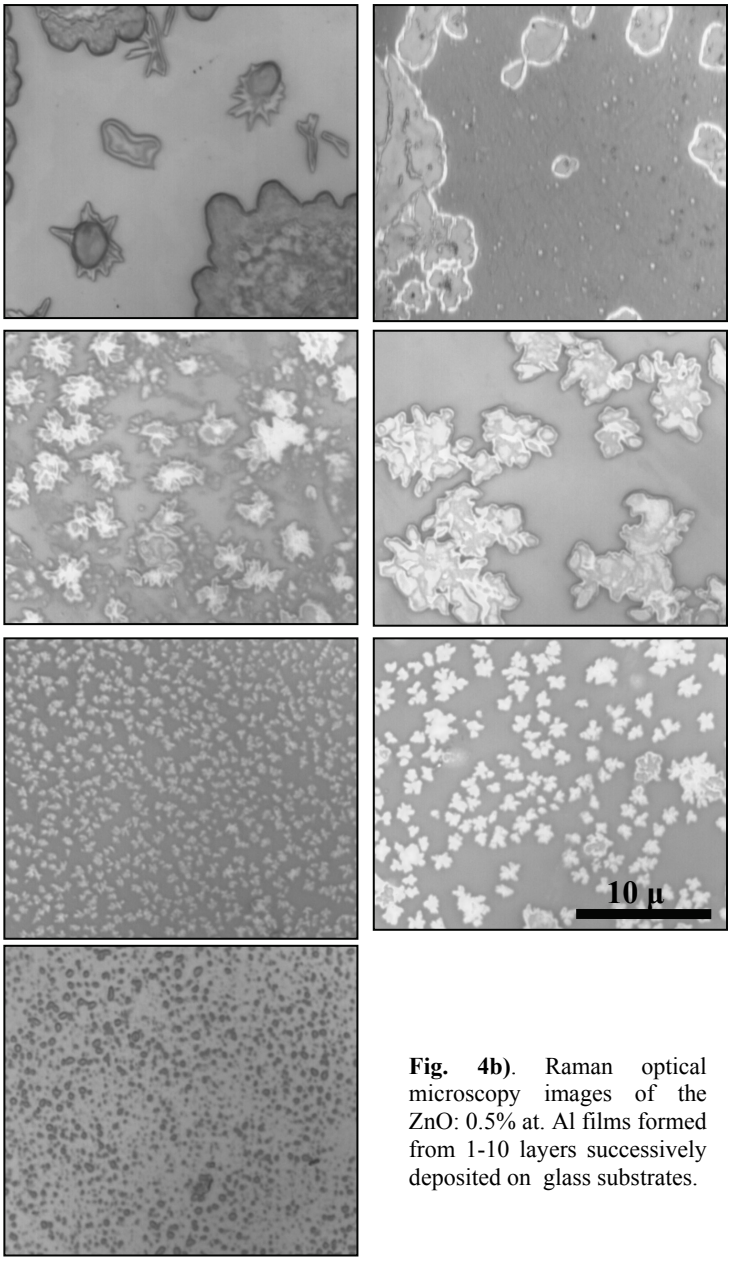

Fig. 4b). Raman optical microscopy images of the ZnO: 0.5% at. Al films formed from 1-10 layers successively deposited on glass substrates.

3.3. *Structural investigation*

The XRD patterns of ZnO:0.5% at. Al doped films consisting of 5 and 10 layers deposited on Si/SiO_2 and glass substrates are presented in Figure 5. The patterns

were indexed according to the wurtzite structure (B4). The films grown on Si/SiO_2 are textured, with the c-axis perpendicular to the substrate, as evidenced by the relative intensity of the (002) reflexion. Note that the intensity of the (002) line increases with the number of deposited layers, clearly pointing to a texture induced by the film growth process. In case the films grow on glass substrate, the orientation gradually changes from (002) to (101) after 5 layers deposition.

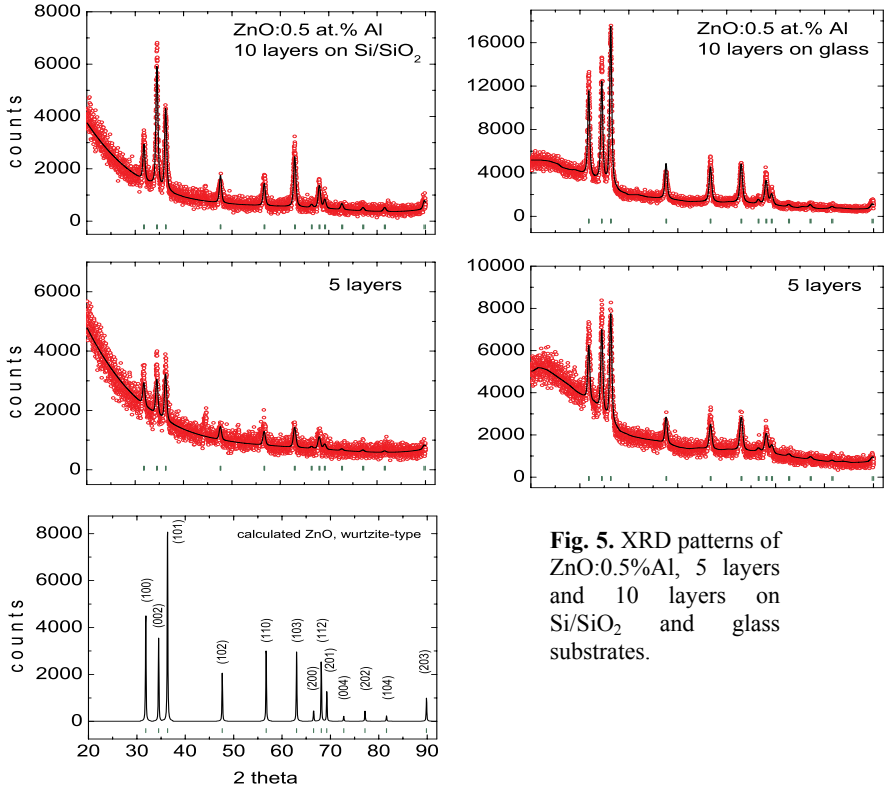

Fig. 5. XRD patterns of ZnO:0.5%Al, 5 layers and 10 layers on Si/SiO_2 and glass substrates.

Figure 6 and Figure 7 display the TEM images and the corresponding selected area diffraction (SAED) of the films with 10 layers deposited on Si/SiO_2 and glass substrates. The films consist of crystalline grains embedded in an amorphous matrix. The HRTEM image presented in the inset in Fig. 6 reveals the lattice fringes of nanocrystals inside a grain in the film deposited on Si/SiO_2 substrate. The interplanar distances of 2.84 Å and 2.45 Å, corresponding to the planes (100) and (101) in ZnO wurtzite structure are indicated. Thus, the micrographs support a (002) texture perpendicular to the film plane, in accordance with the XRD results.

An inspection of the HRTEM image of the film grown on glass (see Fig.7), shows that the lattice fringe is about 2.48 Å and 1.92 Å which corresponds to the

(101) and (102) planes; therefore, the preferred growth direction is along the [100] axis for the films deposited on glass [27, 28].

The diameter of the nanocrystallites in a grain varies in the range 2-15 nm for the films deposited on silicon substrate (Fig. 6), and 6-10 nm in the case of the films deposited on glass substrate (Fig. 7). The HRTEM images also show that the crystallization of a grain in the film deposited on Si/SiO_2 is better than in the case of the film deposited on glass. Not only the size of the crystallites, but also their density in a grain is higher in the former case.

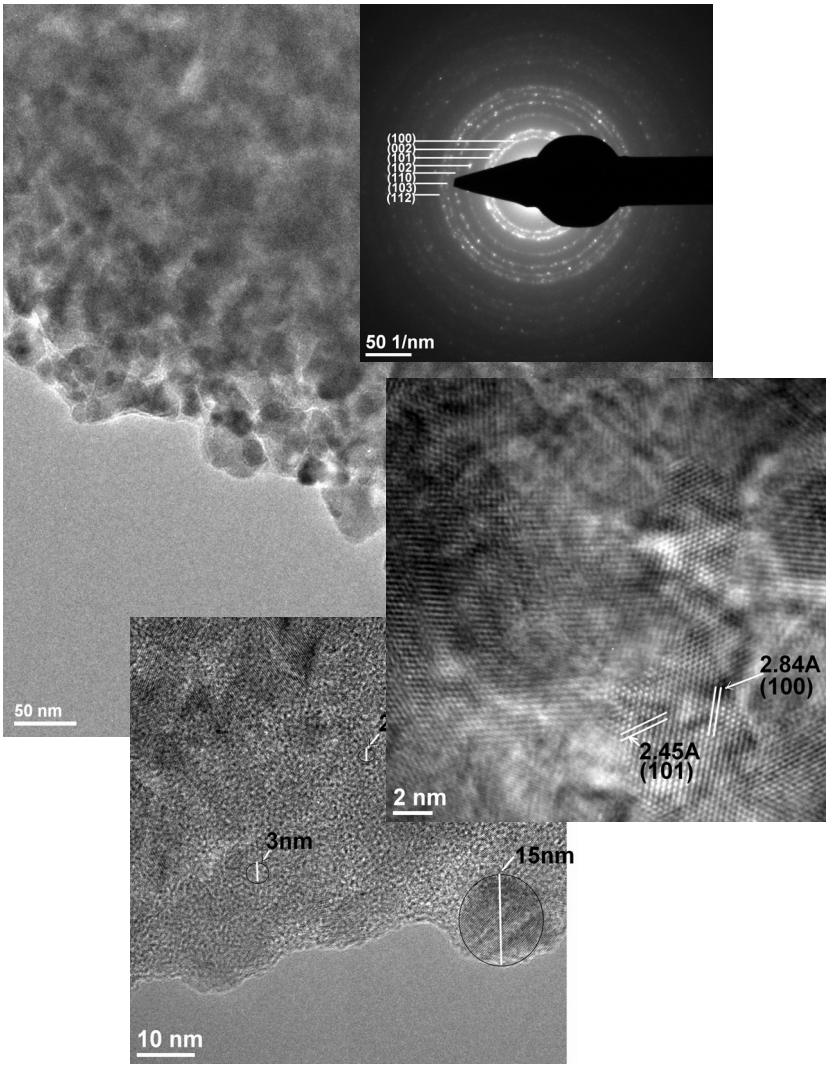

Fig. 6. TEM images and the corresponding selected area diffraction (SAED) of the films with 10 layers deposited on Si/SiO_2.

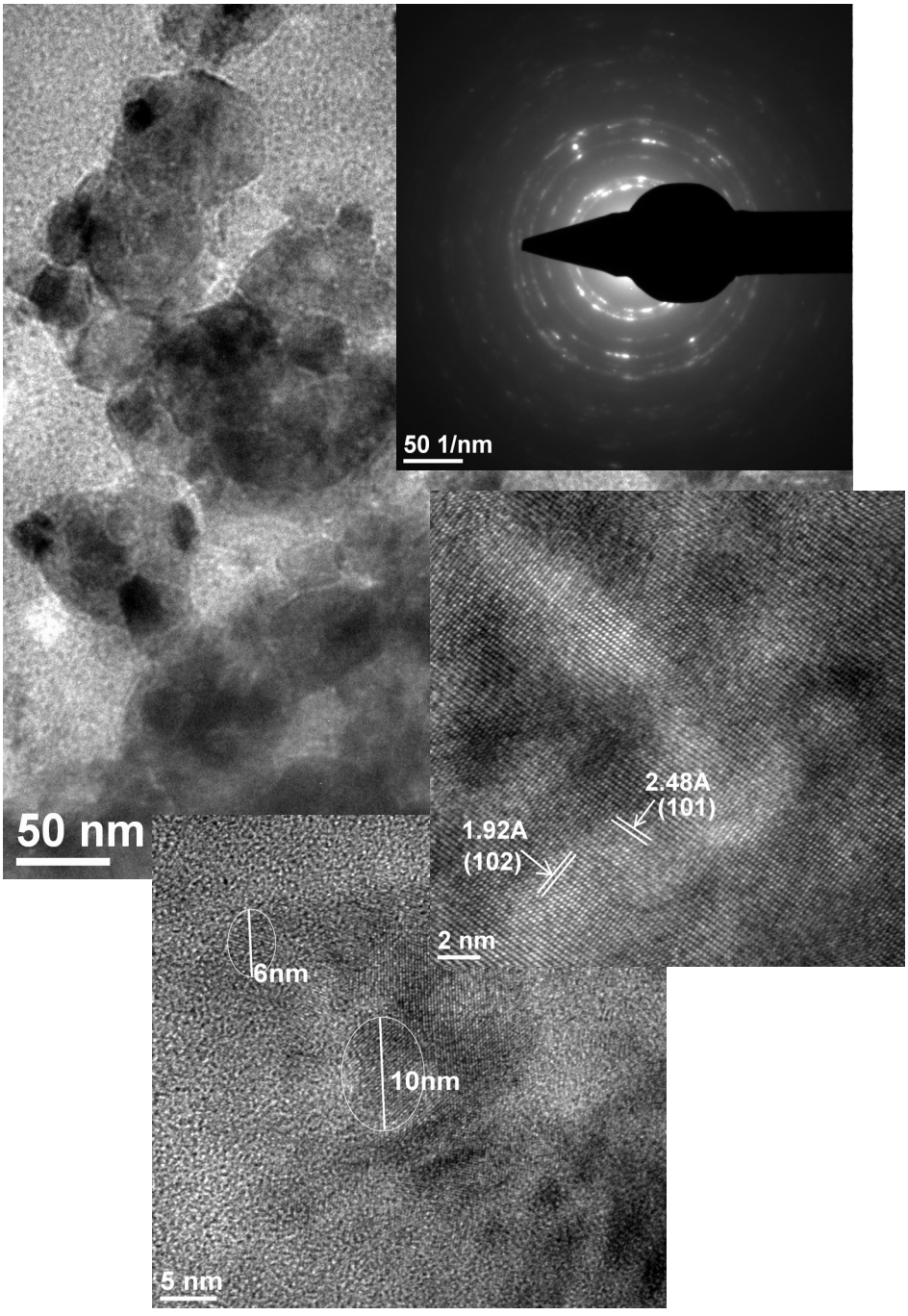

Fig.7. TEM images and the corresponding selected area diffraction (SAED) of the films with 10 layers deposited on glass.

EDX analysis was performed to study the elemental composition of the ZnO:0.5% at. Al doped films. The average concentration of Al in the films is 0.40 ±0.10 at. %. The concentration of the elements in a selected area of the film with 5 layers deposited on a Si/SiO_2 substrate is presented in *Table 2*. The EDS spectra corresponding to qualitative and quantitative analysis are showed in Figures 8 (a) and (b). The film with 10 layers demonstrates a concentration of 0.57 at.% in a plan view selected area, while in a cross section area corresponding to a nanocrystalline grain (see Figure 9), Al concentration is 0.13 at.%.

Table 2. Concentration of Al in the ZnO:0.5% at. Al with 5 layers

Element	Weight %	Atomic %	Uncert. %	Correction	k-Factor
O(K)	32.76	66.41	0.76	0.49	2.008
Al(K)	0.31	**0.37**	0.08	0.92	1.030
Zn(K)	66.92	33.20	0.92	0.99	1.68

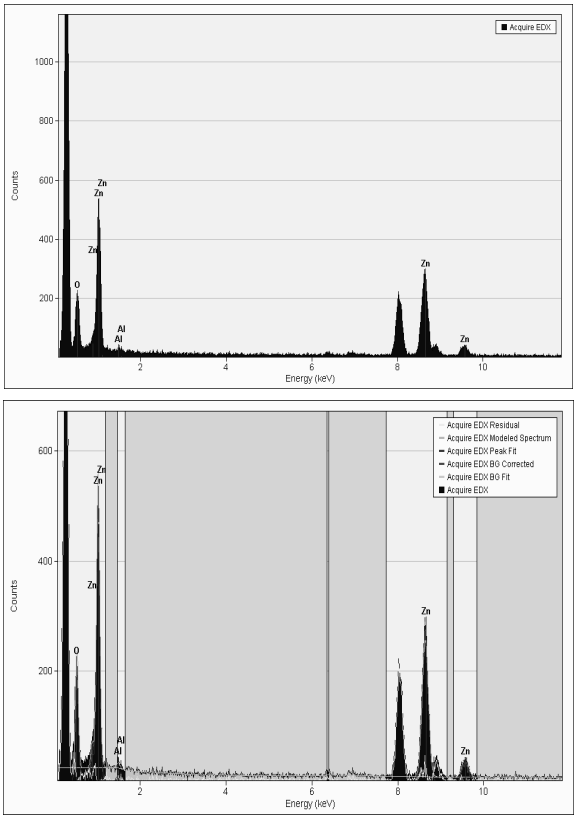

a)

b)

Fig. 8. Energy dispersive spectra (EDS) spectra of ZnO:0.5% at. Al film with Cantitative microanalyse (view of quantization spectrum). 5 layers. (a) Calitative microanalyse; (b).

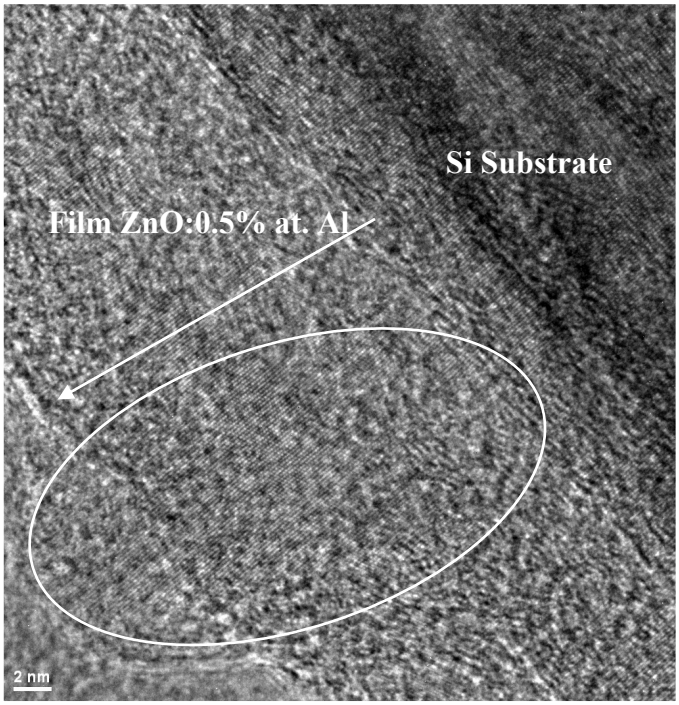

Fig. 9. HRTEM cross section image of the film ZnO:0.5% at. Al, formed from 10 layers. The nanocrystalline grain in the film is pointed out.

3.4. *Optical investigation*

The optical transmission and absorption spectra of the films doped with 0.5 % at. Al and 5 % at. Al, recorded in the wavelength region 200-900 nm are plotted in Figures 10 (a) and (b). The optical transmission spectra of the undoped films with 1 layer and 4 layers are included for comparison (Fig. 10 (a)). It can be observed that the optical transmittance of the films varies in the range of 80%-95%. The transmittance decreases when it's increased the number of the layers in the case of the 0.5% at. Al doping, but it remains almost constant for 5% at.Al doping as well as for the undoped films. For the same number of deposited layers, the transmittance decreases when Al concentration increases. The present result is in conceptual agreement with previously reported data [28] on the transmittance of multilayer films doped with Al in the range 0.25 % to 4 %. The optical absorption spectra of the films are shown in Figure 10 (b). The optical band edge of ZnO: Al doped films calculated from transmission spectra are shifted comparatively to the value 3.92 eV obtained for undoped films. The values of 3.76 eV and 4.12 eV were calculated for 0.5 % at. Al and 5 % at. Al doped films, respectively. The shift of the absorption band edge to higher energies in Al doped ZnO films was observed for

Al concentration up to 3 at. % [29]. The optical band gap value (E_{opt}) increases from 3.27 eV up to 3.33 eV, then decreases to 3.28 eV [30]. Also, enhanced E_{opt} values of 3.70-3.87 eV were reported for 5 mol% and 8 mol% Al doped films prepared by sol-gel method, whereas the E_{opt} of the undoped films was 3.70 eV [31]. The higher values of E_{opt} for undoped and doped films obtained in our experiment comparatively to previously reported results can be related to structural differences, particularly to the porosity observed in our films, which affects the optical constant.

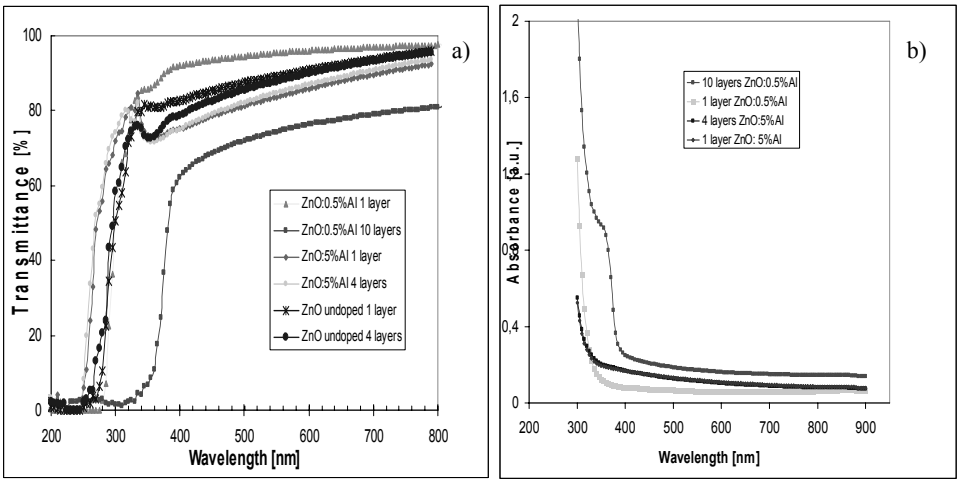

Fig. 10. Optical transmission (a) and absorbtion (b) spectra of ZnO, ZnO: 0.5% at. Al and ZnO: 5% at. Al doped multilayers films.

The films refractive index, n(λ), and the thickness were determined from spectroscopic ellipsometry measurements of optical constants in the wavelength range 250-850 nm. Figure 11 shows n(λ) for 1, 4, 10 layers of 0.5 % Al: ZnO. For all the samples the refractive index values are lower, n =1.6-2, comparatively with the refractive index of an epitaxial ZnO layer in the visible region (n = 1.9-2.1) [32]. This difference can be attributed to a lower density of our films.

The dependence of the film thickness versus the number of depositions for ZnO:5 % Al is shown in the plot in Fig. 12. The curve shows a slight deviation from a linear dependence for up to 5 depositions and then deviates stronger for 5 to 10 depositions. The same trend is also observed for the 0.5 % Al concentration, but with a lower rate of the layer deposition. We obtained a thickness of 31 nm per deposited layer for 5 % Al and only 16 nm per layer for 0.5% Al concentration. Comparatively, the thickness of an undoped layer was 8 nm. The dependence of the observed deposition rate on the dopant concentration shows that the Al ions act as nucleation centers.

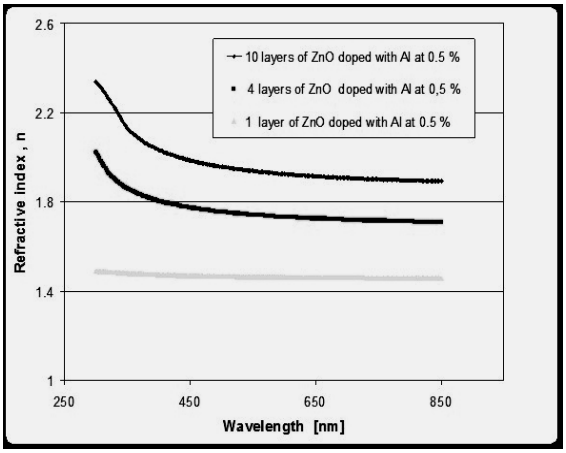

Fig. 11. Refractive index of N=1, 4, 10 layers ZnO:0.5% at. Al films.

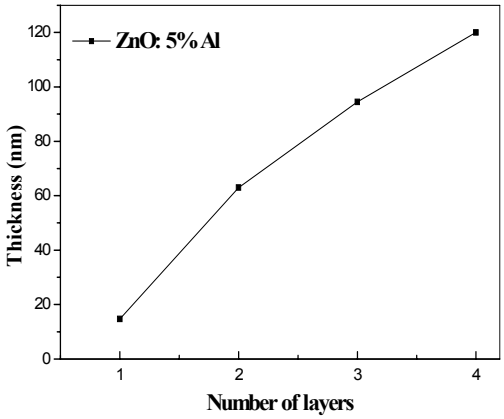

Fig. 12. Film thickness versus the number of depositions for ZnO:5% Al doped films.

3.5. *Raman spectroscopy*

Fig. 13 shows the Raman spectra of the ZnO:0.5 % Al films with 4 and 10 layers deposited on Si/SiO2 substrate. For comparison, the Raman spectrum of ZnO micro-rods grown by CVD is included in the same figure. The wurtzite structure belongs to space group C6v and, according to group theory, the optical phonons at the Γ point of the Brillouin zone are A1+2B1+E1+2E2 [34]. The A1, E1, 2E2 modes are Raman active while 2B1 are silent. The polar phonons of A1, E1 modes are split into longitudinal optical (LO) and transversal optical (TO) components - A1 (TO), A1 (LO), E1 (TO), E1 (LO). Non-polar phonon modes, E2, have two frequencies: E2 (low) associated with non-polar vibration of the heavier Zn atoms sublattice and E2 (high) mode with lighter oxygen atoms. The Raman

spectra were recorded with the laser beam focalized on the dendritic structures, covering an area with a diameter of about 1 μm. The peak located at 437 cm^{-1} in the spectra of the ZnO:0.5% at. Al films can be assigned to the E2 (high) mode of non-polar optical phonons. This is the characteristic peak of hexagonal wurtzite phase and for the bulk ZnO is situated at 439 cm^{-1}. The Raman peak corresponding to E2 (high) mode in the spectra of the ZnO nanocrystals is redshifted compared with bulk material. The redshift effect has been previously attributed to the relaxation of the selection rules in the case of small particles, such as nanocrystallites with 20 nm size, or due to the doping effect [35]. In the latter case, one may also expect a broadening of the Raman peak. The local heating produced by the laser has also been considered to be at the origin of the red shift [36].

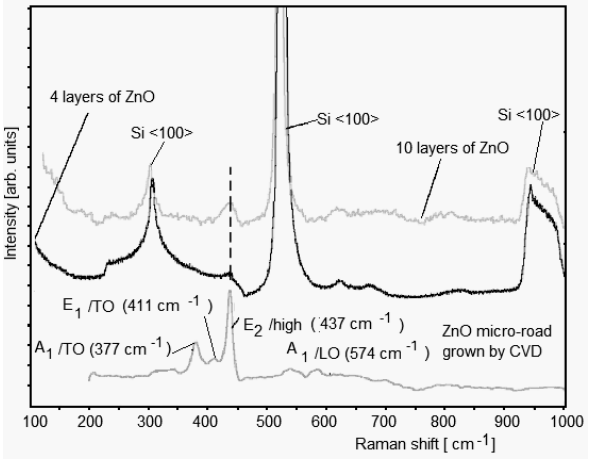

Fig. 13. Ran spectra of 0.5% Al:ZnO films with 4 and 10 layers. For comparison, the Raman spectrum of ZnO micro-rods grown by CVD [ref 26] is also presented.

In the Raman spectra plotted in Fig. 13, the peak associated with the E2 (high) mode appears red shifted for all the samples. However, the broadening effect can be observed only for the peaks in the spectra of the sol-gel deposited films and it is likely to be caused by dopant impurities. No other modes are visible in the spectra of the films, most likely due to the presence of free carriers in the samples or due to the hidden effect caused by the high intensity of the Raman peaks from the Si substrate. The increase in the peak intensity of the E2 (high) mode with the number of the deposited layers confirms the nanocrystallinity of the films deposited layer by layer.

3.6. *UV-VIS Fluorescence*

The fluorescence spectra of the films obtained by deposition of 1-10 layers on Si/SiO_2 and glass substrates are shown in Figure 14 (a) and (b). Two emission bands are present in the spectra, one situated at 383 nm (3.23 eV) and the other

situated in the blue region at 400-450 nm (3.1-2.75 eV). Comparatively, the fluorescence spectra of undoped films (not shown here) are dominated by the optical transitions at 386 nm (3.21 eV) in the case of the films grown on Si/SiO_2 and 387 nm (3.20 eV) in the case of the films grown on glass. A blue shift is observed in the fluorescence emission spectra of the doped films. The optical band gap shift towards the shorter wavelength can be ascribed to Burstein-Moss effect [37]. The increase in carrier concentration in the doped films leads to the occupation of the conduction band bottom, then, the lowest states in the conduction band are forbidden for the occurrence of optical transitions. Previously, it was reported that the optical band gap in ZnO shifts from 3.40 eV to 3.55 eV, for a doping concentration of 0.95% at Al, [37]. In our case the blue shift is smaller, in consistency with the smaller Al concentration in our films. It is worth to observe the intense blue emission bands in the plots in Fig.14. We suggest that these bands correspond to transitions involving defect levels induced by Al doping [38-41].

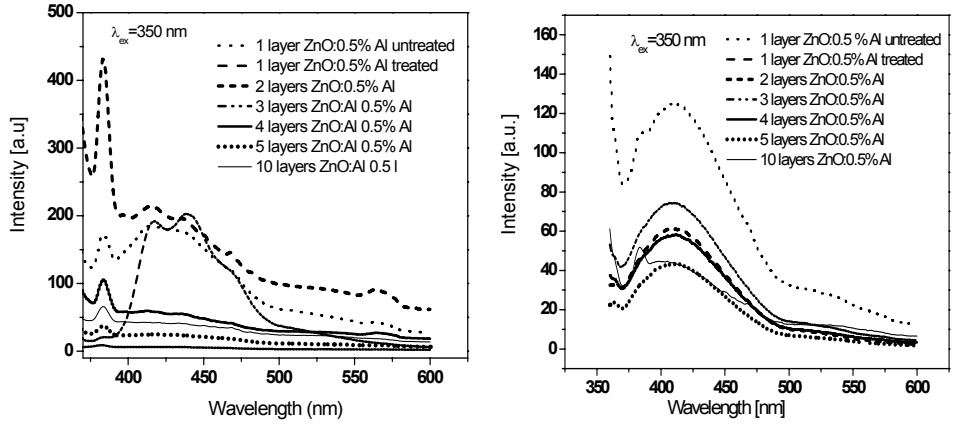

Fig. 14. Fluorescence spectra of ZnO: 0.5% at. Al multilayer films on Si/SiO_2 (a) and glass substrates (b) at an excitation wavelength of 350 nm.

3.7. *DFT study of the electronic structure of $M_xZn_{1-x}O$ (M=Al, Ti, Mn)*

We performed calculations of the electronic band structure of wurtzite-type ZnO modified by M=Al, Ti and Mn doping, aimed at disentangling the impurity effects on conductivity and magnetism in these disordered matrices [42, 43]. We used the exchange and correlations functional in the parameterization of Perdew and Wang [44] and a 16×16×16 integration grid in the Brillouin zone to account for possible Fermi surface effects, having in view the donor character of Al and Ti. We performed the calculations at the experimental volume, assumed the impurity substitutional character and considered no lattice relaxation, hence we refer only to the electronic effects due to the substitutions.

Al and Ti substitution for Zn leads to the appearance of donor states in the system. The valence band shifts to lower energy and a density of states, N (E_F), arises at the Fermi level, increasing with the dopant concentration. The evolution of the band structure as a result of Al and Ti doping may be observed in the element and angular momentum-projected DOS plots displayed in Figure 15 and Figure 16, respectively. The present results indicate that Al-doped ZnO is already metallic for x= 2%. The Al 3s and 4s states are partially occupied and form a narrow band localized at the valence band minimum, see Figure 15. Al contribution to N(E_F) at the Fermi level is almost negligible for 2 at.% Al. Therefore, we associate the conductivity increase in Al-doped ZnO films mostly with the presence at the Fermi level of the electronic charge from O 2p dangling orbitals.

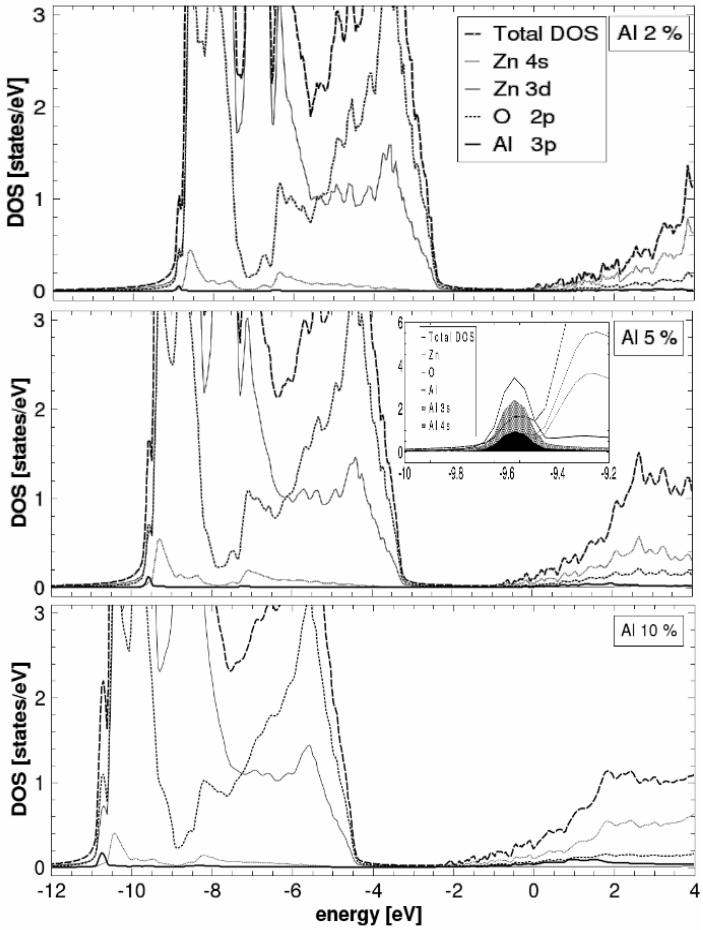

Fig. 15. Tott and l-projected DOS of ZnO doped with: i) 2 % Al top panel, ii) 5 % Al middle panel and iii) 10 % Al bottom panel. Inset middle panel: Enlarged image of the valence band bottom showing Al 3s and 4s states. Note that the Al states are scaled.

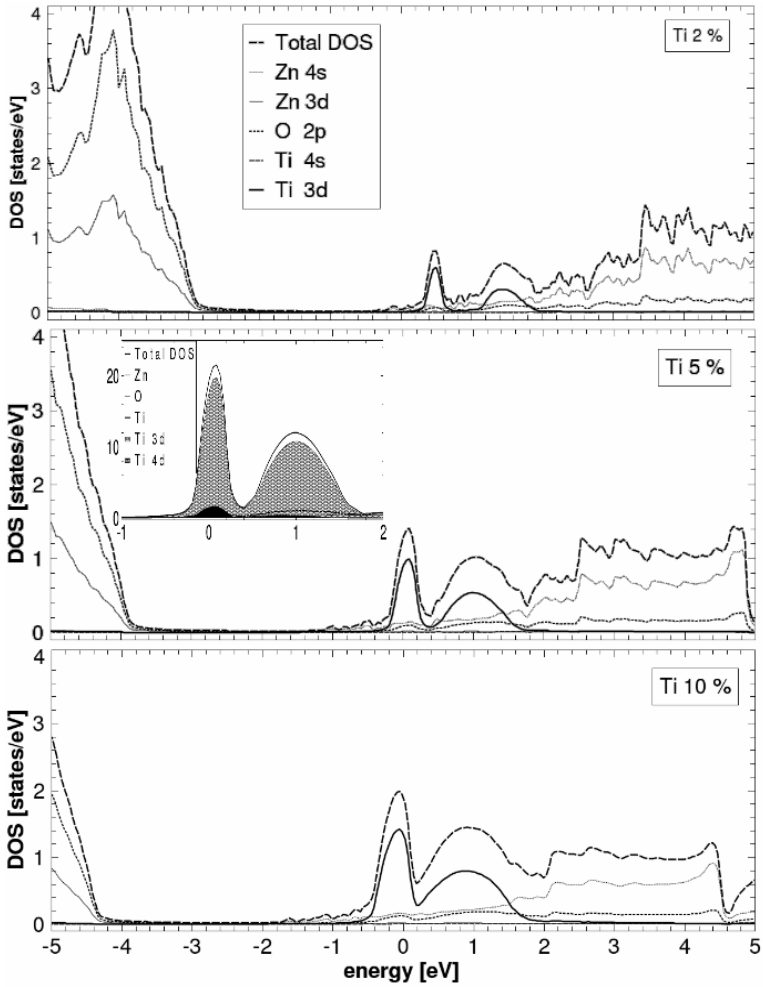

Fig. 16. LDA total DOS and element and l-projected DOS of ZnO doped with: i) 2 % Ti, top panel, ii) 5 % Ti, middle panel and iii) 10 % Ti, bottom panel. Inset middle panel: Enlarged image of the region at the Fermi energy showing the contribution of Ti 3d and 4d states at the $N(E_F)$.

The LDA results for Ti doping show a peak in the density of states at the Fermi level, due to Ti(3d) states, mainly, and also Ti(4d) states, secondarily, see Fig. 5; these states also contribute to a peak situated at approx. 1 eV in the CB, see Inset in Figure 16. $N(E_F)$ shows a variation determined by the shift of the Fermi level toward the CB; thus, $N(E_F)$ increases uniformly from 0.04 states/eV for 2% Ti, to 1.93 states/eV for 10% Ti. Our results predict a non magnetic ground state for Al doped ZnO, derived from a comparison of total energy in spin unpolarized and spin

polarized calculations, in consistency with reported results. In the case of Ti doping the impurity band at the Fermi level is exchange split and the calculations predict a magnetic ground state, in agreement with previous experimental [45] and first principles [46] results. Previously, it has been established that carrier mediated ferromagnetism is responsible for the magnetism in diluted magnetic semiconductors (DMS) [47].

The Mn-doped system retains its semiconductor character for x up to 10%; at that concentration it is at the limit of undergoing an insulator-to-metal transition. The Mn majority spin t_{2g} and e_g states (fully occupied) are situated in the band gap, whereas the (unoccupied) minority spin states are in the conduction band. In the case of Ti doping the LSDA magnetic moment increases from 0.90 to 1.13 to 1.28 μ_B/Ti at. for x=2%, 5% and 10%, respectively, pointing to Ti^{2+} configuration, whereas in the case of Mn the magnetic moment is constant, 4.71 μ_B/Mn at. (high spin Mn^{2+} configuration) in the 2-10% concentration range.

4. Conclusions

- Al-doped ZnO multilayered films ($N \leq 10$ and Al concentration 0.5 and 5 %) with wurtzite structure were grown by sol-gel route on Si/SiO_2 and glass substrates.
- The films are polycrystalline with the grain size of about 44.5-48.7 nm on both types of substrates. The growth process takes place by the nucleation of dendritic structures which coalesce; this process leads to grains with a certain degree of porosity.
- The transmittance of the 1-10 layers of Al:ZnO is 80-95% and decreases when increasing the number of layers. The optical band edge of ZnO is shifted to a shorter wavelength (blue shift) when Al concentration increases. The thickness of a layer increases with Al concentration, from 8 nm for the undoped film, to 16 nm for 0.5% Al and to 31 nm for 5 % Al.
- The E2 (high) Raman mode shows 2 cm^{-1} red shift and appears as a broad peak in the Raman spectra of the multilayered films. The peak intensity of the E2 (high) mode increases with the number of the deposited layers; therefore it brings evidence on the nanocrystallinity of the films deposited layer by layer.
- Fluorescence emission of the films doped with 0.5% at. Al shows the presence of defects, interstitial Zn, and oxygen vacancies (OVs) with the associated emission bands. We assigned the observed blue emission in the region 400-450 nm to transitions involving defect levels induced by the Al substitution for Zn.
- A shift of the fluorescence band at 383 nm to ultra-violet region is determined for Al concentration of 0.4 ±0.1 % with respect to the undoped ZnO. The optical band edge of ZnO is shifted to a shorter wavelength

when increasing Al concentration (blue shift) according with the Moss–Burstein theory.

- Ab-initio calculations predict that in wurtzite-type ZnO systems modified by M= Al, Ti and Mn: i) Al, Ti, Mn behave as donors; ii) Al, Ti, Mn demonstrate different effects on conductivity and magnetism; iii) local magnetic moments appear in Ti and Mn doped ZnO.

Acknowledgements. This work was supported by Projects 11-048/2007-2010 NANOXI, and ERA-NET/MNT 7-029/2010, funded by the National Authority for Scientific Research, Romania.

References

[1] DJURIŠIĆ A.B., NG A.M.C., Chen X.Y., *ZnO nanostructures for optoelectronics: Material properties and device applications*, Progress in Quantm Electronics **34**, pp. 191–159, 2010.

[2] JANOTTI A. and WALLE VAN de C.G., *Fundamentals of zinc oxide as a semiconductor*, Rep. Progr. Phys. **72**, 126501(29), 2009.

[3] JAGADISH C. and PEARTON S., (Editors), *Zinc Oxide Bulk, Thin Films and Nanostructures*, Elsevier, 2006.

[4] SAGAR P., KUMAR M., MEHRA R.M., *The Meyer–Neldel rule in sol–gel derived, polycrystalline ZnO:Al thin films*, Solid State Commun, **147**, pp. 465–469, 2008.

[5] DING J.J., MA S.Y., CHEN H.X., SHI X.F., ZHOU T.T., MAO L.M., I*nfluence of Al-doping on the structure and optical properties of ZnO films*, Physica B **404**, pp. 2439–2443, 2009.

[6] ELILARASSI R., CHANDRASEKARAN G., *Effect of annealing on structural and optical properties of zinc oxide films*, Mater. Chem. Phys. **121**,pp. 378–384, 2010.

[7] LIN -moh K., CHEN Y.-Y., CHOU K.-Y., *Solution derived Al-doped zinc oxide films: doping effect, microstructure and electrical property*, J. Sol-Gel Sci. Technol. **49**, pp. 238–242, 2009.

[8] LU J.J., TSAI S.Y., LU Y.M., LIN T.C., GAN K.J., *Al-doping effect on structural, transport and optical properties of ZnO films by simultaneous RF and Dc magnetron sputtering*, Solid State Commun. **149**, pp. 21777–2180, 2009.

[9] QIANG X.Z., HONG D., YAN L., HANG C., *Al-doping effects on structure, electrical and optical properties of c-axis-orientated ZnO: Al thin films*, Mat. Sci. Semicon. Processing **9**, pp. 132–135, 2006.

[10] ZHU M.W., GONG J., SUN C., XIA J.H., JIANG X., *Investigtion of correlation between the microstructure and electrical properties of sol-gel derived ZnO based thin films*, J. Appl. Phys. **104**, pp. 073113–7, 2008.

[11] LUPAN O., CHOW L., SHISHIYANU S., MONAICO E., SHISHIYANU T., SONTEA V., ROLDAN CUENYA B., NAITABDI A., PARK S. and SCHULTE A., *Nanostructured zinc oxide films synthesized by successive chemical solution deposition for gas sensor applications*, Mat. Res. Bulletin **44**, pp. 63–69, 2009.

[12] WALLE Van de C.G., *Computational studies of conductivity in wide-band-gap semiconductors and oxides*, J. Phys.: Condens. Matter **20**, pp. 064230–7, 2008.

[13] IUSAN D., KNUT R., SANYAL B., KARIS O., ERIKSSON O., COLEMAN V.A., WESTIN G., MAGNUS J., SVEDLINDH P., *Electronic structure and chemical and magnetic interactions in ZnO doped with Co and Al: Experiments and ab-initio density-functional calculations*, Phys. Rev.B **78**, pp. 085319-1–9, 2008.

[14] PALACIOS P., SANCHEZ K., WAHNON P., *Ab-initio valence band spectra of Al, In doped ZnO*, Thin Solid Films **517**, pp. 2448–2451, 2008.

[15] SHELKE V., SONAWANE B.K., BHOLE M.P., PATIL D.S., *Effect of annealing temperature on the optical and electrical properties of aluminum doped ZnO films*, J. Non-Cryst. Solids **355**, pp. 840–843, 2009.

[16] MALDONADO F., STASHANS A., *Al-doped ZnO: Electronic, electrical and structural properties*, J. Phys. Chem. Solids **71**, pp. 784–787, 2010.

[17] EHRMANN N., REINEKE-KOCH R., *Ellipsometric studies on ZnO: Al thin films: Refinement of dispersion theories*, Thin Solid Films **519**, pp. 1475–1485, 2010.

[18] CHUAN YAO P., TSE HANG S., SHUAN LIN Y., TSAI YEN W., CHENG LIN Y., *Optical and electrical characteristics of Al-doped ZnO thin films prepared by aqueous phase deposition*, App. Surf. Sci. **257**, pp. 1441–1448, 2010.

[19] ZNAIDI L., *Sol–gel-deposited ZnO thin films: A review*, Mat. Sci. Eng. B **174**, pp. 18–30, 2010.

[20] KOEPERNIK K. and ESCHRIG H., *Full-potential nonorthogonal local-orbital minimum-basis band-structure scheme*, Phys. Rev. B **59**, pp. 1743–1757, 1999.

[21] KOEPERNIK K., VELICKÝ B., HAYN R. and ESCHRIG H., *Self-consistent LCAO-CPA method for disordered alloys*, Phys. Rev. B **55**, pp. 5717–5729, 1997.

[22] MIHAIU S., GARTNER M., VOICESCU M., GABOR M., MOCIOIU O., ZAHARESCU M., *Characterization of the ZnO thin films obtained by chemical route*, Optoelectron. Adv. Mater. Rapid Communications **3**, pp. 884–890, 2009.

[23] MIHAIU S., TOADER A., ATKINSON I., ANASTASESCU M., VASILESCU M., ZAHARESCU M., PLUGARU R., *Al–doped ZnO nanocoatings obtained by sol-gel route*, Proceedings of SPIE Advanced Topics in Optoelectronics, Microelectronics, and Nanotechnologies V, **7821**, pp. 7821–70, 2010.

[24] BEHERA D., ACHARYA B.S., *Nano-star formation in Al-doped ZnO thin film deposited by dip-dry method and its characterization using atomic force microscopy*, electron probe microscopy, photoluminescence and laser Raman spectroscopy, J. Luminescence **128**, pp. 1577–1586, 2008.

[25] ZHANG H., DU N., WU J., MA X., YANG D., ZHANG X., YANG Z., *A novel low-temperature chemical solution route for straight and dendrite-like ZnO nanostructures*, Mater. Sci. Eng. B **141**, pp. 76–81, 2007.

[26] XIE J., LI P., WANG Y., WEI Y., *Synthesis of needle- and flower-like ZnO microstructures by a simple aqueous solution route*, J. Phys. Chem. Solids **70**, pp. 112–116, 2009.

[27] KIM S., KANG H.-G., CHOI J., *Surfactant-free preparation of ZnO dendritic structures by electrochemical method*, Current App. Phys. **10**, pp. 740–743, 2010.

[28] HUANG J., XIA C., CAO L., ZENG X., *Facile microwave hydrothermal synthesis of zinc oxide one-dimensional nanostructure with three-dimensional morphology*, Mat. Sci. Eng. B **150**, pp. 187–193, 2008.

[29] LIN -moh K., CHEN Y.-Y., CHOU K.-Y., *Solution derived Al-doped zinc oxide films: doping effect, microstructure and electrical property*, J. Sol-Gel Sci. Technol. **49**, pp. 238–242, 2009.

[30] DING J.J., MA S.Y., CHEN H.X., CHEN X.F., SHI X.F., ZHOU T.T., MAO L.M., *Influence of Al-doping on the structure and optical properties of ZnO films*, Physica B **404**, pp. 2439–2443, 2009.

[31] RATANA T., AMORNPITOKSUK P., RATANA T., SUWANBOON S., *The wide band gap of highly oriented nanocrystalline Al doped ZnO thin films from sol–gel dip coating*, J. Alloys Compounds **470**, pp. 408–412, 2009.

[32] SUN X.W., KWOK H.S., *Optical properties of epitaxially grown zinc oxide films on sapphire by pulsed laser deposition*, J. Appl. Phys. **86**, pp. 408–411, 1999.

[33] LIN -moh K., TSAI P., *Parametric study on preparation and characterization of ZnO: Al films by sol–gel method for solar cells*, Mat. Sci. Eng. B **139**, pp. 81–87, 2007.

[34] ASHKENOV N., MBENKUM B.N., BUNDESMANN C., RIEDE V., LORENZ M., SPEMANN D., KAIDASHEV E.M., KASIC A., SCHUBERT M., GRUNDMANN M., WAGNER G., NEUMANN H., DARAKCHIEVA V., ARWIN H., MONEMAR B., *Infrared dielectric functions and phonon modes of high-quality ZnO films*, J. Appl. Phys. **93**, pp. 126–134, 2003.

[35] BI C., PAN L., XU M., YIN J., GUO Z., QIN L., ZHU H., XIAO J.Q., *Raman spectroscopy of Co-doped wurtzite ZnS nanocrystals*, Chem. Phys. Lett. **481**, pp. 220–223, 2009.

[36] ALIM K.A., FONOBEROV V.A., SHAMSA M., BALADIN A.A., *Micro-Raman investigation of optical phonons in ZnO nanocrystals*, J. Appl. Phys. **97**, p. 124313, 2005.

[37] SERNELIUS B.E., BERGGREN K.-F., JIN Z.-C., GRANQVIST C.G., *Band-gap tailoring of ZnO by means of heavy Al doping*, Phys. Rev. **37**, pp. 10244–48, 1988.

[38] DING J.J., MA S.Y., CHEN H.X., SHI X.F., ZHOU T.T., MAO L.M., *Influence of Al-doping on the structure and optical properties of ZnO films*, Physica B **404**, pp. 2439–2443, 2009.

[39] ELILARASSI R., CHANDRASEKARAN G., *Effect of annealing on structural and optical properties of zinc oxide films*, Mater. Chem. Phys. **121**, pp. 378–384, 2010.

[40] PLUGARU R., PLUGARU N., MIHAIU S., VASILE E., *On the electrical conductivity in Al:ZnO layers; experimental investigation and a theoretical approach*, International Semiconductor Conference, Proceedings CAS, pp. 345–348, 2010.

[41] GOSWAMI N., SHARMA D.K., *Absorption and fluorescence emission in the bulk ZnO and nc ZnO*, Physica E **42**, pp. 1675–1682, 2010.

[42] PLUGARU R., PLUGARU N., *First Principles Electronic Structure Study of Disordered Al, Ti, Mn Doped ZnO*, Abstract book "Ψk Conference 2010", p. 349. http://www.psi-k.org/conference 2010.

[43] PLUGARU R., PLUGARU N., *First principles study of the electronic structure of Al/Ti:ZnO Crystal*, International Semiconductor Conference, Proceedings CAS, pp. 383–386. 2009.

[44] PERDEW J.P., WANG Y., *Accurate and simple analytic representation of the electron-gas correlation energy*, Phys. Rev. B **45**, pp. 13244–13249, 1992.

[45] VENKATESAN M., FITZGERALD C.B., LUNNEY J.G., COEY J.M.D., *Anisotropic Ferromagnetism in Substituted Zinc Oxide*, Phys. Rev. Lett. **93**, pp. 177206–4, 2004.

[46] OSUCH K., LOMBARDI E.B., GEBISKI W., *First principles study of ferromagnetism in* $Ti_{0.0625}\ Zn_{0.9375}\ O$, Physical Review B, **73**, p. 075202, 2006.

[47] OHNO H., *Properties of ferromagnetic III-V semiconductors*, J. Magn. Magn. Mat. **200**, () pp. 110–129, 1999.

Nanostructured, Functional Films Prepared Using Thermionic Vacuum Arc

C.P. LUNGU[1], I. JEPU[1], I. MUSTATA[1], V. KUNCSER[2], V. IONESCU[3], V. CIUPINA[3], M. OSIAC[4], G.E. IACOBESCU[4]

[1]INCD pentru Fizica Laserilor, Plasmei si Radiatiei
E-mail: cristian.lungu@inflpr.ro
[2]INCD pentru Fizica Materialelor
[3]"Ovidius" University, Constanta
[4]Faculty of Physics, Craiova University

1. Introduction

Nanostructured magnetoresistive systems based on ferromagnetic materials have been the subject of intensive study due to their relevance both in fundamental physics and in technological applications connected with digital data storage and spintronics, such as reading heads and sensors, high density media, magnetic random access memories. Transport properties in granular structures where ferromagnetic grains are separated by non magnetic spacers are affected by spin-dependent electron confinement and spin filtering, leading to oscillating magnetic coupling and tunneling magnetoresistance.

The structure degree of resistance is extremely variable in the presence of the magnetic field in comparison with the resistance in its absence. The magnetic grains have a super paramagnetic behavior, easily to be oriented to an exterior magnetic field. In its absence, they return to the disordered orientation of the spins they had before the magnetic field application.

The tunneling barrier height depends on the insulator nature; this is why we prepared MgO matrix and the respective MgF_2 matrix magnetoresistive films for a comparative study of the magnetoresistance behavior with the two isolators.

Taking into consideration that the MgF_2 coatings have special optical properties, the so called anti-reflection coatings were prepared with this substance, and we have measured optical absorption of the coated layers in 200-1000 nm domain.

2. Deposition Method

The magnetic metal concentration in the insulator matrix plays a very important role in reaching a tunneling magnetoresistance effect. A mixture of MgF_2 and cobalt was prepared to observe the factors' influence. In order to observe the concentration influence on the magnetoresistance effect, MgF_2 and Co were simultaneously evaporated on 0.5 mm thickness microscope glass slides set above two thermionic vacuum arc evaporation sources as presented in Fig. 1 and more detailed in ref. [2], to both benefit from the coating speed variation and the distance of the evaporation source place.

After that, we heated the MgF_2 and Co anodes keeping the electrical parameters at constant values (the intensity of the filament current, the intensity of the discharge current, and the applied voltage) and the shutter close.

After the electrical parameters remained constant, the shutter screen was removed until the desired thickness was reached. In this case we used the following formula in order to calculate the average density of the prepared compound, the value that must be introduced as parameter of the thickness measurement unit. Let's suppose we intend to prepare a compound with the ratio of the atom concentrations to be **a/b**. We take as reference a volume of 1 cm^3. We suppose that the volume of the material A is V_A and the volume of the material **B** is V_B. We have:

$$V_A + V_B = 1 \tag{1}$$

The masses of the two materials are $\rho_A V_A$ and $\rho_B V_B$ respectively, where ρ is the material density. The number of the atoms of each material will be:

$$n_A = [\rho_A V_A/\mu_A]*N \text{ and respectively } n_B = [\rho_B V_B/\mu_B]*N \tag{2}$$

where N is the Avogadro's number and μ is the respective molar mass.

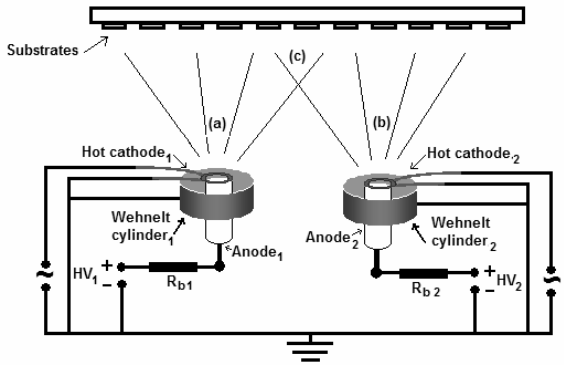

Fig. 1. Experimental set-up. a) Plasma produced in MgF_2 vapors, b) plasma produced in Co vapors, c) zone of mixed plasmas.

Finally we obtain:

$$n_A/n_B = [\rho_A V_A/\mu_A]/ [\rho_B V_B/\mu_B] = a/b \quad (3)$$

Using eq. (3) and eq. (1) we obtain V_A and V_B which are introduced into the following equation:

$$\rho_A V_A + \rho_B V_B = \rho_{med}(V_A + V_B) \quad (4)$$

When two materials are co-deposited the compound density is calculated and settled on the measuring unit.

3. Results and Discussion

The coated films were analyzed by transmission electron microscopy (TEM) using a PHYLIPS CM 120 apparatus at Ovidius University, Constanta where was inferred the nano-metrical structure of the Co magnetic particles uniformly spread in the dielectric matrix of MgF_2. (Fig. 2).

Using TEM, it was observed the nanosize dimension of the magnetic grains (2-3 nm), which leads to the over paramagnetic structure of those domains, very useful in reaching uniform domains through post deposition thermal treatment [3-7]. The selected area diffraction pattern, presented in Fig. 3 shows diffuse rings due to the Co grains embedded in the MgF_2 matrix, as well as specific patterns due to the formation of the crystalline Co grains.

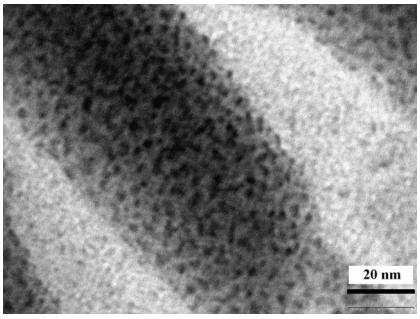

Fig. 2. TEM image of the MgF_2-40at%Co film.

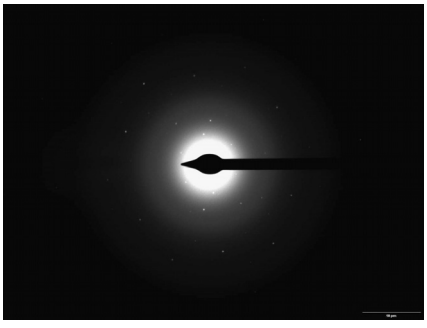

Fig. 3. Selected area diffraction of the $MgF_2$40%atCo film.

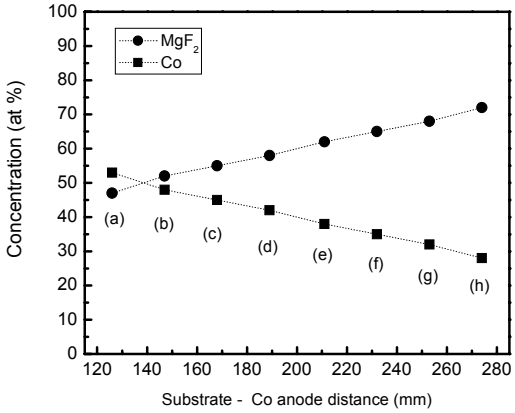

Fig. 4. Co and MgF_2 concentration in the studied samples, measured by energy dispersive spectroscopy (EDS).

The relative amount of Co (at. %), as obtained by EDS measurements on different samples, versus the distance from the Co crucible to the film supports, is presented in Fig. 4 (e.g. sample (a) corresponds to a distance of 125 mm, whereas the sample (h) is the sample placed at a distance: Co anode - substrate of 275 mm). The distance between the two anodes was 150 mm. It was observed the almost linear decrease of the Co concentration with the increasing distance between the substrate and the Co anode.

As a consequence of the different Co contents in the different samples from the sample (a), to the sample (h), it was studied the dependence of the TMR effect and the related structural and magnetic behaviors versus the concentration of the magnetic element. It is worth mentioning that the thickness of the central samples (d) and (e) was 250 nm and the other samples present thicknesses of the same magnitude inside the measuring error bars.

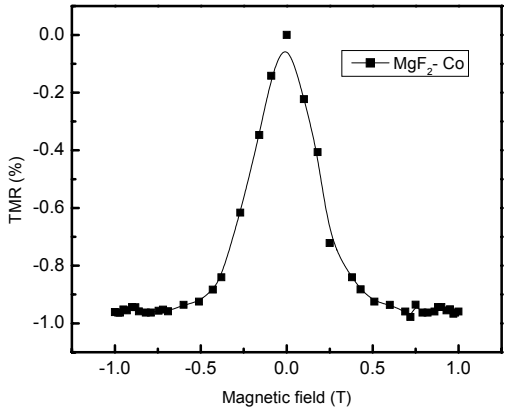

Fig. 5. Tunneling magnetoresistive response of the $MgF_2$40%Co sample film versus the applied magnetic field.

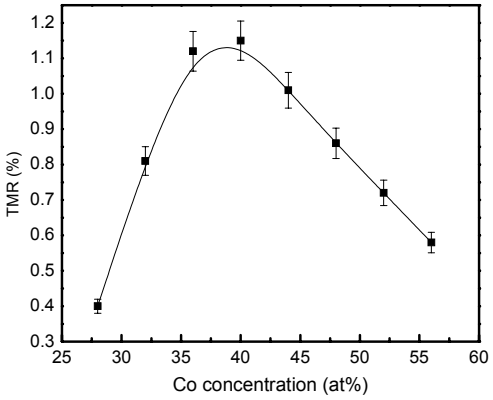

Fig. 6. The room temperature TMR effect for different concentrations of Co in the MgF_2 matrix.

The variation of the TMR effect at room temperature (RT) defined as the $(R_H–R_0)/R_0$ was measured in a current in plane (CIP) arrangement. Fig 5 shows the magnetoresistive response of the MgF_2 40 % Co sample film versus the applied magnetic field, while the TMR response versus the relative content of cobalt in the magnesium fluoride dielectric film is shown in Fig. 6.

It is easily observed that the TMR effect has a maximum value at a given Co concentration (40 at % Co in this case) and decreases much faster at lower Co concentration as compared with the case of higher Co concentrations in the range of 40 to 57 at % Co. Most likely, this effect has to be related with different morphology or size distribution of the Co particles in the dielectric matrix and we will return to this point after providing structural and magnetic data.

Fig. 7 shows the longitudinal magneto-optic Kerr effect (MOKE) hysterezis loop obtained at RT on MgF_2 40 % Co sample.

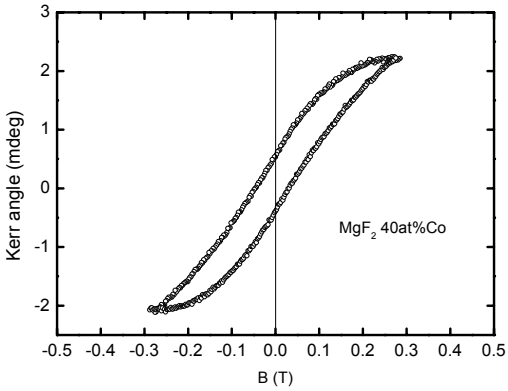

Fig. 7. The magneo-optic Kerr effect behavior of the MgF_2 40 % Co sample versus the magnetic field.

In order to correlate TMR effect and magnetic data, we will further show some structural and magnetic aspects of the film containing MgF_2 40 % Co. Both the as prepared sample, as well as the annealed one were analyzed and processed by a post-deposition thermal treatment, performed at 300^0C for one hour in high vacuum condition (10^{-5} torr).

The EDS spectra collected on the two samples have shown slightly increased oxygen content in the annealed sample as compared with the as-prepared one, which would lead presumably to an increased partial oxidation of the Co particles in the annealed sample. The scanning electron microscopy (SEM) images of the as-deposited and the annealed MgF_2 40 % Co film, presented in Fig. 8 and Fig. 9 respectively, show clearly much larger grains induced by the thermal treatment. Electron diffraction patterns evidence that the structure with well arranged atomic planes belongs to metallic Co grains, of which dimensions are much larger in the thermally annealed sample as compared with the as-prepared one.

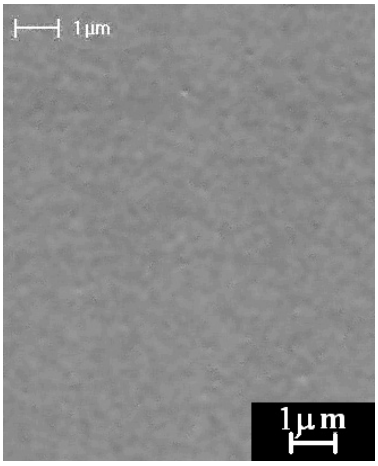

Fig. 8. SEM image of the as-deposited MgF_2 40 % Co sample.

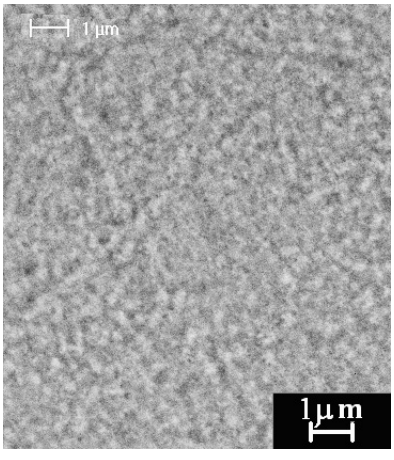

Fig. 9. SEM image of the annealed MgF_2 40 % Co sample.

In addition, the electron diffraction has proven the presence of cobalt oxide (the antiferromagnetic Co_3O_4) in both the as-prepared sample and the annealed sample. The amount of the cobalt oxide is slightly larger in the annealed sample, in agreement with the EDS data proving increased oxygen content in this sample.

The RT MOKE hysteresis loops of the as-prepared and annealed MgF_2 40 % Co films are presented in Fig. 10. One can see that the thermal treatment increases the saturation magnetization of the film as well as its coercive force. Based on this structural/morphologic picture of the two samples, we can interpret the corresponding RT MOKE curves as follows. In the as-prepared sample, there are formed very fine Co grains (about 5 nm) with a thin magnetic dead layer of cobalt oxide, giving rise to a reduced magnetization of the sample (due to both defected spin structure and possible superparamagnetic behavior of the grains of lower dimensions).

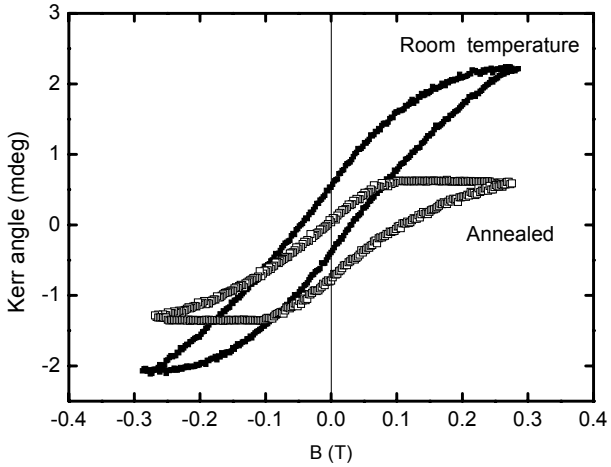

Fig. 10. Room temperature MOKE measurements of the as-prepared and the annealed at 300^{O}C MgF_2 40 % Co film.

After the annealing treatment, the initial clusters agglomerate giving rise to much larger Co crystalline particles. In spite of a slightly thicker cobalt oxide layer on the surface, the Co core is significantly larger than in the case of the as-prepared film, which leads finally to higher average magnetic moment per Co atom, due to both a less defected magnetic structure and reduced magnetic relaxation of the Co particles. Hence, a higher magnetization and coercive field is expected for the annealed sample.

The magnetic field dependent TMR response of the annealed samples showed a decrease of the magnetoresistance in comparison with the as-prepared ones. That is probably due to increased distances between the magnetic grains in the annealed samples (directly connected with formation of much larger magnetic grains), diminishing drastically the tunneling probability in this system. Hence, the thermal

treatment appears to decrease the TMR coefficient in MgF_2 - Co systems, opposite to the effect of similar treatments applied to nanoglobular GMR systems like Co-Cu or Fe-Cu [8].

The above observation can be also extended to the case of the TMR data presented in Fig. 6. The continuous decrease of the magnetization with the Co relative content in the films has to be explained by a reduced average size of the Co grains (and implicitly by an increased particle density) in films of higher Co content. That would explain the fast increase of the TMR effect when increasing the Co content in the film up to the optimal value of 40 at. %. However, by further increasing the Co content, the TMR effect starts to decrease, due to an enhanced magnetic disorder specific to the very large surface area of very fine particles, connected also with a very weak magnetic response to the applied field.

The transmission coefficient decreases in the intervals of 328 nm - 498 nm, Zone I and 500 nm-900 nm, Zone II, respectivelly, with the increase of the Co concentration into the MgF_2 matrix. The maximum peaks of transmission move also from 394 to 370 nm, Zone I, and from 700 nm to 570 nm in Zone II for the films with higher concentration of Co (from 26 a t% Co to 56 at % Co).

Between 970 and 1200 nm, the transmission coefficients of the all films are almost the same, with very high (0.98 to 0.99), with a tendency for the films with higher concentration in Co to be higher than the others.

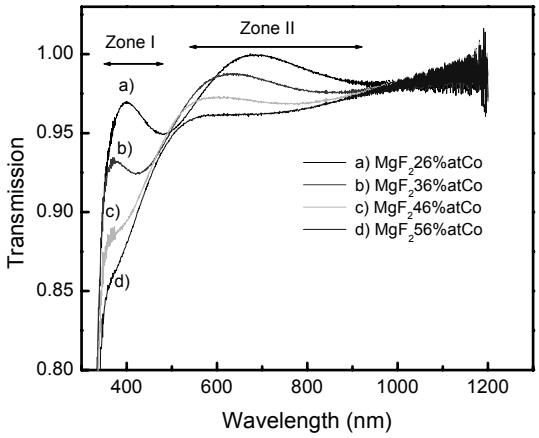

Fig. 11. Transmission spectra of MgF_2-Co films.

This behavior of the transmission could be due to the refraction indices of the films with different concentration of Co magnetic clusters. We expect also the diffraction of the light due to the nanometric grain size of Co clusters embedded into the MgF_2 matrix.

The dependence of the transmission on Co cluster concentration in Zone I and Zone II could be explained as in ref [11] on the trasmission decrease as function of film thickness, in our case the increasing of the Co grain concentration. The

minimum of the transmission will be correlated with the "percolation threshold" - the situation when the Co clusters form a continuum film. The reason why that happens is because the electrons are trapped in individual islands and cannot move freely like in a closed film. The electromagnetic field of an incoming lightwave can excite surface plasmons which lead to absorption [12].

The films could be used as absorption filter on different range of the wavelength, controlled by the magnetic nanometric size and the cluster concentration.

4. Conclusions

MgF_2-Co granular films presenting TMR effects were successfully prepared by the TVA method. The films with different Co cluster concentrations were obtained by settling film substrates at different distances from the Co and MgF_2 evaporation sources. A maximum TMR effect of about 1.2 % was obtained at room temperature for a relative content of 40 at % Co. High resolution TEM and electron diffraction measurements reveal the presence of the crystalline Co grains as well as surrounding shells of cobalt oxide. Post deposition thermal treatments of the Co-MgF_2 films (for one hour, 300^{o}C, 10^{-5} torr) increase substantially the average of the Co grain size and slightly the thickness of the cobalt oxide layers around nanograins. These structural results support the increased magnetization in the room temperature MOKE hysterezis loop in the annealed samples as well as the decreased TMR effect, due to increasing distances among Co nanograins.

The proposed processing method (TVA) allows the fast deposition of TMR granular structures with a large variation of the concentration of the magnetic metal in the insulating matrix. However, the TMR effects in such systems are still low and further work is needed in order to improve them.

References

[1] BADER S.D., ERSKINE J.L., in: B. Heinrich, J.A.C., Bland (Eds.), Ultrathin Magnetic Structures, Springer Verlag, Berlin, 1994.
[2] MUSTATA I., *et al*., Vacuum, ,**76,** p. 131., 2004.
[3] MOODERA J.S. and MESERVEY R.H., 2004 *Magnetoelectronics* Ed M.Johnson, (Academic Press).
[4] JULLIERE M., *Phys. Lett.,* **54 A** 225, 1975.
[5] TSYMBAL E.Y., MRYASOV O.N., LECLAIR P.R., *J. Phys.: Condens. Matter*, **15,** 109, 2003.
[6] KUNCSER V., *et al.*, *Surf.& Coat. Techn*, **1-4**, 980, 2005.
[7] LUNGU C.P., *et al.*, *Surf and Coat. Techn*, **200**, 399, 2005.
[8] ANGHEL A., *et al.*, *Czech J. Phys*., **56 B,** 16, 2006.
[9] KUNCSER V., *et al.*, Journal of Alloys and Compounds, **499,** 23, 2010.
[10] IONESCU V., *et al.*, *Thin Solid Films*, **518**, 3945, 2010.
[11] CHARTON C. and FAHLAND M., *Surf.and Coat. Techn.*, **174-175**, 181, 2003.
[12] ABELÈS F., BORENSZTEIN Y., LÓPEZ-RIOS T., Festkörpeprprobleme XXIV (1984).

The Eukaryote Cell Interaction With Doped TiO_2 Nanoparticles

G.C. CORNEANU[1, 2], C. CRĂCIUN[3], M. CORNEANU[4], C. LAZĂU[5], I. GROZESCU[5], S. TRIPON[3]

[1]University of Craiova, Genetics Dept., 200585-Craiova, Romania
E-mail: gabicorneanu@yahoo.com

[2]West University Vasile Goldiş Living Sciences, Arad, Romania

[3]Babeş-Bolyai University, Electron Microscopy Center, 400006-Cluj-Napoca, Romania
E-mail: ccraciun@hasdeu.ubbcluj.ro; tripon_septimiu@yahoo.com

[4]University of Agronomical Sciences and Veterinary Medicine of Banat, Genetics Engineering Dept., 300645-Timisoara, Romania
E-mail: micorneanu@yahoo.com

[5]I.N.C.-D.E.M.C., 300860-Timisoara, Romania
E-mail: carmenlazau@yahoo.com; grozescu@icmct.uvt.ro

Abstract. The experiment was performed in Mus musculus, being analyzed the liver ultra-structural features, as well as the nanoparticles interaction (single TiO_2 nanoparticles of 10-20 nm, or conjugate with a metal, TiO_2-Fe, TiO_2-Pt or TiO_2-Ag) with the hepatic cell. The small nanoparticles can penetrate in hepatocyte, their effect being dependent on the conjugate metal kinds. The TiO_2-Pt and TiO_2-Ag nanoparticles induced reversible effect, while the TiO_2-Fe nanoparticles altered the hepatocyte ultra-structure. Depending on the metal kinds, the TiO_2-Me nanoparticles can be in relation with smooth and rough endoplasmic reticulum and with mitochondria, or in lipid droplets, being also present in the Kupffer cell.

1. Introduction

Initially, TiO_2 nanoparticles were considered an inert material, because of the very small size of it. Subsequent was the point that TiO_2 nanoparticles can induce lesions at the chromosomes and DNA, as well as at the ultrastructural level. They can migrate in different organs, and induce oxidative stress and cell death. As a result of the studies performed by International Agency for Research on Cancer

(IARC), the TiO_2 toxicity was re-revaluated, and they were moved in the **2B** group of materials, as possible carcinogen for men [1]. The biological reactivity of the TiO_2 nanoparticles is dependent on different features: their crystallization shape (anatase, rutile or broklite), amount, size, a/o. Recently, TiO_2 nanoparticles doped with different chemical elements were obtained, as well as nanoparticles included in liposome. From the noble metals, the mostly used were silver, gold and platinum, as well as other metals (iron, copper, a/o). The noble metals are resistant to oxidation process. In many studies, the silver was deposited on TiO_2 surface, being more reactive than gold or platinum, having the photocatalitic effect proper to TiO_2 nanoparticles, as well as the ability to prevent bacteria development [2].

In the human or animal body, the research was performed to establish an eventual cytotoxic effect depending on different parameters: the nanoparticle size [3], their single presence or doped with other element [4], activation or not by UV rays [5], [6], encapsulated or not in different bioactive substances, a/o. The cyto- and genotoxicity analysis of the ultrafine TiO_2 nanoparticles, in human lymphoblast cell, evidenced that these can induce cyto- and genotoxicity in a significant mode [7]. The analysis of the biological effects of three kinds of nano-TiO_2 of different size (10-20 nm anatase; 50-60 nm anatase and 50-60 nm rutile) on DNA and cell ultrastructure of the 293T and CHO cells, reveal that all three kinds of nano-TiO_2 manifest a higher toxic effect on tumor cells than on normal cells [8]. Also, the nano-TiO_2 from anatase kinds, were observed in the cytoplasm of CHO cells, indifferent on this size (50-60 nm or 10-20 nm).

The biological investigation pointed out different biological effects of the TiO_2-Me nanoparticles, depending on the metal type (silver, golden, copper or platinum). Thus, the use of the TiO_2-Pt and TiO_2-Au nanoparticles, are preferable in comparison with TiO_2-Ag or TiO_2-Cu doped nanoparticles [9].

There are a few studies regarding the TiO_2 nanoparticles' interaction with the eukaryote cell. In a synthesis from 2006 [10], there wasn't present any paper regarding the interaction between the eukaryote cell with the TiO_2 nanoparticles. In previous researches, our groups pointed out the relation between TiO_2 nanoparticles with eukaryote animal cell [11] or vegetal cell [12]. In another paper [8] was underlined that the nano-TiO_2 from anatase kinds was observed in the cytoplasm of CHO cells, indifferent on the size (50-60 nm or 10-20 nm).

In this paper the interaction of titanium dioxide nanoparticles with animal cell (hepatocyte from *Mus musculus*), depending on the chelated metal (single or chelated with silver, platinum, or iron) was analyzed.

2. Materials and Methods

2.1. *The preparation of titanium dioxide nanoparticles*

Undoped and doped titanium dioxide nanocrystals were synthesized by the sol-gel route, using the precursors: titanium isopropoxide, isopropyl alcohol, distilled

water, nitric acid, hexachloroplatinate acid, silver nitrate and ferrous nitrate. Over 30 ml of isopropyl alcohol, 5 ml of titanium isopropoxide were added in drops, under continuous stirring with the magnetic stirrer. After a few minutes of stirring, distilled water was added, continuously controlling the solution pH with nitric acid in order to avoid the precipitation. In the case of platinum-doped and iron-doped TiO_2 ions, after the adjustment of the pH (pH=2.5 for Pt and Ag, pH=5 for Fe), to the previously prepared solutions were added hexachloroplatinate acid for doped with Pt, silver nitrate for doped with Ag and ferrous nitrate for doped with Fe under continuous stirring. In all cases, the gel was dried and washed in order to remove the secondary reaction products. The calcinations was achieved in the oven, at a temperature of 250ºC for undoped TiO_2 and 500ºC for Pt, Ag or Fe-doped TiO_2, for 3 hours.

The obtained materials were characterized by X-ray diffraction (XRD), scanning electron microscopy (SEM) and energy dispersive X-ray analysis (EDAX). XRD spectra were recorded at room temperature with a BRUKER D8 ADVANCE X-ray diffractometer using Cu Kα radiation in θ:2θ configuration. The SEM images were made in an Inspect S scanning electron microscope coupled with EDAX device.

2.2. *Biological material*

The experiments were performed on young females of *Mus musculus*, intra-peritoneal injected with a suspension of titanium dioxide. The animals were intraperitoneal injected (five injections of 0.5 ml each, one two days) with a 0.01% TiO_2 or TiO_2-Me suspension. A day after the last injection, the animals were sacrificed through the carotid artery section, and their liver were used for the electron microscopy investigations.

2.3. *Electron microscopy investigation*

The pieces of about 1 mm^3 of liver, were prefixed in a 2.7% glutaraldehyde solution (2 ½ hours), postfixed in a 1% Millonig solution (1 ½ hour) and then included in Epon 812. The seriated sections of about 60 nm thickness, were contrasted with uranyl acetate and lead citrate, and then analyzed at a TEM JEM JEOL-1010 electron microscope in the Electron Microscopy Centre, *Babes-Bolyai* University (Cluj-Napoca, Romania).

3. Results and Discussions

3.1. *TiO_2 particles feature*

The XRD (Fig. 1) analyses present the crystallization as *anatase* form of the undoped / Pt, Ag or Fe doped TiO_2, even if the calcinations temperatures for the TiO_2 doping surpass the value of 500ºC. The presence of the dopant in the

crystalline network of the titanium dioxide tripped the phase transition from *anatase* to *rutile*. From the diffraction spectra it is noticeable that the dopants did not present separate peaks, which means that this is distributed uniformly in the crystalline network.

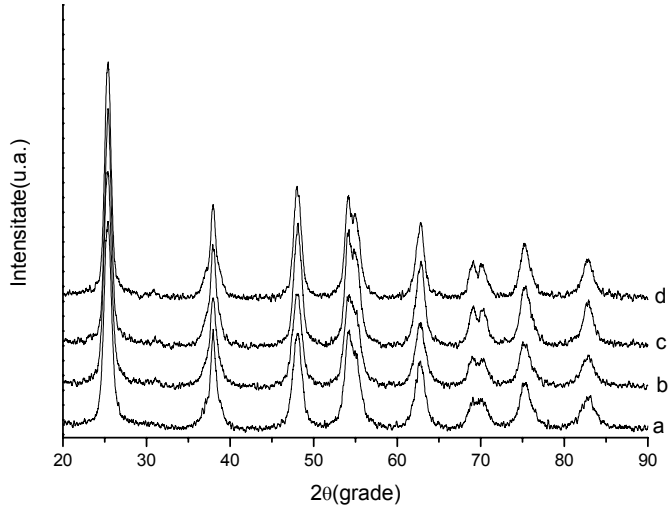

Fig. 1. XRD pattern for: (a) TiO_2 undoped; (b) TiO_2-Fe; (c) TiO_2-Pt; (d) TiO_2-Ag.

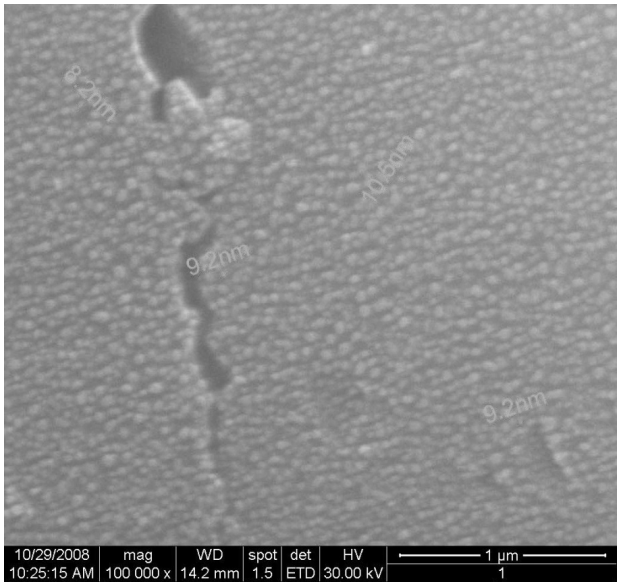

Fig. 2. SEM morphology for TiO_2 undoped.

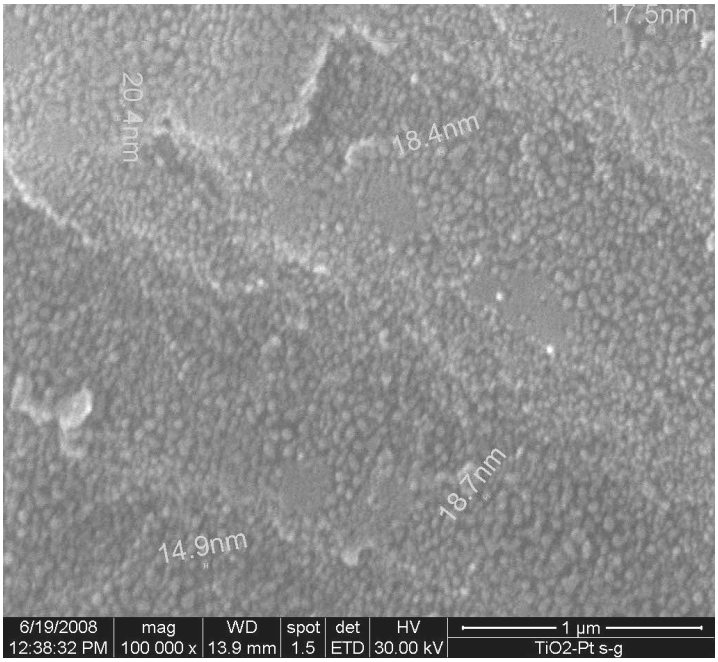

Fig. 3. SEM morphology for TiO_2-Pt.

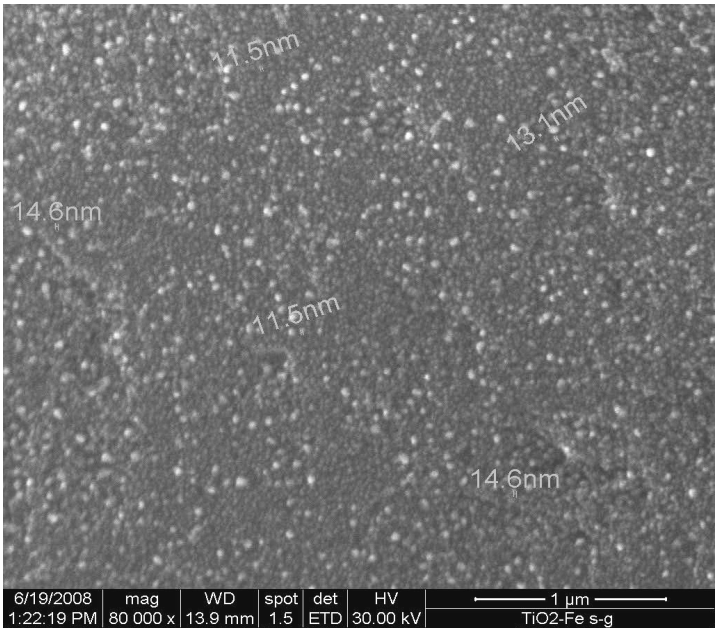

Fig. 4. SEM morphology for TiO_2-Fe.

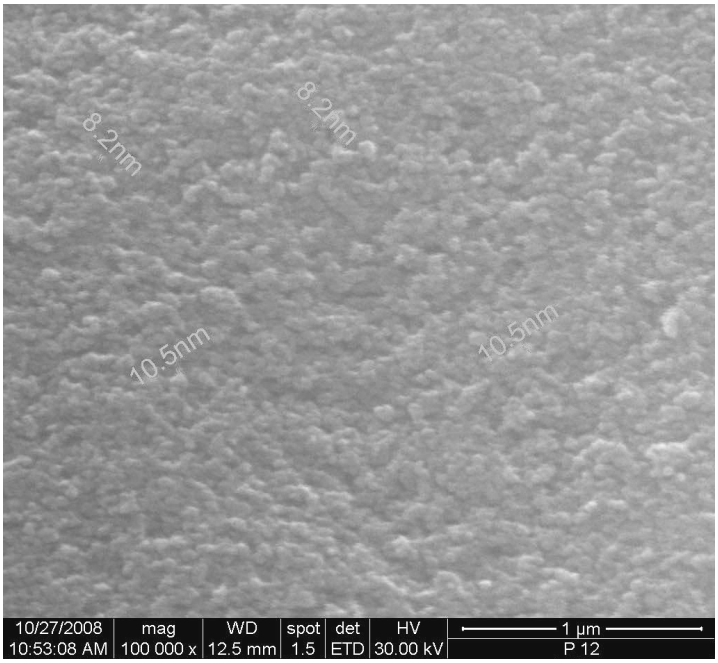

Fig. 5. SEM morphology for TiO_2-Ag.

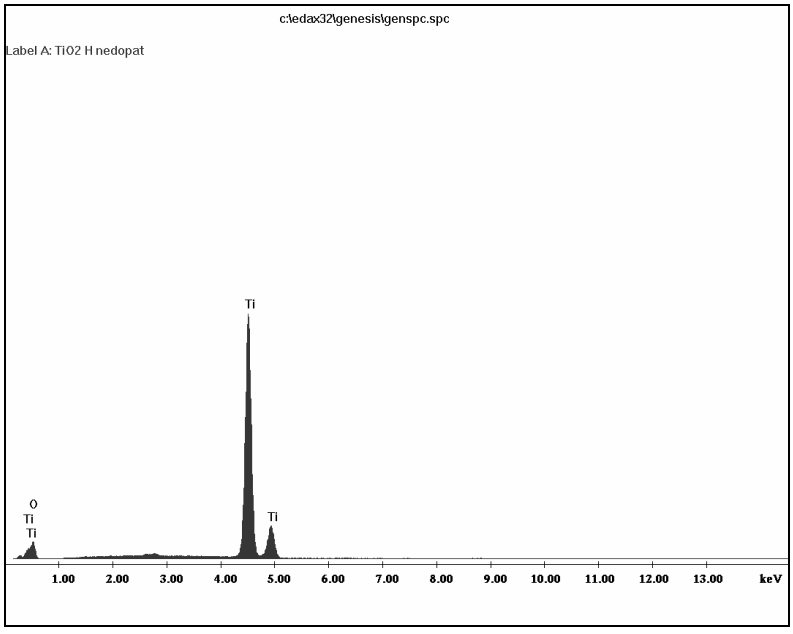

Fig. 6. EDX spectrum for elemental analysis of undoped TiO_2.

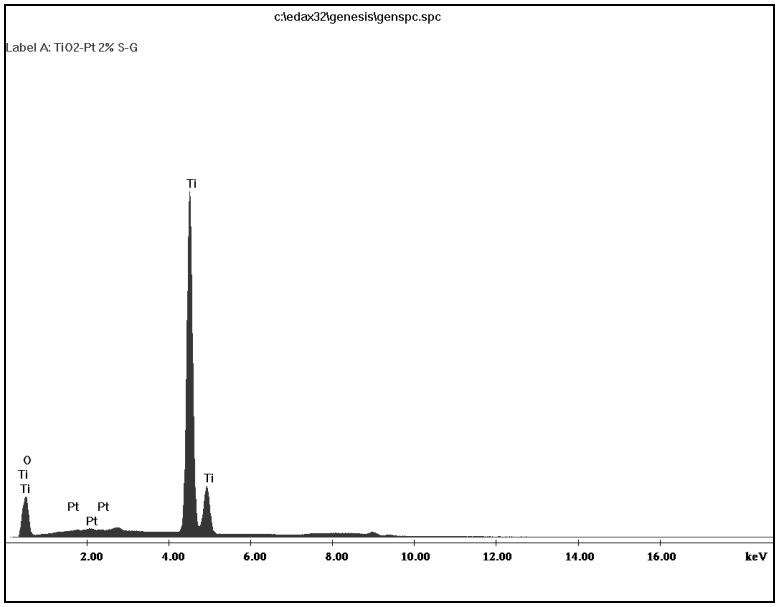

Fig. 7. EDX analysis for elemental analysis of TiO_2-Pt.

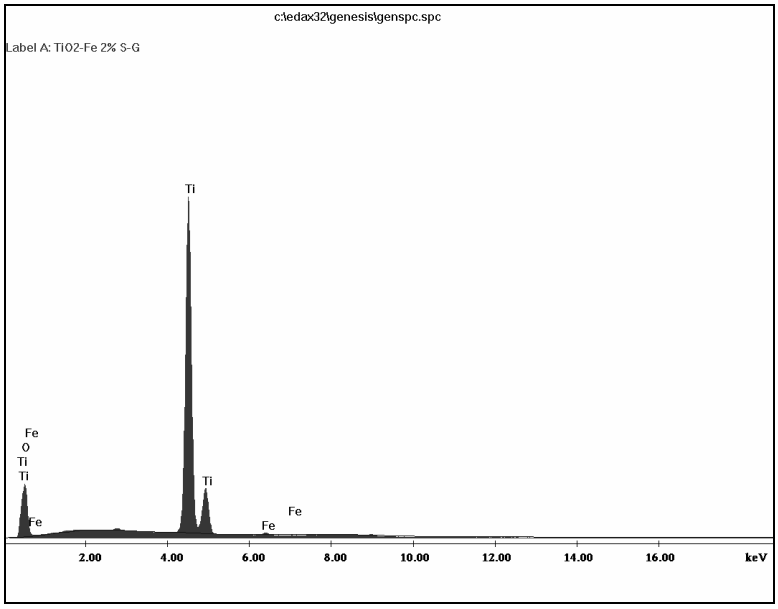

Fig. 8. EDX analysis for elemental analysis of TiO_2-Fe.

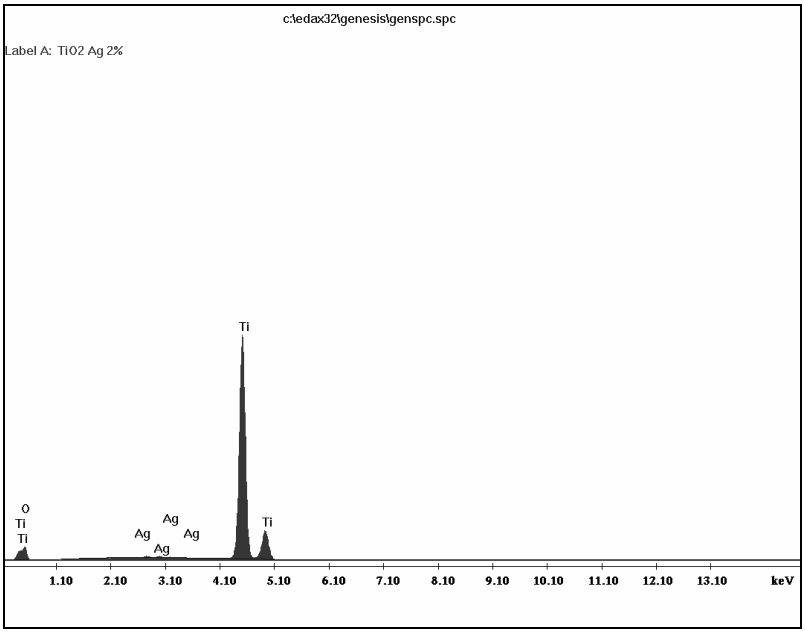

Fig. 9. EDX analysis for elemental analysis of TiO_2-Ag.

From the surface morphology (SEM) it can be observed that the TiO_2, as well as TiO_2-Pt, TiO_2-Ag and TiO_2-Fe nanosphere dimensions range between 10-20 nm, having a spherical shape, indifferent of the chelated metal (Figs. 2-5). EDAX analysis presents undoped TiO_2 nanoparticles, as well as the nanoparticles with Pt, Ag and Fe ions in titanium dioxide structure (Figs. 6-9).

3.2. *TiO_2 nanoparticles interaction with the eukaryote cell*

Normal liver ultrastructure The liver has a normal ultrastructure, similar to other reported data [13], [14]. The hepatocytes present one spherical nucleus (sometimes two), with a regulated outline and heterochromatine disposed in a small electrondense masses, usually under inner envelope (Fig. 10). In cytoplasm there are numerous mitochondria spherical or slightly elongated with cristae disposed transversally, rough endoplasmic reticulum well represented, numerous glycogen particles (Fig. 11), Golgi complex, smooth endoplasmic reticulum (SER) with a discrete presence, having a bigger concentration in the areas with glycogen, a/o. The lipid droplets are very rarely in cytoplasm, as small anelectrondense granules, especially at the vascular pole of the hepatocyte in the vicinity of Ito cell (Fig. 12).

The Kupffer cells are in a normal activity (Fig. 13), having accumulated a small amount of phagocytated material.

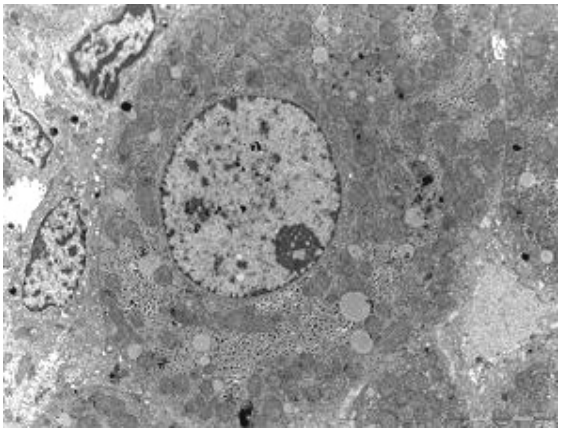

Fig. 10. Control. Hepatocyte with the normal ultrastructure.

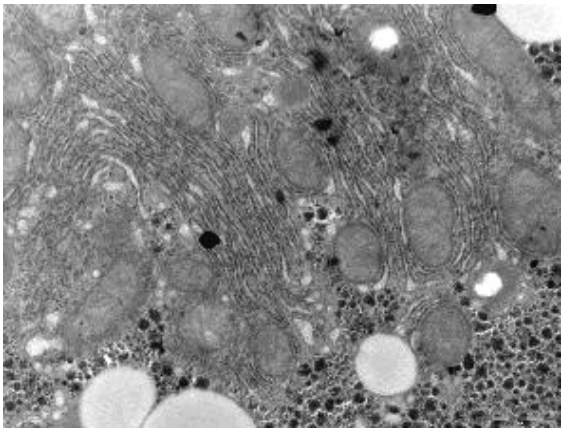

Fig. 11. Control. Cytoplasma with cellular organelles and glycogen.

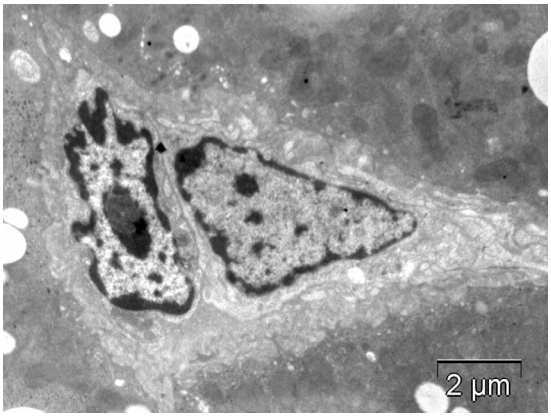

Fig. 12. Control. Vascular pole of hepatocytes and Ito cell.

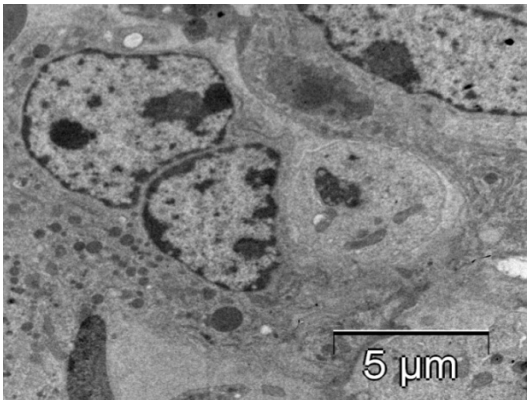

Fig. 13. Control. Kupffer cell in activity.

Undoped TiO_2 Nanoparticles Effect

The presence of undoped TiO_2 nanoparticles has a drastic affect under the metabolism and ultrastructure of the hepatocyte (Figs. 14-17). The nucleus, usually has 3-4 nucleoli, and an unregulated outline with invaginations, the heterochromatin having a parietal disposition, or spread as fine blocks in euchromatine (Fig. 14). The mitochondria are swelled, with matrix and crista rarefied, sometimes being in amitotic division (Fig. 15). The TiO_2 nanoparticles are accumulated in a big amount in the lipid droplets which became electrondense (Fig. 15). Their transit from hepatocyte is practically absent, because they are absent in the Ito cell (Fig. 17). The glycogen microparticles are absent in the cytoplasma of hepatocytes. The cell response at the stress factor, is represented through presence, in a great number, of the vesicles of the smooth endoplasmic reticulum (SER), for counteract of the TiO_2 negative effect (Fig. 16). Also, the Kupffer cell is in metabolic activity.

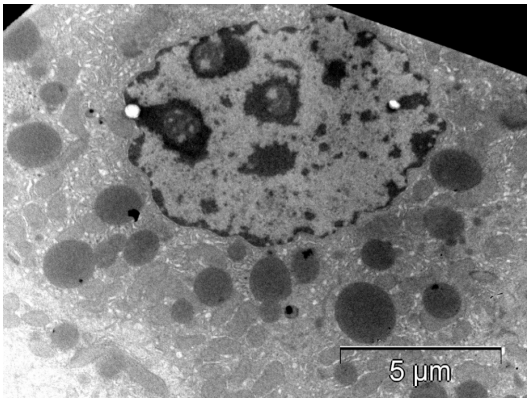

Fig. 14. TiO_2. Aterated nucleus and many SER vesicles.

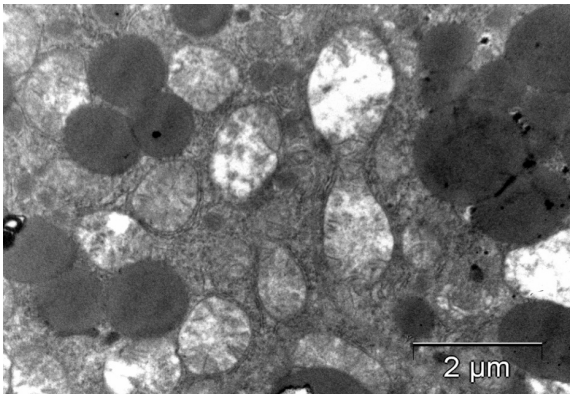

Fig. 15. TiO_2. Affected mitochondria, in amitotic division.

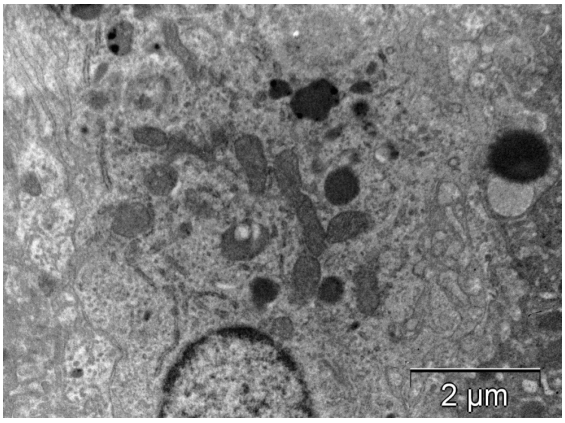

Fig. 16. TiO_2. The cell reacts to stress factor.

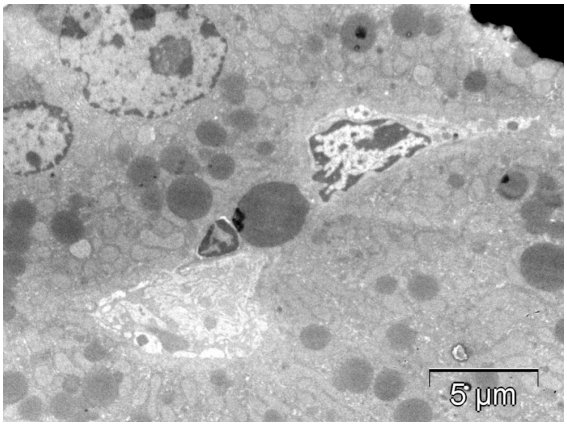

Fig. 17. TiO_2. Ito cell, without lipid droplets.

The TiO_2 – Ag nanoparticles effect

The TiO_2-Ag nanoparticles induce reversible modifications in hepatocytes. The nucleus, with 1-3 nucleoli, presents the heterochromatine with parietal disposition or as fine blocks in its inner (Fig. 18). As a result of the exogenous nanoparticles' presence, the lipid metabolism is altered, hepatocytes having a big amount of lipid droplets (Fig. 18). Lipid droplets contain a moderate amount of TiO_2-Ag nanoparticles (Fig. 18). In some mitochondria, the TiO_2-Ag nanoparticles are massively accumulated (Fig. 19). As a response to this stress factor, the vesicles of smooth endoplasmic reticulum is well represented in proximity (Fig. 19) Also, Golgi complex is present. Practically, the glycogen microparticles are absent from hepatocytes.

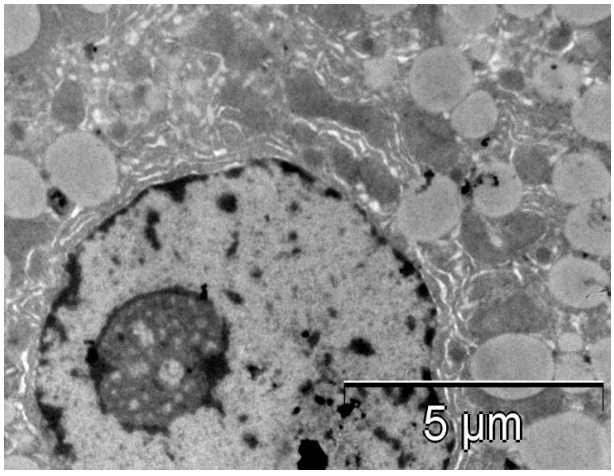

Fig. 18. TiO_2-Ag. Reversible alterations of the hepatocyte ultrastrucure.

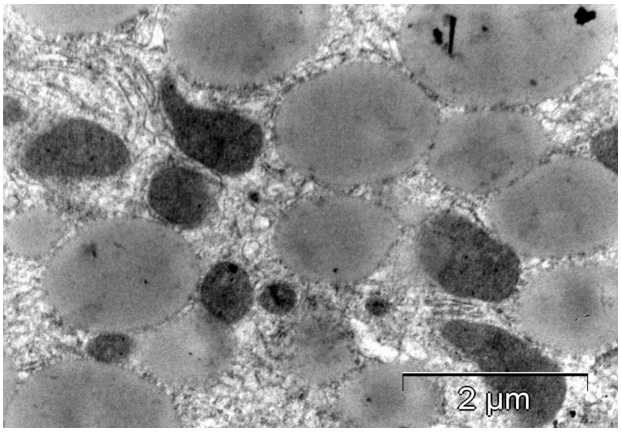

Fig. 19. TiO_2-Ag. Lipid droplets and mitochondria with TiO_2-Ag nanoparticles incorporated.

Other reported researches [13] revealed enhanced photocatalitic reactivity, in comparison with undoped TiO_2 nanoparticles, and for the doped TiO_2 nanoparticles severe alterations in hepatocyte were not induced, as in the case of undoped TiO_2 nanoparticles.

The TiO_2 – Pt nanoparticles effect

The TiO_2-Pt nanoparticles induced minor and reversible ultrastructural modifications. Some nuclei have an undulated outline (Fig. 20), the profiles of rough endoplasmic reticulum (RER) are slightly dilated and the vesicles of the smooth endoplasmic reticulum are slightly proliferated (Fig. 21).

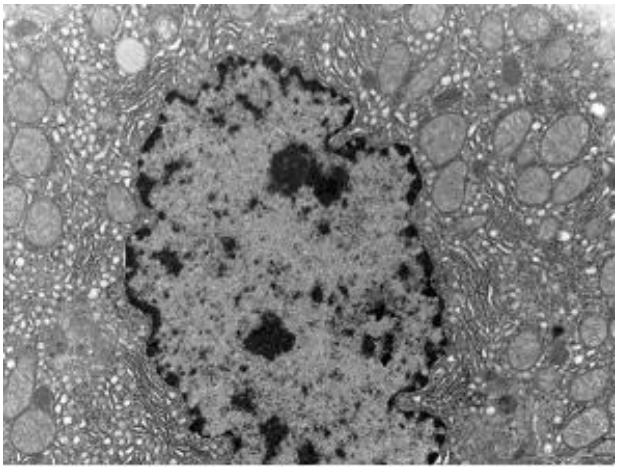

Fig. 20. TiO_2-Pt. Nucleus with unregulated outline.

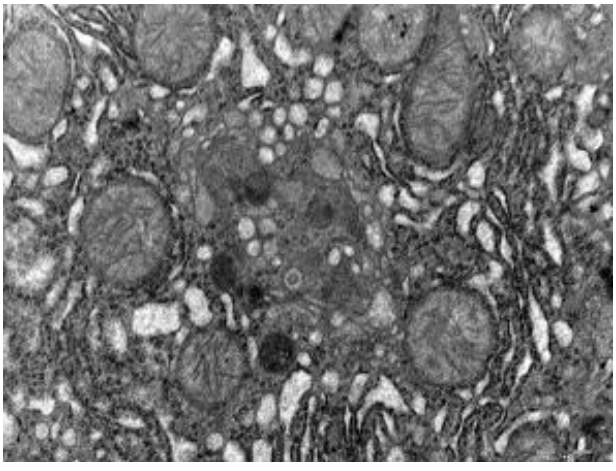

Fig. 21. TiO_2-Pt. Cellular organelles with slightly modifications.

Also, the hepatocytes do not present collagen fibers and cellular destructions. The mitochondria present a normal ultrastructure (Fig. 21). The small TiO_2-Pt nanoparticles penetrate in hepatocytes under shape of electrondense masses, being in strong relation with rough endoplasmic reticulum profiles, smooth endoplasmic reticulum vesicles and especially with mitochondria (Figs. 22, 23). There are mitochondria with a different amount of TiO_2-Pt nanoparticles, respectively much (Fig. 22), or little (Fig. 23). There were not evidenced any ultrastructural alterations of the cell organelles, induced by TiO_2-Pt. Also, in some Kupffer cells, there are many electrondense corpuscles, which probably contain TiO_2-Pt aggregates (Fig. 24).

In the hepatocyte of a mouse, the TiO_2-Pt nanoparticles, manifest a high reactivity, in comparison with TiO_2-Ag nanoparticles. In the first case, the TiO_2-Pt nanoparticles penetrate in mitochondria and endoplasmic reticulum, while the TiO2-Ag nanoparticles are present in a moderate amount in the lipid droplets and massive accumulated in some mitochondria. The analysis of the biological effects of the TiO_2 doped with different metals (silver, golden, copper or platinum), reveals that the TiO_2-Pt and TiO_2-Au chelated nanoparticles, manifest an enhanced effects in comparison with TiO_2-Ag or TiO_2-Cu chelate nanoparticles [9]. Also, the chelated nanoparticles with some metals induced better biological effects in comparison with the unchelated TiO_2 [9].

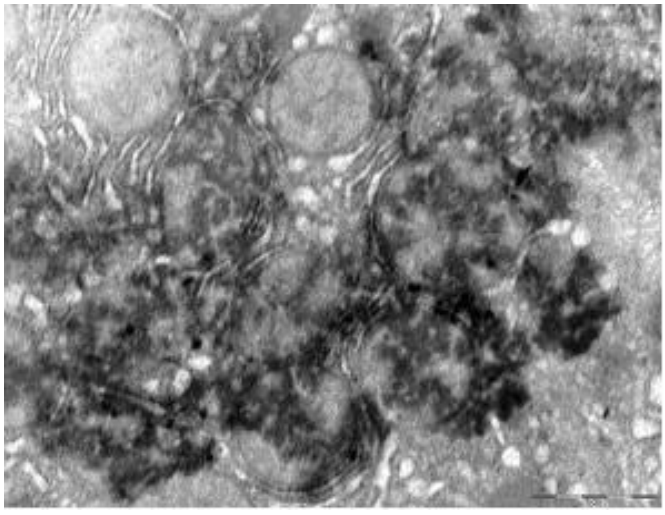

Fig. 22. TiO_2-Pt. Nanoparticles in strong relation with mitochondria and RER.

Some researches, performed with TiO_2-Pt and TiO_2-Au nanocomposites, point out that they also manifested enhanced photocatalitic reactivity [14]. Also, in another experiment was established that, the chelated nanoparticles with some metals, induced better biological effects in comparison with the unchelated TiO_2

[9]. Similarly, when comparing the biological effects of the TiO_2 doped with different metals (silver, golden, copper or platinum), the TiO_2-Pt and TiO_2-Au chelated nanoparticles manifest enhanced effects in comparison with TiO_2-Ag or TiO_2-Cu chelated nanoparticles [9].

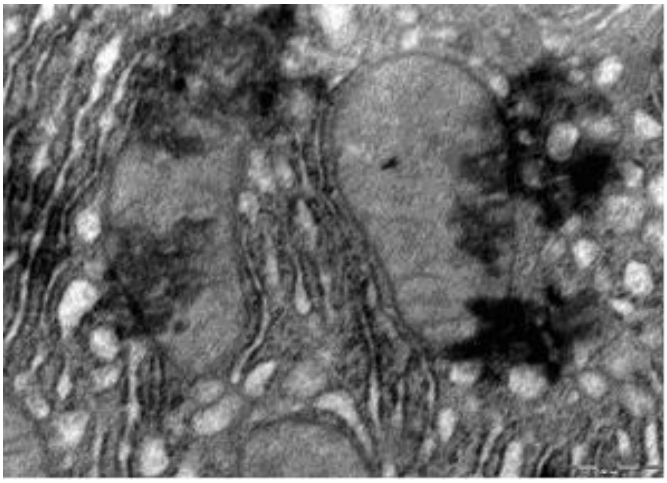

Fig. 23. TiO_2-Pt. Nanoparticles in close relations with mitochondria.

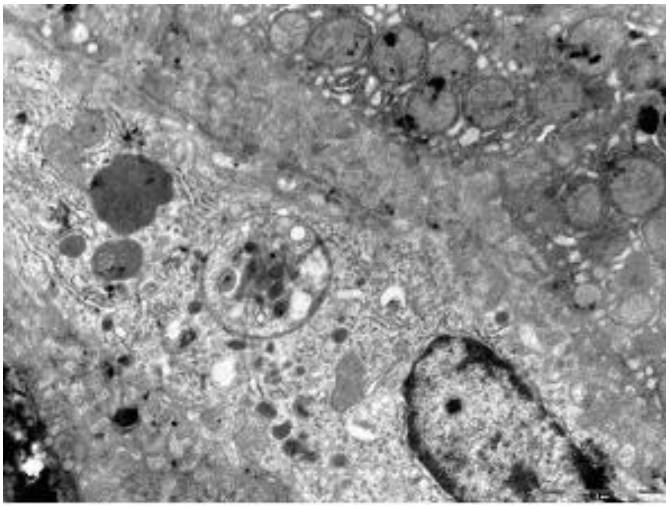

Fig. 24. TiO_2-Pt. Kupffer cell with electrondense granules.

TiO_2-Fe Nanoparticles Effect

The TiO_2-Fe nanoparticles induce complex modifications at the hepatocyte level. The nuclei present deep incisures, having an unregulated outline (Fig. 25),

the rough endoplasmic reticulum is poor represented, but instead the vesicles of smooth endoplasmic reticulum present a proliferation, as response to this stress factor (Fig. 26). Also, the mitochondria present the matrix and the mitochondrial crista rarefied, with slightly tendency to vacuolization (Fig. 26). The TiO_2-Fe nanoparticles are present in some hepatocytes, in relation with cellular organelles and nucleus (Figs. 27, 28). The Kupffer cells manifest an increased activity, having in their cytoplasm numerous electrondense granules represented by TiO_2-Fe and cell remnants (Fig. 29).

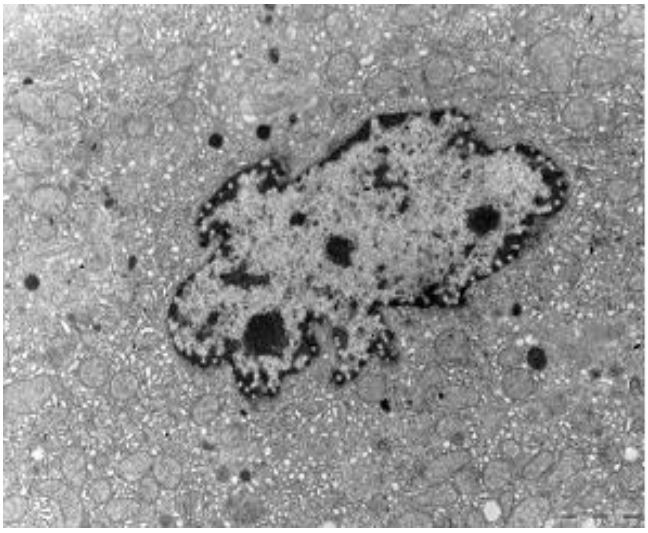

Fig. 25. Nucleus has deep incisures and heterochromatine blocks.

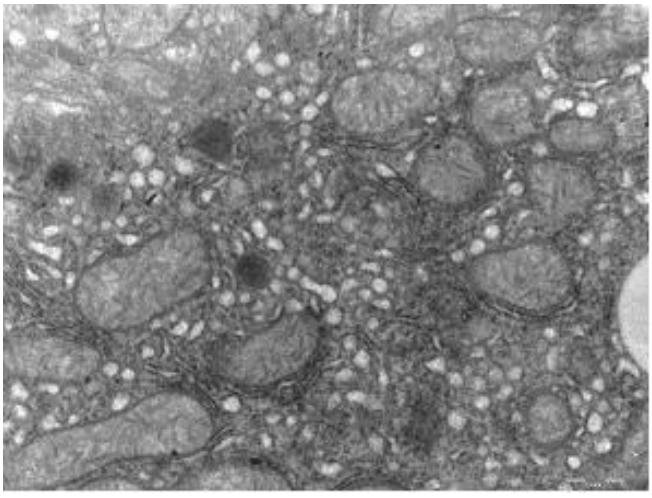

Fig. 26. Cytoplasm with vesicular SER and mitochondria.

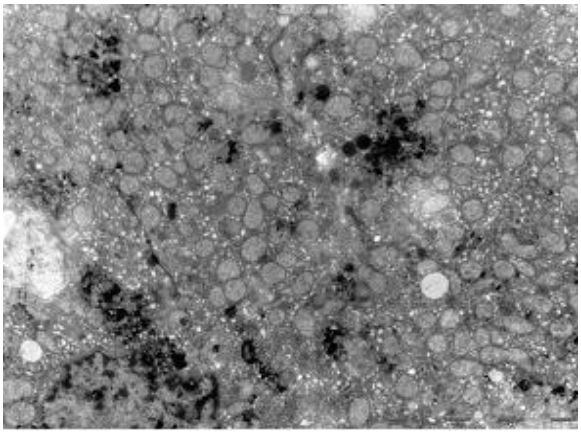

Fig. 27. TiO_2-Fe nanoparticles in hepatocytes.

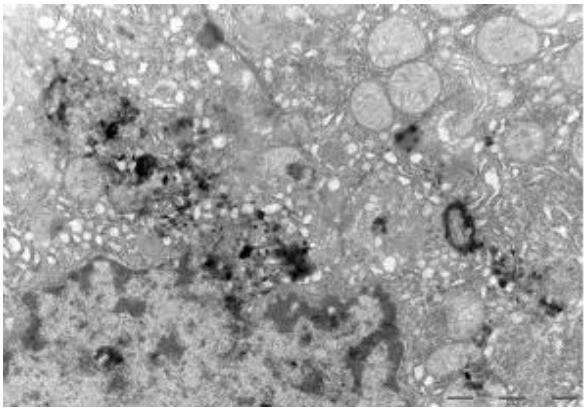

Fig. 28. TiO_2 nanoparticles in relation with nucleus and cellular organelles.

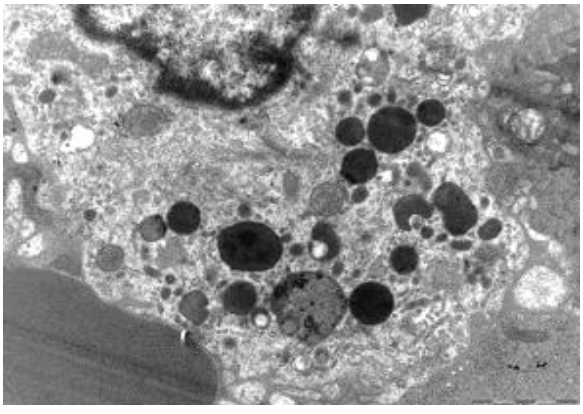

Fig. 29. Kupffer cell with intense activity of phagocytated electrondense bodies.

4. Conclusions

In this experiment was analyzed the TiO_2 nanoparticles effect (*anatase* crystallization form, size of about 10-20 nm), doped or not with a metal, at the liver level in *Mus musculus*, and their interaction with the cellular organelles. The titanium dioxide effect was dependent on the chelated metal. Also, depending on the chelated metal, the TiO_2 nanoparticles penetrate or not the hepatocyte, and they are in different relations with cellular organelles or cellular inclusions (lipid dropletss)

The TiO_2 nanoparticles induced a drastic effect at the hepatocyte level, affecting the nucleus and some ultrastructured organelles (mitochondria especially), as well as the lipid metabolism. The TiO_2 nanoparticles are accumulated in the lipid droplets, as well as in some mitochondria.

The TiO_2-Ag nanoparticles, altered the lipid metabolism, and induced slightly, reversible modifications at the ultrastructural level (dilatation of the rough endoplasmic reticulum, the nucleus outline). In hepatocyte, the TiO_2-Ag nanoparticles, are moderate accumulated in lipid droplets, and massive accumulated in mitochondria.

The TiO_2-Pt nanoparticles, induced also slightly, reversible modifications. They penetrate in some hepatocytes, being in strong relation with rough and smooth endoplasmic reticulum, and with mitochondria. Their excess is accumulated and degraded in the Kupffer cell.

The TiO_2-Fe nanoparticles induced severe alteration of the hepatocytes ultrastructure. They penetrated some hepatocytes, being localized at the rough endoplasmic reticulum and mitochondria level. Their excess was accumulated in the Kupffer cell, as some electrondense bodies.

Acknowledgements. These researches were sponsored by the IMUNONANOMAT Grant 70/2007, financed by the National Council for Programs Management, CNMP-Bucharest (Romania). The authors wish to thank Mrs. Cornelia Rațiu and Paula Sfârloagă (I.N.C.-D.E.M.C.-Timişoara) for their contribution to the preparation of TiO_2 nanoparticles.

References

[1] BAAN R.A., *Carcinogenic hazards from inhalated carbon black, titanium dioxide, and talc not containing asbestos or asbestiform: recent evaluations by an IARC monographs working group*, Inhal. Toxicol., **19** (suppl. 1), pp. 213–228, 2007.

[2] COZZOLI P.D., COMPARELLI R., *Photocatalytic synthetized of silver nanoparticles stabilized by TiO_2 nanorods: a semiconductor/metal nanocomposite in homogenous nonpolar solution*, J. Am. Chemical Soc., **126**(12), pp. 3868–3879, 2004.

[3] LI X.Y., GILMOUR P.S., DONALDSON K., MacNEE W., *Free radical activity and proinflammatory effects of particulate air pollution (PM10) in vivo and in vitro*, Thorax, **51**, pp. 1216–1222, 1996.

[4] CHOI W., LEE J., KIM S., HWANG S., LEE M.C., LEE T.K., *Nano Pt particles on TiO_2 and their photocatalitic reactivity*, J. Industrial and Engineering Chemistry, **9**, pp. 96–101, 2003.

[5] SERPONE N., SALINARIO A., EMELINE A., *Deleterious effect of sunscreen titanium dioxide nanoparticles on DNA: efforts to limits DNA damage by particle surface modification*, Proc. SPIE, **4258**, pp. 86–98, 2001.

[6] UCHINO T., TOKUNAGA H., ANDO M., UTSUMI H., *Quantitative determination of OH radical generation and its cytotoxicity induced by TiO_2-UVA treatment*, Toxicol in Vitro, **16**, pp. 629–0635, 2002.

[7] PARK C., LEE J., KIM H., PARK H., KIMK C., *Highlights from recent literature*, Gold Bulletin, **42**(2), pp. 159–167, 2009.

[8] ZHU R.R., WANG S.L., CHAO J., SHI D.L., ZHANG R., SUN X.Y., YAO S.D., *Bio-effects of nano-TiO_2 on DNA and cellular ultrastructure with different polymorph and size*, Mater. Sci. Engineer. C., **29**, pp. 691–696, 2009.

[9] YONEZAWA T., KAWASAKI H., TARUI A., WATANABE T., ARAKAWA R., SHIMADA T., MAFUNÉ F., *Detailed investigations on the possibility of nanoparticles of various metal elements for surface-assisted laser desorption/ionization mass spectrometry*, Analytical Sciences, **25**, pp. 339–346, 2009.

[10] WOLOSCHAK G., PAUNESCU T., THURN K., MASSERE J., LAU B., *Intracellular localization of titanium dioxide-DNA nanocomposites*, Cornel University, ERL Workshop, 2006.

[11] CORNEANU C.G., CRĂCIUN C., CORNEANU M., LAZĂU C., GROZESCU I., SILOSI I., ROGOZ S., PRODAN G.C., BARDU-TUDORAN L., MIHALI C., ŞTEFĂNESCU I., CORNEANU L.M., *The TiO_2-Pt nanoparticles implication in the immune response and their interaction with the animal cell*, In: *Progress in Nanoscience and Nanotechnologies*, **11** (Eds. I. Kleps, A. Catrinel Ion, D. Dascălu), pp. 183–192, Edit. Academiei Române, Bucureşti, 2007.

[12] CORNEANU G.C., CORNEANU M., CRĂCIUN C., LAZĂU C., GROZESCU I., *The TiO_2-Pt nanoparticles effect on the ultrastructural features of the Allium sativum sagittatm callus*, In: New *Applications of Micro- and Nanotechnologies*, **14** (Eds. M. Zaharescu, L. Giurgiu, D. Dascălu), pp. 140–148, Edit. Academiei Române, Bucureşti, 2009.

[13] YU J.G., XIONG J.F., *Fabrication and characterization of Ag-TiO2 multiple nsanocomposite this films with enhanced photocatalytic activity*, Environmental, **60**(3-4), pp. 211–221, 2005.

[14] YU J.G., YUE L., *Hydrothermal preparation and photocatalytic activity of mesoporous Au-TiO2 nanocomposite microspheres*, J. Colloidal and Interface Science, **334**(1), pp. 58–64, 2009.

Ge Nanodots Embedded in a Silica Matrix

I. STAVARACHE, A.-M. LEPADATU, M.L. CIUREA

National Institute of Materials Physics, 105 bis Atomistilor Street,
Magurele 077125, Romania

Tel: +40-21-3690185; Fax: +40-21-3690177
E-mail: ciurea@infim.ro

Abstract. The properties of GeSiO films consisting of Ge nanodots embedded in SiO_2 matrix, prepared by sol-gel and magnetron sputtering methods, followed by an adequate thermal annealing, are studied and discussed in this paper. Structural investigations were performed by means of transmission electron microscopy and X-ray photoelectron spectroscopy. In the sol-gel films one finds amorphous Ge nanodots distributed in the amorphous matrix, while in the sputtered ones tetragonal Ge nanodots are evidenced. The electrical and photoconductive properties of sol-gel films treated by rapid thermal annealing technique were also studied. For this, measurements of current-voltage and conductance-temperature curves, spectral and bias dependences of the photocurrent were carried out. These films have weak rectifying behaviour and show a very high photoconductivity.

Keywords: Nanodots; Sol-gel; Magnetron sputtering; TEM; XPS; Photoconductive nanostructures; Electrical properties; Photoelectrical properties.

1. Introduction

Much research in recent years has focused on films consisting of Ge nanodots embedded in SiO_2 matrix. Many studies on synthesis methods [1−2], structural aspects [3−6] and optical properties [3−4, 7−8] of these structures were reported. The memory effect related to charge storage [6−7, 9−10], electrical [9−13] and photoconductive [14−15] properties were also investigated. These films can be prepared using different methods: sol-gel [1, 3, 5−6, 16], molecular beam epitaxy [9−10, 14, 17−18], magnetron sputtering [2, 4, 5, 7−8, 12, 19], plasma-enhanced chemical vapor deposition [20], atom beam co-sputtering [21], and Ge implantation [22] and/or combined with neutron irradiation [23]. Different annealing techniques are used for Ge nanodots formation such as furnace annealing [6], rapid thermal annealing (RTA) [6, 16], or microwave annealing [24]. Ge nanodots can be also

embedded in other oxide matrixes, *e.g.* HfO_2 [25−26], Al_2O_3 [27] or TiO_2 [28]. The films of Ge nanocrystals embedded in SiO_2 present a wide range of possible applications, in MOS based gamma radiation sensors [29], heterojunction devices with photovoltaic effects for solar cells [13], MOS-structure photodiodes for optoelectronics [30], and nonvolatile memories [6, 31].

The magnetron sputtering films containing Ge nanodots embedded in silicon dioxide are obtained in a wide range of different deposition and annealing conditions. The deposition conditions depend on the type of the used target and on the ambient atmosphere. One can use a target of SiO_2 covered with Ge pieces [5, 12−13, 19], two targets of SiO_2 and Ge respectively [4, 8], a Si target covered with Ge chips using a reactive co-sputtering [7]. Argon is commonly used as a sputtering gas [8, 12] or a mixture of different gases (Ar, O_2) is used in a reactive sputtering [7]. Other deposition parameters are also important for the structure, microstructure and properties of the films (the RF power, the substrate temperature [7, 13].

Cosentino et al [8] synthesized Ge quantum dots (2–10 nm) embedded in silica by magnetron co-sputtering of SiO_2 and Ge, in Ar atmosphere, followed by annealing at 600–800°C in N_2. Zhang et al [13] obtained thin films composed of quasi-spherical Ge nanocrystals (3.8–8 nm), with diamond structure, distributed in SiO_2, by magnetron co-sputtering from a fused quartz plate partially covered with Ge chips (undoped or doped with Ga or Sb). During the deposition, the substrates were heated at 380^{o}C and, then, the obtained films were annealed by RTA method in N_2 at 650–800°C. Ray et al [7] prepared nearly spherical Ge nanocrystals (4–7 nm) embedded in SiO_2 matrix by reactive RF magnetron co-sputtering from a n-type Si wafer target covered with Ge pieces, using a mixture of oxygen and argon. Then, the deposited films were annealed in N_2 for 1h at 600–900°C. Kolobov et al [4] prepared films of Ge nanocrystals (5–20 nm) embedded in SiO_2 also by co-sputtering of Ge and SiO_2, with a subsequent annealing at 800^{o}C in Ar. The films contain 25, 40 or 60 mol% of Ge in the SiO_2 matrix. The authors found that the size of nanocrystals strongly depends on the type of the used substrate, Si (100). Ge nanocrystals with two shapes were observed, ones are spherical with multiple twinning defects and the other ones are faceted single crystals. They have also evidenced a gradient of Ge nanocrystals concentration with the depth of the film. At the film's surface, there are no Ge nanocrystals, and at the bottom part, i.e. at the interface with the Si substrate, a higher density of Ge nanocrystals was evidenced. The authors observed the presence of single faceted nanocrystals in the layer, whereas at the interface with the Si substrate, spherical nanocrystals with multiple twinning defects are present. The films deposited on quartz substrates have Ge nanocrystals with smaller sizes that form a continuous network. Shen et al [19] obtained Ge nanocrystals (2.1–27.2 nm) with diamond structure by co-sputtering of SiO_2 and Ge, followed by an annealing in N_2 at different temperatures (300–1100^{o}C). They remarked the out-diffusion of Ge atoms in the samples

annealed at 1100°C. The same system was prepared by Fujii *et al* [12] using a thermal annealing at 800°C in vacuum, resulting Ge nanocrystals with sizes of 3.8–8.9 nm.

Cosentino et al studied the influence of surfaces states on the photon absorption in films formed of Ge nanoclusters embedded in silica [8]. The authors found an optical bandgap of 1.6 eV, independent on the quantum dot size (for size in 2−10 nm range) and the structural phase, amorphous or crystalline (diamond) of Ge nanoclusters. They showed how the absorption is influenced by surface states. The authors also observed the Ge out-diffusion through the surface.

Zhang et al studied the electrical properties of undoped and doped thin films of Ge nanocrystals embedded in SiO_2 [13]. The undoped films treated by RTA exhibit a p-type conductivity (σ), with about three orders of magnitude higher than those as-deposited. They measured current – voltage (*I–V*) characteristics of films treated in 650–800°C range. The *I–V* curves are linear except the one with RTA at 800°C which presents a small non-linearity at low voltages. This behaviour was attributed to the acceptor-like surface states which produce the holes accumulation in nanocrystals. They evidenced a thermally activated process, given by the $\ln \sigma \sim T^{-1}$ law, explained by a hopping process from one nanocrystal to its nearest neighbour one. In the (Ga or Sb) doped layers, similar electrical behaviour was found, explained by the major influence of surface states which determine a dominant hole conduction, too. They evidenced a clear photovoltaic effect given by the heterojunction between p-type SiO_2 films with Ge nanocrystals and n-type silicon wafer.

Ray *et al* investigated a trilayer MOS capacitor [7] that consists of a tunnel oxide thermally grown on a p-Si substrate, an intermediate layer composed of Ge nanocrystals with 20–30 nm diameters, and a cap gate oxide. These structures annealed by RTA exhibit a strong and broad photoluminescence (PL) at room temperature (RT), attributed to quantum confinement of carriers in Ge nanocrystals. If the annealing time is increased, the films present a narrower PL spectrum.

Electroluminescence (EL) was investigated by Shen et al [19] in a metal-insulator-semiconductor (MIS) structure. The films treated by RTA at different temperatures in the range of 300–1100°C present a broad maximum centred at 590 nm. For the films annealed at 600°C, the EL intensity (590 nm) is much higher. Also, the EL intensity rapidly decreases with the nanocrystal size increase. The authors explained the EL curves by a radiative recombination in the small Ge nanocrystals.

Fujii *et al* [11−12] find variable range hopping (VRH) conduction mechanism, $\ln \sigma \propto T^{-1/4}$, through localized states associated with Ge clusters, in the as-deposited films of Ge clusters embedded in SiO_2. In the annealed films, containing Ge nanocrystals, the $\ln \sigma \propto T^{-1/2}$ dependence was evidenced [12].

They explained the electrical conduction as due to the tunneling of carriers between neighboring nanocrystals.

Other method to prepare films formed of Ge nanodots embedded in SiO_2 matrix is the sol-gel method [1, 3, 5−6, 15−16]. Different precursors for Ge and Si were used, germanium tetraethoxide $Ge(OC_2H_5)_4$ [6], 3-trichlorogermanium propanoic acid Cl_3−Ge−C_2H_4−COOH [3] or $GeCl_4$ 1, 5, 15] and/or silicon tetraethoxide TEOS $Si(OC_2H_5)_4$ [1, 3, 5−6, 15−16] or dimethyldiethoxysilane $(CH_3)_2Si(OC_2H_5)_2$ [6] respectively. The values of the Ge/Si molar ratio in solution are relatively small, in the interval of 3 – 15 % [1, 3, 5, 15−16]. The SiO_2-GeO_2 gel films are deposited either by means of dip coating method [6] or spin coating [5, 15−16] on different substrates, commonly used being Si (100) wafers [5−6, 16]. After the deposition, the films are annealed under different conditions of temperature and gas atmosphere: 400 – 800^{o}C, in a flowing mixed gas of H_2 and N_2 [1, 3, 5−6] or 800^{o}C and 950^{o}C in Ar and N_2 atmosphere [15−16].

Investigations of structure and microstructure and optical studies were performed on the sol-gel films consisting of Ge nanodots embedded in SiO_2. The crystallinity of Ge nanodots was evidenced by high resolution transmission electron microscopy (HRTEM) and selected area electron diffraction (SAED). Thus, Ge nanodots with diamond structure [1, 3], amorphous Ge nanodots distributed in the SiO_2 amorphous matrix [16] and Ge nanodots with tetragonal phase [5, 15] were reported in literature. Knebel et al [6] observed two shapes of Ge nanocrystals, ones being globular and the others strongly faceted with tetrahedral form. However, films with small spherical Ge nanodots (up to 10 nm) dispersed in the amorphous matrix are usually obtained [1, 5, 15−16].

These films exhibit PL: Nogami *et al* reported visible PL [1] at liquid nitrogen temperature and Yang *et al* [3] observed a strong visible PL at RT. Surprisingly, the films with Ge nanocrystals having a diamond structure are not photoluminescent.

In this paper, we present the properties of GeSiO films consisting of Ge nanodots embedded in amorphous SiO_2 matrix, prepared by sol-gel and magnetron sputtering methods. Structural investigations were performed by means of transmission electron microscopy (TEM) and X-ray photoelectron spectroscopy (XPS) methods. In the sol-gel films we obtained amorphous Ge nanodots distributed in the amorphous matrix, while in the sputtered ones appeared both tetragonal Ge nanodots and a network of Ge-rich amorphous nanostructures. The electrical and photoconductive properties of sol-gel GeSiO films treated by RTA technique were also studied. To do that, measurements of $I - V$ and conductance-temperature ($G - T$) curves, spectral ($I_f - \lambda$) and bias dependences ($I_f - V$) of the photocurrent were carried out. These films have weak rectifying behaviour and show a very high photoconductivity.

2. Experimental: Preparation and Measurements

In order to prepare GeSiO thin films, two conventional methods, *i.e*. the sol–gel [15−16, 32] and the radio frequency magnetron sputtering methods [5, 32] were used. The film deposition was followed by an annealing process in order to allow Ge segregation as well as Ge nanodots formation.

The sol-gel method for the preparation of GeSiO layers, $GeCl_4$ and tetraethyl orthosilicate $Si(OC_2H_5)_4$ (TEOS) as precursors**,** dissolved in ethanol were used. The two sols of GeO_2 and SiO_2 were mixed, for different values of the Ge/Si molar ratio, in the 3 – 12 % interval, depending on the desired Ge content in the film. The final mixture was stirred at RT, and then, it was deposited on silicon substrates by using the spin coating method. After this stage, the films were dried and heated in air at 400 – 600^{o}C in order to remove the organic solvent. The resulting GeO_2-SiO_2 films were compact and homogeneous. Then, some films were annealed in N_2 atmosphere at 800 – 950^{o}C, using a RTA for 5 – 15 min. An alternative annealing was made in N_2 at 1000^{o}C for 7 h in a heater, or in H_2 (at 2 atm and 500^{o}C). The thickness of the GeSiO layers ranged between 200 and 300 nm. Al electrodes were deposited in a planar geometry on RTA annealed samples, for electrical and photoconductivity measurements.

The sputtered GeSiO films were prepared by using a target consisting of a SiO_2 disk with germanium pieces fixed on it. The Ge area covering the sputtering active zone was chosen in order to obtain a desired mass concentration of Ge/SiO_2 of 40 %. The deposition was performed in high purity argon atmosphere (99.99 %). An argon pressure of 0.3 Pa was maintained during the deposition. A constant power of 150 W RF was used at a generator frequency of 1.78 MHz. These films were deposited on silica substrates, placed at 35 mm above the target. Again, similarly with the sol-gel case, the films were annealed in a H_2 atmosphere (at 2 atm and 500^{o}C). The sputtered GeSiO films are much thicker (about 3 μm) than the sol-gel ones.

The microstructure of the GeSiO layers with different Ge concentrations was investigated by means of TEM and HRTEM. Two different methods were used for the preparation of the TEM sol-gel specimens: some of them were prepared by a cross section method, and those used for plan view investigations by ion milling using a Gatan PIPS 691 apparatus. In the case of magnetron sputtered GeSiO layers, being much thicker, the TEM specimens were prepared by extraction of small micro-fragments from the film. For this, the film surface was scratched with a thin diamond tip and the fragments were collected on holey carbon grids [33]. These fragments present edges with very small angles, so that, the TEM observation guarantees large transparent area useful for HRTEM images. The TEM images and SAED patterns were obtained using a Jeol TEM 200CX instrument, while for the HRTEM images was used a Topcon 002B electron microscope,

working at 200 kV. Cross-section TEM (XTEM) images were also obtained on sputtered samples.

The XPS measurements were performed in a complex Specs GmbH surface science setup that includes a photoemission chamber. The GeSiO samples were analyzed by using both an unmonochromatized Al K_α radiation (1486.61 eV) and a monochromatized Ag L_α radiation (2984.3 eV).

Electrical and photoconductivity investigations were performed on sol-gel samples, annealed by RTA, only. The setup used for these measurements contains a Janis CCS-450 cryostat (10 – 500 K), Keithley 6517A electrometer, Stanford SR 830 double lock-in amplifier, Newport monochromator, Newport light source 1000 W (Xe) (UV-VIS-NIR), LakeShore 331 temperature controller and Stanford SR 540 chopper. All measurements were performed on a computer-assisted set-up using a LabVIEW 8.5.1 development environment.

3. Results and Discussion TEM Investigations

The cross section TEM images showed that the GeSiO sol-gel layers are formed of amorphous nanodots with diameters in the range of 2 – 10 nm, uniformly distributed in an amorphous SiO_2 matrix, see Fig. 1 (Reprinted from Digest Journal of Nanomaterials and Biostructures **6** (1), 67-73 (2011), "Study of Ge nanoparticles embedded in an amorphous SiO_2 matrix with photoconductive properties", A. M. Lepadatu, I. Stavarache, T. F. Stoica, M. L. Ciurea, Figure 1, Copyright 2011, with permission from © INCDFM).

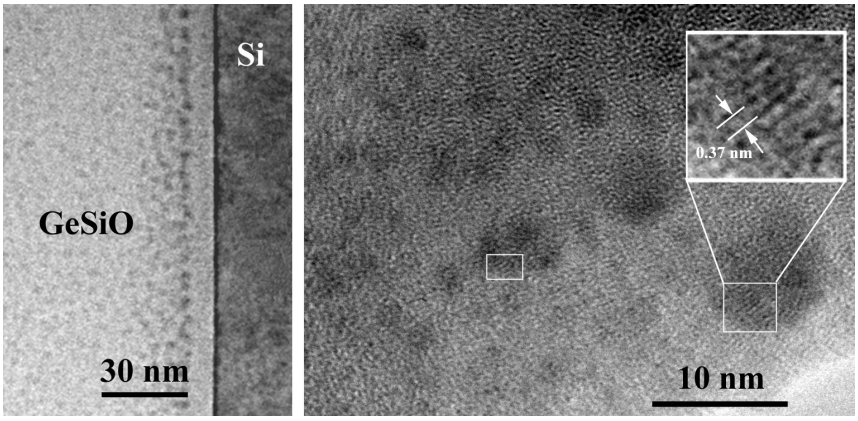

Fig. 1. XTEM image of a GeSiO (3 % Ge) sol-gel film annealed by RTA in N_2. Morphology of the interface with the Si substrate (left); some nanodots have small areas with lattice fringes like contrast, enlarged in the square frame (right) [15].

The interface between the nanodots and the SiO_2 matrix is not well defined, which is expected in the case of amorphous films. Thus, one can infer that the nanodots are Ge rich regions because the TEM contrast is dependent on the local

density and on the *Z* value of the atomic species. The density and size of nanodots are practically constant in the film thickness, except for the region near the interface with the silicon substrate (see Fig. 1 left). In this bottom region of the film, a SiO_2 band without nanodots, with a thickness of approximately 10 nm, is clearly visible. In its vicinity one finds Ge nanodots with larger sizes and density in comparison with the rest of the film.

One interesting feature is the presence of some nanodots which have small areas with lattice fringes like contrast (see Fig. 1 right). The periodicity of the lattice fringes is 0.36 ± 0.02 nm, that corresponds very well to the (111) lattice interfringe of tetragonal germanium phase. The most of the nanodots are amorphous, as the SAED pattern confirmed.

Another characteristic of the sol-gel films is the presence of coalescence starting-points (Fig. 2). No structural difference is observed between the samples annealed in N_2 and H_2. The main difference between various GeSiO sol-gel films is related to the variation of the nanodot density. The nanodot sizes slightly vary: for example if the Ge concentration grows from 3 % to 12 %, the average size of the nanodots increases from 3.8 to only 4.3 nm. The interfaces between all GeSiO sol-gel films and the Si substrate look similar. The SiO_2 clear band formed at the bottom of the film was attributed to the oxidation of the silicon substrate during the annealing process. In our opinion, this band is formed by nucleating of Ge rich nanodots that there are at the original interface and the increase of these nanodots by collecting of Ge species, so that no Ge diffusion takes place during the growing of SiO_2 band.

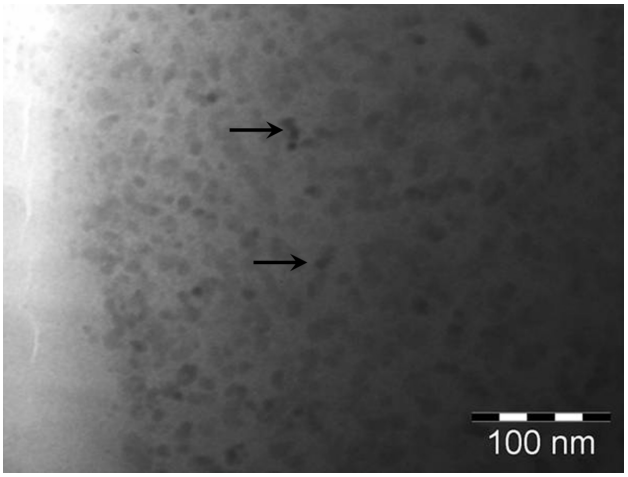

Fig. 2. Plan view TEM image of a sol-gel layer (12 % Ge) annealed in H_2. Some of the nanodots are connected (arrows).

In the case of the magnetron sputtered films, a more complex structure is evidenced. The concentration of Ge is of 40 %, a much larger value than that

obtained in the sol-gel layers. The morphology of these films is different of that of the sol-gel ones: thus, there are big Ge rich nanodots (20–50 nm) embedded in the amorphous SiO_2 matrix besides the smaller ones (5–15 nm) that are homogeneously distributed, as one can see in Fig. 3. The average size of 20 nm is evidenced. The low magnification XTEM image, presented in Fig. 3, shows the morphology of the layer in the middle of the GeSiO sputtered sample.

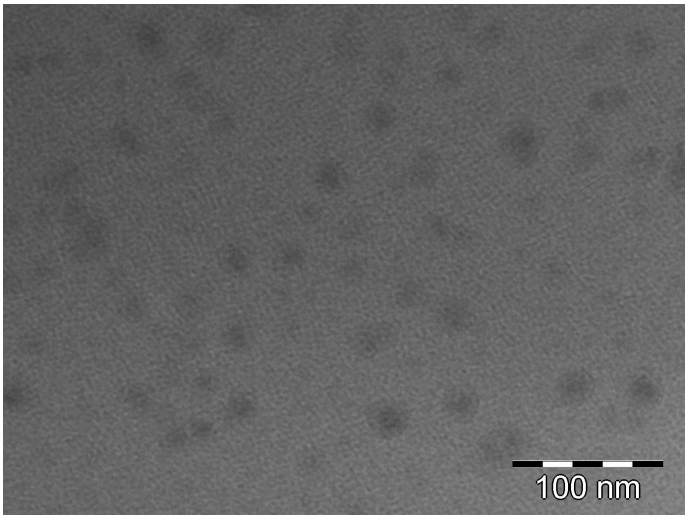

Fig. 3. Low magnification XTEM image in the middle of the GeSiO (40 % Ge) sputtered sample.

The large nanodots show a well defined interface with the SiO_2 amorphous matrix. The local change of the TEM contrast in large nanodots at the slight tilting of specimen in the microscope gives a clear indication of the presence of a crystallized structure. This fact is confirmed by a SAED pattern, in Fig. 4 (Reprinted from Springer – Journal of Nanoparticle Research **13** (1), 221-232 (2011), "Structural investigations of Ge nanoparticles embedded in an amorphous SiO_2 matrix", I. Stavarache, A.-M. Lepadatu, N.G. Gheorghe, R.M. Costescu, G.E. Stan, D. Marcov, A. Slav, G. Iordache, T.F. Stoica, V. Iancu, V.S. Teodorescu, C.M. Teodorescu, and M.L. Ciurea, Figure 6, Copyright 2011, with kind permission from Springer Science+Business Media B.V.), where one can see that the main diffraction spots originate from the big nanocrystals, those with sizes larger than 40 nm.

The experimental data obtained from the SAED pattern measured on the GeSiO sputtered films were compared with the expected crystalline phases of germanium. The tetragonal phase of germanium was found to be the most suitable one for the sputtered films. It is already known from literature that this phase is metastable and appears under high pressure conditions only [34].

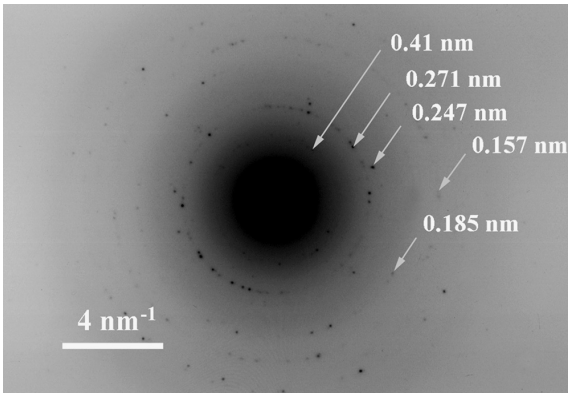

Fig. 4. SAED pattern of a sputtered film fragment: a number of clear reflections could be measured in spite of the low contrast due to the massive amorphous matrix [5].

The high resolution images of the sputtered GeSiO layers reveal two types of Ge nanostructures (see Fig. 5, Reprinted from Springer – Journal of Nanoparticle Research **13** (1), 221-232 (2011), "Structural investigations of Ge nanoparticles embedded in an amorphous SiO_2 matrix", I. Stavarache, A.-M. Lepadatu, N.G. Gheorghe, R.M. Costescu, G.E. Stan, D. Marcov, A. Slav, G. Iordache, T.F. Stoica, V. Iancu, V.S. Teodorescu, C.M. Teodorescu, and M.L. Ciurea, Figure 7, Copyright 2011, with kind permission from Springer Science+Business Media B.V.). One consists of tetragonal Ge nanocrystals of approximately 10 nm diameter (Fig. 5 left), with the lattice interfringe of about 0.45 nm [35]. The other forms a network of Ge-rich nanostructures in the amorphous matrix (Fig. 5 right). In our opinion, the high pressure tetragonal phase of Ge appears due to the stress field developed in the GeSiO films during the annealing.

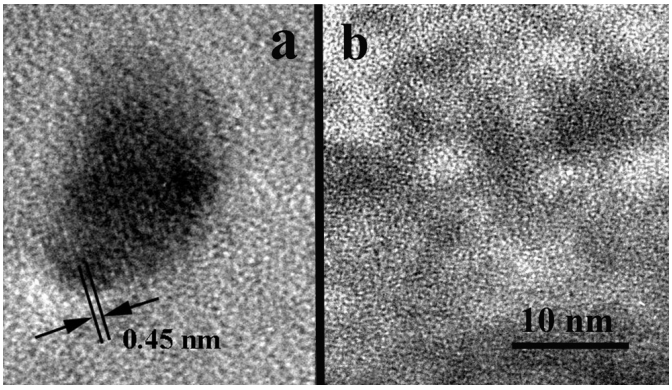

Fig. 5. HRTEM images on the sputtered specimen: a – crystallized nanodot showing lattice fringes, b – a network of Ge-rich nanostructures in the amorphous matrix [5].

We correlated the tetragonal phase of Ge with the stress field developed in the GeSiO layers due to contraction of the film structure during the annealing. Most likely, the preparation of TEM sample, namely the extraction of small micro-fragments from the film, permits us to put in evidence the tetragonal phase. In our opinion, the stress field could relax, during the preparation of TEM specimens by ion milling.

The wide-range survey XPS spectrum (shown in Fig. 6, Reprinted from Springer – Journal of Nanoparticle Research **13** (1), 221-232 (2011), "Structural investigations of Ge nanoparticles embedded in an amorphous SiO_2 matrix", I. Stavarache, A.-M. Lepadatu, N.G. Gheorghe, R.M. Costescu, G.E. Stan, D. Marcov, A. Slav, G. Iordache, T.F. Stoica, V. Iancu, V. S. Teodorescu, C.M. Teodorescu, and M.L. Ciurea, Figure 8, Copyright 2011, with kind permission from Springer Science+Business Media B.V.) measured for a magnetron sputtered GeSiO sample, using monochromatized Ag L_α, showed the presence of Ge, Si and O elements. One may observe traces of contaminants such as Zn or Na. The extracted binding energies were: 101,6 eV, 123,9 eV, 151,2 eV, 181,5 eV, and 1220,7 eV for the core levels Si 2p, Ge $3p_{3/2}$, Si 2s, Ge 3s, and Ge $3p_{3/2}$, respectively.

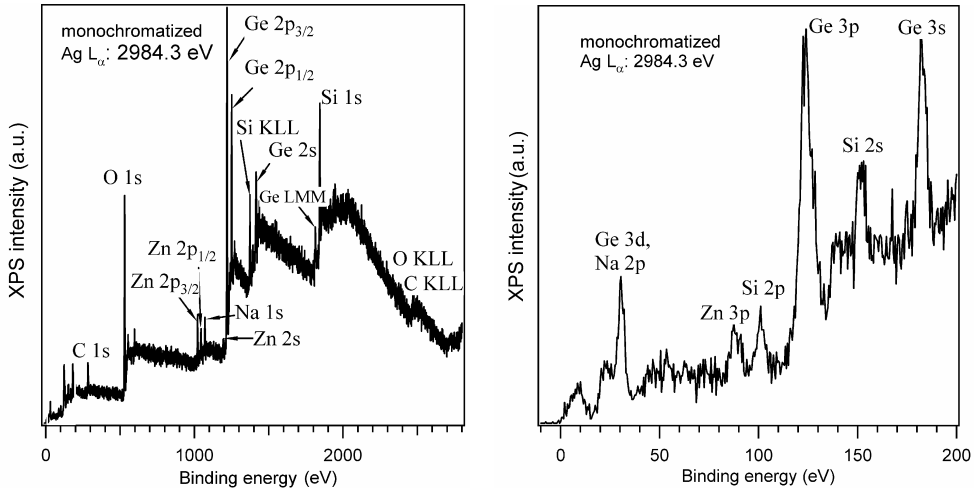

Fig. 6. a) Survey scan on a magnetron sputtered GeSiO layer, b) Detail of the survey scan in the region with binding energies lower than 200 eV. A monochromatized Ag L_α radiation was used [5].

In the case of sol-gel samples, a spectrum comprising the region of Si 2p-2s and Ge 3p-3s core levels was measured using unmonochromatized Al K_α radiation (see Fig. 7, Reprinted from Springer – Journal of Nanoparticle Research **13** (1), 221-232 (2011), "Structural investigations of Ge nanoparticles embedded in an amorphous SiO_2 matrix", I. Stavarache, A.-M. Lepadatu, N.G. Gheorghe,

R.M. Costescu, G.E. Stan, D. Marcov, A. Slav, G. Iordache, T.F. Stoica, V. Iancu, V.S. Teodorescu, C.M. Teodorescu, and M. L. Ciurea, Figure 9, Copyright 2011, with kind permission from Springer Science+Business Media B.V.). The extracted binding energies were: 104,2 eV, 126,2 eV, 155,2 eV, and 1221,3 eV for the core levels Si 2p, Ge $3p_{3/2}$, Si 2s, and Ge $3p_{3/2}$, respectively. This spectrum was compared with the ones corresponding to a clean Si (001) sample, to an oxidized germanium sample, and to a germanium sample after cleaning by ion sputtering.

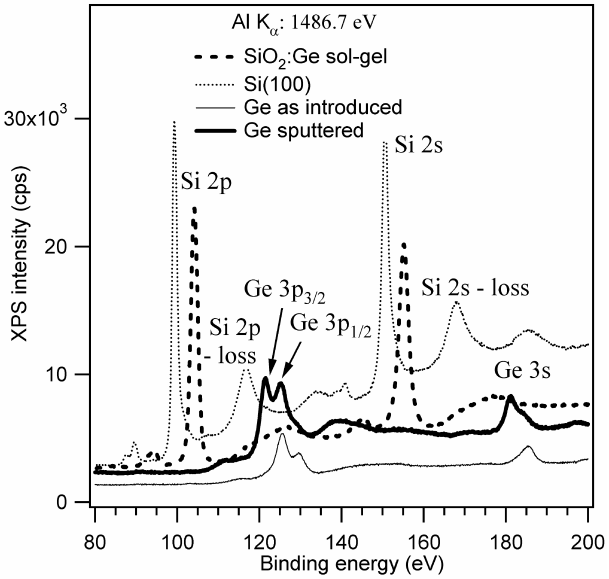

Fig. 7. Si 2p-2s and Ge 3p-3s core levels measured on a sol-gel prepared sample. This spectrum was compared with the ones corresponding to a clean Si (001) sample, to an oxidized germanium sample, and of a germanium sample after cleaning by ion sputtering [5].

The Ge $2p_{3/2}$ core level, shown in Fig. 8 (Reprinted from Springer – Journal of Nanoparticle Research **13** (1), 221-232 (2011), "Structural investigations of Ge nanoparticles embedded in an amorphous SiO_2 matrix", I. Stavarache, A.-M. Lepadatu, N.G. Gheorghe, R.M. Costescu, G.E. Stan, D. Marcov, A. Slav, G. Iordache, T.F. Stoica, V. Iancu, V.S. Teodorescu, C.M. Teodorescu, and M. L. Ciurea, Figure 10, Copyright 2011, with kind permission from Springer Science+Business Media B.V.), was measured on sol-gel and magnetron sputtered GeSiO films, and also on both an oxidized Ge crystal and a cleaned one by Ar^+ sputtering. The monochromatized Ag L_α radiation of 2984.3 eV was used. One can see that at the surface of the samples (the outermost 2 – 3 nm due to the finite photoelectron escape depth) only Ge in oxidised state can be found.

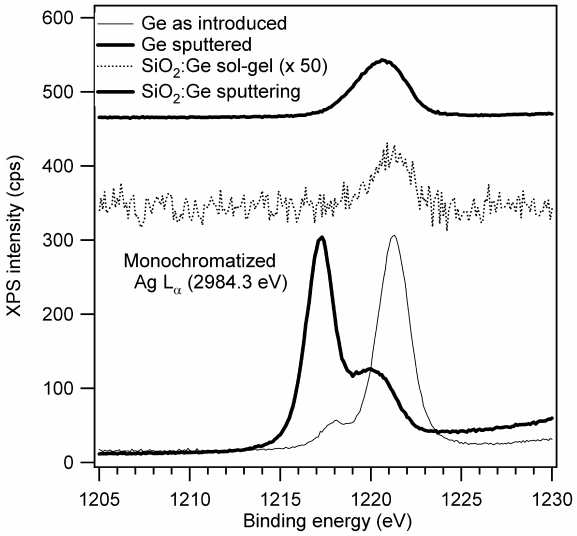

Fig. 8. Ge $2p_{3/2}$ core level measured, with monochromatized Ag L_α radiation, on sol-gel and magnetron sputtered GeSiO layers, and together with a Ge crystal as introduced and later cleaned by Ar^+ sputtering. The sol-gel spectrum is multiplied by 50, and the magnetron sputtered one is intentionally shifted upwards by + 450 cps [5].

The O 1s core level in oxidized Si (001) was compared with the corresponding spectrum in sol-gel GeSiO layer (see Fig. 9, Reprinted from Springer – Journal of Nanoparticle Research **13** (1), 221-232 (2011), "Structural investigations of Ge nanoparticles embedded in an amorphous SiO_2 matrix", I. Stavarache, A.-M. Lepadatu, N. G. Gheorghe, R. M. Costescu, G. E. Stan, D. Marcov, A. Slav, G. Iordache, T. F. Stoica, V. Iancu, V. S. Teodorescu, C. M. Teodorescu, and M. L. Ciurea, Figure 11, Copyright 2011, with kind permission from Springer Science+Business Media B.V.). One found a value of 533.7 eV for the binding energy of O 1s in GeSiO sample, and 532.3 eV for the oxidized silicon respectively. Comparing the experimental results with the ones from the NIST X-ray photoelectron spectroscopy database, one finds that silicon has a larger electronegativity in solid state than germanium.

The obtained values for core level binding energies are in good agreement with data reported in literature for clean Si and Ge samples. We found that the Si 2p core level binding energy of 101.6 eV, for magnetron sputtered samples fits well with the reported data for SiO [36] of 101.7 eV or for several SiO_x/Si structures [37]. Thus, in the magnetron sputtered GeSiO sample, silicon suboxides are formed. On the contrary, in the sol-gel sample, silicon oxide is formed.

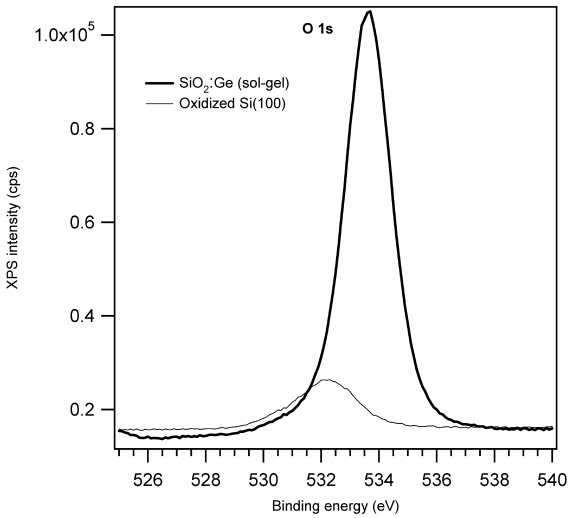

Fig. 9. O 1s core level in sol-gel film compared with the one obtained on oxidized Si(001) [5].

In the sputtered sample, a lower binding energy (123.9 eV) for Ge is observed in comparison with the value corresponding to the oxidized Ge (125.6 eV) and to the data reported in literature for GeO_2, e.g. 125.3 eV [38]. This shows that at the surface of the magnetron sputtered samples germanium suboxides are also present. One can state that, the surface of the magnetron sputtered GeSiO films contains germanium and silicon suboxides, whereas the sol-gel one is composed of a mixture of GeO_2 and SiO_2. When one uses a target of amorphous SiO_2 covered with Ge pieces, it is typical to find suboxides at the surface of the deposited films. One can also see why the magnetron sputtered films are easier to be reduced than the sol-gel ones under equivalent conditions.

If one investigates in more detail the Si 2p, Ge $2p_{3/2}$ and $3p_{3/2}$ levels, by using the atomic sensitivity factors (ASF), as obtained empirically [39], will obtain 6 % of Ge/Si ratio at the sol-gel GeSiO (3 % Ge) sample surface, whereas at the magnetron sputtering sample surface the Ge concentration is three times higher than the Si one.

The $I - V$ characteristics, measured on sol-gel samples treated by RTA are presented in Fig. 10 (Reprinted from Digest Journal of Nanomaterials and Biostructures **6** (1), 67-73 (2011), "Study of Ge nanoparticles embedded in an amorphous SiO_2 matrix with photoconductive properties", A. M. Lepadatu, I. Stavarache, T. F. Stoica, M. L. Ciurea, Figure 2, Copyright 2011, with permission from © INCDFM). These curves were taken at RT, in the interval 0 – 1 V, for both bias polarities. These samples, as already stated, are formed by amorphous Ge nanodots embedded in amorphous SiO_2 matrix. In these films are also present ordered Ge clusters close to Ge tetragonal phase that are produced during the RTA

treatment. A typical $I - V$ curve is asymmetric and has a weak rectifying behaviour, mainly given by the junction formed between the GeSiO film and Si substrate. This behaviour can be understood if we take into account that Ge nanodots, located at the interface SiO_2 clear band/GeSiO layer, can induce a depletion layer into the Si substrate. For a bias higher than 0.4 V, a linear dependence of the $I - V$ characteristic appears, so that this behaviour is dominated by the series resistance of the film.

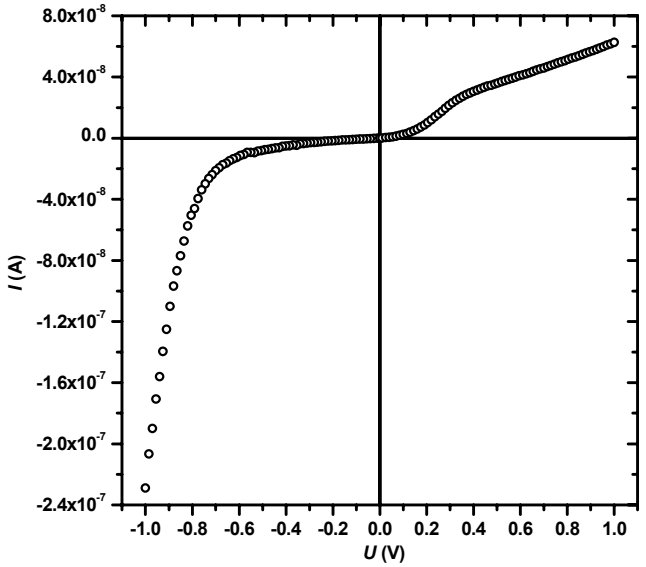

Fig. 10. Dark I – V curve taken at RT on a sol-gel sample treated by RTA [15].

The experimental curve was fitted (Fig. 11, Reprinted from Digest Journal of Nanomaterials and Biostructures **6** (1), 67-73 (2011)), "Study of Ge nanoparticles embedded in an amorphous SiO_2 matrix with photoconductive properties", A. M. Lepadatu, I. Stavarache, T. F. Stoica, M. L. Ciurea, Figure 3, Copyright 2011, with permission from © INCDFM) with the equation [40]:

$$I = I_S \exp\left(\frac{q(V - I \times R_S)}{nkT}\right)\left[1 - \exp\left(\frac{-q(V - I \times R_S)}{kT}\right)\right] \qquad (1)$$

where I_S represents the reverse current at zero bias, q is the electron charge, n is the ideality factor, and R_S is a suitable series resistance. We found I_S = 39 pA, n = 1.30, and R_S = 0.2 MΩ.

On a reversed polarity, the process of thermionic emission is considered together with the electron-hole recombination in the depletion region that appears in the Si substrate, at the interface with the GeSiO film. For voltages higher than 0.4 V, the film contribution is dominant, thus the $I - V$ curve becomes linear.

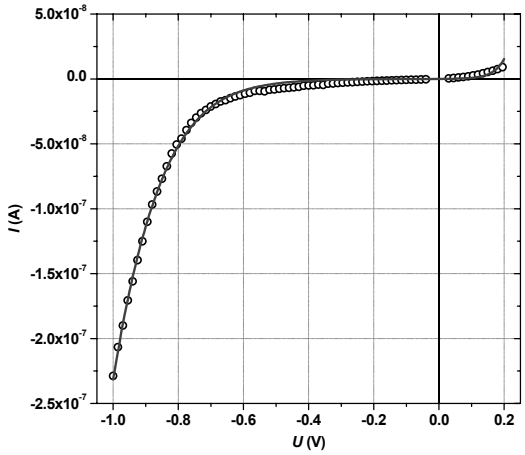

Fig. 11. The experimental dark I – V characteristic (open circles) compared with the fit curve (continuous line) [15].

The temperature dependence of the conductance fits well the Mott law $\sigma \propto \exp\left[-\left(T_0/T\right)^{1/4}\right]$, which describes the transport mechanism of the VRH in amorphous materials. This is true only in the absence of dominant Coulomb interactions. A typical characteristic taken for a bias of 0.8 V is shown in Fig. 12. The curves measured for 0.5 and 0.9 V have a similar behaviour. The VRH transport in GeSiO sol-gel films can be explained by the hopping of electrons on localized states present in the amorphous film, including those associated with Ge clusters [11].

The photoconductive properties of the sol-gel films annealed under different conditions were investigated. The sol-gel films annealed by RTA show a very high photoconductivity, but those annealed in a heater under the same conditions (at the same temperature and atmosphere) are not photoconductive. Illuminating a sample annealed by RTA with white light from an incandescence lamp of 40 W, a big photocurrent appears. It is with 2 – 3 orders of magnitude bigger than the dark current. The spectral dependence of the photocurrent (I_f) was measured at RT in the 350–900 nm wavelength range. The curves were taken for different constant biases from 0 to 1 V, using modulated light, with an 80 Hz chopping frequency. The curves of the spectral dependence of the photocurrent, corresponding to both a not normalized to the incident light intensity and to a normalized ones are given in Fig. 13 a) and b) (Reprinted from Digest Journal of Nanomaterials and Biostructures **6** (1), 67-73 (2011), "Study of Ge nanoparticles embedded in an amorphous SiO_2 matrix with photoconductive properties", A.M. Lepadatu, I. Stavarache, T.F. Stoica, M.L. Ciurea, Figure 5, Copyright 2011, with permission from © INCDFM). One can see that the curves present a fine structure. The most important five maxima are located at 513, 724, 773, 804 and 862 nm.

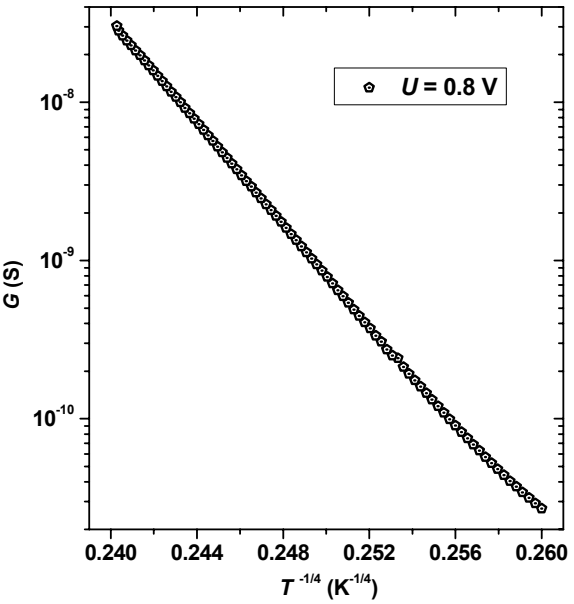

Fig. 12. Temperature dependence of the conductance taken for a bias of 0.8 V.

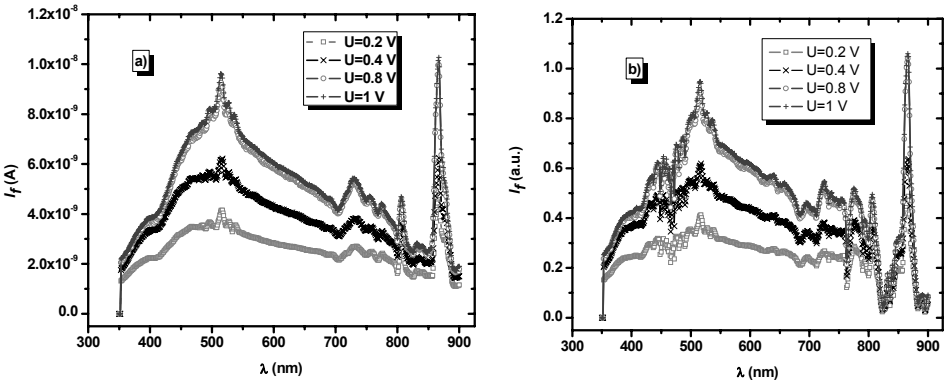

Fig. 13. Spectral dependence of the photocurrent measured at 0.2, 0.4, 0.8 and 1 V, corresponding to both a) not normalized to the incident light intensity and b) to normalized ones, [15].

For the wavelengths corresponding to these maxima, photocurrent-voltage ($I_f - V$) characteristics were measured, using a continuous monochromatic light. The obtained curves are presented in Fig. 14 (Reprinted from Digest Journal of Nanomaterials and Biostructures **6** (1), 67-73 (2011), "Study of Ge nanoparticles embedded in an amorphous SiO_2 matrix with photoconductive properties", A.M. Lepadatu, I. Stavarache, T.F. Stoica, M.L. Ciurea, Figure 6, Copyright 2011,

with permission from © INCDFM) together with the dark $I - V$ one. These characteristics are not normalized to the incident light intensity. Looking at the curve measured under illumination with monochromatic light (862 nm), the photocurrent is with two orders of magnitude bigger than the dark current, if the sample is biased with 1 V.

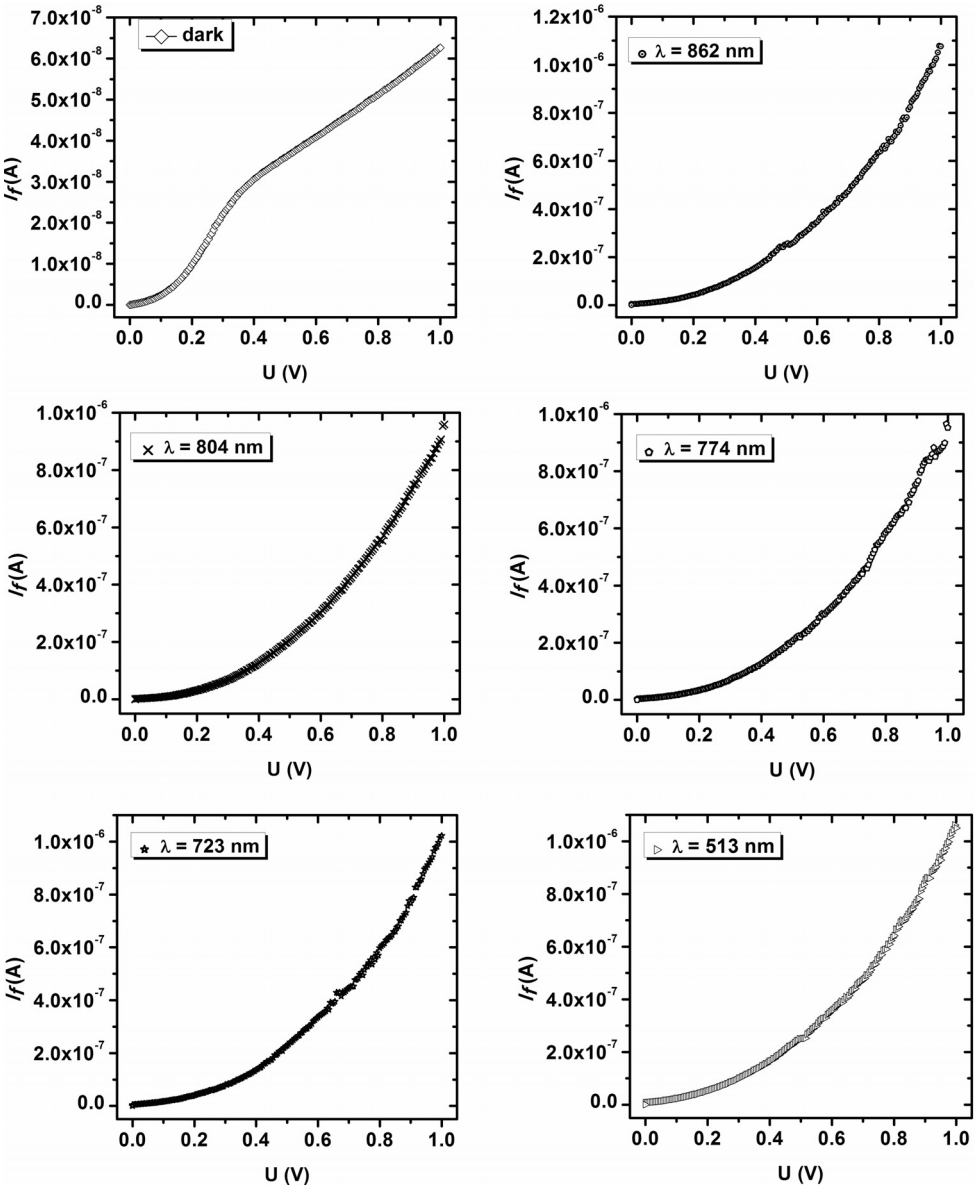

Fig. 14. $I_f - V$ characteristics for the wavelengths corresponding to the most important five maxima of the photocurrent in Fig. 13 b) and I – V curve in dark [15].

The high photoconductivity can be explained by taking into account the Ge clusters and localized states (defects), produced during the RTA process, on which, the light absorption takes place [41]. The defects can also act as traps for a type of carriers (e.g electrons), thus increasing the lifetime of the other type (holes). The carriers with a longer lifetime will contribute in the photoconductivity. Also, different localized states/defects present in the film will produce the fine structure of the spectral curves.

4. Summary and Concluding Remarks

Films consisting of Ge nanodots embedded in amorphous SiO_2 matrix were prepared using two conventional deposition methods, sol-gel and magnetron-sputtering. Different investigations, namely structural investigations by TEM and XPS, electrical and photoconductivity measurements, were performed.

In the sol-gel films the major part of the Ge nanodots are amorphous. The average diameter gradually grows from 3.8 nm to 4.3 nm with the increase of Ge concentration from 3% Ge to 12% Ge. A 10 nm thick band of clear SiO_2 matrix, without nanodots, is present at the interface with the silicon substrate. This clear band was attributed to the oxidation of the silicon substrate during the annealing process. Near this band, one finds larger nanodots than in the rest of the film. In the sol-gel films, some of the nanodots present small areas with traces of (111) lattice interfringes corresponding to the tetragonal phase of germanium. No structural difference was observed between the samples annealed in N_2 and H_2.

In the case of sputtered GeSiO (40 % Ge) films two different Ge nanostructures were evidenced. One part of Ge forms big tetragonal nanocrystals, while the second part forms a network of Ge-rich amorphous nanostructures in the amorphous matrix. The magnetron sputtered layers consist of big Ge rich nanodots (20 – 50 nm) embedded in the amorphous SiO_2 matrix as well as smaller ones (5 – 15 nm) that are homogeneously distributed.

The tetragonal phase of germanium was found in the sputtered samples. This phase is metastable and appears under high pressure conditions only. The high pressure phase of Ge appears due to the stress field developed in the GeSiO layers during the annealing. Most likely, the preparation of TEM sample, namely the extraction of small micro-fragments from the film, permits us to put in evidence the tetragonal phase. Perhaps the stress field could relax, during the preparation of TEM specimens by ion milling.

The XPS measurements showed the presence of Ge, Si and O elements in the sol-gel and magnetron-sputtering films. At the surface of sol-gel films one finds a mixture of GeO_2 and SiO_2, whereas the sputtered ones contain germanium and silicon suboxides. The surface of GeSiO samples consist of a greater Ge concentration than the one present in the volume of the films.

The $I - V$ characteristics, measured on sol-gel samples treated by RTA, are asymmetric and have a weak rectifying behaviour, mainly given by the junction formed between GeSiO film and Si substrate. The transport mechanism of the variable range hopping in amorphous materials was evidenced. This can be explained by the hopping of electrons on localized states present in the amorphous film, including those associated with Ge clusters.

The GeSiO sol-gel films annealed by RTA show a very high photoconductivity. The curves of spectral dependence of the photocurrent present a fine structure with five main maxima. The high photoconductivity can be explained by taking into account the Ge clusters and localized states (defects) produced during the RTA process, on which, the light absorption takes place.

Acknowledgements. This work was supported by the Romanian National Authority for Scientific Research through the CNCSIS –UEFISCDI Contract No. 471/2009 (ID 918/2008).

References

[1] NOGAMI M. and ABE Y., Appl. Phys. Lett. **65**, p. 2545, 1994.
[2] ZHANG B., SHRESTHA S., GREEN M.A., and CONIBEER G., Appl. Phys. Lett. **96**, p. 261901, 2010.
[3] YANG H., YAO Xi, WANG X., XIE S., FANG Y., LIU S., and GU X., J. Phys. Chem. B **107**, p. 13319, 2003.
[4] KOLOBOV A.V., WEI S.Q., YAN W.S., OYANAGI H., MAEDA Y., and TANAKA K., Phys Rev. B **67**, p. 195314, 2003.
[5] STAVARACHE I., LEPADATU A.-M., GHEORGHE N.G., COSTESCU R.M., STAN G.E., MARCOV D., SLAV A., IORDACHE G., STOICA T.F., IANCU V., TEODORESCU V.S., TEODORESCU C. M., AND CIUREA M.L., J. Nanopart. Res. **13**, p. 221, 2011.
[6] KNEBEL S., KYRIAKIDOU A., BRACHT H., RÖSNER H., and WILDE G., Appl. Phys. A: Mater. Sci. Process, DOI 10.1007/s00339-010-6156-4.
[7] RAY S.K. and DAS K., *Opt. Mater*. **27**, p. 948, 2005.
[8] COSENTINO S., MIRABELLA S., MIRITELLO M., NICOTRA G., LO SAVIO R., SIMONE F., SPINELLA C., and TERRASI A., Nanoscale Res. Lett. **6**, p. 135, 2011.
[9] GACEM K., El HDIY A., TROYON M., BERBEZIER I., SZKUTNIK P.D., KARMOUS A., and RONDA.A., J. Appl. Phys. **102**, p. 093704, 2007.
[10] El HDIY A., Gacem K., Troyan M., Ronda A., Bassani F., and Berzebier I., J. Appl. Phys. **104**, p. 063716, 2008.
[11] FUJII M., INOUE Y., HAYASHI S., and YAMAMOTO K., Appl. Phys. Lett. **68**, p. 3749, 1996.
[12] FUJII M., MAMEZAKI O., HAYASHI S., and YAMAMOTO K., J. Appl. Phys. **83**, p. 1507, 1998.
[13] ZHANG B., YAO Y., PATTERSON R., SHRESTHA S., GREEN M.A., and CONIBEER G., Nanotechnology **22**, p. 125204, 2011.
[14] CASTRUCCI P., GOBBO Del S., SPEISER E., SCARSELLI M., De CRESCENZI M., AMIARD G., RONDA A., and BERBEZIER I., J. Non-Cryst. Solids **356**, p. 1940, 2010.
[15] LEPADATU A.M., STAVARACHE I., STOICA T.F., ANDand CIUREA M.L., Digest J. Nanomater. Bios. **6**, p. 67, 2011.

[16] STOICA T.F., GARTNER M., TEODORESCU V.S., and STOICA T., J. Optoelectron. Adv. Mater. **9**, p. 3271, 2007.
[17] KANJILAL A., LUNDSGAARD HANSEN J., GAIDUK P., NYLANDSTED LARSEN A., CHERKASHIN N., CLAVERIE A., NORMAND P., KAPELANAKIS E., SKARLATOS D., and TSOUKALAS D., Appl. Phys. Lett. **82**, p. 1212, 2003.
[18] ZHANG L., YE H., HUANGFU Y.R., ZHANG C., and LIU X., Appl. Surf. Sci. **256**, p. 768, 2009.
[19] SHEN J.K., WU X.L., TAN C., YUAN R.K., and BAO X.M., Phys. Lett. A **300**, p. 307, 2002.
[20] PEIBST R., SOUSA de J.S., and HOFMANN K.R., Phys. Rev. B **82**, p. 195415, 2010.
[21] SRINIVASA RAO N., PATHAK A.P., SATHISH N., DEVARAJU G., SAIKIRAN V., KULRIYA P.K., AGARWAL D.C., SAI SARAVANAN G., AVASTHI D.K., Solid State Commun. **150**, p. 2122, 2010.
[22] FUKUDA H., SAKUMA S., YAMADA T., NOMURA S., NISHINO M., HIGUCHI T., and OHSHIMA S., J. Appl. Phys. **90**, p. 3524, 2001.
[23] CHEN Q., LU T., XU M., MENG C., HU Y., SUN K., and SHLIMAK I., Appl Phys Lett **98**, p. 073103, 2011.
[24] SRINIVASA RAO N., PATHAK A.P., DEVARAJU G., SAIKIRAN V., Vacuum **85**, p. 927, 2011.
[25] DAS S., SINGHA R.K., GANGOPADHYAY S., DHAR A., and RAY S.K., J. Appl. Phys. **108**, p. 053510, 2010.
[26] DAS S., SINGHA R.K., MANNA S., GANGOPADHYAY S., DHAR A., and RAY S.K., *J.* Nanopart. Res. **13**, p. 587, 2011.
[27] BULJAN M., PINTO S.R.C., ROLO A.G., . MARTÍN-SÁNCHEZ J, GOMES M.J.M., GRENZER J., MÜCKLICH A., BERNSTORFF S., AND HOLÝ V., Phys. Rev. B **82**, p. 235407, 2010.
[28] CHATTERJEE S., J. Phys.: D Appl. Phys. **41**, p. 055301, 2008.
[29] AKTAĞ A., YILMAZ E., MOGADDA N.A.P., AYGUN G., CANTAS A., TURAN R., Nucl. Instr. *Meth.* Phys. Res **B 268**, p. 3417, 2010.
[30] TZENG S.S. and LI P.W., Nanotechnology **19**, p. 235203, 2008.
[31] HONG S.H., KIM M.C., JEONG P.S., CHOI S.-H., and KIM K.J., Nanotechnology **19**, p. 305203, 2008.
[32] STAVARACHE I., LEPADATU A.-M., TEODORESCU V., STOICA T., PASUK I., STAN G., IANCU V., AND CIUREA M.L., CAS 2010 Proceedings IEEE CN CFP10CAS-PRT; 33nd International Semiconductor Conference (CAS 2010, Sinaia, 11–13 October), **1**, p. 77, 2010.
[33] TEODORESCU V.S. and BLANCHIN M.G., Microscopy and Microanalysis **15**, p. 15, 2009.
[34] WOSYLUS A., PROTS Y., SCHNELLE W., HANFLAND M., and SCHWARZ U., Zeitschrift für Naturforschung B **63b**, p. 608, 2008.
[35] Powder Diffraction File, PDF No: 18-0549. Available via http://www.icdd.com.
[36] NGUYEN T.P. and LEFRANT S., J. Phys. Cond. Matter. **1**, p. 5197, 1989.
[37] KERKHOF F.P.J., MOULIJN J.A., and HEERES A., J. Electron. Spectrosc. Relat. Phenom. **14**, p. 453, 1978.
[38] MORGAN W.E. and WAZER Van J.R., J. Phys. Chem. **77**, p. 964, 1973.
[39] WAGNER C.D., DAVIS L.E., ZELLER M.V., TAYLOR J.A., RAYMOND R.M., and GALE L.H., Surf. Interf. Anal. **3**, p. 211, 1981.
[40] RAY A.K., MABROOK M.F., NABOK A.V., and BROWN S., J. Appl. Phys. **84**, p. 3232, 1998.
[41] YANG H., YAO X., XIE S., WANG X., LIU S., FANG Y., GU X., and WANG F., Opt. Mater. **27**, p. 725, 2005.

Defect Assisted Localization of Mn^{2+} Activating Ions in the Core of the ZnS Quantum Dots

S.V. NISTOR, M. STEFAN, L.C. NISTOR, D. GHICA and C.D. MATEESCU

National Institute of Materials Physics, Atomistilor 105 bis,
077125 Magurele-Ilfov, Romania
E-mail: snistor@infim.ro

Abstract. Multifrequency electron paramagnetic resonance (EPR) and high resolution transmission electron microscopy (HRTEM) investigations were performed on cubic ZnS:Mn quantum dots (QDs) of 2 nm, synthesized by a surfactant-assisted liquid-liquid reaction. The EPR spectra reveal the presence of Mn^{2+} ions localized substitutionally and at the surface of QDs. Based on accurate EPR spectra analysis we demonstrate that the substitutional Mn^{2+} ions are localized in the core of the ZnS QDs at Zn^{2+} sites, next to an extended lattice defect. Their presence, confirmed by HRTEM measurements, seems to be essential in the incorporation of Mn^{2+} activating ions in cubic II-VI semiconductor QDs.

1. Introduction

Activating impurities, in particular transition ions, play an essential role in fulfilling the expected exceptional properties of semiconducting nanocrystals. To understand the mechanisms responsible for their incorporation and the resulting quantum properties one needs to know the precise location of the doping impurities in the nanocrystals (NCs) lattice. In the case of wide band-gap nanocrystalline II-VI semiconductors, which are prepared at relatively low temperatures (< 350^oC), such information could also help in understanding the still unclear mechanisms responsible for the incorporation of activating impurity ions such as Mn^{2+} or Co^{2+} [1, 2].

Electron paramagnetic resonance (EPR) spectroscopy can accurately determine the localization of the paramagnetic impurities and the resulting changes in the neighboring ligands configuration [3]. In the case of luminescent cubic ZnS (cZnS) NCs [4], it was for quite long accepted [1,5-10] that the substitutional Mn^{2+} ions

are localized at the cation (Zn^{2+}) sites with local cubic T_d symmetry, similar to the case of cZnS single crystals [11]. Despite this assumption, in the publications dedicated to this subject [6-10] the spin Hamiltonian (SH) describing the EPR spectra also included, besides the cubic Zeeman and hyperfine interaction terms with parameter values centered around $g = 2.002$ and $|A| = 64 \times 10^{-4}$ cm^{-1} [11], additional axial and even rhombic zero-field-splitting (ZFS) terms characterized by the D and E parameters, respectively. The corresponding reported values were spread over a two orders of magnitude range [6-10], a situation which can be explained by the low accuracy of the procedures used to determine the SH parameters and the low resolution of the experimentally obtained EPR spectra. One should also mention that no clear explanation for the presence of the reported non-cubic ZFS terms was given.

In an effort to improve this situation, we could synthesize by a surfactant-assisted liquid-liquid reaction at room temperature (RT) small cZnS NCs doped with Mn^{2+} self-assembled into a mesoporous structure with a tight size distribution, centered around 2 nm and an improved lattice quality [12, 13]. Such small size NCs, to be further called quantum dots (QDs), in which quantum confinement (QC) effects are expected to take place, exhibited EPR spectra with the smallest line-width reported so-far and a corresponding increased spectra resolution, beyond the best reported data available in the literature [14, 15]. These properties were attributed to the self-assembling.

As will be shown here, the full quantitative analysis of the resulting low and high frequency EPR spectra resulted in accurate SH parameters for the substitutional, as well as for the surface Mn^{2+} centers, which confirmed, in the case of the substitutional center, the presence of an axial ZFS term and an accurate determination of the characteristic D parameter value. Moreover, by comparing the resulting spectral parameters with those reported in early experimental investigations concerning EPR parameters of Mn^{2+} ions in strongly defective ZnS single crystals, we could demonstrate that the local axial crystal field component at the substitutional Mn^{2+} ion is due to the presence of a neighboring extended lattice defect (ELD) in the form of a stacking fault or twin. We have also concluded that the ELD play an essential role in the incorporation and localization in the cubic ZnS NCs lattice of the Mn^{2+} impurity ions. Based on previously published EPR results it is proposed that a similar extended lattice defects assisted (ELDA) mechanism of impurities incorporation is acting in the case of other cubic II-VI semiconductor NCs doped with Mn^{2+} ions as well.

2. Experimental

The QDs of cZnS:Mn were synthesized by precipitation in a surfactant-assisted liquid-liquid reaction, at room temperature [12, 13]. In the initial stage 0.2% mol manganese acetate [$Mn(CH_3COO)_2 \cdot 4H_2O$] has been added to a zinc acetate

$[Zn(CH_3COO)_2 \cdot 2H_2O]$ solution and further mixed for 15 minutes. Afterwards the resulting solution was co-precipitated with sodium sulfide $[Na_2S \cdot 9H_2O]$ in the presence of Tween 20 (polyoxyethylene sorbitan monolaurate), a nontoxic additive used in the food industry. In the post synthesis steps the precipitate was filtered, washed with bi-distilled water and methanol and dried at 50°C for 24 h. The concentration of the Mn^{2+} ions at isolated sites in the nanocrystalline ZnS has been estimated from EPR measurements, using concentration standards of MgO:Mn^{2+} crystalline powders, to be in the 2-400 ppm range.

The X-ray diffraction (XRD) characterization of the resulting material shows (Figure 1a) the formation of a mesoporous structure consisting of nanocrystals of ZnS with cubic (sphalerite) structure of 1.9 nm average diameter. The transmission electron microscopy (TEM) images and electron diffraction (ED) patterns (Figure 1b) confirmed the above conclusions, revealing the details of the structure of the mesoporous material with walls consisting of cubic ZnS nanocrystals with uniform size, of 2.1 nm average diameter. This value was obtained by measuring de size of 259 nanocrystals.

The EPR investigations were performed on QDs of cZnS doped with 0.2% mol Mn^{2+}, self-assembled into a mesoporous structure, which were prepared at room temperature (RT) by a surfactant-assisted liquid-liquid reaction [12]. The preparation procedure, as well as the results of structural and preliminary X-band EPR and optical characterization of the presently investigated sample batch was reported elsewhere [13, 14].

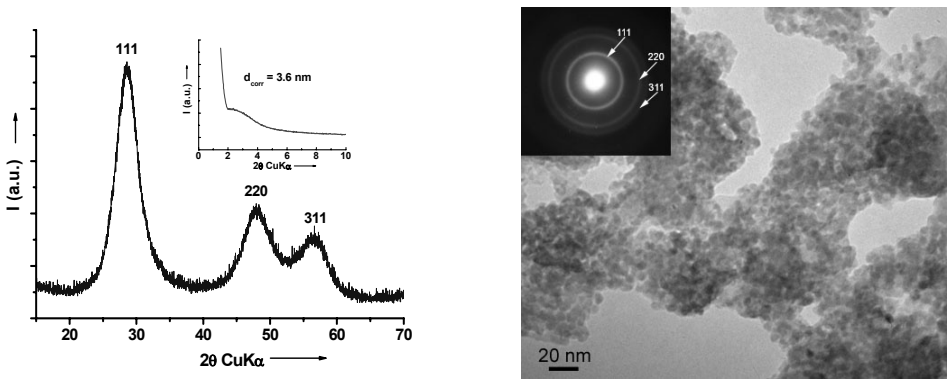

Fig. 1. The microstructure of the presently investigated cZnS:Mn QDs as revealed by: Left - wide-angle XRD diffractogram. Inset - the low angle range reflecting the mesoporous structure of the resulting nanomaterial; and (b) Right – TEM image revealing the mesoporous morphology of the cZnS:Mn sample. Inset - the corresponding ED pattern indexed with the cubic (sphalerite) ZnS structure.

The X (9.8 GHz)- and Q (34 GHz)-band measurements were performed at RT on Bruker EMX-plus and ELEXSYS 500Q spectrometers, respectively, at the

Research center for advanced ESR techniques (CetRESav - http://cetresav.infim.ro/) from NIMP. High frequency W (95 GHz)-band measurements were performed on a Bruker E600 spectrometer from the Department of Physics – ECMP, University of Antwerp, Belgium. The SH parameters were determined by lineshape simulations and fitting procedures with the SIM specialized program graciously provided by Prof. H. Weihe of the University of Copenhagen and the publicly available EasySpin v. 3.1 program.

3. Results and Discussion

We have identified in the preliminary X-band EPR investigations of the cZnS:Mn QDs the presence of a substitutional Mn^{2+} center, called Mn(I), which does not change its concentration by thermal treatments, and two surface centers, called Mn(II) and Mn(III) [13, 15]. The Mn(III) centers were found to transform into Mn(II) centers during heating, by the temperature activated desorption of water molecules from the nanocrystals surface [14]. Figure 2 illustrates such a situation, where the X- and Q – band EPR spectra from samples of the same batch, but with a different thermal history, exhibit a different relative concentration/ lines intensity of the Mn(II) and Mn(III) centers. The transition fields attributed to the Mn(I), Mn(II) and Mn(III) centers are marked with vertical lines, namely 6 allowed (M_s: -1/2↔1/2, $\Delta M_I = 0$) and 10 forbidden (M_s: -1/2↔1/2, $\Delta M_I = \pm 1$) hyperfine transitions for the Mn(I) centers and only the 6 allowed hyperfine transitions for the Mn(II) and Mn(III) centers. These observed features are typical for the Mn^{2+} ions in crystalline powders [3, 16]. One can see that in the case of the left hand side X-band spectrum the intensities of the lowest magnetic field lines from the two surface centers are comparable. Meanwhile, in the other spectrum from a sample with a different history (recorded in the Q-band), the concentration/ lines intensity of the Mn(II) surface center is much smaller compared to the concentration/ lines intensity of the Mn(III) surface center.

The EPR spectrum of the Mn^{2+} centers in nanocrystalline cZnS is described by the following SH, with usual notations [3]:

$$\boldsymbol{H} = \mu_B \vec{\boldsymbol{S}} \hat{\boldsymbol{g}} \vec{\boldsymbol{B}} + \vec{\boldsymbol{S}} \hat{\boldsymbol{A}} \vec{\boldsymbol{I}} + \boldsymbol{CF} \tag{1}$$

Here the first two terms represent the main interactions of the $S = 5/2$ electron spin +with the external magnetic field and the hyperfine interaction with the $I = 5/2$ nuclear spin of the ^{55}Mn (100% abundance) isotope, respectively. The last zero field splitting (ZFS) term describes the interaction of the electron spin with the local crystal field, characterized in the case of a local cubic symmetry, typical for cubic ZnS single crystals, by the *a* parameter and in the case of lower symmetry by additional axial and rhombic ZFS terms with the *D* and *E* parameters, respectively [3].

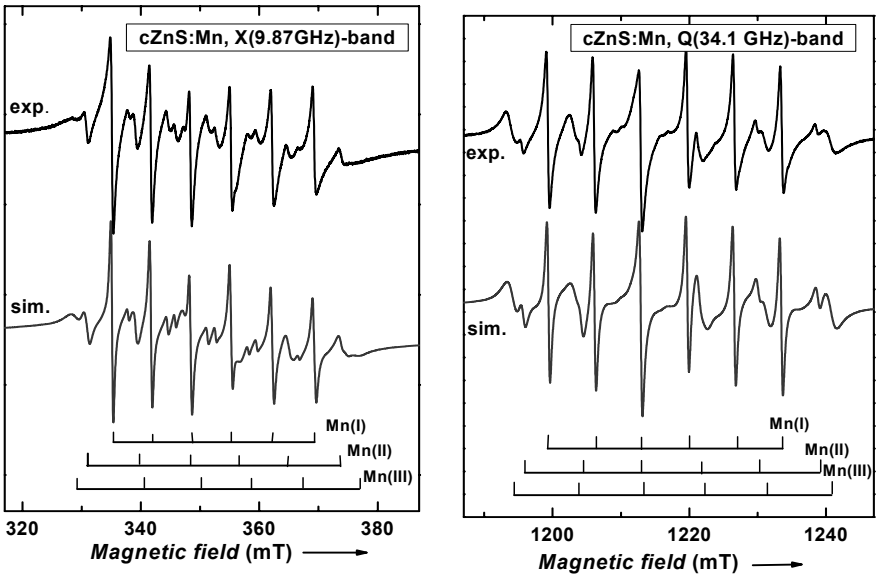

Fig. 2. The X- and Q-band EPR spectra of cZnS:Mn QDs powder samples with a different thermal history. The upper curves represent the experimental spectra while the lower curves are, in each case, the sum of the simulations of the Mn(I), Mn(II) and Mn(III) spectra calculated with the SH parameters given in Table 1.

We have been able to obtain accurate SH parameter values for the Mn^{2+} centers in the cZnS:Mn QDs (Table 1) by fitting both low and high frequency experimental EPR spectra with line shape simulations which took into account the forbidden transitions and the line broadening effects, both strongly influenced by the non-cubic crystal ZFS terms. The increased accuracy of the SH parameters determinations was also possible due to the narrower lines exhibited by our EPR spectra, i.e. 0.4 mT linewidth for the Mn(I) center in the X-band, as compared to the best reported value of 0.6 mT [7]. The two steps procedure for determining the SH parameters was described in Ref. [17]. In the first step the g and A parameters were determined with high accuracy from fitting the line positions in the Q-band spectrum with transition fields calculated with a SH consisting of only the first two terms of SH (1). At higher magnetic fields the contributions of the ZFS terms to the line positions were found to be negligible (within the experimental errors). An accurate value for the D parameter was further determined from fitting the line shape of the X-band spectrum, more sensitive to the ZFS terms. One should also mention that in the case of a local axial crystal field, the cubic fourth order ZFS term characterized by the a-parameter should be in principle replaced by an axial fourth order term characterized by the a-F parameter [3]. However, because of the small values of the fourth order ZFS terms, the strong line broadening effects, included as fluctuations in the ZFS parameter values to fit both X- and Q-band spectral line shapes, were practically wiping out their contribution, making it

impossible to determine accurate values. Therefore, in our calculations we considered the cZnS single crystal value $a = 7.987\times10^{-4}$ cm^{-1} [11].

Table 1. The SH parameters at RT of the substitutional Mn^{2+} ions in cZnS:Mn QDs, called the Mn(I) centers, as well as of the surface Mn(II) and Mn(III) centers, are presented and compared with previously reported values in cZnS NCs and similar values from substitutional Mn^{2+} ions in ZnS single crystals. The hyperfine (A) parameter and the cubic (a), axial (a-F, D) and rhombic (E) ZFS parameters are given in 10^{-4} cm^{-1} units.

Lattice host/ Mn^{2+} center	Ref.	g	A	$\|D\|$	a
cZnS:Mn QDs / Mn(I)	[17,18]	2.0022	-63.7	41	7.987
cZnS:Mn QDs / surface Mn(II)	[17,18]	2.0012	-80.5	~10-80	
cZnS:Mn QDs / surface Mn(III)	[17,18]	2.0009	-86.8	~ 10-90	
cZnS:Mn NCs/ NC1	[5]	2.003	-64.5		
cZnS:Mn NCs / SI	[6]	2.0010	-63.9	1.0	
ZnS:Mn NCs/ center I	[7, 8]	2.0024	-64.5	91.0	
cZnS:Mn NCs /samples 1 and 2	[9]	g_{xx} = 2.0064 g_{yy} = 2.0064 g_{zz} = 2.0066	A_{xx} = -63.9 A_{yy} = -64.0 A_{zz} = -64.4	37.4 |E| = 12.47	
cZnS:Mn NCs / Ib	[10]	$g_{\square}$ = 2.0075 $g_{\|\|}$ = 2.0040	$A_{\square}$= -63.8 $A_{\|}$= -65.2	37.4 |E| = 12.47	
cZnS:Mn single crystal / substitutional Mn^{2+}	[11]	2.00225	-63.88	0	7.987
Mixed polytype ZnS:Mn single crystal / trig. Mn^{2+} (PN center)	[20,21]	2.0018	-64.9	36.1	7.35 a-F = 7.4
Microtwined cZnS:Mn single crystal / trig. Mn^{2+} (PN center)	[22]	2.0016	-64.5	37.85	a-F = -7.5

The quality of the fitting with the experimental spectra (see Fig. 2) demonstrates that the substitutional Mn(I) center EPR spectra are well described by the SH (1), which includes, besides the cubic terms with g and A values very close to those found in the cZnS single crystals, the axial ZFS term with $|D| = 41\times10^{-4}$ cm^{-1}. The resulting SH parameters presented in Table 1 are also in good agreement with the

values we have previously obtained from the analysis of the X- and W-band EPR spectra [17]. As discussed in Ref. [18], which was dedicated to their structure and properties, the two surface Mn(II) and Mn(III) centers represent Mn^{2+} ions localized at the surface of the cZnS:Mn NCs in partly oxidized areas, without or with an adsorbed water molecule attached, respectively.

The additional axial ZFS term involved in describing the EPR spectrum of the substitutional Mn^{2+} ions in the investigated cZnS:Mn QDs is related with the presence of a local axial crystal field component (or local distortion of the lattice) at the cation Zn^{2+} site, with otherwise pure cubic (T_d) symmetry in the bulk cZnS single crystals [11]. The resulting value of the *D* parameter suggests a unique configuration with a neighboring defect, either as an unintentional impurity, or as an intrinsic lattice defect. A neighboring natural impurity seems unlikely, because the estimated ~200 ppm concentration of Mn^{2+} ions in our cZnS:Mn QDs is too high compared to the trace impurity levels in the starting materials. A neighboring intrinsic point defect (vacancy/interstitial) is also unlikely, in view of the similar electrical charges and close radii of the Mn^{2+} impurity and substituted Zn^{2+} cation. Also, a local axial crystal field resulting in a ZFS term with finite *D* parameter value could not be caused by the presence of size induced strains in the QDs [19]. The random character of such strains can only contribute to the experimentally observed inhomogeneous broadening of the EPR lines in QDs.

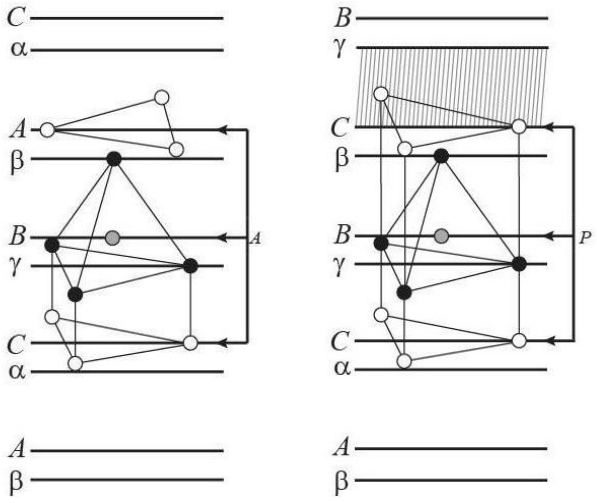

Fig. 3. The local structure at the substitutional Mn^{2+} ions, shown in the left hand side drawing for a pure cubic ZnS single crystal lattice and in the right hand side drawing for a Zn^{2+} lattice site perturbed by the presence of a neighboring stacking fault (shaded area) resulting in a trigonal distortion at the Mn^{2+} ion (grey), called the PN center. In both drawings the Zn^{2+} cations and S^{2-} anions are represented by open and filled circles, respectively, aligned as {111} layers, and the substitutional Mn^{2+} at a Zn^{2+} cation site by a shaded circle.

A more plausible explanation is obtained by comparing the SH parameters of the substitutional Mn(I) center with the corresponding parameters of the substitutional Mn^{2+} (PN) center with local trigonal symmetry and very close SH parameter values, reported in mixed polytype ZnS or micro-twined cZnS single crystals [20-22]. As shown from correlated theoretical calculations and optical investigations, the PN center consists of a substitutional Mn^{2+} ion at a Zn^{2+} site where the normal stacking sequence of layers along the sphalerite <111> direction (equivalent to *c*-axis in wurtzite), at the third order neighboring ligands, was changed by the gliding of a neighboring layer due to a stacking fault or twin [20-22]. From the close values of the axial ZFS parameter *D* of the PN center in ZnS:Mn single crystals and the Mn(I) center in the cZnS QDs (see Table 1) one concludes that in the later case the substitutional Mn^{2+} impurity is localized in a {111} layer, which contains the Mn^{2+} ion and its tetrahedrally coordinating sulfur ligands, lying next to a stacking fault or twin. The resulting PN center–type configuration, illustrated on the right hand side in Figure 3 is characterized by the presence of a local axial (trigonal) crystal field at the substitutional Mn^{2+} impurity ion, which leads to the additional axial ZFS term in the SH (1). The small differences in the measured SH parameters of the substitutional Mn(I) centers in the cZnS QDs and of the PN center in the defective ZnS single crystals (see Table 1) are attributed to experimental errors and/or possible slight differences in the arrangement of the first neighboring ligands in the single crystals and nanocrystals, respectively.

In order to confirm the validity of the proposed ELD model of localization of the Mn^{2+} ions in the cZnS:Mn QDs we had to prove that a rather large concentration of such defects exists in the investigated QDs. In crystals with a sphalerite structure planar stacking defects such as stacking faults and twins are known to occur along the {111} planes. To reveal the stacking defects in the cZnS:Mn QDs we performed high resolution transmission electron microscopy (HRTEM) investigations. One should mention that the atomic structure of the extended defects can be imaged by HRTEM only if the defects exhibit translation symmetry along the viewing direction. For crystals with sphalerite structure this condition is fulfilled along the [110] viewing direction. Figure 4 shows HRTEM images of very thin parts of cZnS:Mn QDs which were extracted from a cZnS:Mn nanocrystalline sample previously investigated by EPR spectroscopy. As shown in the picture some of the cZnS QDs exhibit planar extended defects such as twins (T) or stacking faults (SF), marked by arrows. Any substitutional impurity localized in a cation site next to these defects (Figure 3) will be therefore in a disturbed neighborhood, with regard to the perfect cubic lattice, in agreement with our EPR investigations.

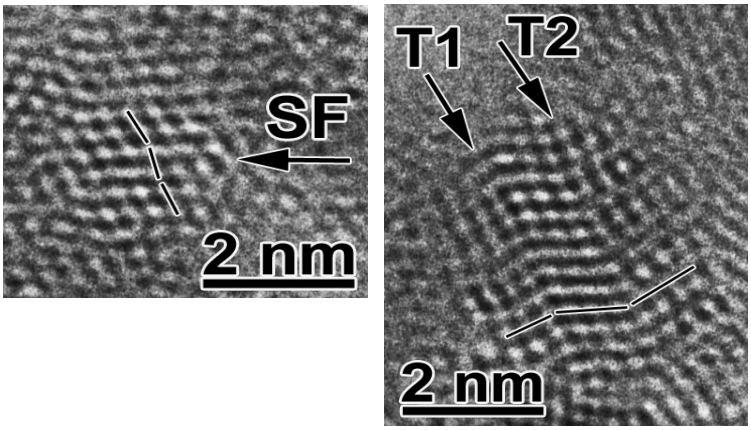

Fig. 4. HRTEM image of cZnS:Mn QDs from a sample previously investigated by EPR spectroscopy revealing in some crystallites (marked by arrows) planar defects such as twin interfaces (T) and stacking faults (SF).

By examining several HRTEM images we found out that a rather large amount (at least 30%) of the cZnS:Mn QDs oriented along [110] contain planar extended defects in the form of stacking faults and twins. Considering that the ZnS:Mn nanocrystallites are arbitrarily oriented in the investigated sample it results that a corresponding fraction of them contain such extended defects, which represents more than enough to explain the observed concentration of the substitutional Mn(I) centers. The observation of the extended defects by HRTEM also confirms the simulation results based on a Debye function analysis, which has shown [23] that the presence in the small cZnS nanocrystals of extended defects in the form of twins is essential for an accurate fitting of the experimental XRD patterns.

4. Conclusions

Considering that no sizable amount of substitutional Mn^{2+} ions localized at unperturbed Zn^{2+} cation sites with T_d symmetry could be identified in our investigated cZnS:Mn QDs, it results that the ELDs in the form of stacking faults and twins are essential in the localization of the Mn^{2+} ions in the cZnS QDs.

The presence of a local axial ZFS term of comparable magnitude in the SH describing the EPR spectrum of substitutional Mn^{2+} ions has been reported in cubic CdS nanocrystals [24] as well and occurs very likely in ZnSe:Mn nanocrystals, which also exhibit forbidden hyperfine transitions in the Mn^{2+} EPR spectrum [25]. Therefore, it is reasonable to assume that a similar localization of the substitutional Mn^{2+} ions involving a neighboring extended defect is valid for other cubic II-VI semiconducting nanocrystals doped with Mn^{2+} and possible with other divalent cations such as Co^{2+}.

The localization of the substitutional Mn^{2+} in the II-VI semiconductor QDs next

to ELDs has some very important fundamental and applicative implications. Thus, it demonstrates that the ELDs play an essential role in the incorporation of Mn^{2+} and possibly of other divalent impurities in the very small nanocrystals, which usually do not exhibit well defined facets, considered [2] essential for activating the diffusion assisted incorporation of impurities. On the other hand, it is well known that extended defects such as steps on the surfaces or dislocations, which emerge when the extended defects intersect the nanocrystals surface, are very likely to "attract" impurities [26]. Therefore, one expects the doping to be mainly controlled by the trapping of impurities at the steps and dislocations at the surface of the growing nanocrystals, a mechanism which was not considered up to now.

The large fraction of planar extended defects observed in our investigated cZnS:Mn QDs samples can also explain the relatively high fraction of the doping Mn^{2+} impurities (more than 10%) found in the investigated cubic II-VI semiconductor QDs [25] and still unexplained, as well as the high concentrations of Mn^{2+} impurities, including the formation of impurity aggregated states at higher dopant concentrations, previously reported in ZnS nanocrystals of comparable size [6-8, 10].

We should also mention that, according to our results, at higher dopant concentrations one expects the impurities to aggregate preferentially in {111} planes parallel to the extended defects, resulting in properties specific for 2D systems, a subject to be further investigated.

In summary, we conclude that the high doping levels of Mn^{2+} ions in the cubic II-VI semiconductor QDs prepared by colloidal growth are very likely controlled by the proposed mechanism of extended lattice defects assisted (ELDA) incorporation of impurities. This mechanism also explains the reported localization of Mn^{2+} impurities at cation sites situated next to an extended lattice planar defect, resulting in a local crystal lattice deformation at the impurity ion, which should also be taken into consideration in the description of the local quantum states and resulting optical, electrical and magnetic properties.

Acknowledgements. The present research was supported by CNCSIS-UEFISCSU, project number PN-II-ID-523/2008, and ANCS in the frame of the project Nucleu PN09-450102.

References

[1] ERWIN S.C., ZU L., HAFTEL M.I., EFROS A.L., KENNEDY T.A. and NORRIS D.J., Nature **436**, pp. 91–94, 2005.
[2] NORRIS D.J., EFROS A.L. and ERWIN S.C., Science **319**, pp. 1776–79, 2008.
[3] ABRAGAM A. and BLEANEY B., Electron Paramagnetic Resonance of Transition Ions, Clarendon Press, Oxford, 1970.
[4] HU H. and ZHANG W., Opt. Mat. **28**, pp. 536–50, 2006.
[5] KENNEDY T.A., GLASER E.R., KLEIN P.B. and BHARGAVA R.N., Phys.Rev. B **52**, pp. R14356–59, 1995.

[6] BORSE P.H., SRINIVASA D., SHINDE R.F., DATE S.K., VOGEL W. and KULKARNI S.K., Phys. Rev. B **60**, pp. 8659–64, 1999.
[7] IGARASHI T., IHARA M., KUSUNOI T., OHNO K., ISOBE T. and SENNA M., J. Nanoparticles Res. **3m**, pp. 51–56, 2001.
[8] IGARASHI T., ISOBE T. and SENNA M., Phys. Rev. B **56**, pp. 6444–45, 1997.
[9] GONZALEZ BEERMANN P.A., MCGARVEY B.R., MURALIDHARAN S. and SUNG R.C.W., Chem. Mater. **16,** pp. 915–18, 2004.
[10] GONZALEZ BEERMANN P.A., MCGARVEY B.R., SKADTCHENKO B.O., MURALIDHARAN S. and SUNG R.C.W., J. Nanoparticles Res. **8**, pp. 235–41, 2006.
[11] NISTOR S.V. and STEFAN M., J. Phys.: Condens. Matter **21**, 145408 (7pp), (2009) and references cited therein.
[12] NISTOR L.C., MATEESCU C.D., BIRJEGA R. and NISTOR S.V., Appl. Phys. A **92**, pp. 295–301, 2008.
[13] NISTOR S.V., NISTOR L.C., STEFAN M., MATEESCU C.D., BIRJEGA R., SOLOVIEVA N. and NIKL M., Superlatt. and Microstruct. **46**, pp. 306–11, 2009.
[14] NISTOR S.V., STEFAN M., NISTOR L.C., MATEESCU C.D., BIRJEGA R., J. Nanosc. Nanotechn. **10**, pp. 1–6, 2010.
[15] NISTOR S.V., NISTOR L.C., STEFAN M., GHICA D., MATEESCU C.D. and BIRJEGA R., Rom. Rept. Phys. **62**(2), pp. 319–28, 2010.
[16] RUBIO J.O., MUNOZ P.E., BOLDU O.J., CHEN Y. and ABRAHAM M.M., J. Chem. Phys. **70**, pp. 633–38, 1979.
[17] NISTOR S.V., STEFAN M., NISTOR L.C., GOOVAERTS E., and TENDELOO Van G., Phys. Rev. **B 81**, 035336 (6pp), 2010.
[18] STEFAN M., NISTOR S.V., GHICA D., MATEESCU C.D., NIKL M., and KUCERKOVA R., Phys. Rev. **B 83,** 045301 (11 pp), 2011.
[19] QADRI S.B., SKELTON E.F., HSU D., DINSMORE A.D., YANG J., GRAY H.F. and RATNA B.R., Phys. Rev. B **60**, pp. 9191–939, 1999.
[20] LAMBERT B., BUCH T. and CLERJAUD B., Sol. State Commun. **10**, pp. 25–27, 1972.
[21] BUCH T., CLERJAUD B., LAMBERT B. and KOVACS P., Phys. Rev. B **7**, pp. 184–91, 1973.
[22] YAKUNIN A., SHTAMBAR I.V., KUSHNIR A.S. and OMELCHENKO S.A., Russian Phys. J. **16**, pp. 1375–79, 1973.
[23] VOGEL W., BORSE P.H., DESHMUCK N. and KULKARNI S.K., Langmuir **16**, pp. 2032–37, 2000.
[24] COUNIO G., ESNOUF S., GASCOIN T. and BOILOT J.P., J. Phys. Chem. **100**, pp. 20021–26, 1996.
[25] NORMAN Jr.T.J., MAGANA D., WILSON T., BURNS C., ZHANG J.Z., CAO D. and BRIDGES F., J. Phys. Chem. B **107**, pp. 6309–17, 2003.
[26] AMELINCKX S., *The Direct Observation of Dislocations*. In Solid State Physics: Advances in Research and Applications. Suppl. **6**, pp. 55–89, Seitz F. & Turnbull D., Eds., Academic Press: New York, 1964.

Growth and Characterization of Ultrathin Fe Magnetic Layers Deposited on Atomically Clean Si(001) by Molecular Beam Epitaxy

N.G. GHEORGHE, M.A. HUSANU, G.A. LUNGU, D. MACOVEI, V. KUNCSER, R.M. COSTESCU, D.G. POPESCU, C.M. TEODORESCU

National Institute of Material Physics Bucharest-Magurele, Atomistilor
E-mail nicoleta.gheorghe@infim.ro

Abstract. We present the very first surface physics experiments performed in ultrahigh vacuum (UHV) in Romania. A technology for cleaning Si(001) wafers was achieved by using annealing at 900-1000°C in UHV. Fe layers grown on the Si(001) single crystal surface are characterized by low energy electron diffraction, reflection high energy electron diffraction, and Auger electron spectroscopy. The clean sample contamination and the interface reactivity are assessed by these combined techniques, whereas magnetism of Fe is investigated by magneto-optical Kerr effect. Higher deposition temperatures yield better surface ordering, but also enhance Fe and Si interdiffusion and decrease the Fe magnetic moment.

1. Introduction

A key test of most surface science UHV apparatuses, and especially of MBE installations, is the cleaning of semiconducting samples, of which Si(111) and Si(001) are the most used examples. This allows the setup and comissioning of standard characterization devices, such as (i) for structural characterization: LEED, RHEED; (ii) for chemical characterization: AES, XPS. Usually, silicon substrates are prepared by flashes at very high temperatures (1200 – 1400°C) [1-3], cycles of Ar^+ sputtering and annealing [4-6], cleavage under UHV [7], RCA (Radio Corporation of America) method and other wet chemical methods [8-9], gas source MBE [10], laser ablation [11-12]. Any of these methods has specific disadvantages. Sputtering introduces defects, very high temperature flashes induces the risk of melting the sample, cleavage is rarely reproducible, gas source MBE is using high risk gases, etc.

In this paper we investigate a novel and cheap method for preparing atomically clean samples of Si(001) just by annealing them in ultrahigh vacuum. Once established, the method may be repeated several times with reproducible results in obtaining low-contamination, well characterized surfaces of Si(001). The characterization was mainly performed by LEED and AES, but also RHEED was used for investigating the cleanliness of the sample and the surface reconstruction. Consistent investigation and analysis of AES allowed derivation of the kinetics of contamination and the nature of the reacted compounds formed at the surface.

Iron layers deposited on silicon have been subject of numerous investigations in the past, since this interface involves both the most common pure ferromagnetic metal and the most used semiconductor in the industry. One of the global aims of our research is to provide recipes for fabrication of ferromagnetic contacts on semiconductors for spin injection. However, spin injection efficiency is strongly dependent on the reactivity at interface. At the same time, the magnetism of the layers is strongly perturbed by the interface reactivity [13].

In the present paper we will address Fe/Si(001) interfaces, for which fewer studies combining reactivity with magnetism are reported up to the present moment.

When the Fe deposition is performed at room temperature, Si diffusion into the Fe film promotes a layer of approximate composition Fe_3Si [14], which becomes ferromagnetic for coverages exceeding 3.6 ML ≈ 5 Å [15] or about 7 Å [16-17].

The aim of this paper is to investigate the long- and short-range ordering, composition and magnetic properties of Fe deposited onto Si(001) in order to see which are the correlations between magnetic properties, interface reactivity and local atomic order. The long-range order was investigated by LEED, the chemical reactivity and the intermixing by Auger electron spectroscopy (AES), and the magnetic properties by magneto-optical Kerr effect (MOKE).

2. Experimental Aspects

2.1. *Description of the experimental cluster for surface and interface science*

The Cluster represents one of the most complexes such systems in Europe, which makes possible the preparation and characterization *in situ* of surfaces and interfaces, and consists of four units, of which the first three are mutually coupled (Fig. 1):

- The MBE (Molecular Beam Epitaxy) Chamber
- The STM (Scanning Tunneling Microscope) Chamber
- The Spin- and Angle-resolved Photoelectron Spectroscopy (SARPES)
- The PEEM (Photoemission Electron Microscopy) and LEEM (Low Energy Electron Microscopy) System.

All devices operate in ultra-high vacuum (1-2 x 10^{-10} mbar). It is possible to perform *in situ* characterization by low energy electron diffraction (LEED), reflection high energy electron diffraction (RHEED), Auger electron spectroscopy (AES), quadrupole mass spectroscopy (QMS), classical and high-resolution X-ray photoelectron spectroscopy (XPS), ultraviolet photoelectron spectroscopy (UPS), etc.

The performance of the complex system described above is illustrated in Fig. 2 for high resolution photoelectron spectroscopy (line widths comparable to that obtained with synchrotron radiation sources) and in Fig. 3 for scanning tunneling microscopy with atomic resolution. Further, Fig. 4 shows the first results obtained for the visualization of the monatomic terraces of Si(001) by low energy electron microscopy (LEEM). The ultimate resolution achieved with the LEEM in darkfield mode is 4.1 nm (20-80 % criterion).

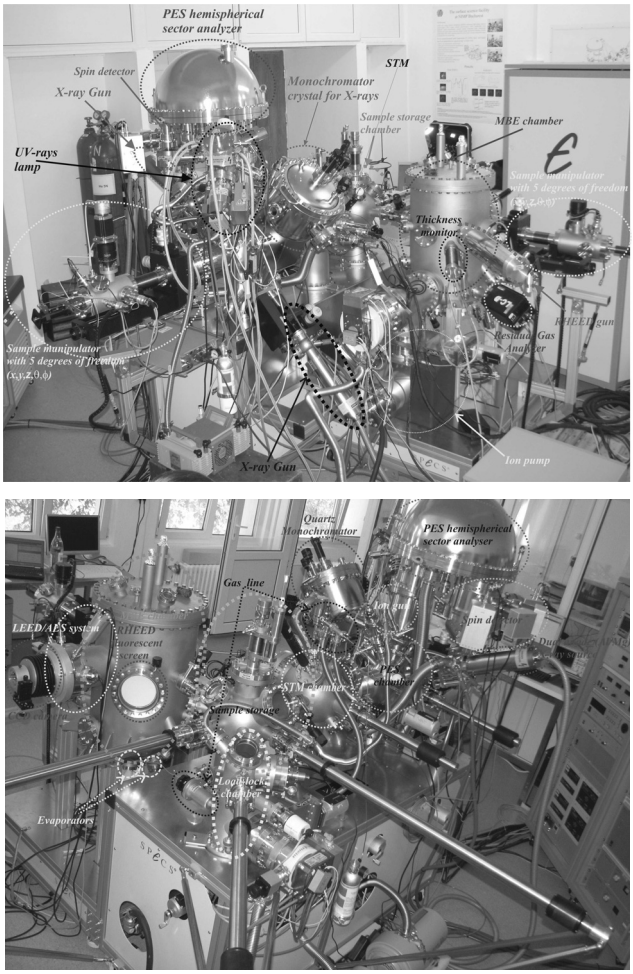

Fig. 1. Experimental measurement cluster for surface and interface science.

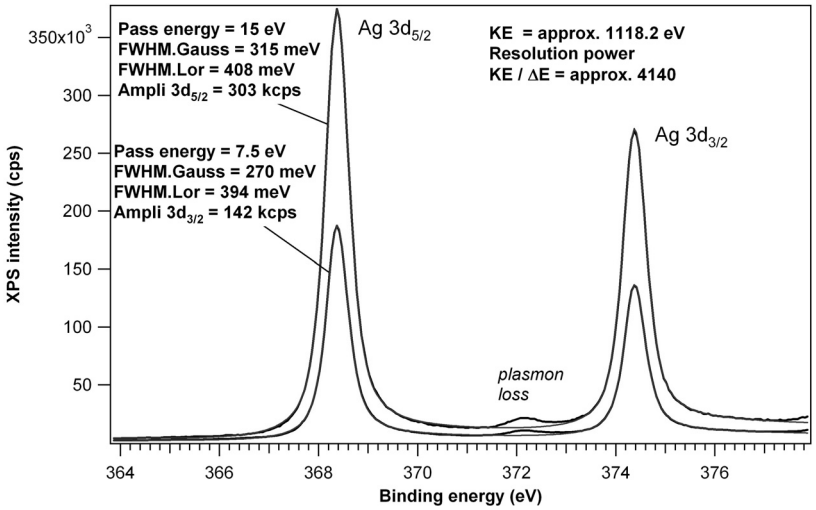

Fig. 2. High resolution XPS spectra for an Ag foil using a monochromatized X-ray source.

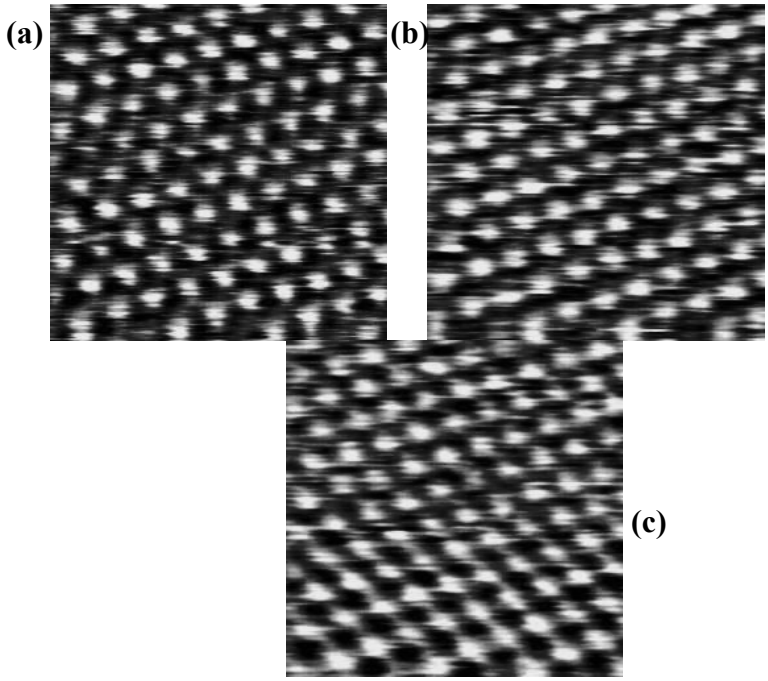

Fig. 3. Scanning Tunneling Microscopy (STM) images with atomic resolution obtained on highly oriented pyrolytic graphite (HOPG) (0001), with different tip voltages: (a) 630 mV; (b) 713 mV; (c) 884 mV.

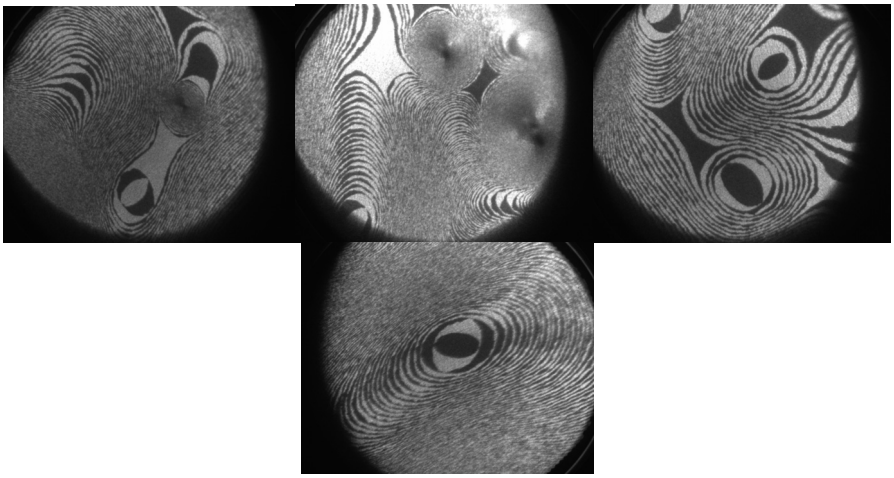

Fig. 4. LEEM darkfield images on one of the diffraction spots (1/2, 0) of the Si(001) surface reconstruction. The size of the image (field of view, FOV) is 3 μm.

In approximately 18 months of surface and interface operation, there have been a significant number of scientific papers published in ISI ranked journals with significant impact factor. To date, outstanding contributions using this setup were reported on catalytic systems [18-21], oxides with photocatalytic or diluted magnetic behavior [22-26], nanoparticle systems [27-28], ferroelectrics [29-30], silicon carbide/silica heterostructures [31], and hydrogen storage materials [32].

2.2. *Preparation of atomically clean Si(001)*

Two-domain Si(001) single crystal wafers were cleaned by repeated cycles of annealing at 900-1000°C. The typical time of an annealing step is 30 min. The composition of the residual gas was monitored with the QMS. After each cycle of annealing, the state of the surface contamination was checked by AES, and its crystallinity by LEED and RHEED. RHEED was proven to be a less surface sensitive technique: RHEED spots started to appear well before achieving the surface cleaning at atomic level. By contrast, LEED patterns were visible only when the sample was almost clean. Also, only the clean sample showed visible RHEED lines, denoting a flat surface [13, 33].

Achieving a LEED pattern also allowed inspection of the whole surface of the sample and practically the whole surface presents long range ordering. This was not the case with samples prepared by Ar^+ sputtering or by very high temperature annealing [1-2], where only a part of the sample presented a well-defined LEED pattern.

2.3. *Growth of Fe layers by molecular beam epitaxy*

Ultrathin Fe layers were prepared on atomically clean Si(001) in the molecular beam epitaxy chamber operating in the pressure range of low 10^{-10} mbar. The samples are investigated *in situ* by Auger electron spectroscopy (AES) (Fig. 5 presents AES survey spectra of the as-prepared Si(001) and of the 6.7 nm Fe deposition on Si(001), respectively) and low-energy electron diffraction (LEED). Single crystals of Si(001) were cleaned by heating Si(001) wafers at 1200 °C for 30 minutes in a vacuum not exceeding 5×10^{-9} mbar, then waiting for the vacuum recover back to low 10^{-10} mbar.

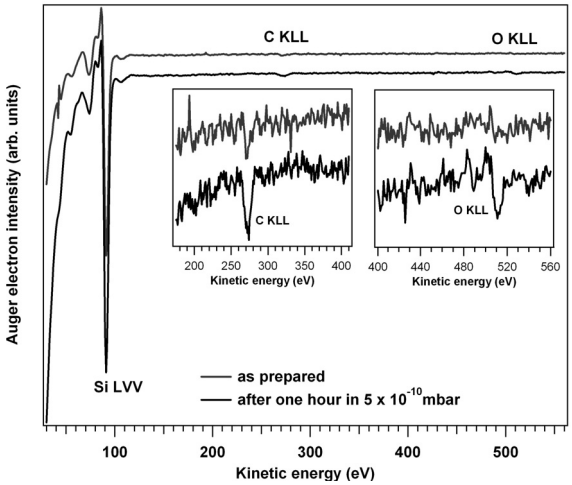

(a)

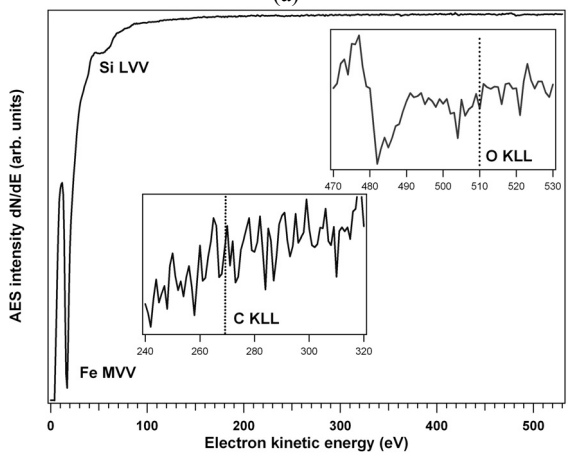

(b)

Fig. 5. Survey scans of Auger electron spectroscopy (a) on the as-prepared Si(001) sample and (b) on a layer of 6.7 nm Fe immediately after its deposition on Si(001).

Fe was evaporated from a Specs EBE-4 electron bombardment source at a rate of 0.06 Å/s and at normal incidence. The base pressure was in the low 10^{-9} mbar range during deposition. 1 monolayer (ML) of Fe is equivalent to about 1.43 Å, as indicated by the thickness monitor set with Fe parameters (density, *Z*-factor).

After the deposition, the samples were capped with 30 Å of Au (deposited also near normal incidence) and characterized *ex situ* by MOKE, using a setup manufactured by AMACC Anderberg and Modéer Accelerator AB. The maximum applied field was 0.6 T and the measurements were performed at room temperature.

3. Results and Discussions

3.1. *Clean Si(001)*

Fig. 6 presents AES recorded during the sample cleaning. We note a considerable shift of around 15 eV towards higher kinetic energies for the as-introduced sample. For instance, the Si-O peak results at 90 eV, value very close to the Si-Si peak of 92 eV, well known in literature [4, 11], although some authors report slightly lower values: 91 eV [3, 5] or even 90 eV [10]. We attribute this shift to the inherent contamination layer from the as-introduced sample, which behaves like an insulator and becomes charged by the primary electrons produced by the spectrometer. After the first annealing cycle, the Si^0 line moves its position to 91-92 eV, whereas the oxidized Si^{4+} line shifts towards 78 eV, in good agreement with data from literature [3, 5]. Subsequent annealing cycles do not change the situation drastically; whereas after the fourth annealing a diffuse LEED pattern appears and the Si LVV AES looks quite different (see Fig. 6). A last cycle of annealing resulted in the vanishing of the Si^{4+} (78 eV) line, a strong reinforcement of the Si^0 (92 eV) line, and the disappearance of the oxygen KLL line (see Fig. 6, black curve). The carbon KLL line did not disappear, but decreased in intensity. By using Auger atomic sensitivity factors [34] it is estimated that the remaining carbon represents about 4 ± 2 % of a single atomic layer. This contamination is possible to appear during the time interval between the achievement of the preparation procedure and the measuring of this line (15-20 min. are elapsed between these two events).

At the end of the cleaning procedure, sharp LEED patterns were obtained, as evidenced in Fig. 2. Also, the spots belonging to both (2×1) and (1×2) reconstructions are quite well observed, since the wafer was not miscut as to provide single domain reconstruction [35]. Fig. 8 presents the

RHEED pattern obtained along the <110> axis on the clean sample. Although the mounting of the sample on the sample holder was such as no direct observation along the highest symmetry axis <100> was possible, the <110> RHEED also provided fractionary spots, which reconfirmed the (2 × 1) - (1 × 2) reconstruction of the surface.

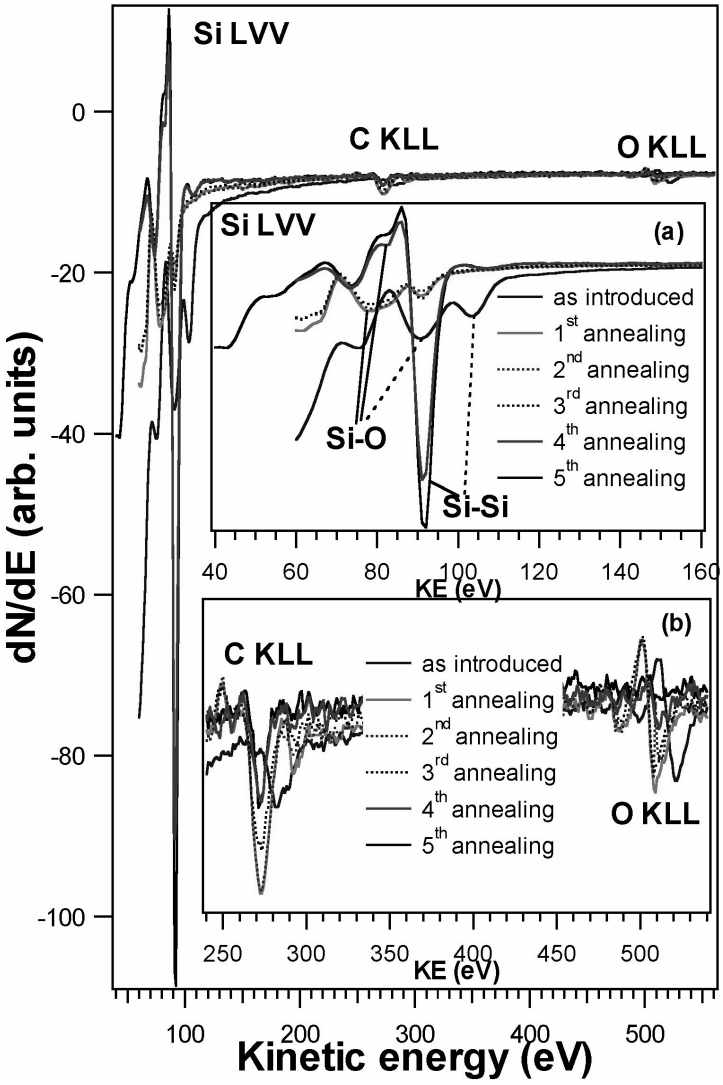

Fig. 6. Auger electron spectra of the Si(001) sample during the annealing cycles. Inserted are (a) detail of the Si LVV lines; (b) detail of the C KLL and O KLL lines.

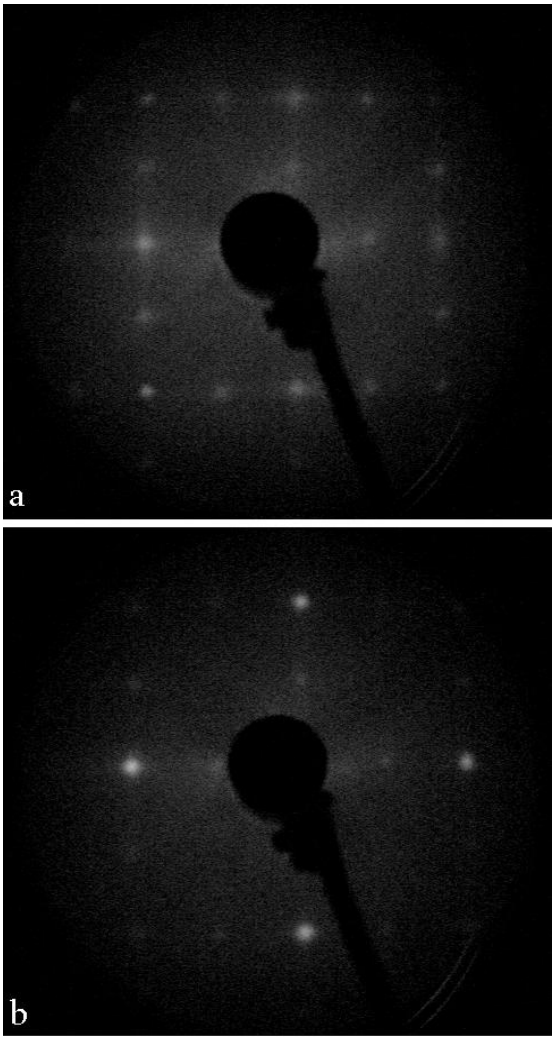

Fig. 7. LEED patterns obtained with primary electrons at 55.9 eV (a) and 43.8 eV (b). The (01) spots are the brigthest ones from (b). One may also observe distinct (0 1/2) spots.

3.2. *Surface contamination in ultrahigh vacuum*

After successful preparation, the sample was measured continuously by AES. The composition of the residual gas during these measurements is represented in Fig. 9. The influence of these molecules results in contamination of the sample, as demonstrated in Fig. 10. The Si^0 LVV peak decreases in intensity, the Si^{4+} LVV peak (or oxidized silicon) starts to manifest [see Fig. 10(b)], whereas the carbon and oxygen KLL peaks increase [see Fig. 10(c)].

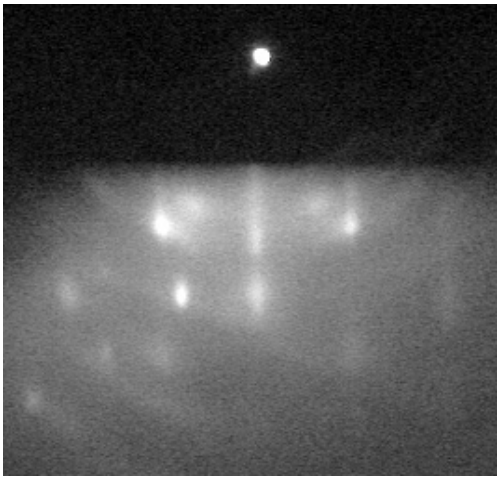

Fig. 8. RHEED pattern along one <110> axis.

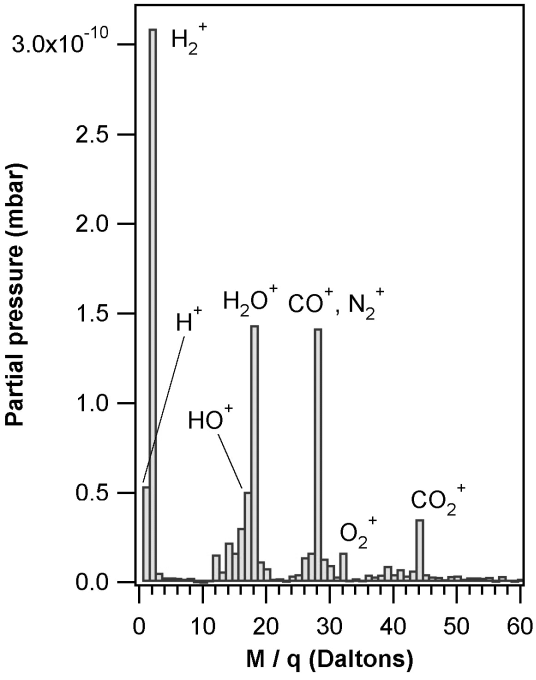

Fig. 9. Typical residual gas analysis (mass spectrum) recorded during AES measurements.

The contamination evolves by primary surface chemical reactions [7], but might also be induced by electron impact from the Auger spectrometer [3]. The next step was to plot the evolution of the intensity of the different peaks (Si4+ LVV, Si0 LVV, C KLL and O KLL), versus time. Consequently, we had to introduce a curve fitting in order to derive the intensity, defined as the minimum value from which the maximum value is subtracted (resulting in a net negative value).

The peaks are asymmetric; therefore a deconvolution with a symmetric function, such as a Voigt profile [36] was not successful. In Fig. 10(c), the C and O Auger spectra were fitted by using an analytical approximation of the convolution of the Beutler-Fano profile with a Gaussian lineshape accounting for the finite resolution of the spectrometer [37].

The use of the Beutler-Fano profile has the following explanation: the Auger effect is an autoionization process, result of a de-excitation of a discrete resonance (creation of a core hole) embedded in a continuum of multiparticle ionization [38]. In Fig. 11 the evolution of the five signals of interest (Si^{4+} LVV, Si^{0} LVV, C KLL and O KLL) are represented as function of time. The data were fitted with exponential decays, such as $I(t) = I(0) + A \exp(- t / \tau)$. The resulting fitting parameters are represented in Table 1. We observe that the Si^{4+} LVV signal may be well approximated by a saturation formula of the type Const. x $\{1 - \exp(- t / \tau)\}$ (note that Const. is a negative value), whereas the Si^{0} LVV signal is better approximated by a formula on the type Const. x $\{1 + \exp(- t / \tau)\}$. This is somehow confusing, since one expects that with infinite contamination (or time spent in the chamber) the clean surface signal should disappear completely. Also, from the carbon contamination one obtains a C KLL signal of - 1.661 + 0.320 = -1.341 units, which is inherently present on the sample from the very beginning. This produces a contamination of some -1.341 / (-50.46 - 54.58) ≈ 0.0128, but this has to be multiplied with the ratio between the Auger sensitivity factors: 0.924 for Si LVV and 0.282 for C KLL [36]. This results in an overall contamination of ~ 4.2 %. Finally, the O KLL signal obeys a saturation-like law, but with a very long lifetime. This suggests that the well known Si^{4+} LVV signal at 78 eV may be due not only to formation of Si-O bonds (therefore the lifetimes of this signal and that of oxygen KLL should be similar), but rather to the formation of Si-CO complexes. Finally, we try to explain the unexpected behavior of the clean silicon signal.

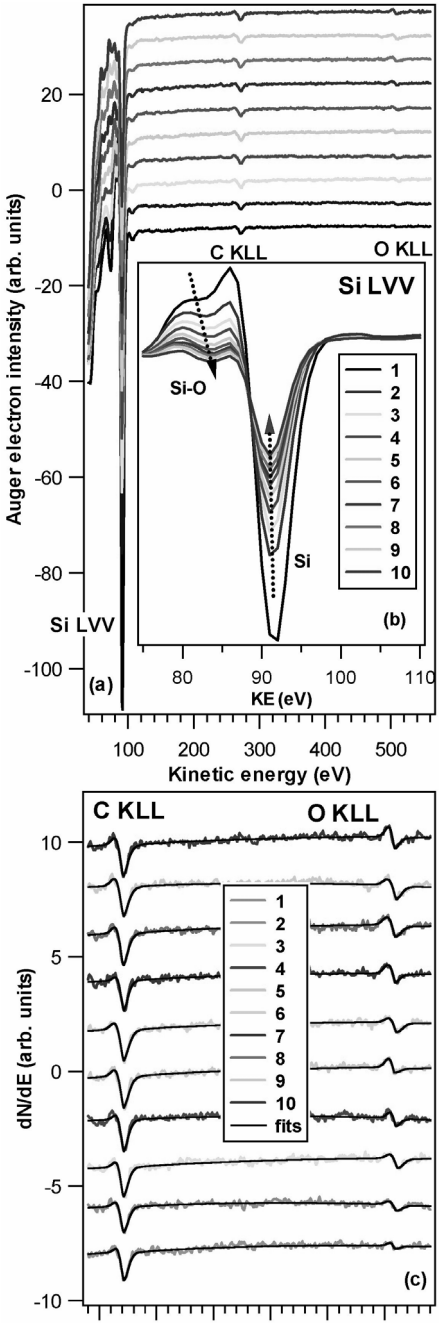

Fig. 10. AES spectra taken progressively in UHV, in order to monitor the sample contamination. (a) Represents an overview scan, (b) the Si LVV region, and (c) the C and O KLL regions.

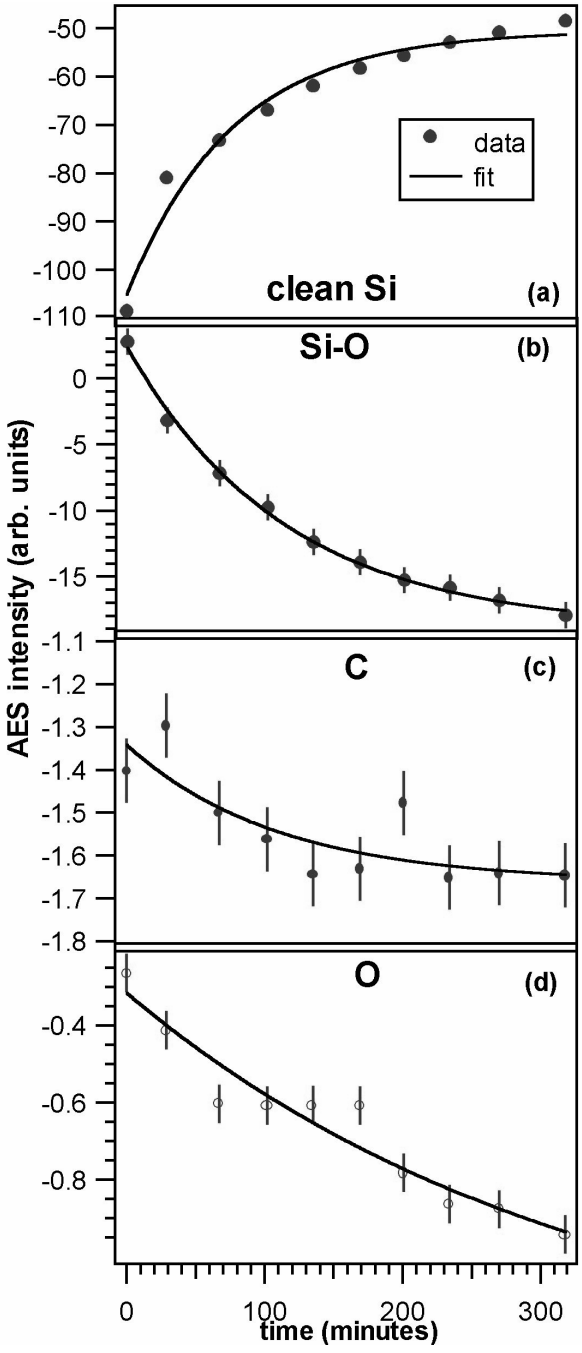

Fig. 11. Time evolution of the signals from Si^{0} LVV (a), Si^{4+} LVV (b), C KLL (c), and O KLL (d), together with exponential fits (see text for details).

Table 1. Values of parameters derived from the fitting of the temporal dependence of Auger signals

AES signal	I (0) [arb.]	A [arb.]	τ [minutes]
Si^0 LVV	- 50.46	-54.58	76.16
Si^{4+} LVV	-18.90	+21.22	115.21
C KLL	-1.661	+0.320	109.89
O KLL	-1.319	+1.004	331.13

In what follows, we supposed that the remaining $I(0)$ peak, representing the Si^0 signal after waiting an infinite time with the sample in the UVH chamber, doesn't show clean silicon, but silicon bonded to carbon, or SiC. Formation of silicon carbide onto clean silicon was reported recently [40], but earlier studies evidenced contamination of Si(111) surfaces in ultrahigh vacuum and formation of SiC islands [9]. Also, the lineshape of the C KLL signal is quite similar to the lineshape of diamond-like nuclei on Si(001) and Si(111) [41]. In Fig. 12 we represented a detail of the Si^0 LVV signal from the spectrum of the clean sample and from the spectrum of the sample at the last AES scan.

A final remark is that even after 300 min of measurements plus 10-12 hours spent in the UHV chamber, the sample still exhibited a broad (1 × 1) LEED pattern and its cleaning was straightforward. This suggests that the silicon carbide-like compound formed at the surface exhibits long range order (results investigated also by STM and high resolution electron energy loss spectroscopy (HREELS) some years ago [9]).

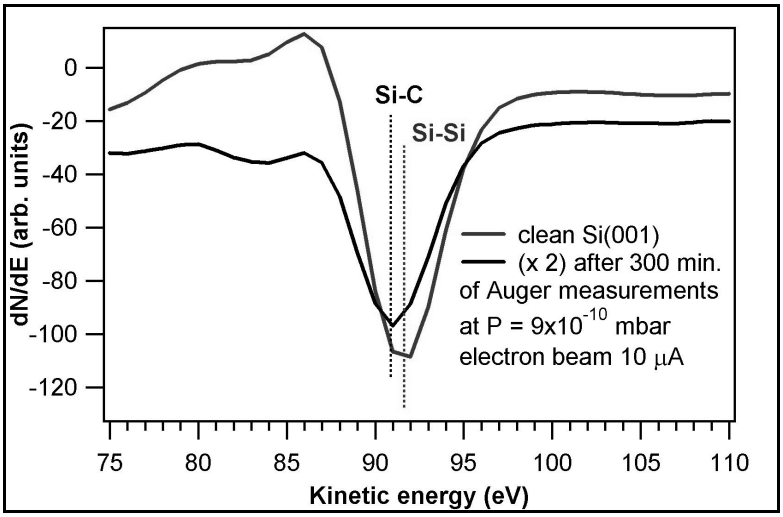

Fig. 12. Detail in the Si^0 AES signal with the spectrum of the clean sample and with the spectrum obtained after 300 min of measurements in UHV under electron impact. The vertical lines represent estimated position of the AES minimum, attributed to clean silicon and to silicon reacted with carbon.

3.3. *Growth of Fe on Si(001)*

3.3.a. *Structure and long range order*

Fig. 13 presents the evolution of LEED patterns when the deposition is achieved at an elevated temperature (500°C). The as-prepared sample exhibits well-defined (2×1) and (1×2) reconstructions. As soon as Fe is deposited, the LEED pattern weakens and broadens and for 2.8 Å deposited, which represents roughly 2 single atomic layers of Fe, only a broad (1×1) pattern is visible. When the deposition is performed at room temperature, the LEED pattern disappears for the lowest quantity of Fe deposited, 0.7 Å, which roughly corresponds to half a monolayer.

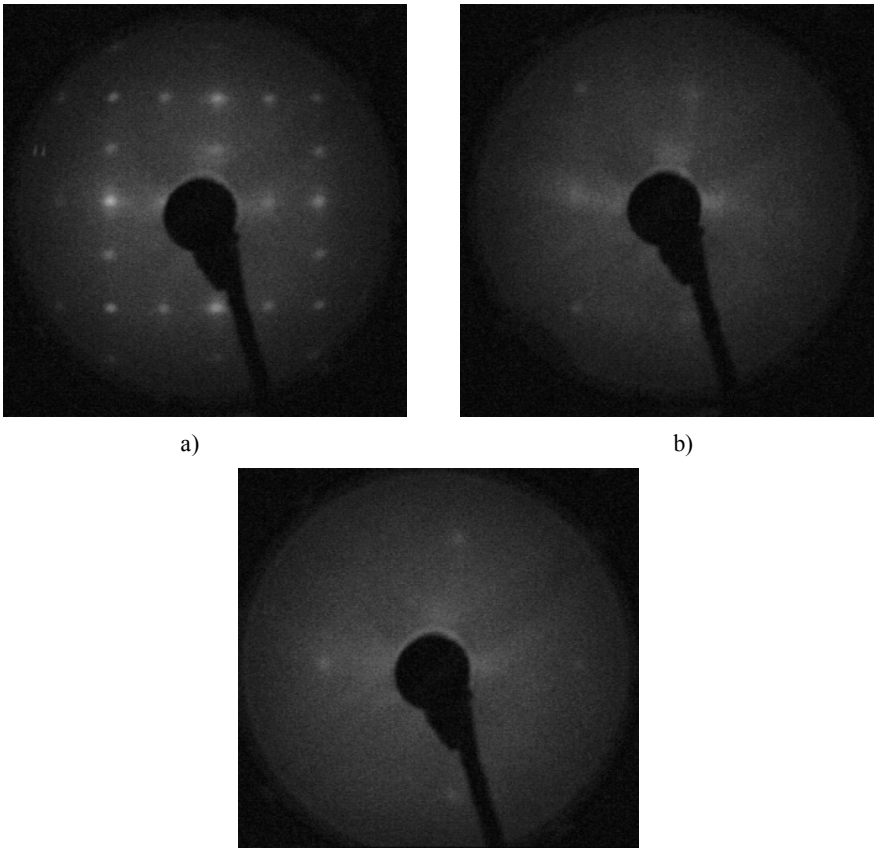

a) b)

c)

Fig. 13. Evolution of LEED patterns with Fe deposition at 500°C.
(a) clean Si(001); (b) 2.1 Å Fe deposited; (c) 8.4 Å Fe/Si(001).

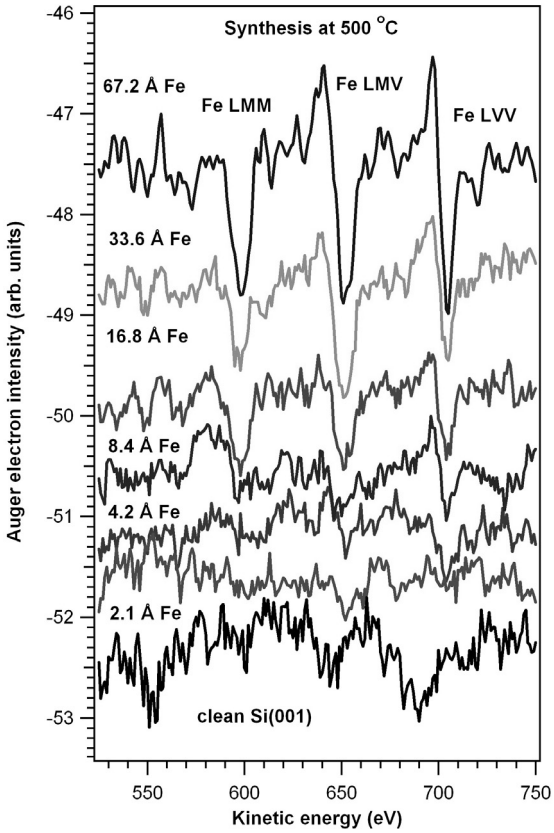

Fig. 14. Auger electron spectra of the Fe LMM, LMV, and LMV signals.

By considering the coherence length of about 25 nm corresponding to electrons of around 50 eV kinetic energy [42], this implies that at room temperature deposition islands with considerable lower lateral dimension are formed on the surface, with increasing surface roughness on the same order of magnitude.

3.3.b *Intermixing and reactivity at the interface*

Fig. 14 presents Auger electron spectroscopy (AES) results obtained from the Fe LMM-LMV-LVV lines for the samples synthesized at high temperature (500 °C). The electron inelastic mean free path (IMFP) is estimated at 9 ± 2 Å in the latter case [43].

For the room temperature deposition, the IMFPs λ_{Si} and λ_{Fe} are close enough and also close to the accepted values for this energy range [43]. Consequently, one may infer that the Fe layer is situated over the Si substrate and that low intermixing occurs. There are some Si atoms diffused into the Fe layer.

3.3.c *Magnetic properties*

Fig. 15 represents MOKE hysteresis loops obtained in both cases of room- and high-temperature. For synthesized at room temperature samples a detectable MOKE signal is observed. Moreover, this signal is different when the applied magnetic field is parallel to one of the <100> or to <110> directions. An uniaxial magnetic anisotropy is observed, although this sample did not exhibit any long range order. The Fe nanoparticles formed whose lateral dimensions are below 20 nm, are in well defined positions with respect to the crystallographic axes of the substrate.

In the case of room temperature deposition, we obtained about 6 mdeg of MOKE signal, which corresponds to 2.4 ± 0.6 nm metal Fe layers. We may infer that the Fe layer is highly likely magnetic and the Fe average magnetic moment in this layer is close to the bulk value of 2.2 μ_B, or perhaps slightly less (1.8-1.9 μ_B). This value is quite similar to the reported value of Fe layers on GaAs(001) or InAs(001), once the interface reaction ends [13].

For the sample synthesized at 500°C, the saturation MOKE signal is one order of magnitude lower than at room temperature, whereas the estimated bulklike Fe layer is about 2 nm. Therefore, an average Fe atomic magnetic momentum of about 0.12 ± 0.03 μ_B is obtained in this case. This is about 5.4 % of the bulk Fe magnetic momentum. Therefore, we might infer that by depositing at high temperature some Fe is still magnetic, but with a very low magnetic momentum.

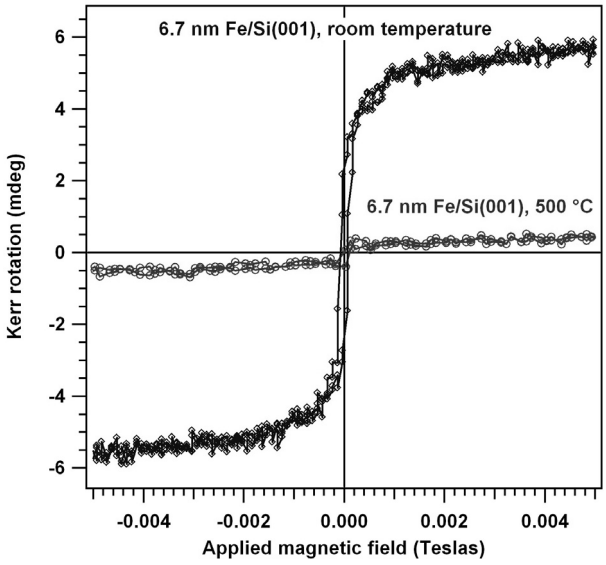

Fig. 15. MOKE hysteresis loops obtained on the samples synthesized (a) at room temperature and (b) at 500°C.

4. Conclusions

The cleaning and contamination processes of Si(001) were reviewed by using a new MBE-XPS installation, permanently monitored by LEED, AES and RHEED. A huge kinetic energy shift of 15 eV was detected between the as-introduced sample and the sample when the cleaning procedure has started. A simple cleaning procedure consisting of successive annealing at not too elevated temperatures was set up, tested and proven. Fair LEED patterns were observed on the clean samples, with (2 × 1) - (1 × 2) reconstructions. Another result was the unexpected success in simulating Auger lineshapes with a convolution between a Beutler-Fano profile and a Gaussian. The systematic study of sample contamination in ultrahigh vacuum exhibited the saturation-like behaviour of the oxidized silicon and of the oxygen signals; however, the evolution of the signal attributed to "clean" silicon cannot be explained unless one assumes that a quite similar energy is obtained from silicon reacted with carbon. In a partial pressure of some 3×10^{-10} mbar of contaminants, the sample is contaminated in slightly more than one hour. Therefore, the sample contamination is quicker than one expects, and the contamination rate, together with the measured partial pressures of contaminants, suggests a sticking coefficient close to unity (assuming that 1×10^{-6} mbar corresponds roughly to a contamination of one atomic layer per second).

New results are also reported concerning the long range order, interface reactivity, and magnetic properties of Fe/Si(001). By growing at room temperature no long range order is detected; however, these small metal Fe particles exhibit noticeable ferromagnetism and uniaxial magnetic anisotropy. When the growth is performed at higher temperatures, Fe reacts completely with Si forming a long range ordered Fe silicide with weak, though detectable, ferromagnetism.

This study constitutes one of the rare ones combining MBE deposition with *in situ* AES and LEED characterization, and with *ex situ* magnetic. We do believe that the facts presented in this paper will contribute to the elucidation of the interface formation in the highly studied Fe/Si(001) system.

Acknowledgements. This work was performed in the framework of the CNCSIS PCCE ID_76/2009 Project.

References

[1] MASCARAQUE A., AVILA J., TEODORESCU C.M., ASENSIO M.C., MICHEL E.G., Phys. Rev. B **55**, p. R7315, 1997.
[2] AVILA J., MASCARAQUE A., TEODORESCU C., MICHEL E.G., ASENSIO M.C., Surf. Sci. **856**, p. 377, 1997.
[3] XU J., CHOYKE W.J., TALES Jr.J.T., J. Appl. Phys. **82**, p. 6289, 1997.
[4] SEFSAF B., CARRIERE B., DEVILLE J.P., Microsc. Microanal. Microstruct. **3**, p. 15 1992.
[5] VISCIDO L., HERAS J.M., J. Phys. Cd. Matter. **5**, p. A159, 1993.
[6] WESTERMANN J., NIENHAUS H., MÖNCH W., Surf. Sci. **311**, p. 101, 1994.

[7] ZAÏBI M.A., LACHARME J.P., SEBENNE C.A., Surf. Sci. **639**, p. 377, 1997.
[8] MARTIN M.G., AVILA J., GRUYTERS M., TEODORESCU C., DUMAS P., CHABAL Y.J., ASENSIO M.C., Appl. Surf. Sci. **156**, p. 123, 1998.
[9] XIE F., BLANCKENHAGEN von P., WU J., LIU J.-W., ZHANG Q.-Z., CHEN Y.-C., WANG E.-G., Appl. Surf. Sci. **139**, p. 181, 2001.
[10] SHIMOSHIKIRYO F., TAKAKUWA Y., MIYAMOTO N., Appl. Surf. Sci. **123**, p. 130, 1998.
[11] LARCIPRETE R., BORSELLA E., J. Electr. Spectrosc. Relat. Phenom. **76**, p. 607, 1995.
[12] CRUZ M.P., DIAZ J.A. and SIQUEIROS J.M., Int. J. Mod. Phys. B **18**, p. 3169, 2004.
[13] TEODORESCU C., CHEVRIER F., ILAKOVAC V., HECKMANN O., LECHEVALIER L., BROCHIER R., JOHNSON R.L., HRICOVINI K., Appl. Surf. Sci. **166**, p. 137, 2000; C.M. Teodorescu, F. Chevrier, R. Brochier, C. Richter, O. Heckmann, V. Ilakovac, P. De Padova, K. Hricovini, Surf. Sci. **482-485**, p. 1004, 2001; C.M. Teodorescu, F. Chevrier, R. Brochier, V. Ilakovac, O. Heckmann, L. Lechevalier, K. Hricovini, Eur. Phys. J. B **28**, p. 305, 2002; C.M. Teodorescu, D. Luca, Surf. Sci. **600**, p. 4200, 2006.
[14] GALLEGO J.M., GARCIA J.M., ALVAREZ J., MIRANDA R., Phys. Rev. B **46**, p. 13339, 1992.
[15] ZAVALICHE F., WULFHEKEL W., XU H., KIRSCHNER J., J. Appl. Phys. **88**, p. 5289, 2000.
[16] PRONIN I.I., GOMOYUNOVA M.V., MALYGIN D.E., VYALIKH D.V., DEDKOV Y.S., MOLODSOV S.L., J. Appl. Phys. **104**, p. 104914, 2008.
[17] PRONIN I.I., GOMOYUNOVA M.V., MALYGIN D.E., VYALIKH D.V., DEDKOV Y.S., MOLODTSOV S.L., Appl. Phys. A **94**, p. 467, 2009.
[18] VERZIU M., El HASKOURI J., BELTRAN D., AMOROS P., MACOVEI D., GHEORGHE N.G., TEODORESCU C.M., COMAN S.M., PARVULESCU V.I., Top. Catal. **53**, p. 763, 2010.
[19] PARVULESCU A.N., MORES D., STAVITSKI E., TEODORESCU C.M., BRUIJNINCX P.C.A., KLEIN GEBBINK R.J.M., WECKHUYSEN B.M., J. Amer. Chem. Soc. **132**, p. 10429, 2010.
[20] NEGOI A., WUTTKE S., KEMNITZ E., MACOVEI D., TEODORESCU C.M., PARVULESCU V.I., COMAN S.M., Angew. Chem. Intl. Ed. **49**, p. 8134, 2010.
[21] NEATU F., PROTESESCU L., FLOREA M., PARVULESCU V.I., TEODORESCU C.M., APOSTOL N., TOULLEC P.Y., MICHELET V., Green Chemistry **12**, p. 2145, 2010.
[22] TEODORESCU C.M., SOCOL G., NEGRILA C., LUCA D., MACOVEI D., J. Exper. Nanosci. **5**, p. 509, 2010.
[23] Enculescu I., Matei E., Vasilache V., Teodorescu C.M., Phys. Stat. Sol. (a) **207**, p. 2517, 2010.
[24] NEAMTU J., GEORGESCU G., MALAERU T., GHEORGHE N.G., COSTESCU R.M., JITARU I., FERRÉ J., MACOVEI D., TEODORESCU C.M., Digest J. Nanomater. Biostr. **5**, p. 873, 2010.
[25] MARDARE D., NICA V., POHOATA V., MACOVEI D., GHEORGHE N., LUCA D., TEODORESCU C.M., Thin Solid Films, *accepted*, 2010.
[26] GHEORGHE N.G., COSTESCU R.M., TEODORESCU C. M., Physica E: Low-dimensional Systems and Nanostructures, *submitted*, 2010.
[27] STAVARACHE I., LEPADATU A.M., GHEORGHE N.G., COSTESCU R.M., STAN G., MARCOV D., SLAV A., IORDACHE G., STOICA T.F., IANCU V., TEODORESCU V.S., TEODORESCU C.M., CIUREA M.L., J. Nanopart. Res. **13**, p. 231, 2011.
[28] LUNGU G.A., MACOVEI D., TEODORESCU C.M., Digest J. Nanomater. Biostr. **5**, p. 85, 2010.
[29] CERNEA M., VASILE B.S., GANEA P., RADU R., MIHALACHE V., HUSANU A., J. Amer. Ceramic Soc. **94**, p. 736, 2011.

[30] GALCA A.C., STANCU V., HUSANU M.A., DRAGOI C., GHEORGHE N.G., TRUPINA L., ENCULESCU M., VASILE E., Appl. Surf Sci., accepted 2010, doi:10.1016/j.apsusc.2011.01.056.
[31] PINTILIE I., TEODORESCU C.M., MOSCATELLI F., NIPOTI R., POGGI A., SOLMI S., LØVLIE L.S. and SVENSSON B.G., J. Appl. Phys. **108**, p. 024503, 2010.
[32] PALADE P., LUNGU G.A., HUSANU A.M., J. Alloys Compds. **505**, p. 343, 2010.
[33] TEODORESCU C., CHEVRIER F., ILAKOVAC V., HECKMANN O., LECHEVALIER L., BROCHIER R., JOHNSON R.L., and HRICOVINI K., Appl. Surf. Sci. **166**, p. 137, 2000.
[34] BRIGGS D., SEAH M.P., eds., *Practical Surface Analysis by Auger and X-ray Photoelectron Spectroscopy*, Wiley, New York, 1983.
[35] ENTA Y., SUZUKI S., KONO S., SAKAMOTO T., Phys. Rev. B **39**, p. 5524, 1989.
[36] TEODORESCU C.M., ESTEVA J.M., KARNATAK R.C., El AFIF A., Nucl. Instrum. Meth. Phys. Res. A **345**, p. 141, 1994.
[37] TEODORESCU C.M., ESTEVA J.M., KARNATAK R.C., El AFIF A., Womes M., J. Phys. B: At. Mol. Opt. Phys. **30**, p. 4293, 1997.
[38] CONNERADE J.P., LANE A.M., Rep. Prog. Phys. **51**, p. 1439, 1988.
[39] COLETTI C., FREWIN C.L., SADDOW S.E., HETZEL M., VIROJANADARA C., STARKE U., Appl. Phys. Lett. **91**, p. 061914, 2007.
[40] SIMONS J.K., DUEVEL R.V., FRIGO S.P., TAYLOR J.W., ROSENBERG R.A., J. Appl. Phys. **76**, p. 5481, 1994.
[41] MARTIN M.G., AVILA J., GRUYTERS M., TEODORESCU C., DUMAS P., CHABAL Y.J., ASENSIO M.C., Appl. Surf. Sci. **123**, 156 (1998).
[42] HÜFNER S., *Photoelectron spectroscopy. Principles and applications*, 3rd Ed.-Springer, Berlin, 2003.

Magnetic Nanoclusters Synthesized by a Novel Method of Aggregation in Ultra High Vacuum; Applications in Nanoelectronics and Nanomedicine

O. Crisan, A.D. Crisan

National Institute for Materials Physics, P.O. Box MG-7
077125 Bucharest-Magurele, Romania
E-mail: ocrisan@yahoo.com

Abstract. A novel method for producing metal clusters as building blocks for nanoscale devices is reported and its advantages for nanoelectronics and biomedical applications are highlighted. The method, which is a derivative from the wider range of techniques called the gas / cluster aggregation methods, is suitable to synthesise nano-clusters of various nature (metallic, oxides, hybrid core-shell architectures) in a wide range of sizes, from submonolayers (few hundreds of atoms clusters) to continuous thin films. More important, these clusters may be subsequently modified and functionalized *in-situ* by adding atoms/molecules of different nature, on the surface of readily formed clusters. The cluster size is extremely well controlled by the vapor pressure of the picked-up species. Moreover, the method is versatile, since it allows multiple pick-up processes within the same rare gas cluster to produce, for example, core-shell nanoparticles with metal core and non-metallic shell or vice-versa, nano-onions, with different species successively attached to the surface of the initial picked-up cluster, and so on. Initial formation of Fe gas-stabilised clusters and core-shell nanoparticles with Fe core and Fe oxide shell, as well as their structure and morphology, are presented and discussed. The core-shell nanoparticles show incipient self-organization into hexagonal cluster superlattice. Structural, magnetic and Mössbauer spectroscopy investigations have been performed on the Fe cluster samples. The magnetic properties of supported Fe clusters show marked differences compared to the bulk. A small hysteresis is observed in the parallel applied field while in the perpendicular case, lack of saturation at the highest applied field is noticed. Such behaviour has been also observed in FeRh [1] and AgCo [2] bimetallic nanoparticles. This behaviour marks the occurrence of a strong planar magnetic anisotropy in the sample and may also be a consequence of increased surface spin disorder and finite size effects, which are typical for nanoparticles in the reported size range.

Keywords: Nanoclusters, Core-shell nanoparticles, Surface-functionalization, Gas/cluster aggregation method

1. Introduction

The production and functionalization of nanometric sized materials with outstanding magnetic, optic and electronic properties has attracted a large interest

in the last years. The more and more developed methods of synthesis allow now complex architectures of nano-objects to be created. Moreover, these systems may be functionalized with molecules, free radicals, and so on, for a wide range of applications. Magnetic clusters may be produced with a strict size and shape control and may serve as templates for surface attachment of molecules for specific biomedical applications. For example, such metallic clusters may be surface-functionalized for the use in biomedical applications as DNA markers, as contrast-enhancement agents in magnetic resonance imaging or as drug delivery media [3]. The magnetic properties of such clusters are highly dependent on the size of the clusters. It has been shown [4] that such clusters are ferromagnetic for the smallest sizes: clusters with less than 30 atoms the magnetic moments are close to the atomic value, while if size is increased up to 700 atoms, the magnetic moments approach the bulk limit. Very large orbital moments were obtained for Co clusters on Pt [5], or Fe clusters on Cu [6] and Mo [7]. Also, bimetallic clusters of Co-Mn were reported to have enhanced magnetic moments compared with the bulk [8] and Co clusters embedded in Mn have been shown to exhibit exchange bias effect [9]. It is of interest to note that the magnetic properties of such systems are different if studied as free clusters or supported onto various surfaces. Different magnetic configurations resulting from the interplay of various interparticle interactions are possible, depending on a wide range of factors, from the nature, size and shape of clusters, to the nature of supporting substrate, density and volume fraction of the magnetic nano-objects and so on. It has been shown that in isolated Fe nanoparticles with strong surface anisotropy, the surface spin configuration evolves towards a throttled spin state that imposes altered magnetic properties on the whole system [10]. Also, in the case of bimetallic AgCo core-shell nanoparticles, strong non-saturation effects on the magnetization, due to the particular coronal shape of the magnetic element (Co) were observed [11]. Fe nanoclusters produced from the gas phase [12] exhibit an enhancement of both orbital and spin moments as compared to the bulk. Subsequent coating of Fe clusters with Co creates a further increase of the spin moment without significantly changing the orbital moment [12]. It has been shown [13] that depending on the volume fractions of Fe clusters, the interplay of dipolar and exchange coupling interactions create a wide range of possible magnetic configurations. These configurations range from superparamagnetism (SPM) with or without interactions, for low cluster volume fraction, up to collective blocking and correlated spin glass states, for high cluster volume fractions [13].

The cluster aggregation methods, is an extremely versatile path for producing isolated, small clusters of aggregated atoms, molecules, free radicals and so on. The principle of this method is based on producing a beam of cold rare gas in supersonic expansion. The beam is produced in the source chamber and picks-up single atoms and molecules from an evaporator in a UHV multi-chamber. The technique, developed for fundamental studies of free clusters of atoms and

molecules, that employs Ag clusters [14, 15] or liquid He droplets [16, 17], has been proven to be also effective in producing magnetic metal clusters [18]. The paper reports on the gas-stabilized free cluster aggregation method, the production of free and supported Fe clusters on mica, their structural and morphological properties as well as their correlation with the magnetic behavior of the samples.

2. Experimental

Previous studies on metal clusters have shown that the properties of the clusters are different if studied in molecular beams, or on surfaces or embedded in solid matrices. The method we present hereafter has the advantage of a very rapid pick-up process of the metal vapor by the cold rare gas supersonic beam, followed by a quick (1 ms) condensation inside the beam. For clusters deposited on surfaces and in matrices, the temperature is well known and can be easily varied; however, the substrate or matrix perturbs the clusters. Since a large fraction of the atoms are in surface states, this perturbation can dominate the desired properties.

The synthesis method of cluster aggregation implies the use of a beam of rare gas molecules (Ar), formed within a source chamber. The beam passes through a liquid nitrogen cooled nozzle, which ensures the supersonic flow of the cold rare gas in a region of low-pressure metal vapor (pick-up chamber), created by a resistive heated metal evaporator (crucible). Metal vapors are collected or picked up by the large rare gas molecules in the pick-up zone, are condensed within 1 ms, and cold metal clusters are thus formed within the gas beam. The pick-up process is governed by a Lennard-Jones interaction potential that depends on the nature of the metal vapor to be picked up by the cold rare gas cluster. This beam passes through the plates of a time-of-flight (TOF) mass spectrometer where it is investigated, and / or collected onto suitable placed substrates or grids, in order to determine *ex-situ* their structural features and other properties. The cluster size is extremely well controlled by the vapor pressure of the picked-up species, which in turn is controlled by the temperatures of the heated crucible. The method is versatile, since, by using several aligned evaporators, it allows multiple pick-up processes within the same rare gas cluster beam to produce, for example, core-shell nanoparticles or multiple shells to form nano-onions. Successive layer formation on the initial (metal) core is controlled by partial pressures of the evaporated constituents.

Schematics of the preparation facility

Fig. 1 represents the schematics of the UHV multi-chamber facility used for the production of the free Fe clusters. The first chamber of the UHV facility is the source chamber where the gas beam is formed. This chamber is cooled with liquid nitrogen, through an external shielding. In the middle, the Ar gas is purged towards

the nozzle situated at the other extremity of the chamber. The gas beam enters the pick-up chamber through the skimmer and hits the metal ions that are evaporated by the crucible. The metal vapors are picked up by the rare gas molecules from the incipient beam and are condensed. The gas beam containing the cold metal clusters is investigated in the TOF chamber.

In the specific case presented here, the sample holder, where the TEM grids and substrate for depositing the clusters, was mounted instead of the second evaporator, right in front of the metal crucible, in order to minimize the pathway of the beam and maximize the area exposed to the metal beam. The cluster beam was first investigated in the TOF spectrometer (the sample holder is firstly kept below the incipient cluster beam so as to allow the beam to reach the TOF).

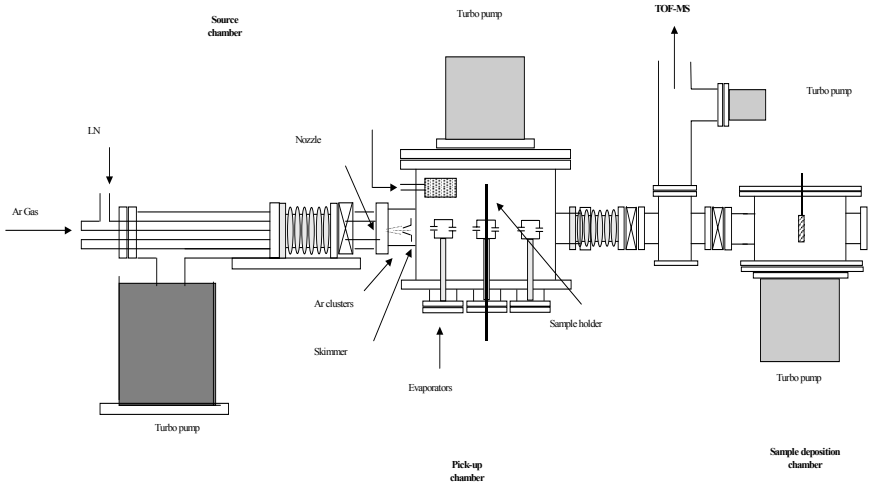

Fig. 1. Schematics of the cluster aggregation UHV multi-chamber facility

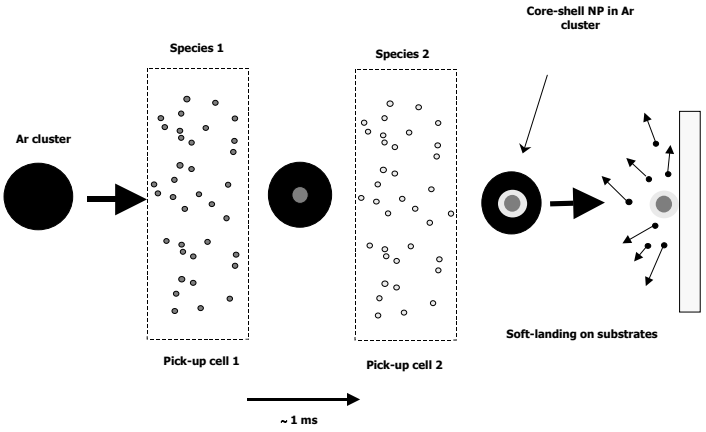

Fig. 2. Schematics of the multiple pick-up process that leads to the production of core-shell NP's.

Inside the main chamber there are several aligned evaporators. As mentioned above, this allows multiple pick-up processes, within the same rare gas beam, to produce core-shell nanoparticles. The schematics of the multiple pick-up processes that take place in the cold rare gas beam are represented in Figure 2. The supersonic beam of Ar molecules penetrates inside the first pick-up zone and loses its kinetic energy by multiple collisions with the metal vapors. These vapors are almost instantly condensed and are retained inside the Ar molecules. The size of the metal clusters is strictly controlled by the partial pressure inside the pick-up zone. Then the beam hits the second pick-up zone and the metal (or other species) vapors from the second evaporator are at their turn embedded into the rare gas molecules, either by forming core-shell nanoparticles or, depending on the degree of miscibility, bimetallic nanoparticles, or, if second species is a molecule or a ligand, a suface-functionalized nanoparticle.

Synthesis conditions and experimental characterization techniques:

The Fe clusters were synthesised as mentioned above, following the fast pick-up / condensation process inside the rare gas supersonic beam. In order to investigate thoroughly their structure and morphology, the beam was directed onto TEM grids where clusters were deposited and thermalized. The subsequent adhesion of the Fe clusters on the grid was eased by an inert gas-flow stabilization process. The synthesis method requires formation of a rare gas beam produced by expansion in a supersonic jet that passes through a conical nozzle into the ultra-high-vacuumed pick-up chamber. The parameters of the cluster beam are essentially related to the shape of the nozzle used. If the nozzle temperature and gas pressure are accurately determined, scaling laws [19,20] allow to precisely determine the size of the rare gas clusters. In our case, the conical nozzle has a throttle diameter of 300 microns and a conical aperture of 15° half-angle. The nozzle temperature was kept at 90K, by the liquid nitrogen flowing in the shielding layer of the cluster source. The input Ar gas pressure was 10^{-3} mbar. The substrates used in the first experiment were TEM copper grids (300 mesh Cu) coated by carbon film. The metal evaporator was carefully out-gassed at high temperature (but well below the melting point) for 12 h. The initial pressure inside the main pick-up chamber was between 10^{-7} and -10^{-8} mbar (depending on the evaporator temperature). Before deposition, the crucible temperature was increased and, in several experiments, varied between 1400K and 1500K so as to ensure a low metal vapor pressure between 10^{-5} and 10^{-4} mbar. The as-formed rare gas beam formed inside the source chamber is sputtered through the nozzle into the pick-up chamber where it undergoes several pick-up processes and is projected onto the TEM grids. Embedding metal atoms into the rare gas beam occur after multiple collisions with the metal vapors. At each collision with the metal atoms, part of the gas atoms from the beam evaporates and upon reaching the target (substrate) the metal cluster

is already formed, as the pick-up processes are much faster than the travel time until the beam reaches the substrate. The pick-up process is governed by the binding energy of the cluster as well as by the Lennard-Jones interaction potential between the gas atoms and picked-up species. Precise *xyz* alignment of the nozzle and implicitly of the direction of the cluster beam was performed, and the nozzle-crucible distance was optimized by measuring the intensities in TOF spectra given by the gas beam, prior to the deposition process. The exposure time for the TEM grids was 5 minutes and the Fe clusters formation of was observed, stabilized on the grids by the subsequent long-time low-pressure rare gas flow. The experimental techniques that we used for structural characterization of the as-obtained samples were:

- Time-of-Flight (TOF) mass spectrometer: as an in-situ rare gas and metal clusters analyser;
- Transmission electron microscopy (TEM): - JEOL 2100 microscope, 2kV acceleration potential, in bright field and high-resolution modes;
- Electron diffraction patterns (EDP): Fourier transforms (reciprocal space map) of TEM images, to identify the crystal symmetry;
- Energy dispersion spectroscopy (EDS): to obtain chemical quantitative analysis of samples;
- Atomic force microscopy: to investigate the topography and morphology of cluster arrangements

3. Results and Discussion

Occurrence of Fe clusters inside the rare gas beam. TOF mass spectrometry

Fig. 3 depicts the TOF mass spectra obtained when only the supersonic Ar gas beam (left) passes through the TOF plates, compared to the one where the metal clusters are condensed and embedded within the original supersonic gas beam. The TOF spectra show the formation of Ar clusters in the beam that passes through the cooled nozzle. Nevertheless, the intensities of the harmonics depicting the formation of gas clusters up to the 14th order are not so high, compared with the gas pressure input into the main chamber.

The conclusion is that the supersonic beam is mostly formed by Ar molecules, with a small fraction of Ar clusters, therefore the pick-up process that allows production of metal clusters is in fact a mixture of gas aggregation and cluster aggregation principles. The right graph depicts the TOF spectrum collected for the gas + metal clusters when the metal evaporator is set at 900K (or 10^{-5} mbar metal vapor pressure). When the gas beam contains also the cold Fe clusters, these Fe clusters are harder to identify in the TOF spectra, mainly due to the high noise level arising from multiple scattering processes inside the TOF, as the partial vapor

pressure is quite high for the TOF measurements. Nevertheless, the peak corresponding to the Fe atomic mass (near 56 atomic mass units) can be seen in the right TOF spectrum. The TOF measurements confirmed that indeed the desired metal clusters are formed inside the rare gas molecular beam.

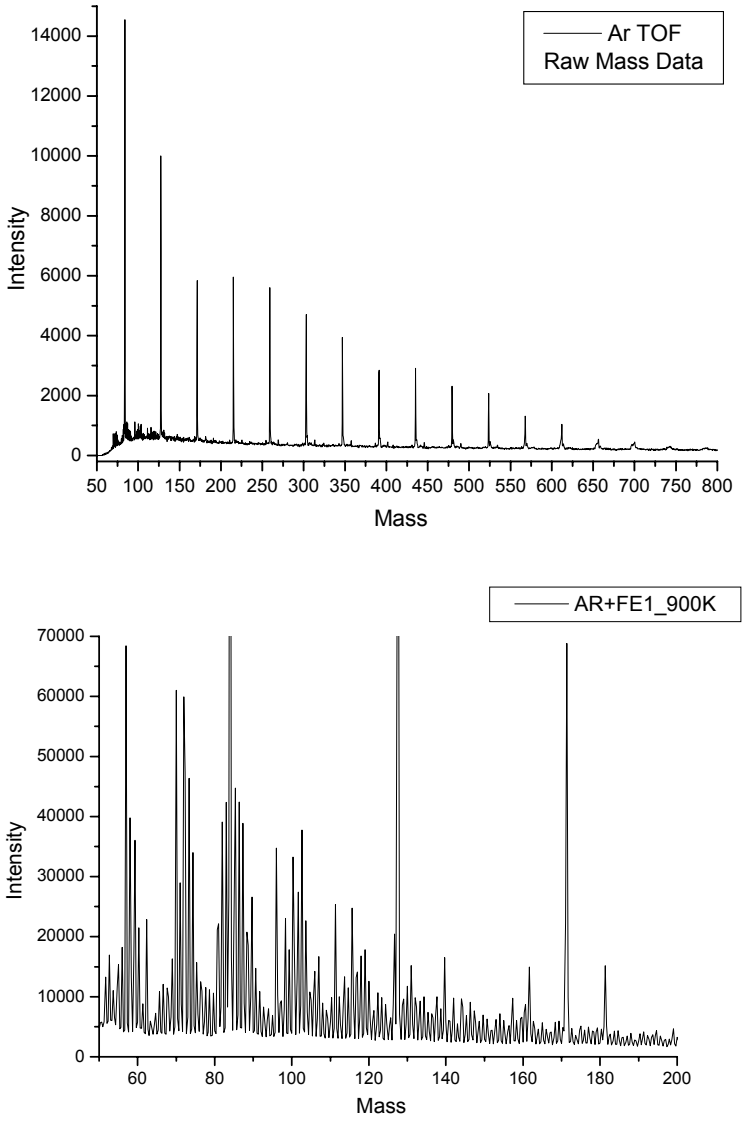

Fig. 3. Time-of-flight mass spectra of the Ar molecular gas beam (top) and the molecular gas beam after picking up the Fe clusters (bottom) evaporated at 900K (10^{-5} mbar).

Structure of Fe clusters on TEM Cu grids

The influence of the metal vapor pressure onto the structure and morphology of the Fe clusters deposited in the above-described UHV facility onto TEM grids, has been largely described elsewhere [22]. Three different deposition experiments with the same exposure time for the grid, but with different partial metal vapor pressures have been performed. The pressure was established by controlling the evaporator temperature. A well-known charted proportional relationship exists between the crucible temperature and the resulted metal vapor pressure [19]. For example, the temperature of 1400K of the metal evaporator corresponds to a metal vapor pressure of 10^{-5} mbar. In the TEM images [25] the as-deposited Fe aggregates are mostly spherical with sizes that increase when the metal vapor pressure increases. No apparent ordering is observed.

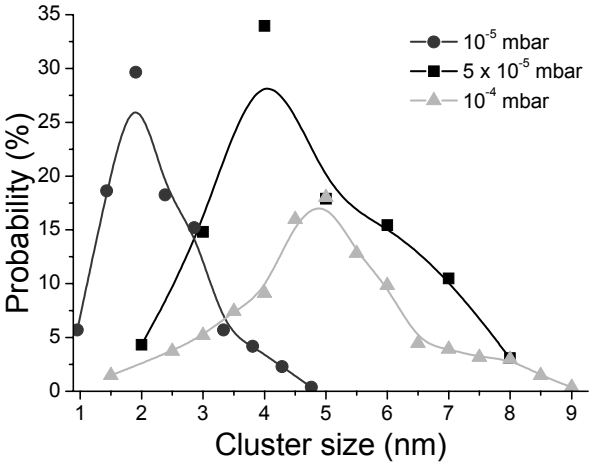

Fig. 4a. The cluster size distributions for samples sputtered at various metal vapor pressures.

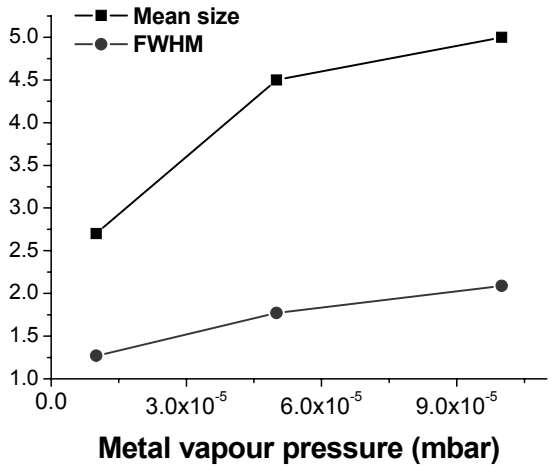

Fig. 4b: The average size obtained by the histographic technique and the width of the log - normal distributions obtained after numerical fittings.

These observations have now been made quantitative. A large number of images have been studied and, using a histographic method, the size distribution for all 3 samples has been derived. The size distributions are plotted in Fig. 4 (a). Average sizes obtained for the Fe clusters were 2.7, 4.5 and 5.1 nm for vapor pressures of 10^{-5}, 5 x 10^{-5} and 10^{-4} mbar respectively. The cluster size distributions approximately obey a log-normal profile law. The average size as well as the full-width-at-half-maximum (FWHM) of the log-normal distributions obtained after numerical fittings is plotted in Figure 4 (b). It can be seen that the size distribution of the obtained Fe clusters are shifted towards larger cluster sizes as the metal vapor pressure increases. Distributions are also larger as the metal vapor pressure increases, as both the average particle size and width of the distribution increases with the vapor pressure. With further increase of the vapor pressure, distributions seem to exhibit tendency towards a bimodal character. It is expected that higher densities and volume fractions (higher exposure times) will lead to cluster aggregation and change of crystal symmetry.

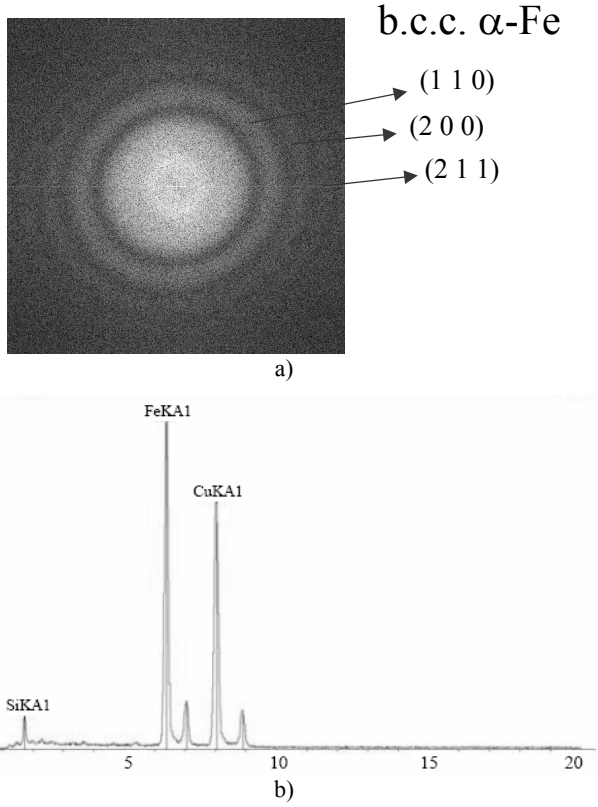

Fig. 5a. Electron diffraction pattern of the Fe clusters showing 3 Bragg reflections of the b.c.c. α-Fe phase symmetry. b. Energy dispersion spectrum of Fe clusters on Cu grid, obtained under a metal vapor pressure of 10^{-4} mbar inside the pick-up chamber.

It is also worthwhile mentioning that in the electron diffraction (EDP) patterns of all samples, recorded during TEM imaging and presented in the Fig. 5a, we have unambiguously identified the diffraction rings corresponding to (1 1 0), (2 0 0) and (2 1 1) Bragg reflections of the body-centred-cubic α-Fe. It seems that the deposited Fe clusters have a cubic symmetry whatever the metal vapor pressure during the deposition, at least up to 10^{-4} mbar. As mentioned above, it is expected that higher metal vapor pressures and / or exposure times (with impact on the effective volume fraction of the film) would lead to changes in the structural symmetry of the Fe clusters. Also, during TEM imaging, energy dispersion X-ray spectroscopy (EDX) was undertaken in order to check the chemical elemental composition of the grids. An example of such spectra is plotted in Fig. 5b. It has been observed that only Fe $K\alpha_1$ and Cu $K\alpha_1$ peaks appear in the spectra. At this point, no oxidation was observable through the chemical analysis of the Fe clusters on the TEM grids.

Structure of core-shell Fe / Fe oxide nanoclusters

The Fe/Fe oxide core-shell nanoparticles were also produced in a very simple way, by allowing the Fe containing rare gas molecular supersonic beam to enter a region with controlled partial pressure of oxygen. In the way described earlier, with successive pick-up processes, we expected to see a core-shell structure where the Fe core is surrounded by a Fe oxide layer of uniform size. That was indeed the case, as it is shown in the bright field TEM image of these Fe/Fe oxide clusters. In Figure 5 it is shown a TEM image of the core-shell Fe/Fe oxide nanoparticles, formed by the gas-stabilization method. In this image, and also in the following ones, one can observe the occurrence of multiple-faceted core-shell NP's of a white core and a dark shell, with a somehow regular coronal thickness, as intended. It is clear that in the first step, of metal vapor condensation, inside or on the surface of the rare gas molecule, a spherical metal cluster is formed. Afterwards, the metal oxide surrounding the metal core is grown as a complete covering coronal layer onto the metal core surface, simply by allowing controlled pressure of oxygen to enter the UHV pick-up region. The oxygen pressure was 1.1×10^{-3} mbar. The TEM grid was subjected to the oxygen pressure for about 1 hour, time long enough to grow a continuous oxide layer around the metal core, and then the oxygen flux was switched off. A beginning of an ordering seems to occur as in the highlighted part of the image. Hexagonal "crystals" of Fe clusters self-organized into what looks like an icosahedral-type superlattice. It seems that during the oxidation process, a stable (minimum energy) configuration is achieved, and the core-shell clusters commence to self-organize. This phenomenon has been observed to occur in Ag-Au bimetallic nanoclusters [23] and the array formed, of an icosahedral symmetry, has been named as "cluster of clusters". The phenomenon, explained by the balance between kinetic energy of the incoming clusters hitting the substrate and

the thermal energy gained by the evaporation of the gaseous carrier (the rare gas cluster) allow a commencement of the self-organization process into a quasi-regular array of icosahedral symmetry. Nevertheless, the energy gained via the stabilization process is not enough to allow periodic arrangement onto larger arrays, as it is the case during the stabilization of chemically obtained nanoparticles during the colloidal crystallization from solution [11,24], that allows the observation of large periodic arrays of monodispersed nanoparticles, practically onto the whole area of the substrate. However, the purpose of the experiment, i.e. the production of core-shell nanoparticles with metal core and continuous, uniformly thick shell of metal oxide, has been accomplished.

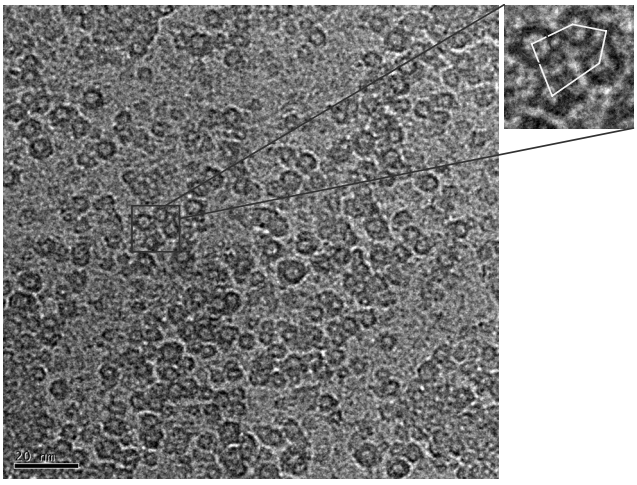

Fig. 6. TEM image of an assembly of Fe / Fe oxide dispersed nanoparticles. Inset: formation of icosahedral- type superlattice, taken from [25].

In order to provide more complete morpho-structural characterization of the core-shell clusters, we have performed atomic force microscopy using an Omicron instrument in high vacuum. The grids were mounted on stainless steel holder and a cantilever with Si tip was used for scanning the grid surface. An AFM image recorded during the experiment together with a cross section line profile is shown in Fig. 7.

The atomic force microscopy image shows columnar-like growth of aggregates of sizes compatible with TEM observations. Their intrinsic features are hidden by the averaging of the atomic potential, developed by the cantilever tip, over the surface. The height of the cluster aggregates observed in the image is about 10 nm, a value comparable with the cluster sizes obtained from TEM, taking into account also the tip-surface interaction that gives slightly higher topographical features. A 4 nm periodicity is observed in the line profile of the Fe clusters (Figure 7b), which again, is comparable to the average cluster size observed in TEM.

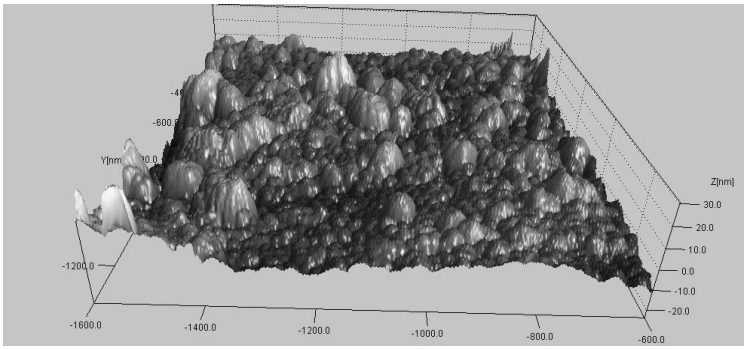

a)

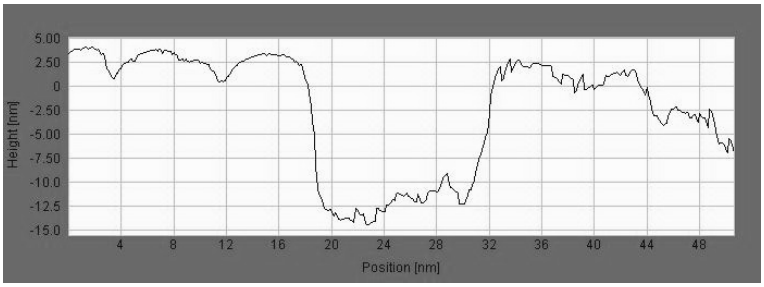

b)

Fig. 7. Atomic force microscopy of core-shell nanoparticles (a) and cross - section line profile of the imaged topography (b).

This first experiment to produce core-shell clusters in our cluster aggregation UHV facility opens wide perspectives into production of several types of core-shell clusters and other nano-architectures including, for example cores with multiple shells. These surface shells may be furthermore surface-functionalized for example, by attaching molecules, ligands, proteins, receptors, for a huge number of biomedical applications, but also for other kind of technological applications such as catalysis or nanosensors. One of the envisaged future applications is formation of high anisotropic – high magnetic moment core surrounded by Au layer coating, and attachment onto this coating of various biological proteins as DNA markers or tumor markers such as aptamers or folic acid [3].

Structure of the Fe clusters supported on mica substrate

In order to further investigate other macroscopic properties, samples of Fe clusters were also deposited onto mica substrate. In this experiment, instead of TEM grids, pure muscovite clean sheets were mounted onto the holder. Metal vapor pressure was fixed at 10^{-4} mbar with a crucible temperature of 1500K. Due to the fact that, for other types of measurements, such as Mossbauer or magnetism,

larger amounts of Fe clusters are necessary in order to observe a noticeable effect, we have chosen to increase the exposure time up to 30 minutes. The structure of the as-obtained Fe clusters on mica was examined *ex-situ* by powder X-ray diffraction using Cu Kα radiation (wavelength: λ=1.54Å). A well-resolved spectrum with sharp Bragg peaks is obtained, as seen in Figure 8. It may be noticed that a very strong contribution to the XRD spectrum arises from the mica substrate. This is an expected effect since the mass of the mica substrate is much lager than the amount of supported Fe clusters.

As depicted in the Figure 8, the Bragg reflections attributed to the $2M_1$ phase structure of mica (muscovite) are indexed. In spite of that, we have been able to identify the contribution from the supported Fe clusters, too. The diffraction peaks arising from the (1 1 0), (2 0 0) and (2 1 1) Bragg reflections of the body-centred-cubic α-Fe structure are also observed and correctly indexed. These results are in agreement with TEM observations of free Fe clusters, synthesised at a much lower exposure time (5 min compared to 30 min). The two measurements may thus be correlated in spite of the exposure time difference since no change in crystal symmetry is observed, compared to the free Fe clusters.

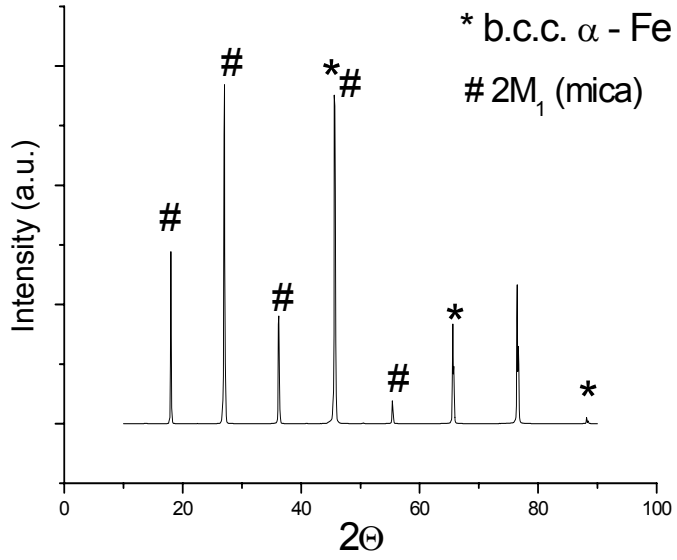

Fig. 8. X-ray diffraction spectrum of the supported Fe clusters on mica.

Mössbauer data on supported Fe clusters on mica

One of the reasons for choosing mica as the substrate for the supported Fe clusters was its transparency to the γ-rays, so that the sample could be investigated by Mössbauer spectroscopy. The Mössbauer spectrum recorded at room temperature in transmission geometry is presented in Fig. 9.

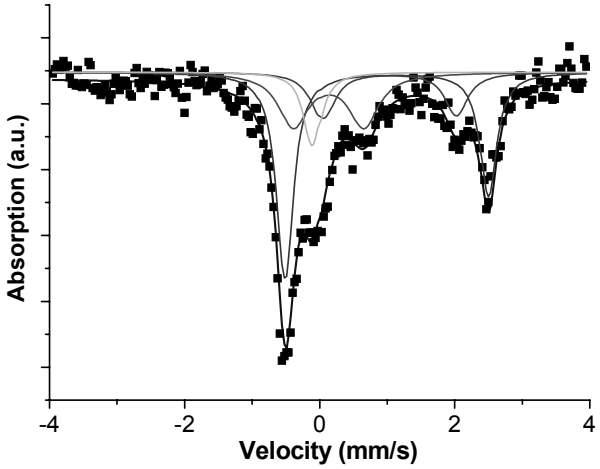

Fig. 9. Mössbauer spectrum of Fe clusters supported on mica.

We first noticed that the supported Fe clusters are not ferromagnetic at room temperature, since there was no magnetic Zeeman splitting of the Mössbauer spectrum. This is an expected effect since the volume fraction is not so large, even at 30 minutes time of exposure to the cluster beam. As the metal vapor pressure was kept at a relatively low value (10^{-4} mbar) the deposition rate was low. Four different contributions were revealed from the fitting of the Mössbauer spectrum. Two doublets with high quadrupole splitting were fitted to the experimental spectrum and attributed to the octahedral Fe^{2+} cis and trans sites of the $2M_1$ structure of mica. Another doublet with lower quadrupole splitting has been attributed to the octahedral Fe^{3+}. This assignation is in agreement with previously reported site population of the Fe-muscovite from Mössbauer data [26]. The singlet in the central part of the spectrum, having an isomer shift value close to 0, is attributed to the superparamagnetic metallic Fe clusters having a b.c.c. structure. The Fe clusters contribution observed in the Mössbauer spectrum has an abundance of 10%. These results are in agreement with TEM observations of free Fe clusters and XRD structural data. From Mössbauer data it seems that the clusters behave as an assembly of non-interacting superparamagnets. All the hyperfine parameters obtained from the Mössbauer spectrum fitting are presented in Table 1.

Table 1. Hyperfine parameters of the Mössbauer spectrum of Fe film on mica.

	Isomer shift (mm/s)	Quadrupole splitting (mm/s)	Relative area (%)
I: $2M_1$ octahedral Fe^{2+} cis	1.12	2.98	46
II: $2M_1$ octahedral Fe^{2+} trans	1.16	1.96	17
III: $2M_1$ octahedral Fe^{3+}	0.26	1.01	27
IV: SPM metallic Fe (b.c.c.)	0.03	0.00	10

Magnetic properties

The room temperature hysteresis loops for supported Fe clusters on mica were measured in a vibrating sample magnetometer at an applied field of up to 0.8 Tesla, both parallel and perpendicular to the substrate plane. As it is well known, bulk Fe in the b.c.c. crystalline symmetry is magnetically soft with virtually no hysteresis, and high saturation magnetization. As it can be seen in the two hysteresis loops, plotted in Figure 10, a quite different behavior from the bulk is obtained.

The hysteresis loop recorded parallel to the substrate plane exhibits interesting magnetic behavior. In the case of the parallel loop, a significant coercivity is obtained (270 Oe). This feature is more encountered in harder ferromagnets. This confirms once again that in the case of low-dimensional magnetic systems, different properties and magnetic features are obtained, compared with their bulk counterpart. The occurrence of the coercivity in our sample is a sign of a strong planar magnetic anisotropy that makes magnetic moments harder to reverse during the applied field switching.

This strong planar anisotropy is proven also by the perpendicular-to-plane loop that shows completely different feature than the parallel loop (much slower approach to saturation). Such behavior is due to the interplay between various competing inter-cluster interactions, as well as to the enhanced surface contribution arising from the high fraction of atoms that are in surface states. The effective anisotropy constant may be estimated from the ratio between the area encompassed by the two hysteresis loops, following the Cullen & Callen [21] approach for cubic ferromagnets.

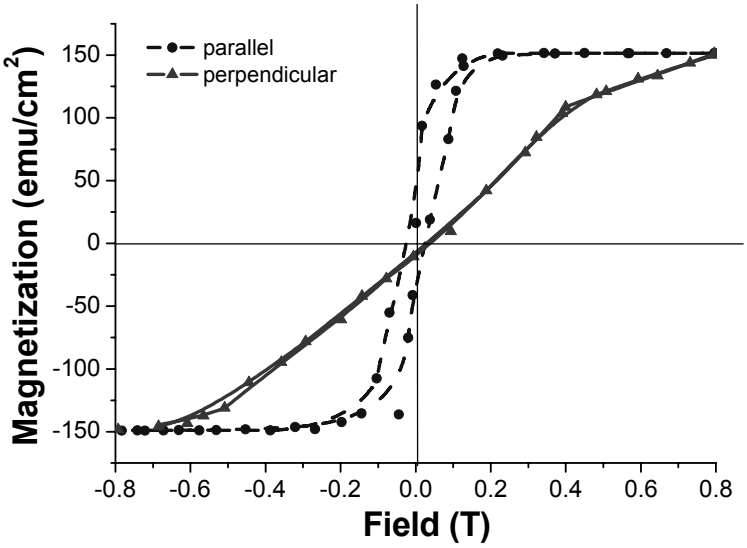

Fig. 10. Room temperature hysteresis loops with applied field parallel and perpendicular to the sample plane, for supported Fe clusters on mica.

4. Conclusions

A novel gas-stabilized cluster aggregation method was presented together with the schematics of the UHV multi-chamber facility and the principle of pick-up processes that allows creation of supersonic molecular gas beam that is subsequently used for pick-up and condensation of very fine metal clusters. Using such a method, we have been able to produce free and supported Fe clusters, core-shell Fe / Fe oxide clusters with controlled sizes. Moreover, their morpho-structural properties are thoroughly investigated.

We have proven that the cluster size is readily controlled by the metal vapor pressure inside the pick-up chamber. In its turn, this parameter is controlled by the evaporator temperature of the picked-up species (in our case the metallic Fe). By using detailed transmission electron microscopy, we showed that when the metal vapor pressure ranges between 10^{-5} and 10^{-4} mbar, the obtained Fe clusters have average cluster sizes between 2.7 and 5 nm. Electron diffraction patterns showed that the crystal symmetry is of a body-centred-cubic type and atomic force microscopy scans allow to determine that the growth mode of the Fe clusters onto the Cu grids is columnar with revealed aggregates of 10 nm size.

Using a simple method of oxidation by allowing the Fe containing molecular supersonic beam to enter a region with controlled partial pressure of oxygen, we succeeded to produce core-shell nanoparticles with metal core and continuous, uniformly thick, shell of metal oxide. These Fe / Fe oxide core-shell clusters achieve by self-organization a complex superlattice (icosahedral-type) structure, by forming multiple faceted hexagonal nanoparticles.

Supported Fe clusters on mica have the crystal structure of body-centred-cubic metallic Fe, and are superparamagnetic at room temperature, as has been revealed by X-ray diffraction and Mossbauer spectroscopy. The magnetic measurements have revealed that Fe clusters on mica exhibit pronounced coercivity, due to strong planar magnetic anisotropy exerted in the substrate plane, anisotropy induced during the deposition process.

The possibility to produce core-shell clusters using the gas-stabilised cluster aggregation UHV facility opens wide perspectives into production of several types of core-shell clusters and other nano-architectures including, for example cores with multiple shells. The extreme versatility of the method allows almost any kind of material, solids or even molecules, to be evaporated and attached to a solid core. By using multiple pick-up processes, these surface shells may be furthermore surface-functionalized for example, by attaching molecules, ligands, proteins, receptors, for a large number of biomedical applications, but also for other kind of technological applications such as: catalysis or nanosensors. The facility may as well be useful in template-assisted growth of nanoparticles to produce, for example, metal-coated complex molecules, or for synthesis of other unusual core-shell structures. For example, hydrogen-filled hollow spheres with metallic shells

have obvious technological applicability and may have huge impact as an effective hydrogen storage material.

Acknowledgements. Part of the work has been performed by O.C. at the Department of Physics, University of Leicester, UK. The financial support by the Romanian Ministry of Research under the research project PNCDI II 12-129 / 2008 is gratefully acknowledged.

References

[1] ZITOUN D., RESPAUD M., FROMEN M.C., CASANOVE M.J., LECANTE P., AMIENS C., CHAUDRET B., Phys. Rev. Lett. **89**, pp. 037203-1, 2002.

[2] CRISAN O., ANGELAKERIS M., NOGUÈS M., PAPAIOANNOU E., FLEVARIS N.K., KOMNINOU PH., KEHAGIAS TH., SOBAL N., GIERSIG M., MAGN J., Magn. Mater. **272-276,** pp. e1253-e1254, 2004.

[3] For a review of magnetic nanoparticles applications in medicine, please see: Wilfried Andrä and Hannes Nowak (Eds.) "Magnetism in Medicine: A Handbook", Wiley-VCH Interscience 2006, New York, and references therein

[4] BILLAS I.M.L., CHATELAIN A., HEER de W.A., Science **265,** p. 1682, 1994.

[5] GAMBARDELLA P., RUSPONI S., VERONESE M., DHESI S.S., GRAZIOLI C., DALLMEYER A., CABRIA I., ZELLER R., DEDERICHS P.H., KERN K., CARBONE C., BRUNE H., Science **300**, p. 1130, 2003.

[6] BOEGLIN C., STANESCU S., DEVILLE J.P., OHRESSER P., BROOKES N.B., Phys. Rev. B **66**, p. 014439, 2002.

[7] BODE M., PIETZSCH O., KUBETZKA A., WIESENDANGER R., Phys. Rev. Lett. **92**, p. 67201, 2004.

[8] KNICKELBEIN M.B., Phys. Rev. Lett. **86**, p. 5255, 2001.

[9] DOMINGO N., TESTA A.M., FIORANI D., BINNS C., BAKER S., TEJADA J., MAGN J., Magn. Mater.**316**, p. 155, 2007.

[10] LABAYE Y., CRISAN O., BERGER L., GRENECHE J.M., COEY J.M.D., J. Appl. Phys. **91**, p. 8715, 2002.

[11] CRISAN O., ANGELAKERIS M., KEHAGIAS TH., SIMEONIDIS K., GIERSIG M., FLEVARIS N.K., Acta Materialia **54**, p. 5251, 2006.

[12] BINNS C., BAKER S.H., LOUCH S., SIROTTI F., CRUGUEL H., PRIETO P., THORNTON S.C., BELLIER J.D., Applied Surface Science **226**, p. 249, 2004.

[13] BINNS C., MAHER M.J., PANKHURST Q.A., KECHRAKOS D., TROHIDOU K.N., Phys. Rev. B **66**, pp. 184413, 2002.

[14] RUTZEN M., KAKAR S., RIENECKER C., PIETROWSKI VON R., MÖLLER T., Z. Phys. D. **38**, p. 89, 1996.

[15] LINDBLAD A., BERGERSEN H., RANDER T., LUNDWALL M., ÖHRWALL G., TCHAPLYGUINE M., SVENSSON S., BJÖRNEHOLM O., Phys. Chem. Chem. Phys. **8**, p. 1899, 2006.

[16] YANG S., BRERETON S., WHEELER M., ELLIS A., MATTER S., Phys. Chem. Chem. Phys. **7**, p. 4082, 2005.

[17] YANG S., BRERETON S., ELLIS A., Int. J. Mass Spectrom. **253**, p. 79, 2006.

[18] IEVLEV D., RABIN I., SCHULZE W., ERTL G., Eur. Phys. J. D **16**, p. 157, 2001.

[19] HAGENA O.F., Z. Phys. D **4**, p. 291, 1987.

[20] BUCK U., KROHNE R., J. Chem. Phys. **105**, p. 5408, 1996.

[21] CULLEN J., CALLEN E., Phys. Rev. B **30**, p. 181, 1984.

[22] CRISAN O., HAEFTEN VON K., ELLIS A.M., BINNS C., Nanotechnology **19**, p. 505602, 2008.
[23] TEO B.K., ZHANG H., Proc. Nat. Acad. Sci. **88**, p. 5067, 1991.
[24] SUN S., MURRAY C.B., WELLER D., FOLKS L., MOSER A., Science **287**, p. 1989, 2000.
[25] CRISAN O., HAEFTEN VON K., ELLIS A.M., BINNS C., J. Nanopart. Res.**10**(1), p. 193, 2008.
[26] SHABANI A.A.T., RANCOURT D.G., LALONDE A.E., Hyp. Int. **117**, p. 117, 1998.